TECHNISCHE UNIVERSITÄT MÜNCHEN

Fakultät für Chemie

Lehrstuhl für Technische Elektrochemie

Understanding Degradation Mechanisms of Lithium- and Manganese-Rich Layered Oxide Cathodes for Lithium-Ion Batteries

Tobias Maximilian Teufl

Vollständiger Abdruck der von der Fakultät für Chemie der Technischen Universität München zur Erlangung des akademischen Grades eines

Doktors der Naturwissenschaften (Dr. rer. nat.)

genehmigten Dissertation.

Vorsitzender:	Prof. Dr. Lukas Hintermann
Prüfer der Dissertation:	1. Prof. Dr. Hubert A. Gasteiger
	2. Prof. Dr. Tom Nilges

Diese Dissertation wurde am 12.06.2019 bei der Technischen Universität München eingereicht und durch die Fakultät für Chemie am 15.07.2019 angenommen.

„Nichts ist mächtiger als eine Idee, deren Zeit gekommen ist.“

Victor Hugo (1802 – 1885)

Abstract

In order to enable future electromobility, new cathode materials for lithium-ion batteries need to be developed to both, decrease cost and increase energy density. Li- and Mn-rich layered-oxide cathode active materials (CAMs) are considered as a promising class of future cathode materials, while their performance still suffers from serious issues. The scope of this thesis is to understand not only the degradation mechanisms on a materials level, but also to delimitate the challenges for the overall cell chemistry. The main technique used in this study is on-line electrochemical mass spectrometry (OEMS), in conjunction with several electrochemical techniques, such as charge/discharge cycling and impedance spectroscopy. As a first step, the electrochemical properties of the material are investigated in detail and the oxygen release from layered-oxide CAMs during the initial cycles is carefully quantified. Furthermore, the failure mechanisms that govern the full-cell cycling performance of these materials at room temperature and at elevated temperature are analyzed. In the end, we show a potential path how oxygen release can be mitigated for layered-oxides by washing a Ni-rich layered cathode active material in an aqueous solution.

Kurzfassung

Um Elektromobilität in Zukunft nachhaltig zu gestalten, müssen neue Kathodenmaterialien für Lithium-Ionen-Batterien entwickelt werden, welche kostengünstig sind und gleichzeitig eine Erhöhung der Energiedichte ermöglichen. Li- und Mn-reiche Schichtoxide gelten als vielversprechende Strukturklasse für zukünftige Kathodenmaterialien, weisen jedoch noch Unzulänglichkeiten in der praktischen Anwendung auf. Das Ziel dieser Arbeit ist es nicht nur die Degradationsmechanismen auf Materialebene zu verstehen, sondern auch die Herausforderungen für die gesamte Zellchemie. Hierzu wird einerseits „on-line electrochemical mass spectrometry“ (OEMS) verwendet, als auch verschiedene elektrochemische Analysetechniken, wie zum Beispiel Lade-/Entladezyklentests und Impedanzspektroskopie. Zuerst werden die elektrochemischen Materialeigenschaften untersucht und die Sauerstofffreisetzung während der ersten Zyklen quantifiziert. Darüber hinaus werden die Probleme der Lebensdauer auf Zellebene sowohl bei Raumtemperatur, als auch bei erhöhter Temperatur analysiert. Außerdem wird ein möglicher Weg aufgezeigt wie die Sauerstoffabgabe von Schichtoxiden verhindert werden kann, nämlich durch Waschen dieser Materialien in wässriger Lösung, was anhand eines Ni-reichen Kathodenmaterials gezeigt wird.

Contents

List of Acronyms

ASR	area specific resistance
BET	Brunauer-Emmett Teller
(B)EV	(battery) electric vehicle
CAM	cathode active material
CC	constant current
CEI	cathode electrolyte interface
CV	constant voltage
DCIR	direct current internal resistance
DEC	diethyl carbonate
DEMS	differential electrochemical mass spectrometry
DoE	U.S. Department of Energy
EC	ethylene carbonate
EIS	electrochemical impedance spectroscopy
FEC	fluoroethylene carbonate
FFT	fast Fourier transform
GC	gas chromatography
GEIS	galvanostatic electrochemical impedance spectroscopy
GITT	galvanostatic intermittent titration technique
GWRE	gold-wire reference electrode
HE-NCM	high-energy lithium nickel cobalt manganese oxide ($Li_{1+x}Ni_aCo_bMn_cO_2$; a+b+c = 1)
HFR	high frequency resistance
(HR)TEM	(high-resolution) transmission electron microscopy
HVS/LNMO	high-voltage spinel ($LiNi_{0.5}Mn_{1.5}O_2$)
ICP	inductively coupled plasma
LCO	lithium cobalt oxide ($LiCoO_2$)
LNO	lithium nickel oxide ($LiNiO_2$)
MS	mass spectrometry

NCA	lithium nickel cobalt aluminum oxide ($LiNi_aCo_bAl_cO_2$; a+b+c = 1)
NCM	lithium nickel cobalt manganese oxide ($LiNi_aCo_bMn_cO_2$; a+b+c = 1)
NMR	nuclear magnetic resonance
OEMS	on-line electrochemical mass spectrometry
OCV	open circuit voltage
PEIS	potentiostatic electrochemical impedance spectroscopy
PITT	potentiostatic intermittent titration technique
SEI	solid-electrolyte-interface
SHE	standard hydrogen electrode
SLP	single-layer pouch cell
SOC	state-of-charge
TGA	thermogravimetric analysis
TM	transition metal
VC	vinylene carbonate
XPS	x-ray photoelectron spectroscopy
XRD	x-ray diffraction

1. Introduction

More than 100 years ago, Henry Ford and Thomas Edison were already enthusiastic about the idea of electric vehicles for mass production, that time based on nickel-iron batteries.[1, 2] However, the driving range and the weight of these early electric vehicles was not competitive, leading to a triumph of internal combustion engines, while electric vehicles nearly completely disappeared from the market.[1] Since those times, many batteries based on different cell chemistries have been evaluated, starting from lead-acid and nickel-iron systems, leading to the investigation of more recent nickel-metal-hydride batteries, and finally ending up with state-of-the-art lithium-ion batteries.[2] Due to its low molecular weight, the small ionic radius and its low potential (-3.04 V vs. SHE), lithium was proven to be one of the best elements for designing secondary batteries with a high energy density and reasonable reversibility.[3] Early work on rechargeable lithium-ion batteries was carried out by M. Stanley Whittingham and John B. Goodenough. In 1976, Whittingham presented a Li//TiS_2 cell that could be reversibly charged and discharged under realistic conditions, obtaining a cell voltage of ≈2.2 V vs. Li^+/Li;[4-6] with $LiPF_6$ dissolved in propylene-carbonate as electrolyte,[4] which makes these cells already quite similar to modern lithium-ion battery cells. In order to increase the energy density of the positive electrode, Goodenough's group investigated the so called "layered-oxides", having the sum formula $LiMO_2$ (M = Cr, Co, Ni),[5] whereas especially $LiCoO_2$ showed good structural stability during reversible lithium insertion and extraction at rather high voltages of >4.0 V vs. Li^+/Li.[7] While $LiCoO_2$ was proven to be a very good positive electrode material, the search for a suitable negative electrode material for lithium-based batteries was obviously much more complicated.[8] At the beginning, simply lithium metal was suggested as negative electrode, showing high energy densities due to its low potential and its high gravimetric capacity.[3, 8] In the late 1980s, Moli Energy commercialized the first cells based on a MoS_2 positive electrode and on lithium metal as negative electrode.[2] However, dendritic growth of lithium on the negative electrode led to short-circuits and finally to explosions of the cells, leading to a dramatic backlash of lithium-based battery technologies.[9] After intensive ongoing research for alternative negative electrode materials and pioneering work carried out by Nishi et al.[10] and Dahn et al.[11], Sony

achieved the breakthrough using graphite as negative electrode.[12] Consequently, Sony could commercialize graphite//$LiCoO_2$ cells with organic carbonate electrolytes for consumer electronics in 1991.[13] While lithium-ion batteries, mainly based on $LiCoO_2$ and graphite, have been used for more than 20 years in portable consumer electronics,[8] the requirements for the application of lithium-ion batteries in electric vehicle (EV) applications have changed drastically.[14]

Motivated by the seeking to reduce consumption of fossil fuels and to reduce emissions of CO_2 and other greenhouse gases, causing air pollution and global warming, the interest in electrical energy storage for power grid and automotive applications rapidly grew during the last years.[14-16] In order to make battery electric vehicles (BEV) commercially successful for mass production, the driving range has to be improved significantly while lowering the cost at the same time.[17] Recently, the Tesla Model 3, a mid-price state-of-the-art electric vehicle, has entered the market. The currently available battery option for the Model 3, with a battery energy of ≈60 kWh, offers a driving range of ≈415 km at a prize starting from 44.500 €.[18] Furthermore, the latest version of the BMW i3 has a battery size of ≈40 kWh, resulting in a maximum driving range of ≈360 km under optimum conditions, and at a cost of 38.000 €.[19] This shows that reasonable driving ranges are already achievable for mid-priced EVs; however, EVs have not yet reached mass market penetration. According to the long-term goals of the US Department of Energy, a driving range of 480 km (300 miles) needs to be exceeded at acceptable cost in order to make electrified cars competitive with combustion engines for the mass market.[17] In order to achieve a driving range of >480 km, it is predicted that the energy density needs to be improved to about 250 Wh/kg on battery pack level.[17] Furthermore, also the cost of the battery pack is critical and needs to be decreased to achieve high driving ranges also for lower priced EVs.[20] Targeting a battery cost of 125 $/kWh until 2025 seems to be a realistic and feasible goal and would enable sufficient driving ranges at acceptable cost; this may be compared to a battery cost of 250 $/kWh in 2015.[17, 20, 21] With the target of 125$/kWh, the cost of a battery cell with a nominal energy of 40 kWh, as used in the current BMW i3, would decrease to an absolute cost of 5.000 $, which would make lithium-ion battery technology also attractive for entry-level vehicles.

In order to both increase the energy density and decrease the cost of lithium-ion batteries, especially the development of new cathode active materials is a key challenge.[14] On the one hand, current cathode active materials have a rather limited capacity and on the other hand, they contain expensive transition metals that are a significant cost driver of current lithium-ion batteries. Amongst these transition metals, cobalt is the most crucial one, as the high cobalt price (≈34 $/kg) leads to high raw material cost for Li-ion batteries.[22] Furthermore, cobalt is also critical from an ethical point of view, due to non-sustainable mining conditions and artisanal mining in the Democratic Republic of Congo.[23] For these reasons, one of the current development trends focuses on the development of nickel-rich cathode active materials with a limited cobalt content. These nickel-rich layered oxides ($LiMO_2$; M = Co, Ni, Mn), also referred to as NCMs, cannot only lower the cost by reduction of the cobalt content, but can also increase the energy density of the cell due to higher capacities at similar upper cutoff potentials. However, these nickel-rich materials still suffer from several technical hurdles that need to be mitigated in order to commercialize them. One of the most serious issue of these materials are safety concerns, caused by their structural instability in their delithiated state that can lead to heat release and ultimately to a thermal runaway of the battery cell.[24-26] While the nickel raw metal price (≈12 $/kg) is already a factor of 3 lower compared to cobalt (≈34 $/kg), manganese-based cathode materials could further decrease the cathode cost due to the low manganese metal cost (≈2 $/kg). Therefore, another focus in battery R&D is the development of Li- and Mn-rich NCM materials which are an attractive option for future battery applications, because of their low metal cost and their high reversible capacities. There are still some serious drawbacks that still hinder the application of Li- and Mn-rich NCMs and that need to be overcome before this class of materials becomes a viable option for energy storage in EVs.[27] For this reason, the main scope of this thesis is to establish a detailed understanding about the capacity and voltage fading mechanisms of Li- and Mn-rich NCMs and their long-term stability challenges in lithium-ion battery cells. Based on the main fading mechanisms, a promising path how these issues can be solved and how the performance of this type of materials can be improved will be shown in this thesis.

1.1. Lithium-ion battery working principle

State-of-the-art lithium-ion batteries are based on the so called "rocking-chair" concept, which was established by M. Stanley Whittingham in the 1970s.[4] Based on this concept, the positive and the negative electrode material serve as intercalation host to reversibly intercalate and deintercalate lithium-ions that can be transported between the two electrodes[2-4] in an electrolyte with sufficient Li^+ mobility; in general, the electrolyte is contained within the pores of a porous polymeric separator, placed between the electrodes in order to prevent a short circuit. Figure 1 depicts the typical setup of a lithium-ion battery during the discharge of the cell, whereas the negative electrode is commonly referred to as anode and the positive electrode as cathode: a layered oxide cathode, a liquid electrolyte, and a graphite anode are shown, which essentially describes the first lithium-ion battery commercialized by Sony in 1991.[13] The redox reactions occurring at the graphite (C_6) anode during charge/discharge can be written as follows:

$$C_6 + Li^+ + e^- \leftrightarrow LiC_6 \qquad [1.1]$$

During charge, Li^+ is intercalated from the electrolyte into the graphite host structure, accompanied by an uptake of electrons from the external circuit, forming a variety of Li-C compounds and ultimately yielding LiC_6. This process is found to be highly reversible. As cathode material, lithium-cobalt-oxide ($LiCoO_2$) was used in the first lithium-ion batteries commercialized by Sony and is still used in consumer electronics due to its high volumetric capacity and its good reversibility.[8, 13] $LiCoO_2$ can also serve as intercalation host, leading to the following reaction on the cathode side:

$$LiCoO_2 \leftrightarrow Li_{1-x}CoO_2 + xLi^+ + xe^- \qquad [1.2]$$

In this case, Co^{3+} is oxidized to Co^{4+}during charge as Li^+ is extracted from the structure; during discharge, Li^+ is incorporated into the host structure and $Co^{4+}$is reduced back to Co^{3+}. This means that the Co^{3+}/Co^{4+} redox couple serves for charge compensation during the charge/discharge of the cell, while the initial layered structure is preserved during lithium deintercalation and reintercalation.[7] Therefore, considering that the amount of graphite is

generally balanced such that LiC_6 is formed upon complete cell discharge, the overall reaction, taking place in a graphite//$LiCoO_2$ battery cell can be written as follows:

$$xC_6 + LiCoO_2 \leftrightarrow xLiC_6 + Li_{1-x}CoO_2 \qquad [1.3]$$

Li^+ always migrates as charge carrier through the electrolyte within the pores of the porous polymeric separator between the electrodes, while the electrons are transported through an external circuit between the electrodes. In the following sections, the different types of organic electrolytes will be discussed, as well as the most common and most promising anode and cathode active materials.

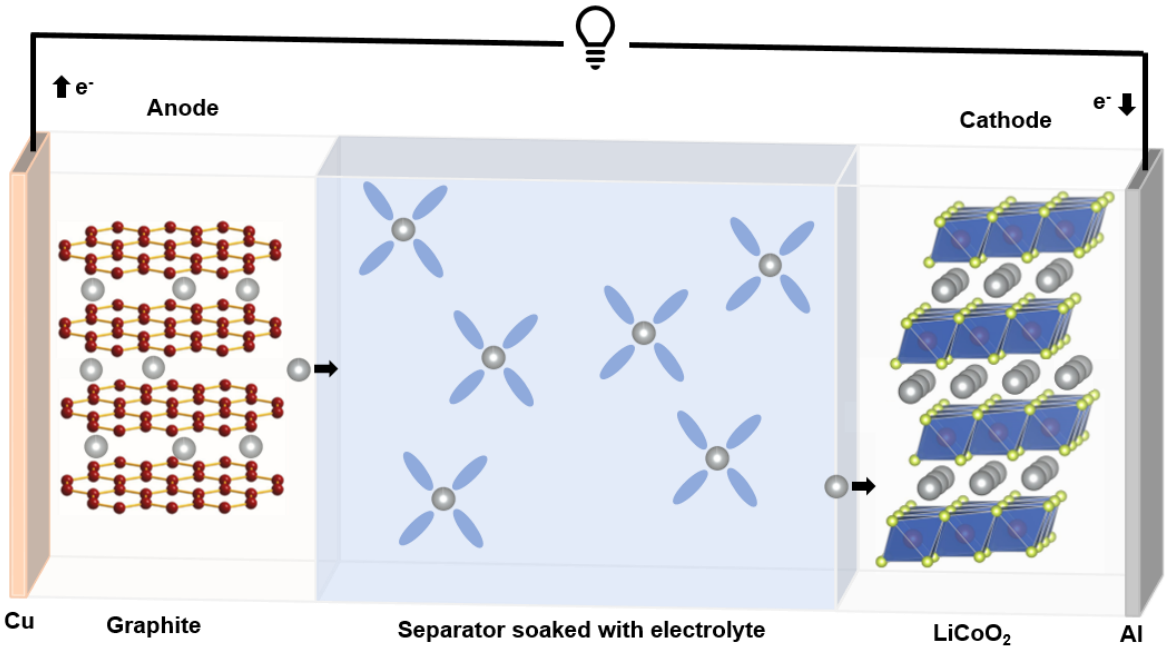

Figure 1. Schematic of the main components and the working principle of a lithium-ion battery during discharge. Lithium can be reversibly intercalated into the anode and cathode active material host structures. While electrons are transported through the external circuit, the Li^+-ions migrate through the electrolyte between the electrodes. This sketch is derived from that shown by Dunn et al.[3]

1.2. Electrolyte solutions

To enable Li^+ transport between the electrodes and to minimize reactions between lithiated graphite and the electrolyte, non-aqueous liquid consisting of organic carbonates with a Li-salt are used.[28] State-of-the-art electrolytes consist of a mixture of a linear carbonate, a cyclic carbonate, and a conductive salt, which is mostly $LiPF_6$ at a concentration of around 1M.[28] While the linear carbonate solvent has a low viscosity and a low conductivity, the cyclic carbonates, such as ethylene carbonate (EC), have high dielectric constants at the cost of a very high viscosity.[28] However, by changing the ratio between linear and cyclic carbonate and the concentration of the salt, the physical properties of the electrolyte can be easily tuned and optimized for different applications. The carbonate-based electrolyte systems offer sufficient electrochemical stability for the current generation of cathodes active materials that are operated at potentials of <4.5 V vs. Li^+/Li,[28] while their reductive stability is limited to potentials of >0.8 V vs. Li^+/Li.[11, 29] However, their reductive instability on graphite anodes is not an issue, due to the formation of a protective insulating layer on a graphite anode, which was at first recognized by Dahn et al.,[11] while the initial observation of a so called "solid-electrolyte-interphase" (SEI) was already reported by Peled in the late 1970s.[30] This SEI layer can electronically insulate the anode from the liquid electrolyte and thus prevent further electrolyte reduction, while showing a good Li^+ diffusivity which is required for the lithium intercalation reaction.[30, 31] For the use with graphite anodes, a good SEI formation is not only required to prevent electrolyte reduction, but also to protect the graphite anode from solvent intercalation and a concomitant exfoliation of the anode active material, which would lead to a rapid degradation of the cell performance.[11, 31] Among the classical cyclic and linear alkyl carbonates, only EC was able to form a stable SEI,[11] before certain SEI forming additives were developed to improve the SEI stability and the efficiency during SEI formation, compared an EC derived SEI.[28] The best SEI forming additives that are known nowadays are FEC (fluoroethylene carbonate) and VC (vinylene carbonate),[32, 33] which are normally added to the electrolyte in rather small amounts and are typically consumed on the graphite anode during the first formation cycles. The challenges that electrolytes will face with future cell chemistries are discussed later on. Especially, increased charge voltages will pose challenges for the electrolytes.[34, 35]

1.3. Anode active materials

In order to maximize the energy density of a lithium-ion battery, a suitable anode material should have a low reaction potential and a high specific capacity, as both parameters define the overall cell energy density. Commonly used anode materials are classified in Figure 2 with respect to their potential and their specific capacity; the red area indicates the potential region of reductive instability of the carbonate electrolytes, typically at potentials of <0.8 V vs. Li^+/Li.[29] At the moment, the most important anode material used for state-of-the-art lithium-ion batteries is graphite; due to its low operating potential of ≈0.1 V vs. Li^+/Li and its rather high specific capacity of ≈370 mAh/g, graphite can offer a high specific energy.[10, 13] Furthermore, its low cost and its high abundance makes it interesting for large-scale applications, while its reasonable high density of 2.25 g/cm^3 also leads to good volumetric energy densities, which is a crucial factor for consumer electronics as well as for automotive applications.[10] However, a drawback of a graphite anode is its limited fast-charging capability. Due to its low potential with respect to Li^+/Li, plating of metallic lithium can occur on the graphite anode at high lithium intercalation rates (fast-charging). Typically, lithium plating can be caused by high kinetic overpotentials, so that the anode potential goes below 0 V vs. Li^+/Li. Furthermore, lithium plating can be triggered by lithium salt concentrations that lead to diffusion overpotentials within the electrode and particularly become critical for thick electrodes and high tortuosities.[36, 37]

An anode active material that is capable of high charging rates is lithium-titanate (LTO), owing to its high potential of ≈1.55 V vs. Li^+/Li, so that lithium plating cannot occur. Due to its high potential above the electrolyte reduction potential, no SEI is formed on LTO, which allows the use of LTO-nanoparticles that offer fast kinetics and high rate capability.[38] Due to the absence of electrolyte reduction, LTO is resistant against transition metal deposition from the cathode and shows good capacity retention with high voltage cathode materials.[39] However, as a drawback of the absence of a passivating SEI layer, protons get reduced on LTO anodes, forming H_2 which leads to strong gassing if the materials contain trace water or if protons are formed due to anodic electrolyte oxidation on high voltage cathodes.[40, 41] Furthermore, the high operating voltage of ≈1.55 V vs. Li^+/Li and the low

capacity of ≈155 mAh/g lead to a ≈1.5 – 2 fold lower energy density of LTO based batteries.[38] Therefore, LTO is no choice for automotive applications or consumer electronics, but is rather used for applications were energy density plays a minor role and very long cell lifetimes are required, such as large-scale energy storage systems.

Initially, hard carbons were suggested as anode active material instead of graphite, as they seemed to offer a higher specific capacity of 550 mAh/g and had a lower sensitivity towards lithium plating that would allow higher charging rates for hard carbons compared to graphite anodes.[10] In the end, the sloping voltage profile and the low density of 1.55 g/cm^3 made hard carbons less favorable than graphite, so that graphite had been favored during the last 25 years.[10]

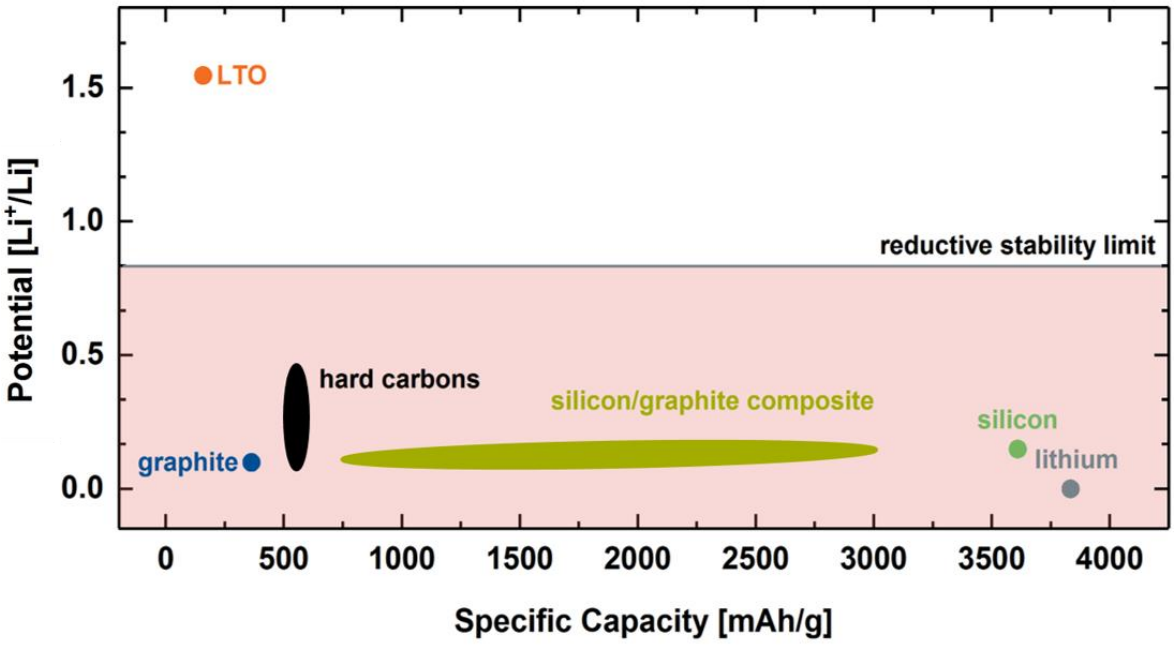

Figure 2. Most relevant anode active materials are classified by their specific capacity and their lithiation potential; references are given in the text. The red area indicates the typical potential region in which carbonate-based electrolytes are being reduced in the absence of a SEI.[29]

For future anodes in lithium-ion batteries, not only the rate capability needs to be improved, but also the specific capacity of the anode active material needs to be increased to

improve the energy density of future battery cells.[14] In this respect, silicon is one of the most promising future anode materials: it can be lithiated electrochemically up to $Li_{15}Si_4$ upon charging, offering high capacities of ≈3590 mAh/g at potentials <0.5 V vs. Li^+/Li, equating to very high gravimetric energy densities.[42] The large volume expansion of ≈310% upon the formation of $Li_{15}Si_4$ leads to destabilization of the protective SEI layer and to breakage of particles, which leads to a loss of cyclable lithium and of silicon active material;[42] both phenomena lead to rapid capacity fading and need to be overcome to make silicon applicable for future lithium-ion batteries. Silicon can also be blended with graphite in different compositions, so that the silicon graphite blends depicted in Figure 2 cover a wide capacity range.

Finally, the in principle most desirable anode with regards to energy density would be a simple lithium metal anode, as was intensively investigated by Moli Energy in the 1980s, but failed due to dendrite formation, leading to short circuits.[9] While lithium metal anodes cannot form a stable SEI and are still prone to dendrite formation in liquid electrolytes, lithium metal anodes are hoped to be a possible anode material for solid state electrolytes and constitute the main driver for the research of all-solid-state-batteries (ASSB).

1.4. Cathode active materials

For the classification of different cathode active materials not only the energy density has to be considered, but also the cost of the transition metals is a crucial factor, as most of the current cathode active materials contain expensive transition metals, such as nickel and cobalt.[14] Therefore, the most commonly discussed cathode materials are mapped in Figure 3 against energy density of the cathode active material (assuming an anode potential of 0 V vs. Li^+/Li) and transition metal cost (excluding lithium). Please note that the energy density trends on a full-cell level can differ due to balancing effects, as shown by Andre et al.[14] However, the energy density on a full-cell level is not considered here, as it is strongly dependent on the cell design and the anode active material used in a full-cell.[14] A practical energy density target of at least ≈675 Wh/kg on a cathode active material level has been set by BMW in order to reach their 2025 energy density target for lithium-ion battery full-cells;[14] this energy density target has been taken into account for the classification of cathode active materials (CAMs) in this thesis. The transition metal costs were calculated based on the market prices on April 26th 2019, which are 34.3 \$/kg for cobalt,[22] 12.3 \$/kg for nickel,[22] 2.0 \$/kg for manganese,[43] 1.8 \$/kg for aluminum,[22] and 0.06 \$/kg for iron.[44]

It can be seen in Figure 3 that the layered $LiCoO_2$ (LCO), that was investigated by Goodenough[7] nearly 40 years ago, still offers a competitive energy density of ≈741 Wh/kg (capacity =190 mAh/g; average voltage ≈3.90 V vs. Li^+/Li),[27] which would already match the 2025 energy density target of BMW. A further advantage of LCO is its high practical press density of ≈3.9 g/cm^3, resulting in an excellent volumetric energy density.[27] However, the huge drawback that hinders the use of LCO in future electric vehicles is the high cobalt content, leading to high metal cost (see Figure 3). While it is clear that LCO is not suitable for future automotive applications due to cost reasons, it is still one of the best materials available for consumer electronics that require only small amounts of cathode active material, and for which safety and volumetric energy density are key factors.[8] A similar trend can be observed for $LiCoPO_4$ (LCP): while its practical energy density (capacity =155 mAh/g; average voltage ≈4.80 V vs. Li^+/Li)[45] is comparable to LCO, the high operating voltages of LCP lead to dramatic drawbacks in cycling stability.[46] LFP ($LiFePO_4$) is another phosphate-

based cathode active material,[47] whereas cobalt is replaced by iron which significantly decreases the transition metal cost, but also substantially lowers the energy density to ≈544 Wh/kg, due to the low operating voltage (capacity =160 mAh/g; average voltage ≈3.40 V vs. Li^+/Li).[8] At the moment, LFP is still used in electric vehicles, but in order to increase the driving range, LFP needs to be replaced by cathode active materials with a higher energy density.[8] However, LFP is still a promising cathode material for applications that require long lifetime and for which lower energy densities are acceptable, such as stationary electrical energy storage systems and electrical busses. A further class of materials is based on spinel structures which are mainly manganese based and represent a cobalt-free and thus cost attractive alternative.[48-50] However, capacities of these structures are limited to ≈140 mAh/g, leading to an energy density of ≈440 Wh/kg (capacity =110 mAh/g; average voltage ≈4.00 V vs. Li^+/Li)[27] for the $LiMn_2O_4$ (LMO) spinel and ≈658 Wh/kg (capacity =140 mAh/g; average voltage ≈4.70 V vs. Li^+/Li)[51] for the so-called high-voltage spinel, where 25% of the manganese is replaced by nickel ($LiNi_{0.5}Mn_{1.5}O_4$). While the high voltage spinel structures offer fast kinetics due to fast 3D Li^+ diffusion, it suffers from rapid capacity fading in full-cell operation which is mainly caused by electrolyte oxidation and manganese dissolution at the high operation potentials.[52, 53]

At the moment, the most promising materials are the so called NCM materials that are still based on the layered LCO structure, but partially replace cobalt by manganese and nickel which leads to a decrease in cost and for high-nickel materials also to an increase in energy density.[14] The first NCM material was the so-called NCM 111 ($LiNi_{0.33}Co_{0.33}Mn_{0.33}O_2$), showing good capacity retention and energy densities of ≈624 Wh/kg (capacity =160 mAh/g; average voltage ≈3.90 V vs. Li^+/Li).[54, 55] In order to increase the energy density at acceptable upper cutoff voltages (≈4.1 – 4.2 V) and to lower the cost at the same time, recent trends tend to an increase of the nickel content (and lower cobalt contents), resulting in NCM 622 ($LiNi_{0.60}Co_{0.20}Mn_{0.20}O_2$, capacity =180 mAh/g; average voltage ≈3.85 V vs. Li^+/Li)[55] and finally in the so-called Ni-rich NCMs, as for example NCM 811 ($LiNi_{0.80}Co_{0.10}Mn_{0.10}O_2$, capacity =210 mAh/g; average voltage ≈3.80 V vs. Li^+/Li).[27] An increasing nickel content provides higher capacities at the same upper cutoff voltage and thus increases the energy density of the NCMs to ≈798 Wh/kg for NCM 811, at acceptable transition metal cost (see Figure 3). For the layered structure, not

only manganese can be used to stabilize the structure, but manganese can also be replaced by aluminum leading to the so-called NCA materials (e.g. $LiNi_{0.80}Co_{0.15}Al_{0.05}O_2$).[56] These can achieve equal energy densities (capacity =200 mAh/g; average voltage ≈3.80 V vs. Li^+/Li for NCA with 80% Ni),[27] with similar metal cost compared to NCMs with same nickel contents. The maximum nickel content for the layered oxides is reached for $LiNiO_2$ (LNO) that shows the highest energy density (capacity =240 mAh/g; average voltage ≈3.70 V vs. Li^+/Li)[57] and the lowest metal cost of all stochiometric layered oxides, but suffers from fast capacity fading during cycling.[57] In addition, with increasing nickel content, the layered structure becomes more unstable, particularly at low degrees of lithation (i.e. in the charged state), which leads to safety issues and strong gas evolution during cell operation.[24, 56]

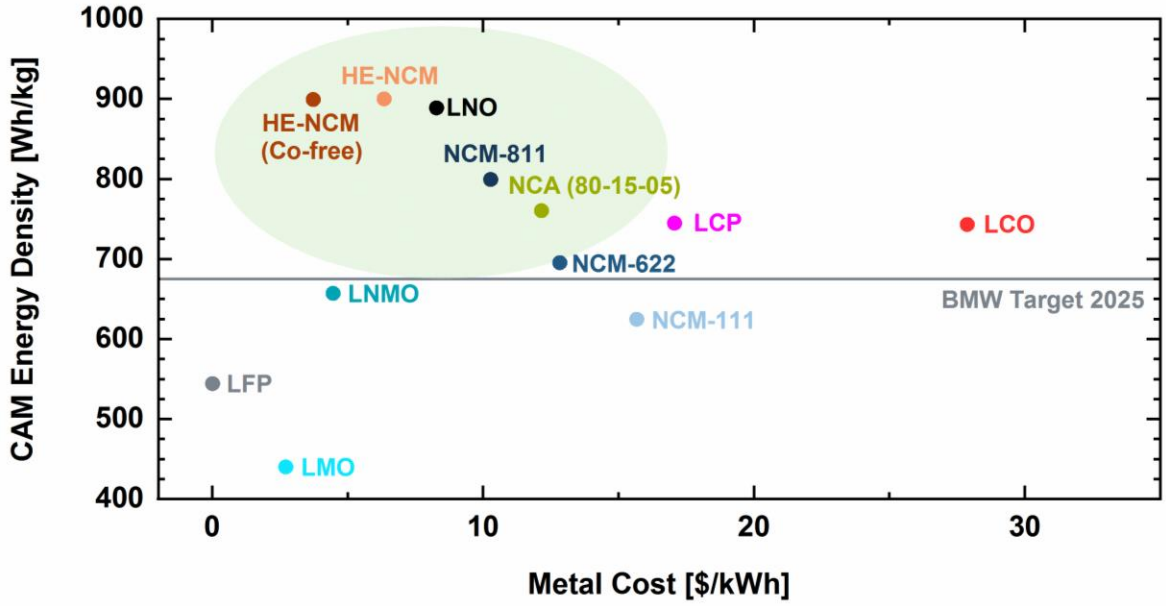

Figure 3. Most relevant intercalation cathode active materials (CAMs), based on layered, spinel and olivine structures are classified by their practical energy density and their transition metal cost (lithium cost are not considered in this representation). For abbreviations and references of the CAMs see text.

A novel concept that was investigated by the researchers at Argonne National Laboratory in the 2000's are the so-called overlithiated NCM materials.[58] Formally, a Li_2MnO_3 domain is added to the stochiometric NCM materials, leading to the nanostructured

two-phase materials described as x Li_2MnO_3 • (1-x) $LiMO_2$ (M = Ni, Co, Mn).[59] Activation of these lithium- and manganese-rich materials at high potentials (≈4.7 – 4.8 V vs. Li^+/Li) leads to high reversible capacities of >250 mAh/g that translate into an energy density of ≈900 Wh/kg (capacity =250 mAh/g; average voltage ≈3.60 V vs. Li^+/Li)[60], as shown in Figure 3. Interestingly, it has been shown in the literature that these materials (often referred to as high-energy NCM or HE-NCM) possibly can be synthesized and stabilized without cobalt, which significantly lowers the metal costs compared to all other layered oxides.[61] However, these materials still suffer from some serious issues that have hindered its commercialization so far; these issues will be a main part of the questions that are addressed in this thesis.[62]

1.5. Challenges for next generation cathode active materials

The research targets for future cathode active materials for lithium-ion batteries aim towards decreasing cobalt contents in order to decrease cost and to increase sustainability, whereas three main material classes are discussed. The first strategy is based on the already commercialized layered NCM materials and focuses on the so-called Ni-rich NCMs.[56] Based on this strategy, the nickel content of the early developed $LiNi_{0.33}Co_{0.33}Mn_{0.33}O_2$ (NCM 111)[54] is increased while lowering the cobalt and manganese content; as example for a Ni-rich NCM in this thesis, $LiNi_{0.85}Co_{0.10}Mn_{0.05}O_2$ (NCM 851005) is used. Instead of manganese it is also possible to use aluminum to stabilize the layered-oxide structure, leading to NCA materials that can also contain 85% nickel or more; these NCA materials are especially used by Tesla in their EVs.[8] The upper limit for the nickel content of these stochiometric layered-oxides is the so-called LNO ($LiNiO_2$) which contains exclusively nickel as transition metal.[57] While the increasing nickel content can also increase reversible capacities at acceptable upper cutoff voltages for a graphite//NCM full-cell (≈4.1 – 4.2 V), the layered structure gets more and more instable with increasing nickel contents, favoring the formation of the NiO rocksalt for very high nickel contents.[25, 26, 55] Thus an increasing nickel content on the one hand leads to increasing bulk instabilities and Ni disorder, [24, 57, 63] and on the other hand leads to pronounced stability issues at the surface of these Ni-rich layered oxides.[24, 55, 64-67] The tendency towards rocksalt formation results in surfaces that are highly unstable during delithiation and are prone to release lattice oxygen during the initial cycles which reacts with the electrolyte and also leads to a resistive rocksalt surface layer.[55, 64] Furthermore, the high nickel content on the surface leads to a very high sensitivity towards moisture and storage conditions, favoring the formation of lithium and transition metal hydroxides and carbonates on the surface of these materials.[65-67] Especially the hydroxide species on the surface do not only alter the cycling performance, but cause gelling of the PVDF binder during electrode processing and strong gassing of the final lithium-ion batteries.[56, 68] Figure 4 shows the voltage profile of NCM 851005; it can be seen that in the typical cycling range between 3.0 – 4.2 V vs. Li^+/Li the electrochemical electrolyte oxidation plays a minor role, which means that the fading mechanisms of Ni-rich cathode materials is

rather due to a chemical degradation process instead of electrochemical electrolyte oxidation.[69]

A very interesting class of next-generation cathode active materials which are not commercialized yet, are the overlithiated Li- and Mn-rich NCMs (HE-NCM), as briefly discussed in the previous section. These materials contain a high fraction of manganese and can potentially open a pathway towards a cobalt free layered cathode material that could strongly decrease cost while increasing the capacity (see Figure 3), as shown by Croy et al.[61] However, these materials suffer from several serious issues that limit the lifetime and the kinetics of these materials.[62] On the one hand, bulk structure instabilities lead to voltage-fading during cycling, to a roughly 1 V hysteresis between charge and discharge, and to comparable slow charge-transfer kinetics and concomitantly poor rate capabilities.[61, 70-72] On the other hand, strong lattice oxygen release leads to a very limited cycle life of overlithiated layered oxides, due to electrolyte degradation and impedance build-up on the surface.[60, 73-75] Furthermore, the voltage profile in Figure 4 shows that HE-NCM is operated at very high potentials that also trigger electrochemical electrolyte oxidation, which especially limits cycle life during full-cell operation at 45 °C, adding another challenge in addition to oxygen release. However, HE-NCM is a very promising material that can deliver high energy densities, while having a low metal cost, but still needs further development prior to commercialization. For this reason, the key part of this thesis will be the detailed analysis of the bulk instabilities and of the interfacial reactions of overlithiated NCMs in order to elucidate these mechanisms and to define a clear path forward to improve the performance of this class of materials.

A different class of material that was suggested as future cathode active material is the so-called high-voltage-spinel (HVS), having the sum formula $LiNi_{0.5}Mn_{1.5}O_4$. At first glance, this material seems quite promising, as the spinel structure is very stable, does not show oxygen release during delithiation, and is rather insensitive towards storage at ambient conditions.[55, 69] However, the main problem can be seen from the voltage profile shown in Figure 4, meaning that the cathode operates over nearly the whole capacity range at potentials where the carbonate electrolytes are not stable anymore, particularly when operated above room temperature, which leads to electrolyte oxidation and to a rapid capacity decay.[52, 76] In

order to overcome this issue and to improve the cycle life, an oxidatively more stable electrolyte system than current state-of-the-art electrolytes would have to be found.[52] For these reasons, an improvement of the HVS cathode active material was out of the scope of this thesis, as this thesis focuses onto the development of the cathode active materials and not on electrolyte development. In this thesis, HVS was only used as a model compound in order to understand degradation mechanisms at high potentials in the absence of oxygen release that is observed for all layered-oxides.[69]

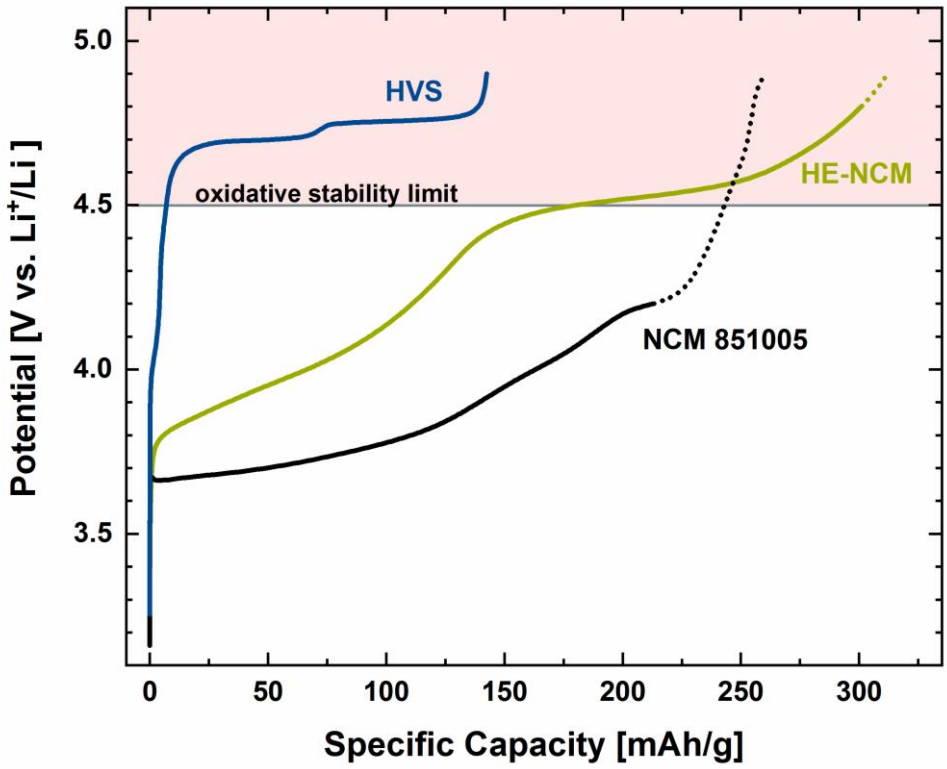

Figure 4. Typical potential profiles for NCM 851005, HVS, and HE-NCM cathodes. The electrode potentials were measured at C/10 rate against a Li-counter electrode. The solid lines show the practical potentials that are used during cell operation, while the dotted lines show the potential vs. capacity relationship for full delithiation (typically not used in a full-cell). The red area indicates the potential region which is beyond the oxidative stability limit of the typical carbonate electrolytes.

The main degradation mechanisms for NCMs and HE-NCMs that are analyzed within this PhD project are schematically summarized in Figure 5. Namely, bulk structural disorder and transition metal migration,[62, 71, 77, 78] electrochemical electrolyte oxidation at potentials of >4.5 V vs. Li^+/Li,[52, 69] side-reactions due to surface hydroxide and carbonate impurities,[65, 68, 79] and lattice oxygen release from the layered-oxide surface that reacts with the electrolyte.[55, 73, 80] In the following these issues will be briefly discussed regarding their relevance for the nickel-rich NCMs as well as for the manganese-rich HE-NCMs. Bulk disorder in Ni-rich layered-oxides occurs mainly during synthesis and lowers the overall capacity of Ni-rich layered-oxides with an increasing disorder.[57] However, by optimizing the synthesis conditions and especially the calcination conditions, it has been shown that Li/TM mixing can be overcome even for LNO.[57] In stark contrast, such Li/TM disordering is triggered by activation and electrochemical delithiation of the overlithiated Mn-rich layered-oxides (HE-NCM), for which reversible and irreversible Li/TM disorder can be observed, causing significant drawbacks in their electrochemical long-term stability.[62, 77, 78] It has been suggested that after activation of HE-NCM, transition metals can migrate reversibly to the tetrahedral site of the Li-layer and irreversibly to the octahedral side of the Li-layer; these processes are schematically shown in Figure 5.[62, 77, 78] In the literature, the reversible migration of transition metals during charge and discharge has been proposed to cause the roughly 1 V hysteresis between the charge and discharge potentials.[62] The gradual irreversible transition metal migration as a consequence of the irreversible movement was shown to be closely linked with the decrease in the average discharge potential during cycle life.[62, 71, 78] Furthermore, these transition metal movements have been proposed to be linked to the activation of the anionic oxygen redox in overlithiated materials, and therefore may be an intrinsic requirement to achieve the high reversible capacities of HE-NCM.[77]

Besides bulk structural changes, the high cutoff potentials of Mn-rich NCMs lead to oxidative instabilities of the carbonate electrolytes, resulting in the electrochemical oxidation of the electrolyte.[28] As shown in Figure 5, the electrooxidation of the carbonate electrolytes generates protons that cause severe issues within a full-cell,[29] such as $LiPF_6$ decomposition and transition-metal dissolution.[81-83] The dissolved transition metals can decompose on the graphite anode, leading to a damage of the SEI-layer which ends up in a consumption of active lithium.[53, 81, 84] While electrooxidation is a minor issue for Ni-rich materials, it has

been shown that the high nickel content on the surface of the materials strongly triggers the chemical decomposition of the electrolyte. One of the main drivers for this reactivity is the increasing tendency of hydroxide formation with an increasing nickel content;[65, 67] these hydroxides can afterwards react with the electrolyte and cause side reactions that significantly compromise cell performance.[65-68, 79] Whereas the nickel content is relatively low for HE-NCM, the formation of surface hydroxides still is a critical issue for HE-NCM, as its BET surface area is about 20-times higher compared to stochiometric NCMs, which results in an overall large amount of surface impurities.[65, 73, 79]

However, not only the surface impurities cause chemical side reactions, but also the layered oxides themselves show structural instability at the surface during delithiation. In particular, from all layered oxides, lattice oxygen is evolved at >80% delithiation which causes formation of a resistive spinel/rocksalt layer on the surface of the cathode active material and chemical oxidation of the electrolyte.[55, 64, 73, 80] In order to utilize the high energy densities (Figure 3) of Ni-rich NCMs and of HE-NCM in practical lithium-ion battery cells this is one of the main issues that needs to be solved.

These above discussed degradation mechanisms will be investigated within this PhD project, they are schematically summarized in Figure 5. It will be the target of this thesis to get a detailed understanding about the capacity and voltage fading mechanisms and to develop a strategy to overcome the surface instabilities of layered oxides.

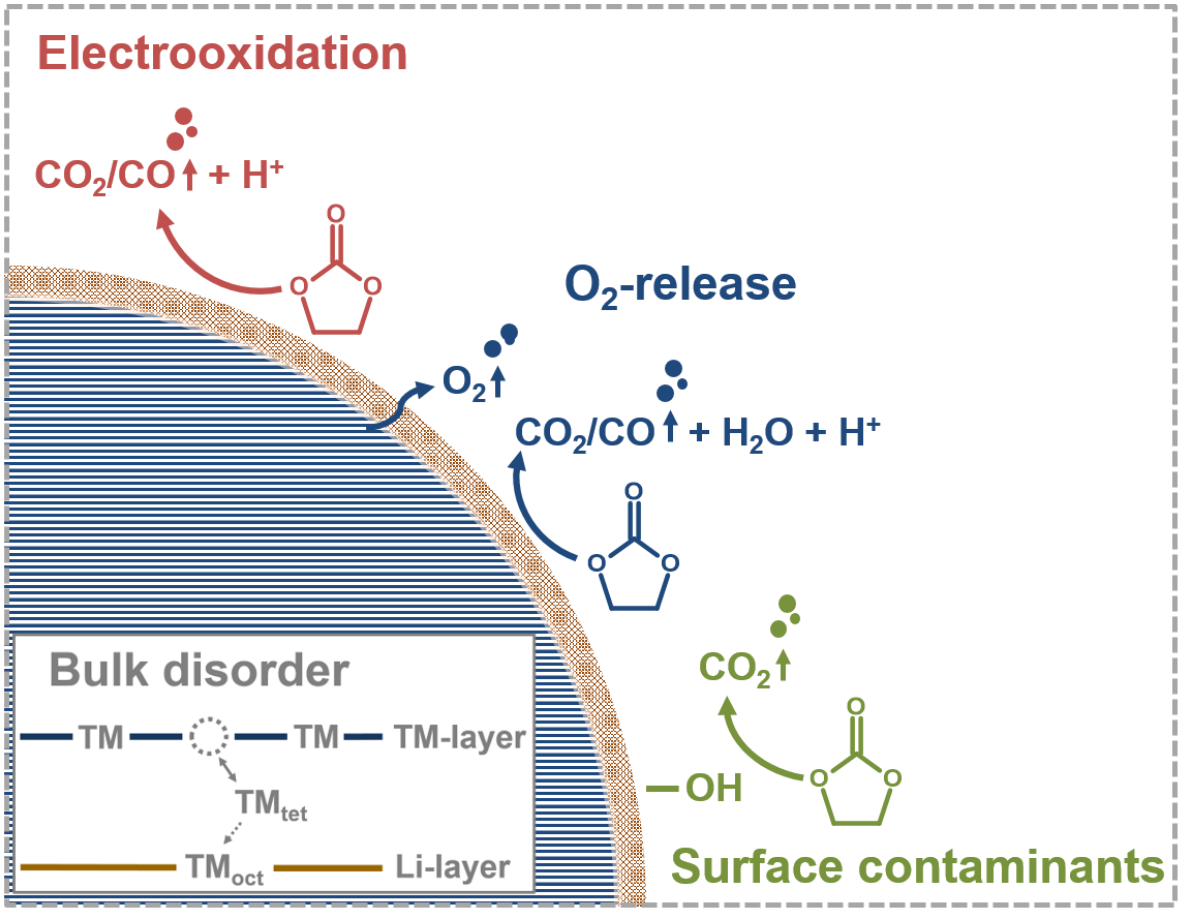

Figure 5. Schematic summary of undesired side-reactions that occur in the bulk and on the surface of stochiometric and overlithiated layered oxides that have been investigated in this PhD thesis. Possible surface reactions are electrochemical electrolyte oxidation,[29, 69] oxygen release,[55, 85] and surface contaminations.[68, 86] In the bulk, reversible and irreversible transition metal disordering (TM) between the transition metal layer (TM-layer) and the lithium layer (Li-layer) is suggested.[62, 78] It is suggested for HE-NCMs that transition metals can reversible occupy the tetrahedral site of the lithium layer (TM_{tet}) upon charge/discharge;[62, 78] over the course of cycling, transition metals can be irreversibly locked in the octahedral side of the lithium layer (TM_{oct}).[62, 78]

1.6. Challenges for next generation electrolytes

The side-reactions shown in Figure 5 also pose new requirements for electrolyte formulations used with high energy cathode materials. Especially, the use of EC-based electrolytes for high-voltage applications has been intensively discussed in the literature. EC-based electrolytes turned out to be very problematic for the full-cell performance, if layered oxides are cycled to cutoff voltages >4.4 V.[87-89] The research group of Jeff Dahn replaced EC by a variety of SEI forming carbonates and showed that the high voltage cycling performance could be significantly increased for EC-free electrolytes.[89-91] Especially fluorination of the electrolyte and the replacement of EC by FEC as co-solvent can strongly improve the lifetime of high voltage cells and is a commonly used approach.[87, 88, 92] However, the exact difference between EC and FEC is not clear at the moment: some researchers suggest that FEC has a better anodic stability and thus is less prone to electrooxidation at high voltages,[92-94] while others claim the formation of a passivating CEI layer on the cathode due to FEC,[95] even though detailed surface analysis by other groups could not prove the existence of such a passivating surface layer.[96] Recently, it has been shown that oxygen release from layered oxide cathode active materials has a significant impact onto electrolyte oxidation and cell performance.[55, 69] Furthermore, the electrolyte can also be affected by surface hydroxides and carbonates on the cathode active material, which can also lead to a deterioration of the cycle life.[65, 66, 68, 79, 97] Against this background, this thesis evaluates not only the differences of EC- and FEC-containing electrolytes regarding electrochemical degradation, but also the effect of chemical degradation on both electrolyte systems. Due to the high cutoff voltages up to 4.8 V vs. Li^+/Li of HE-NCM, also the choice of appropriate additives has to be considered. In particular, vinylene-carbonate (VC), a typical used SEI additive,[32] cannot be used at these high operating voltages due to its anodic instability.[52] This is different for FEC, which shows sufficient electrochemical stability and is also used as co-solvent to replace EC or to enable stable cycling of silicon anodes.[35, 87] However, it turned out that electrolytes containing FEC and $LiPF_6$ show limited thermal stabilities and can produce undesired side-products within the electrolyte.[96, 98] For this reason this thesis will seek to shed some light onto the drawbacks of FEC-based electrolytes used for high voltage applications, especially at elevated temperature.

1.7. Perspectives for lithium-ion batteries

While Ni-rich cathode active materials for lithium-ion batteries are still subject to ongoing development, Tesla already commercialized Ni-rich NCA ($LiNi_{0.80}Co_{0.15}Al_{0.05}O_2$) in 18650 cells for its Tesla Model S back in 2012.[8] Tesla proved with their NCA based batteries in the Model S and Model X that driving ranges >300 miles can already be achieved in the high-price vehicle segment.[99] However, Tesla did not only prove that Ni-rich materials can be used in electric vehicles to achieve high driving ranges, they also proved that battery lifetimes of more than >250.000 km are realizable with nickel-rich cathode materials. The Dutch-Belgium Tesla Forum collects data on the battery lifetime of more than 300 cars and provides them in a publicly accessible google file.[100, 101] Based on these data, it can be seen that the trendline shows a remaining range of more than 90% after 250.000 km, which proves the applicability of nickel-rich cathode materials for electric vehicle.

However, these high driving ranges can still only be provided for high-priced electric vehicles, preventing the large-scale BEV mass market penetration so far.[99] Also, a Tesla Model 3 with a driving range of >300 km still costs ≈45.000 €.[18] To increase driving ranges for low-cost electric vehicles, the cost of the battery pack as well as the weight of the battery pack has to be decreased. To highlight the importance of the cathode active material for decreasing the cost and weight of future lithium-ion batteries, the mass fractions and cost contributions of current electrode and cell materials are shown in Figure 6.[102, 103] It can be seen that the cathode active material does not only contribute ≈50% of the material weight to the battery, but also causes ≈40% of the overall cost of the battery materials (data are derived from Wagner et al.[102] and Pillot[103]; pack components are neglected in this representation). Therefore, it is clear that the development of low-cost and high-capacity cathode materials is a key factor for reaching the 2025 DoE targets, set for lithium-ion batteries required for a large-scale market penetration of BEVs.[17]

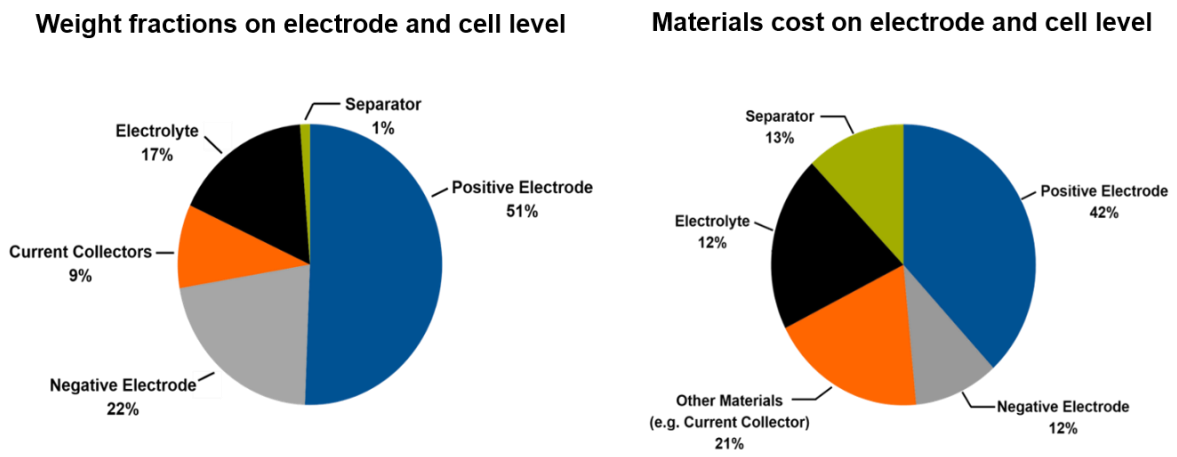

Figure 6. Electrode and cell level weight fractions (left graph) and cost structure (right graph) for a current lithium-ion battery on the materials level. Weight fractions were derived from Wagner et al.[102], based on a cathode active material capacity of 148 mAh/g and an anode active material capacity of 372 mAh/g. Cost contributions were taken from Sanders, and reflect the average cost structure of a lithium-ion cell in 2016.[103] The figure shows only the weight/costs from the battery materials; contributions from the cell assembly process costs and from the pack/cell components were neglected.

The most promising candidates for future cathode active materials are shown in Figure 3, and their issues with regards to performance and durability are discussed in the previous section. From a cost perspective, it is obvious that especially the cobalt content is critical. The trend for the cobalt, nickel, and manganese price over the last decade is shown in Figure 7, proving once more that cobalt is the main cost driver among the raw materials for cathode active materials. But it is not only the current price that makes cobalt so critical, it are also the high fluctuations of the cobalt cost which makes the predictability of the battery cost difficult. Furthermore, the availability of cobalt is rather limited, which gives a high probability of increasing cobalt prices with an increasing production of lithium-ion batteries.[104] While the cost for nickel is much lower compared to cobalt, it is still significantly higher than manganese. Thus, a high share of manganese would be favorable for decreasing battery cost, as indicated in Figure 3.

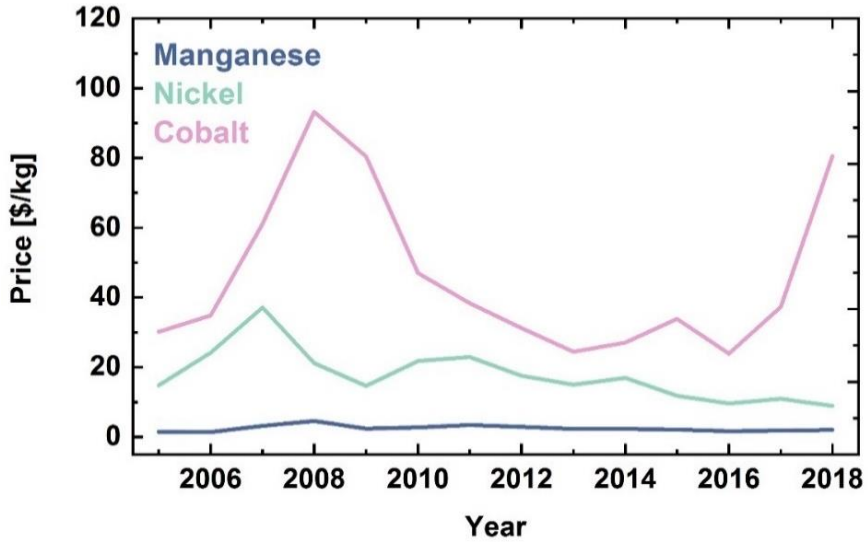

Figure 7. Trendlines for the cobalt, nickel, and manganese cost from 2005 until 2018. Data were taken from metalary.[44]

Due to the high manganese share, Li- and Mn-rich layered oxides (HE-NCM) do not only provide an attractive cathode active material in terms of energy density, but also provide high attractiveness regarding the cost of the material. However, its performance still suffers from practical issues and scientific challenges, such as voltage-fading, voltage-hysteresis and rapid capacity fading.[62] For this reason, we will provide in **Section 3.1** a detailed analysis of the bulk and the surface structural changes of the cathode active material that allows to differentiate the distinct different behavior of the interface compared to the bulk of the material. In **Section 3.2**, we will then show the implications of the oxygen release onto the full-cell performance and discuss the demanding cell chemistry of the system. Finally, **Section 3.3** presents a strategy how the surface of nickel-rich layered oxides can be stabilized against oxygen release. These fundamental insights also reveal new pathways towards the improvement of Li- and Mn-rich cathode active material

2. Experimental

2.1. Electrochemical characterization

To analyze a variety of different ageing and degradation mechanisms in lithium-ion batteries, four different cell setups were used in this thesis. The CR2032 coin-cell is shown in Figure 8a and was mainly used for cycling and lifetime experiments (see **Section 3**). Coin-cells offer a quick and reliable access towards electrochemical data, while only a small amount of material is required. Furthermore, they can be assembled rather as half-cells with a lithium metal counter electrode or as full-cells with a graphite counter electrode, which allows a good flexibility for electrochemical testing. The typical cathode used for the coin-cells in this study has a diameter of 14 mm, the graphite counter electrodes for full-cell testing have a diameter of 15 mm, and the lithium metal for half-cell testing have a diameter if 17 mm. The exact cell components, such as type of separator, electrode loading, and electrolyte volume are separately listed for each of the studies in **Section 3**.

To acquire in-situ impedance measurements during full-cell cycling, a custom-made Swagelok® T-cell that is equipped with a gold-wire reference electrode (GWRE) was used (Figure 8b). This method was developed in our group[105] and allows to separately measure cathode and anode impedance without cell disassembly. The cell consists of an anode and a cathode with the same diameter (both 11 mm), and the reference electrode is placed in between the two electrodes, sandwiched between two separators.[105] As reference electrode, a polyimide coated gold-wire with a diameter of 50 µm (+ 7 µm insulation) is used, which is lithiated prior to cycling in order to obtain a stable potential. The exact setup and procedure can be found in the article by Solchenbach et al.[105] and the exact measurement conditions used in this thesis can be found in **Section 3.1.1**, **Section 3.2.2**, and **Section 3.3**.

Single-layer pouch cells (SLP) assembled in this thesis are depicted in Figure 8c and consist of a cathode with a dimension of 25 x 25 mm and an anode with a dimension of 27 x 27 mm, having an overlap of 1 mm on each side. The cells are assembled with a Celgard® 2500 separator and 1 mL of electrolyte. Single-layer pouch cells can be degassed during cell

formation and operation and offer a higher electrode area compared to coin-cells, thereby minimizing edge effects. In this thesis, the single-layer pouch cells were used for pre-formation of large electrodes, from which coin-cell electrodes were punched out to be used for long term cycling in coin-cells (**Section 3.2.1**). For the analysis of gassing over the course of full-cell cycling, commercial multi-layer pouch cells were obtained from Li-Fun Technologies (China). The cells have a capacity of 200 mAh and were filled with 700 µL electrolyte; these cells are similar to the cells used by the research group of Jeff Dahn.[106] The volume of the gasses evolved during cycling can easily be measured by the Archimedes method, as described by Aiken et al.;[106] the exact formation procedures and materials used are given in **Section 3.2.2**.

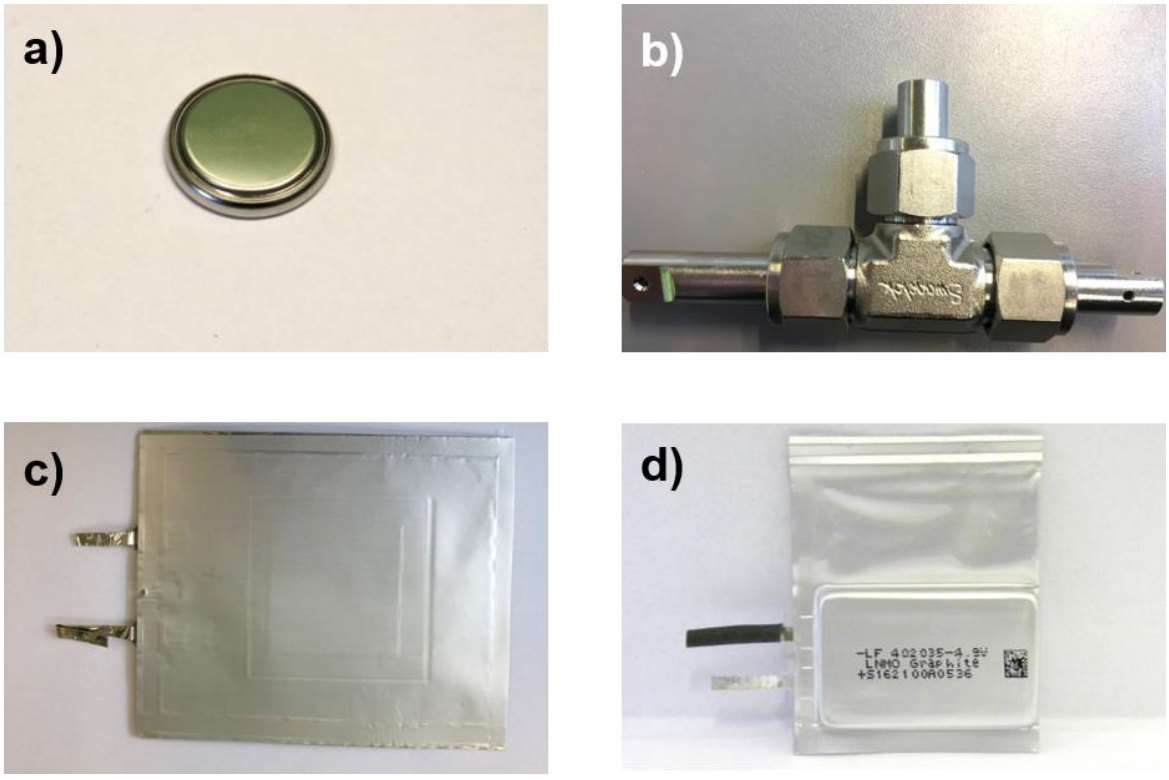

Figure 8. Photograph of the different cell setups used in this study showing a) coin-cell, b) Swagelok® T-cell equipped with a gold-wire reference electrode,[105] c) single-layer pouch cell and d) commercial multi-layer pouch cell obtained from Li-Fun Technologies (China).

Battery cells are charged and discharged in order to analyze their electrochemical properties, such as capacity and lifetime. The capacity of a battery that can be measured during charge/discharge cycling is defined in units of [mAh] and by a commonly used convention the end of life is reached once the capacity falls below 80% of the initial capacity. A typical galvanostatic cycling sequence for a pristine full-cell is shown in Figure 9, consisting of a 2h OCV rest phase, a charge with a positive constant current, followed by a 1h constant voltage phase (during which the current drops) and then by a discharge with a negative constant current. An initial OCV phase of 2h is applied for a pristine cell in order to allow sufficient cell wetting after assembly. The constant current charge is carried out with a certain C-rate, whereas the current for a C-rate of I 1/h is defined as the current required to charge or discharge the theoretical cell capacity in one hour (i.e., for a 200 mAh cell, a C-rate of 1 corresponds to a current of 200 mA). For the case shown in Figure 9, the C-rate is C/15 (i.e. it would take 15 h to galvanostatically charge/discharge the theoretical cell capacity). The charge is carried out until a selected upper cutoff potential is reached. In Figure ***9***, the cell is charged to 4.70 V and then the charge is followed by a constant voltage step (CV-step). During the CV-step, the cell is held at the upper cutoff potential and the current usually drops to small values. Afterwards, the cell is discharged with a constant current step (e.g., C/15) to a selected lower cutoff potential (here 2.00 V). With the sequence shown in Figure 9, the charge and discharge capacity of the cell can be calculated by multiplying the time in [h] by the current in [mA], resulting in a capacity given in [mAh]. The C/rates, as well as the upper and lower cutoff potentials need to be selected and can significantly differ for different materials.

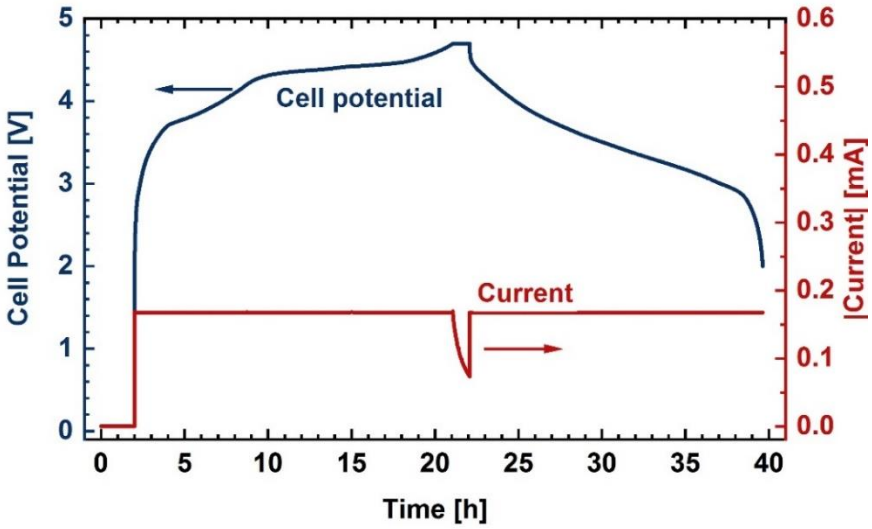

Figure 9. Illustration of a typical cell testing sequence: a galvanostatic charge, followed by a constant voltage step at the upper cutoff cell voltage limit and then by a galvanostatic discharge. The current is shown in red and the resulting voltage is shown in blue.

One electrochemical technique that allows a quick analysis of the cell resistance are current pulses with a specific current and duration, also referred to as direct current internal resistance (DCIR) method.[107] Figure 10 shows a typical DCIR sequence, that consists of an OCV phase for voltage stabilization prior to the current pulse, then a current pulse is applied for 10s and again followed by an OCV phase to monitor the voltage relaxation after the current pulse. During the current pulse, a voltage drop can be observed and the voltages U_1, U_2 and U_3 (see Figure 10) are recorded in order to allow the calculation of the resistance. The cell resistance can be calculated from the values using Ohm's law, by dividing the averaged voltage drop by the current:

$$R = \frac{\frac{U_1+U_3}{2} - U_2}{I} \qquad [2.1]$$

This calculation results in the cell resistance given in [Ohm] that can be converted into the area specific resistance (ASR) in [Ohm cm^2] by dividing the resistance [Ohm] by the geometric electrode area [cm^2]. While commonly used in the battery industry, the resistance obtained from the DCIR measurements is clearly dependent on the duration and the current

of the pulse. Therefore, the DCIR method is benchmarked against impedance spectroscopy in **Section 3.1.1**.

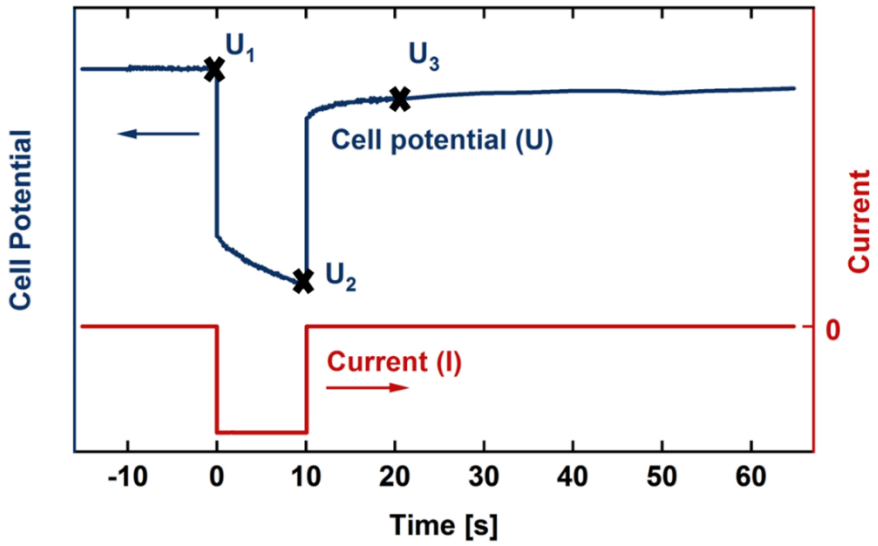

Figure 10. Typical sequence for pulse current testing according to the DCIR method.[107] The current is shown in red and the voltage response is shown in blue, the potentials used for the resistance calculations are marked by U_1, U_2, and U_3.

2.2. Electrochemical impedance spectroscopy

This section gives a brief overview of electrochemical impedance spectroscopy and is mainly based on the lecture of Prof. Gasteiger, who is the supervisor of this thesis[108] and supporting literature.[109] In general, impedance spectroscopy is based on Ohm's law and allows the measurement of resistances and capacitances within an electrochemical cell. Impedance is measured by applying a small sinusoidal voltage perturbation to an electrical/electrochemical system and collecting the current response (potentiostatic mode) or by applying a small current perturbation and measure the voltage response (galvanostatic mode). By using Euler's formula, the complex impedance $Z_{(\omega)}$ is defined as follows:

$$Z_{(\omega)} = \frac{\hat{E}_{AC(\omega)}}{\hat{\imath}_{AC(\omega)}} \cdot \cos(\theta) + j \cdot \left(-\frac{\hat{E}_{AC(\omega)}}{\hat{\imath}_{AC(\omega)}} \cdot \sin(\theta)\right) \qquad [2.2]$$

with the radial frequency $\omega = 2\pi f$ (f = frequency), with $\hat{E}_{AC(\omega)}$ and $\hat{\imath}_{AC(\omega)}$ being the measured/applied voltage and current amplitudes with j defined as $\sqrt{-1}$, and with θ being the phase angle between voltage and current. This complex impedance can be split into a so-called real part of the impedance, $Re_{(Z)}$, and an imaginary part of the impedance, $Im_{(Z)}$. The real and the imaginary part are defined as follows:

$$Re_{(Z)} = \frac{\hat{E}_{AC(\omega)}}{\hat{\imath}_{AC(\omega)}} \cdot \cos(\theta) \qquad [2.3]$$

$$Im_{(Z)} = -\frac{\hat{E}_{AC(\omega)}}{\hat{\imath}_{AC(\omega)}} \cdot \sin(\theta) \qquad [2.4]$$

For analysis of the impedance response, the complex impedance is typically plotted in a so-called Nyquist plot, having the real part of the impedance as x-axis and the imaginary part of the impedance as y-axis, as shown in Figure 11. In principle a Nyquist plot shows the deviation of the magnitude of the impedance ($Z_{(\omega)}$) in dependence of the phase angular.

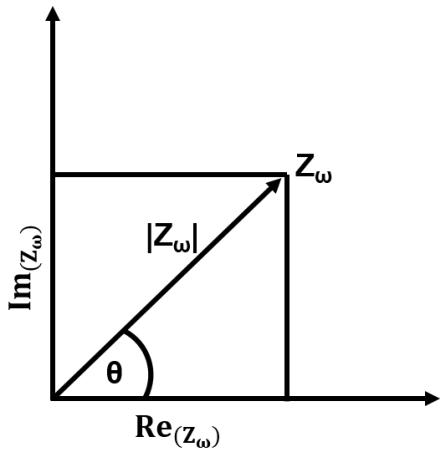

Figure 11. Schematic explanation of the complex impedance plotted in a Nyquist plot, where $|Z_\omega|$ is the magnitude of the impedance, Z_ω, and θ is its phase angle. The vector Z_ω is described by its real part, $Re_{(Z_\omega)}$, and its imaginary part, $Re_{(Z_\omega)}$.

An example Nyquist plot for a typical half-cell measurement within a battery cell is shown in Figure 12. The first part at very high frequencies is the so-called high-frequency resistance (R_{HFR}), which is a purely ohmic resistance and therefore has no Im(ω) contributions, so that it is located on the x-axis. The high frequency resistance is for example caused by ionic resistance of the electrolyte phase within the separator and by electronic contact and clamping resistances. Contact resistances between electrodes and current collector, as well as interfacial resistances, are generally modelled as parallel circuits of a resistor and a capacitor, whose impedance response in a Nyquist plot is a semi-circle with an apex frequency of $f = \frac{1}{2\pi RC}$. Where f is the frequency, R the resistance and C being the capacitance. Such interfacial resistances are for example, the SEI resistance and the charge-transfer resistance. At very low frequencies, diffusive processes show up that result in a 45° line, at the low-frequency end of the Nyquist plot. This impedance is for example caused by bulk Li^+ diffusion within the active materials and is also referred to as Warburg impedance. As the frequencies of the impedance response from the cathode and the anode side are typically close to each other, they overlap if impedance is measured in a full-cell setup, which makes reliable interpretation of the impedance spectra very difficult. For this purpose, a reference electrode can be placed in between the electrodes to record the anode and the

cathode impedance separately. Such a µ-reference electrode was implemented into the previously described Swagelok® T-cell, designed by Solchenbach et al.[105] This reference electrode allows to decouple the impedance contributions from the anode and the cathode side and enables an advanced analysis of the impedance spectra. In **Section 3.1.1** this µ-reference electrode is used to understand the full-cell impedance spectra of a graphite//HE-NCM full-cell.

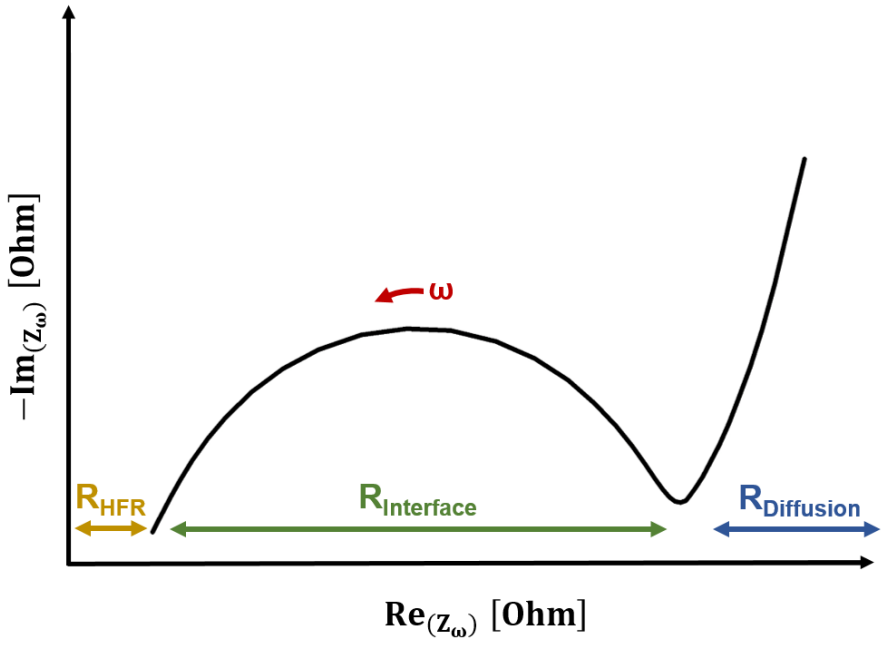

Figure 12. Nyquist plot of a typical impedance measurement for a battery half-cell.

2.3. On-line electrochemical mass spectrometry

On-line Electrochemical Mass Spectrometry (OEMS)[110] is a similar technique as the previously reported differential electrochemical mass spectrometry (DEMS).[111, 112] The distinct difference to a DEMS is that an OEMS operates with a closed measurement cell, where the head-space is connected by a crimped-capillary leak to the mass spectrometer. In contrast, a DEMS measurement cell is continuously or intermittently purged with a carrier gas that transports the gasses in the head-space of the measurement cell to the mass spectrometer inlet. Consequently, the raw data in a DEMS setup represent gas evolution/consumption rates (e.g. in units of µmol/h), while the raw data in an OEMS setup represent quantities of evolved/consumed gases (e.g. in units of µmol) so that evolution/consumption rates must be determined by numerical methods. The OEMS setup has a good time resolution (on the order of 10 – 100 s), a good detection limit, as the gasses are not diluted by a carrier gas stream, that is required for the DEMS method. Furthermore, the reaction gasses in the OEMS are not purged out of the cell, allowing the analysis of crosstalk phenomena during cycling, which is not possible in a DEMS setup. On the other hand, the crimped capillary leak continuously draws gas from the closed OEMS cell, which at a leak-rate of ≈1 µL/min through the capillary limits the measurement time with a 10 mL headspace volume to ≈40 – 50h, whereas a DEMS offers a theoretically unlimited measurement time. However, the measurement time in a DEMS might also be limited by the evaporation of electrolyte into the carrier gas stream, unless the carrier gas stream is pre-wetted, or the DEMS is operated intermittently.

The first OEMS setup was developed by Tsiouvaras et al.[110] and initially used for lithium-air battery research.[113, 114] Afterwards, Metzger et al.[115] adopted it for lithium-ion battery research and developed a sophisticated two-department cell-setup that allows to deconvolute anode and cathode gassing.[29, 116, 117] The OEMS setup, the cell designs and the data analysis methodology are mainly based on the previous work carried out by Tsiouvaras et al.[110] and Metzger et al.[29, 115] As a first step of this PhD project, the same OEMS setup was installed at BASF SE Ludwigshafen and is depicted in Figure 13. The figure shows a photography of the OEMS at BASF, whereas the important parts are labeled, and described

in the figure. Starting from the right-hand side, the custom-made OEMS cell (1) can be seen which is connected to the mass spectrometer (HiQuad QMA 410, Pfeiffer Vacuum, Germany) by a crimped-capillary leak (Vacuum Technology Inc., USA) and connected to a potentiostat (not seen in the image, MPG2, BioLogic, France) for cell cycling. The cell is placed inside a temperature-controlled oven (2, KB23, Binder, Germany) and the vacuum lines towards the mass spectrometer are continuously heated to 100°C; the corresponding heat controllers (5, LC4 D, Julabo, Germany) are placed on top of the climate chamber. Furthermore, a gas supply is available which is used to purge the cell with calibration gasses (3); in order to purge the gas supply lines, an external gas outlet is also available (4). In between the stainless-steel cell and the mass spectrometer, a ceramic insulation (6, Ceramic Seals, UK) is placed within the vacuum lines, which isolates the cell from the MS and avoids parasitic currents. The mass spectrometer itself consists of an ionization source (7), a quadrupole analyzer (8) and a Faraday cup (10) or an SEM (11) for detection and operates under vacuum ($\approx 10^{-7}$ mbar) which is enabled by a turbo pump (12, HiPace 300, HiPace 300, Pfeiffer Vacuum, Germany). Furthermore, a control unit (HiQuad QC 700, Pfeiffer Vacuum, Germany) and a high-frequency generator (QMH 400-1, Pfeiffer Vacuum, Germany) are required, as well as a pre-vacuum pump (HiPace 80, Pfeiffer Vacuum, Germany) to evacuate the lines from ambient pressure which is required to prevent damage to the mass-spectrometer. Those electrical parts of the OEMS setup are placed outside the fume hood and cannot be seen on the image in Figure 13.

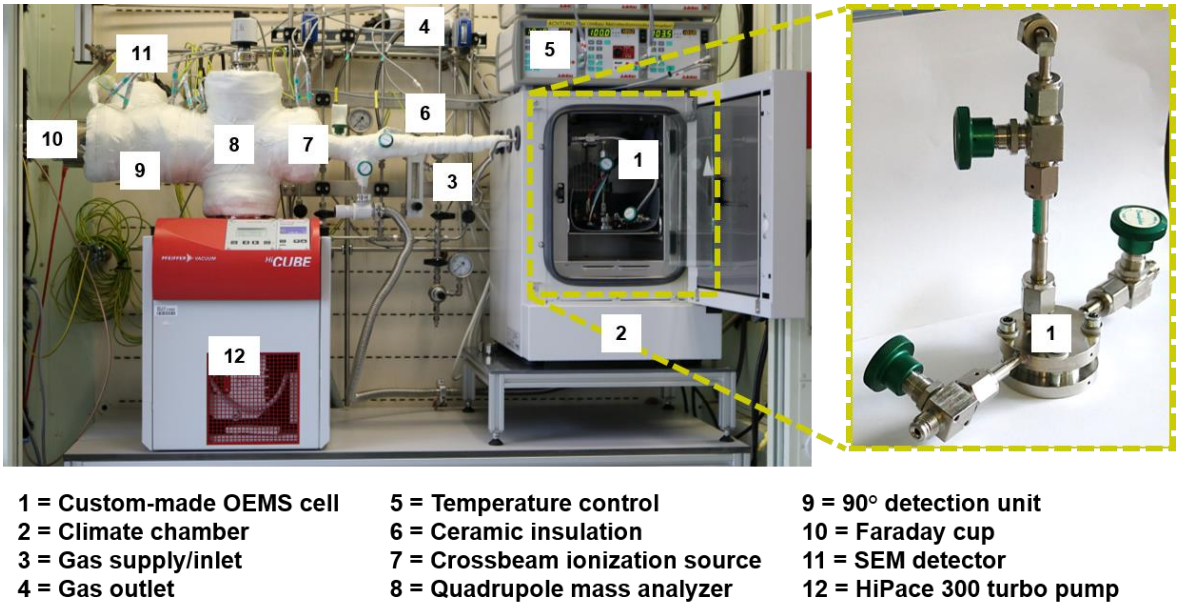

Figure 13. Photograph of the OEMS setup at BASF. The most important parts are labeled by numbers which are described on the bottom. Furthermore, a photograph of the custom-made OEMS cell is shown on the right side.

On the right-hand side of Figure 13, the custom-made stainless-steel OEMS cell (1) is shown. It has a head-space volume of ≈10 mL and is connected to the OEMS by a crimped-capillary leak (Vacuum Technology Inc., USA) that allows to pull out ≈1 µL/min from the cell to the OEMS. The detailed cell design is reported by Tsiouvaras et al.[110] and Metzger et al.[29, 115] The electrode stack assembly in an OEMS cell is similar to that used in a coin-cell (as discussed in **Section 2.1**). Figure 14 shows schematics of a one-compartment and of a sealed two-compartment OEMS cell setup.[29] For both cell designs, a working electrode with a diameter of 15 mm and a lithium metal counter electrode with a diameter of 17 mm is used within this PhD project (note that also other counter electrodes can be used). The working electrodes are coated onto a porous medium, which was a stainless-steel mesh for the cathode materials used in the one-compartment cells and a Celgard® separator for the carbon electrodes in the two-compartment cells; a detailed description of the electrode preparation can be found in **Section 3.1.2**, **Section 3.2.1**, **Section 3.2.2** and **Section 3.3**. For both cell setups, it is important that the working electrode is placed upside down on the electrode stack, with the active material pointing towards the capillary in order to enable

unhindered gas diffusion towards the capillary leak to the mass spectrometer. The main difference between the two cell setups is the edge-sealed Ohara glass (a lithium-ion conducting solid electrolyte) that is placed in between the working and the counter electrode in the two-compartment cell. The sealed Ohara glass can separate the gasses from the lower and the upper compartment and thus allows to detect gas evolution/consumption from the working electrode compartment (here the upper compartment) without interference from gas species evolved/consumed at the counter electrode (here the lower compartment).[29, 118] The one-compartment cell was used in **Section 3.1.2**, **Section 3.2.1**, **Section 3.2.2** and **Section 3.3**; the two-compartment cell was used in **Section 3.2.1** and **Section 3.2.2**. The exact cell components used for the different studies as well as the amount of electrolyte is given separately in each of the studies.

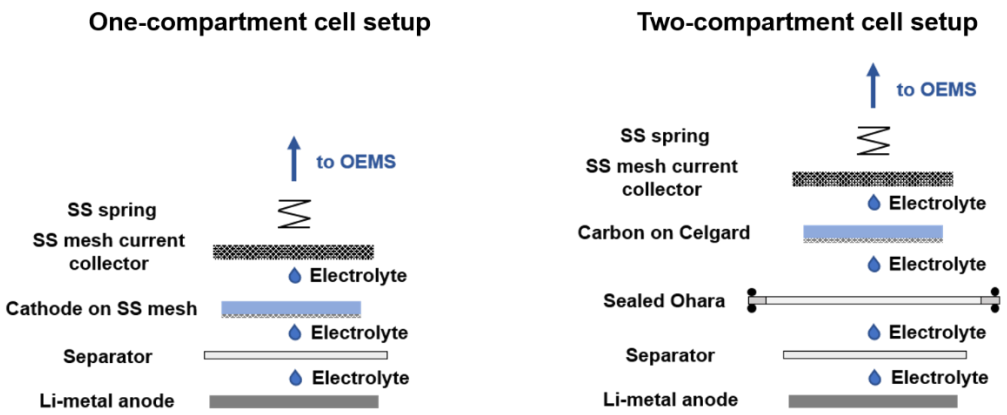

Figure 14. Schematic cell setups for a one-compartment (left panel) and a two-compartment (right panel) OEMS cell with a sealed Ohara glass, as designed by Metzger et al.[29]

A typical raw data set obtained from the mass spectrometer during an OEMS measurement is depicted in Figure 15, showing the ion current signal (m/z) plotted vs. time. To mitigate artefacts due to temperature or pressure fluctuations, the ion current signal is normalized by the signal of the ^{36}Ar isotope (m/z =36), as shown in the y-axis in Figure 15. During the whole procedure, the signals 1-120 are continuously recorded with a dwell time of 100 ms. The OEMS cells are assembled in an argon filled glovebox (O_2 <0.1 ppm, H_2O

<0.1 ppm, MBraun, Germany) and connected to the mass spectrometer. Then, the cell is held for 4h at OCV in order to get a stable background signal prior to the measurement. This background value is then extrapolated as background signal during the actual OEMS measurement (see "Baseline fit" Figure 15). An electrochemical cycling procedure is carried out and allows a measurement time of 40-50 h, as discussed before. After cycling, the cell is purged for 20 min with argon in order to remove the reaction gasses, and a background baseline for the calibration is set. For calibration, the cell is purged for 20 min with a calibration gas mixture containing H_2, O_2, CO_2, C_2H_4, each at a concentration of 2000 ppm. For data evaluation the signals are smoothed with a Savitzky-Golay function and the baseline fit is subtracted from the actual signal during electrochemical cycling. The signal can be quantified with by the calibration routine, resulting in gas amounts in ppm. These values can be translated in [µmol] using the pressure, the cell volume, the temperature, and the molar gas volume.

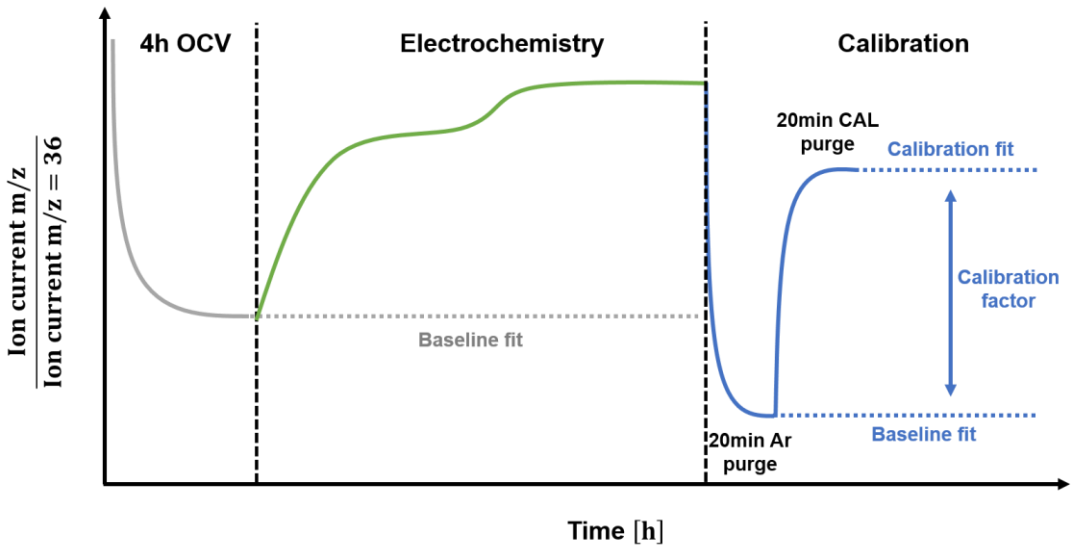

Figure 15. Typical measurement routine of an OEMS measurement with an initial OCV phase, the actual electrochemical measurement and the calibration routine, as described by Metzger.[115]

2.4. Further techniques

In the following, further techniques that were used during this PhD project for material characterization and analysis of failure mechanisms are listed. High-resolution transmission-electron microscopy (HRTEM) was used in **Section 3.1.2** in order to visualize the surface layer of HE-NCM, stemming from material degradation due to O_2-release. Samples for HRTEM were prepared by focused ion beam (FIB) milling using a Strata 400 dualbeam machine (FEI Company, Hillsboro, USA). The samples were immediately imaged at 200 keV by HRTEM on FEI Tecnai G20 and FEI Osiris microscopes. The local crystal structure of oriented crystallites was analyzed by Fourier-analysis of the images using the Digital Micrograph software (Gatan, Pleasanton, USA: version 2.11).

Further techniques that were used for material characterization are listed in the following. X-ray photoelectron spectroscopy (XPS) that was used for surface analysis of the washed NCM samples in **Section 3.3**. BET sorption measurements for the determination of the surface area of the active materials used for the electrochemical experiments in **Section 3.1.1**, **3.1.2**, **3.2.1**, **3.2.2**, and **3.3**. Furthermore, we used ^{1}H-NMR spectroscopy in **Section 3.2.2** to analyze the purity of the carbonate-based electrolyte mixtures. Inductive-coupled plasma attached to a mass spectrometer (ICP-MS) was applied to quantify the amount of transition metals that deposited on the graphite anodes in **Section 3.2.2**. We used gas-chromatography coupled to a mass spectrometer (GC-MS) for the analysis of the reaction gasses evolved from the FEC-containing multi-layer pouch-cells in **Section 3.2.2**.

3. Results

The following section contains the journal articles that were published during this PhD project and manuscripts that are ready for submission. The articles are thematically sorted in three different topics. **Section 3.1** shows a detailed analysis of the material properties of overlithiated layered oxides, whereby one can distinguish between intrinsic bulk reaction mechanisms and oxygen release from the surface of the material. Thus, **Section 3.1.1** presents a careful analysis of the state-of-charge dependent resistance of overlithiated NCMs, and correlating it to the intrinsic bulk properties, such as transition metal migration and oxygen redox. In order to analyze the impact of oxygen release onto the bulk properties of the material, **Section 3.1.2** focuses on the OEMS analysis of the gas evolution from overlithiated NCMs (i.e., HE-NCMs) in the initial charge/discharge cycles. HE-NCMs with different Li_2MnO_3 contents are investigated and the changes of the surface structure of the HE-NCM particles is analyzed by HRTEM and correlated to the oxygen release detected by OEMS.

Based on this understanding of the cathode active material, **Section 3.2** focuses on the compatibility of conventional electrolyte solvents with HE-NCM which is critical for long-term cycling stability. The choice of the cyclic carbonate is discussed in **Section 3.2.1**, using OEMS and full-cell cycling experiments. It turns out that EC-based electrolytes cannot be used due to the high oxygen release from HE-NCM in the first charge/discharge cycles, while FEC as co-solvent shows much better cycling performance. The analysis of the thermal stability of the FEC-based electrolyte is shown in **Section 3.2.2**, suggesting that the use of FEC as co-solvent is only a temporary solution for cycle-life stabilization of oxygen releasing materials. For this, the thermal decomposition mechanism was analyzed in detail analyzed by OEMS, by cycling experiments, and by ^{1}H-NMR.

Based on these mechanistic results, strategies to improve the cycling performance by a surface stabilization of layered oxides rather than by enhancing the stability of the electrolyte are explored. As a viable strategy, aqueous washing of Ni-rich NCM 851005 is investigated in **Section 3.3** and a detailed mechanistic understanding is presented. In this

regard, we can define a promising path forward for all types of layered oxides, showing that oxygen release can be mitigated for Ni-rich NCM by a simple aqueous washing step.

3.1. Distinction between bulk and surface ageing of lithium- and manganese-rich layered oxides

The target of the first step of this thesis is to develop a fundamental understanding about the electrochemical properties and the degradation mechanisms of the cathode active material itself. While electrochemical properties, such as voltage-fading and hysteresis are ascribed to bulk phenomena,[62] it is still unclear how these intrinsic material characteristics depend on the release of oxygen. Initially, it has been suggested that Li_2MnO_3 activation, accompanied by oxygen release, takes place during the activation and causes voltage-fading and hysteresis.[59, 74] However, more recent studies claim that oxygen release occurs as surface phenomenon and leads to a densification of the surface by the formation of a disordered surface layer.[73, 119, 120] In a first step, we show a detailed resistance analysis of Li- and Mn-rich NCMs, where we could correlate the high resistance at low SOCs to a disordered surface layer, while reversible bulk transition metal migration shows up as highly SOC- and path-dependent resistance during discharge. As a second step, we quantified the amount of oxygen released from Li- and Mn-rich NCMs with different Li_2MnO_3 contents and could show oxygen release occurring as surface phenomenon. However, when very high Li_2MnO_3 contents are used, oxygen release starts to occur also in the bulk of the material, which can explain reports that correlate oxygen release to bulk structural changes.[121, 122]

3.1.1. Bulk transition metal migration and resistance build-up

This section presents the article "State of Charge Dependent Resistance Build-Up in Li- and Mn-rich Layered Oxides During Lithium Extraction and Insertion".[123] It was submitted in February 2019 and published in April 2019 as peer-reviewed publication in the *Journal of the Electrochemical Society*. It is published as an open access article and distributed under the terms of the Creative Commons Attribution Non-Commercial Non-Derivatives 4.0 License. The permanent web-link to the article is provided under: http://jes.ecsdl.org/content/166/6/A1275.full. The paper was presented by Tobias Teufl as poster at the GDCh Electrochemistry 2016 (September 26th – 28th, 2016) in Goslar, Germany.

Overlithiated Li- and Mn-rich NCMs (HE-NCM) offer high reversible capacities (≈250 mAh/g)[58, 124] at low material cost, which makes them a promising candidate as future cathode active material for lithium-ion batteries. However, their high degree of delithiation and their high cutoff potentials trigger structural instabilities that lead to several challenges that need to be taken into account before commercialization.[62] One of the issues is a high resistance build-up and a highly SOC dependent behavior of these resistances. While the exact understanding of this behavior of the resistance is essential for practical applications and the design of a battery management system, only a small number of scientific reports focus on the SOC dependence of the resistance.[125-130] In this regard, Gowda et al.[126] showed a high resistance occurring at low SOCs and suggested a correlation to the lithium- and manganese-rich domains, but they could not clarify the exact reason or a detailed mechanism. Furthermore, Assat et al.[125] suggested a path dependency of the kinetics to be caused by anionic oxygen redox. However, there is still a lack of understanding about the exact mechanism of these high resistances and the correlation towards the electrochemical properties of these materials.

In this study, we analyze in detail the resistance of activated and non-activated HE-NCM and can assign the path dependency of the resistance to be caused by the activation process and the associated bulk structural changes. As a first step, we use a micro-reference electrode[105] to deconvolute the impedance within a full-cell and to analyze the individual contributions of the cathode impedance. Based on this analysis, we evaluate the resistance

obtained by 10 s full-cell pulses, which we apply as easily accessible method to measure the resistance during cycling. It is clearly shown that the high resistance and the path dependency of the resistance is only observed for a material that is activated during the first cycle. After activation a high resistance at low SOCs is observed, which is in line with the observations by Gowda et al.[126] We can assign this resistance to an oxygen depleted surface layer which is formed upon activation and cycling of HE-NCM.[60, 73] Furthermore, the analysis of the path dependency of the resistance results in a dependency on the upper cutoff potential, proving that higher cutoff potentials lead to an increased discharge resistance. Based on previous publications,[77, 78, 125] we suggest that the path dependency of the resistance is caused by reversible transition metal migration, which is closely linked to anionic oxygen redox.[77]

Author contributions

T.T. and D.P. carried out the electrochemical experiments. T.T. carried out the data analysis. All authors discussed and commented the data, as well as the conclusions. T.T. wrote the manuscript. M. M. and H.A.G. edited the manuscript.

EDITORS' CHOICE

State of Charge Dependent Resistance Build-Up in Li- and Mn-Rich Layered Oxides during Lithium Extraction and Insertion

Tobias Teufl,[1,2,z] Daniel Pritzl,[2,*] Sophie Solchenbach,[2,*] Hubert A. Gasteiger,[2,] and Manuel A. Mendez[1]**

[1]*BASF SE Ludwigshafen, New Battery Materials and Systems, D-67056 Ludwigshafen, Germany*
[2]*Chair of Technical Electrochemistry, Department of Chemistry and Catalysis Research Center, Technical University of Munich, D-85748 Garching, Germany*

Lithium- and manganese-rich layered oxide-based cathode active materials (often referred to as HE-NCM) exhibit high reversible specific capacity (≈250 mAh/g) and could improve future lithium-ion batteries in terms of energy density and safety, while offering lower cost. Unfortunately, drawbacks such as voltage-fading, hysteresis, and increasing cathode impedance over charge/discharge cycling have so far hindered its commercialization. In this study, we examine the reasons and the implications of the high resistance build-up of this material in graphite//HE-NCM full-cells. Impedances/resistance were obtained either by electrochemical impedance spectroscopy (EIS) with a micro-reference electrode or by current pulse measurements (so-called direct-current internal-resistance (DCIR) measurements). These data show that the so-called activation of the material above 4.5 V vs. Li^+/Li leads to an asymmetric high charge-transfer impedance at low state-of-charge (SOC) between charge and discharge, manifested as an anomalous cell resistance hysteresis which increases over cycling and with increasing upper cutoff potentials. These findings are rationalized by reversible transition-metal migration phenomena.

 [DOI: 10.1149/2.1131906jes]

Manuscript submitted February 15, 2019; revised manuscript received March 29, 2019. Published April 16, 2019.

To address the future demand for sustainable and environmental friendly transportation, alternatives to classical combustion engines are required and lithium ion batteries have become an attractive option, as they offer high energy densities and as they have already been proven in consumer electronics for many years.[1–3] When Sony commercialized the first lithium-ion battery in the early 1990's, it was based on the use of a graphite anode and a $LiCoO_2$ (LCO) cathode.[3,4] Since then, much effort has been expended in developing and implementing new cathode active materials (CAMs) which would offer higher capacities, and promising performance has been shown by stoichiometric layered lithium-nickel-cobalt-manganese-oxides ($LiNi_xCo_yMn_zO_2$, with x+y+z = 1), commonly referred to as NCMs, which also offer the possibility to finetune their properties by changing the ratios between the transition metals.[5–7] Initially, NCM materials with a Ni:Co:Mn ratio of 1:1:1 were investigated (referred to as NCM-111), while more recently nickel-rich materials (e.g., Ni:Co:Mn = 8:1:1, referred to as NCM-811) have been favored, as they offer high capacities at more moderate upper cutoff voltages.[8] However, even with nickel-rich materials, a reversible capacity of 200 mAh/g cannot be exceeded due to structural instabilities at high degrees of delithiation, leading to oxygen release from the surface[9] and, ultimately, to a collapse of the bulk structure.[10]

A promising attempt to further increase the energy density of layered oxide based CAMs are composite materials consisting of x Li_2MnO_3 • 1-x $LiMO_2$ (M = Ni, Co, Mn), so-called overlithiated NCM materials, also referred to as high-energy NCM (HE-NCM).[11–13] A special feature of these materials is the long activation plateau occurring at 4.5 V vs. Li^+/Li during the first charge cycle, whereby charging beyond this plateau leads to high reversible capacities of around 250 mAh/g.[11,14] As the high capacities after activation cannot be explained by classical cationic redox, the material has been extensively studied, seeking to find an explanation for the high reversible capacities. Initially, the activation plateau was associated with a bulk oxygen release from the Li_2MnO_3 domain, leading to electrochemically active $LiMnO_2$,[11–17] and it was suggested that the oxygen release also would initiate phenomena like the 1 V hysteresis of the material[18] as well as the observed voltage-fading over the course of charge/discharge cycling, ultimately leading to a spinel structure in the bulk of the material.[12,13,18–20] Even though it is still subject of ongoing discussions, more recent studies suggest that the bulk and the surface of HE-NCM show distinctly different behaviors: while oxygen release and spinel formation was shown to occur only in surface-near regions,[21–24] there is strong evidence that anionic oxygen redox in the bulk of HE-NCM materials is the cause for the high reversible capacities.[21,22,25–28] Furthermore, it is suggested that irreversible delithiation of the transition-metal layer occurs during the activation plateau[29,30] and triggers disorder and transition-metal migration within the bulk material, which might be the explanation for the charge/discharge hysteresis and for the voltage fading of activated HE-NCM.[31–35]

Besides voltage-fading and charge/discharge hysteresis, another major drawback of HE-NCM that has hindered its commercialization so far is the high impedance of the material,[36–40] particularly at low state-of-charge (SOC).[37,38,41] On the one hand, it has been shown in the literature that sluggish bulk diffusion leads to poor rate capabilities and high resistances;[40,42] on the other hand, there is also clear evidence that restructuration in surface-near regions contributes to a resistive surface layer which slows down lithium diffusion.[24] Furthermore, it has been suggested that lithium re-intercalation into the cathode material during discharge is much more hindered than lithium de-intercalation during charge.[38–40,42] In this context, Zheng et al.[40] remarkably showed that overlithiated oxides have a good rate performance during fast charging, while fast discharging alters the material significantly. Assat et al.[43] recently suggested for the $Li_2Ru_{0.75}Sn_{0.25}O_3$ model compound that high-voltage charging strongly alters the material and leads to a deterioration of the materials kinetics. Furthermore, they suggested that the reversible anionic oxygen redox causes the slow kinetics and the high resistances.[43] However, there is still a lack of understanding to what extent structural changes on the surface versus in the bulk material might be responsible for those high resistances.

In this study, we will examine the resistance build-up mechanisms of HE-NCM, namely of 0.42 Li_2MnO_3 • 0.58 $LiMeO_2$ (Me = Ni, Co, Mn), using electrochemical impedance spectroscopy (EIS) and power pulse testing over 150 charge-discharge cycles in graphite//HE-NCM full-cells. By using a micro-reference electrode,[44] we can deconvolute the impedance of the anode and the cathode to analyze their individual contributions to the cell impedance obtained by EIS, which we then compare to the resistance obtained via 10 s power pulses. The latter

*Electrochemical Society Student Member.
**Electrochemical Society Fellow.
[z]E-mail: tobias-maximilian.teufl@basf.com

will then be applied to analyze the resistance build-up during cycling, as it is more easily accessible and expeditious for full-cell resistance measurements. We show that the activation of HE-NCM leads to high impedance at low SOCs, which is in line with the findings by other groups.[38,39] We ascribe this phenomenon to the reversible lithiation of an oxygen depleted surface layer, whereby this surface layer is formed upon the activation and cycling of HE-NCM.[24] Furthermore, our data reveal that there is a significant hysteresis between the impedance at low SOC, with a higher impedance during discharge compared to charge at the same SOC. Interestingly, this hysteresis gets more pronounced upon extended charge/discharge cycling and can be correlated to distinct discharge features in dQ/dV plots. Here, it should be noted that for non-activated HE-NCM there is no hysteresis in the impedance and that the dQ/dV plot indicates fully-reversible behavior. Finally, we show that the impedance hysteresis at low SOC for activated and cycled HE-NCM increases with increasing upper cutoff potentials and that it disappears once the cells are discharged to 2.0 V. The possible processes which might cause the observed impedance hysteresis and its strong dependence on SOC will be discussed at the end of this work.

Experimental

Electrode preparation.—HE-NCM with the composition 0.42 Li_2MnO_3 • 0.58 $LiNi_{0.38}Co_{0.21}Mn_{0.41}O_2$ was obtained from BASF SE (Germany). For coin-cell testing, inks for cathode electrode preparation contained 92.5 wt.% HE-NCM (BASF SE, Germany), 3.5 wt.% polyvinylidene-fluoride binder (PVDF, Solef 5130, Solvay, Belgium), 2 wt.% conductive carbon (Super-C 65, Timcal, Switzerland; BET area of ≈65 m^2/g), and 2 wt.% graphite (SFG6L, Timcal, Switzerland; BET area of ≈17 m^2/g). These materials were dispersed in N-methyl pyrrolidine (NMP, anhydrous, Sigma-Aldrich, USA) and coated onto aluminum foil (16 μm). Dried electrodes were calendered to a density of 2.3 g/cm^3, resulting in a final electrode thickness of 20 μm. For electrochemical testing, electrodes with 11 mm (for Swagelok T-cells), or 14 mm (for 2032-type coin-cells) were punched out and weighed. The active material loading was ≈6.5 mg/cm^2, corresponding to ≈1.6 mAh/cm^2 (based on a nominal reversible capacity of 250 mAh/g).

Graphite anodes were commercial electrodes with a graphite loading of ≈6.7 mg/cm^2, corresponding to ≈2.4 mAh/cm^2 (based on a theoretical capacity of 360 mAh/g). For electrochemical testing, graphite electrodes with a diameter of 11 mm (for Swagelok T-cells), or 15 mm (for 2032-type coin-cells) were punched out. All anode and cathode electrodes were dried overnight under vacuum in an oven within the glovebox (O_2, H_2O < 0.1 ppm, MBraun, Germany) at 120°C and were not exposed to air after the drying procedure.

Electrochemical characterization.—Two different cell setups were used: i) Swagelok T-Cells with a gold-wire micro-reference electrode (GWRE)[44] were used for the EIS measurements and current pulse measurement validation (based on Figure 3), whereby anode and cathode resistances could be determined individually; ii) coin-cells were used for long-term cycling experiments with current pulse measurements, for which the overall full-cell resistance cold be determined. 2032-type coin-cells were assembled in an argon filled glovebox using a graphite anode (15 mm diameter), two glass fiber separators (200 μm thickness, VWR, Germany), and a HE-NCM cathode (14 mm diameter). The cells were filled with 95 μL of electrolyte, based on FEC:DEC (12:64 v:v) with 1M $LiPF_6$ and 24 $\%_{vol.}$ of an additional fluorinated co-solvent to improve full-cell cycling stability. Swagelok T-Cells were also assembled in an argon filled glovebox using a graphite anode (11 mm diameter), two glass fiber separators (200 μm thickness, VWR, Germany), and an HE-NCM cathode (11 mm diameter). The cells were filled with 60 μL of the same electrolyte that was used for the coin-cells. Furthermore, the Swagelok T-Cells were equipped with a gold micro-reference electrode (for details see Solchenbach et al.).[44]

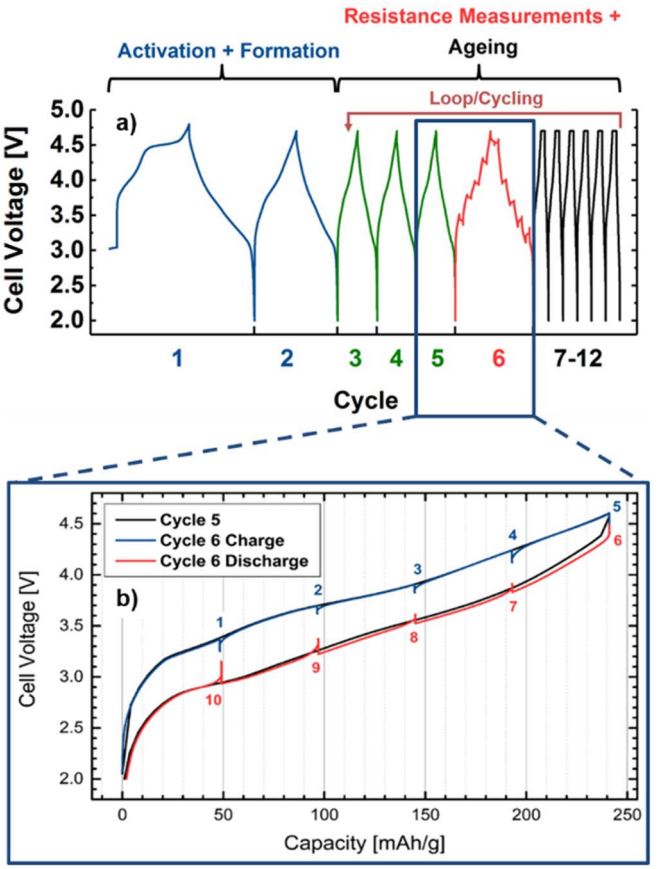

Figure 1. a) Graphic representation of the cycling procedure, with the initial cell activation (2.0–4.7 V at 0.067C CC) and cell formation (2.0–4.6 V at 0.1C CC) in blue. The repeat unit for extended cycling consists of 10 cycles: the green lines depict three slow cycles at 0.2C (2.0–4.6 V) at constant current (CC) to adjust the SOC for the resistance measurements at various SOCs in the fourth cycle at 0.2C, shown in red (2.0–4.6 V), followed by six cycles at fast C-rates for cell aging (2.0–4.6 V) with a charge at 0.5C +1 h CV and a discharge at 1C. b) Voltage versus capacity plots of cycle 5 and 6, marking the points for the resistance/impedance measurements at 20% SOC intervals during charge and discharge. These data were recorded in CR2032-type coin-cells.

All cells were tested at 25°C in a temperature-controlled oven (Binder, Germany) using a battery cycler (Series 4000, Maccor, USA). The cycling procedure is depicted in Figure 1a and consisted of the following steps: i) one activation cycle at a C-rate of 0.067C (2.0–4.7 V) and one formation cycle at a C-rate of 0.1C (2.0–4.6 V), shown in blue; ii) the resistance measurement sequence, consisting of 3 cycles at 0.2C (2.0–4.6 V; green lines) to equilibrate the cell to the different C-rate and to set the actual capacity which is used to adjust the different SOC-values during the fourth cycle at 0.2C (2.0–4.6 V; red lines), where EIS and/or pulse current resistance are being obtained; and, iii) 6 fast cycles (black lines) for cell aging, where the cells were charged/discharged between 2.0–4.6 V with 0.5C (CCCV)/1C (CC), whereby all CV-steps were terminated after 1 h or when the current decreased below 0.01C. The first two cycles (blue lines) were only carried out once, while all other cycle sequences were repeated over the course of extended cycling (as shown in Figure 1). The diagnostic cycles with the resistance measurements where conducted every 10 cycles starting from cycle 6, as shown by the cycling loop in Figure 1a. This means that the resistance was measured after 6, 16, 26, 36, 46 cycles and so on. Note that here all C-rates are referenced to the nominal capacity of the HE-NCM of 250 mAh/g (i.e., 1C ≡ 250 mA/g or 1.6 mA/cm^2).

A typical voltage versus capacity profile is shown in Figure 1b for the cycle at 0.2C just prior to the resistance/impedance

measurements (5th cycle, black line) as well as for a cycle during which resistance/impedance measurements are conducted (6th cycle; red and blue line). A comparison between these two cycles shows that the resistance/impedance measurements do not influence the overall electrochemical performance. For the example shown in Figure 1b, the resistance measurements were conducted in steps of 20% SOC; for the long-term cycling experiments, they were conducted in steps of 10% SOC, otherwise following the very same procedure. Before the resistance/impedance was measured, the cells were set to rest for 1 h at 25°C, which is reflected by the potential relaxations in Figure 1b.

The resistance was measured by two different approaches at 25°C. One was to conduct electrochemical impedance spectroscopy in galvanostatic mode (GEIS) over a wide frequency range (100 kHz to 60 mHz with an amplitude of 0.9 mA), using a potentiostat (VMP300, BioLogic, France). These experiments were done with Swagelok T-cells equipped with a micro-reference electrode, so that anode and cathode impedances could be determined individually. The other approach was based on current pulse measurements, also referred to as Direct Current Internal Resistance (DCIR),[45] which we conducted either Swagelok T-cell with micro-reference electrode or in coin-cells without reference electrode. DCIR measurements were conducted applying a 10 s long negative current pulse of 0.2C (≡0.32 mA/cm^2) to the cell after a 1 h rest at OCV (open circuit voltage); the resistance was calculated from the difference between OCV and the potential at the end of the pulse (i.e., after 10 s) divided by the pulse current, as reported elsewhere.[45] To judge the reproducibility of the resistance/impedance data, at least two independent measurements were carried out, and the here presented cycling and resistance/impedance data show the average values, with the error bars reflecting the maximum and minimum of the measured values.

Results and Discussion

Measurement and validation of the full-cell resistance by DCIR.—It has been reported in the literature that overlithiated oxides show drastic increase in resistance upon cycling,[24] which in term might be caused by sluggish kinetics after the activation of the material. Furthermore, it was proposed that charge and discharge follow different pathways and kinetics for lithium extraction and insertion show distinct differences.[38,43] To explore the different contributions to the resistance in graphite//HE-NCM full-cells, we assembled Swagelok T-cells with a micro-reference electrode.[44] This lithiated gold micro-reference electrode allows to differentiate between anode and cathode impedance in a full-cell without disassembling the cell. With this setup, EIS data and current pulse responses were measured after according to the cycling procedure outline in Figure 1 for several SOCs. Figure 2 shows exemplary Nyquist plots for the measurement at 20% SOC during charge for both the cathode (Figure 2b) and the anode (Figure 2c), whereby the red dots represent the measured data and the blue lines are the results from the fitting. The Nyquist plot for the cathode impedance (Figure 2b) shows a high frequency resistance of ≈6 Ωcm^2 as well as two distinct semi-circles, one at high frequencies that has a resistance of ≈4 Ωcm^2 and one at lower frequencies that has a resistance of ≈28 Ωcm.^{2} The impedance spectra were fitted with the equivalent circuit model shown in Figure 2a, whereby the high frequency resistance is described by a simple resistor (R_{HFR}) and the two semi-circles where fitted with two R/Q elements (R = resistor, Q = constant phase element). Note that when using the micro-reference electrode, R_{HFR} of the cell is split into two essentially equal HFR contributions from the anode ($R_{HFR,anode}$) and cathode ($R_{HFR,cathode}$).[44] Previous studies have shown that the first semi-circle of the cathode impedance (R_1/Q_1) shows up at high frequencies (>5 kHz) and can be assigned to a contact resistance at the interface of the cathode electrode with the aluminum current collector.[24,46–48] This can be rationalized by considering the electrode capacitance corresponding to this first semi-circle:

$$C_1 = \frac{1}{R_1\ 2\ \pi\ f_{max}} \quad [1]$$

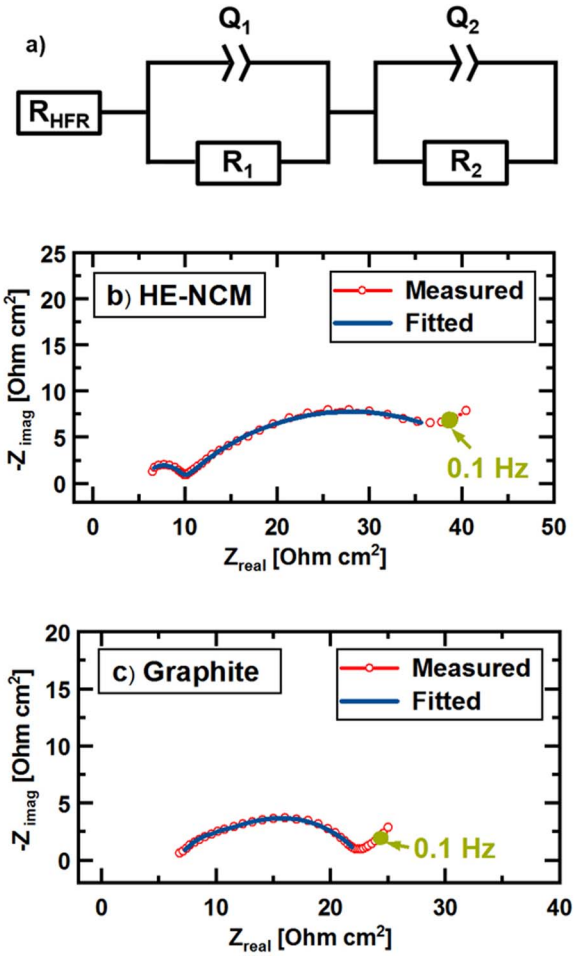

Figure 2. a) Equivalent circuit model for the fitting of the anode and the cathode impedance spectra. Exemplary Nyquist plots obtained from a graphite// HE-NCM full-cell with a micro-reference electrode[44] at 20% SOC during charge (for cycle 6 in Figure 1) are shown for individually for: b) the cathode and c) the anode. The measured data are shown by the red dots and the fitted data are represented by blue lines, while the green dots mark the impedance at 0.1 Hz. Galvanostatic impedance spectra were measured at 25°C from 100 kHz to 60 mHz with an amplitude of 0.9 mA.

where C_1 is the capacitance (approximated from the constant phase element Q_1), R_1 is the diameter of the semi-circle, and f_{max} is the frequency corresponding to the apex of the first semi-circle. For the data shown in Figure 2b, the resistance is R_1 ≈4 Ω and f_{max} ≈31 kHz, equating to an electrode capacitance of ≈1 μF. To examine its origin, the capacitance can be normalized either to the geometric surface area of the aluminum current collector (≈0.95 cm^2) or to the surface area of the cathode electrode (≈450 cm^2, based on mass and BET surface area of the HE-NCM and the conductive carbons within the electrode). This equates to normalized capacitances of either ≈1.1 μF/cm^2 or ≈0.002 μF/cm^2. Comparing these to a typical double-layer capacitance, which is in the order of ≈10^1 μF/cm^2,[49] it is clear that the first semi-circle must correspond to a contact resistance at the interface between the cathode electrode and the current collector ($R_{contact}$). Detailed analysis onto the origin of these contact resistance can be found elsewhere.[46–48] The second somewhat depressed semi-circle of the cathode impedance (R_2/Q_2), occurring in the lower frequency region, can be assigned to the charge-transfer resistance of the cathode ($R_{CT,cathode}$). Thus, the cathode impedance can be defined as:

$$R_{cathode} = R_{HFR,cathode} + R_{contact,cathode} + R_{CT,cathode} \quad [2]$$

The Nyquist spectra of the anode impedance (Figure 2c) shows a high frequency resistance of $R_{HFR,anode}$ ≈ 7 Ωcm^2 and a superposition

of two semi-circles with a total diameter of ≈15 Ωcm^2, which was fitted with the same equivalent circuit model (Figure 2a), containing two R/Q elements. The first R/Q element (R_1/Q_1) can be assigned to the SEI resistance/capacitance and the second R/Q element (R_2/Q_2) describes the charge-transfer resistance. Thus, the anode impedance can be defined as:

$$R_{anode} = R_{HFR,anode} + R_{SEI,anode} + R_{CT,anode} \quad [3]$$

Furthermore, the full-cell resistance can then be defined as the sum of anode and cathode resistance:

$$R_{cell} = R_{cathode} + R_{anode} \quad [4]$$

Simple current pulses are often used in order to have an easy and fast method to determine the cell resistance and the resistance build-up;[36,38] this method is also referred to as DCIR method (Direct Current Internal Resistance).[45] As the response to current pulses is strongly dependent on the current and the pulse duration, we carefully chose the duration and the current of the pulse in order to minimize changes of the SOC and to receive results that are comparable to the low frequency resistance obtained by EIS measurements. Therefore, the pulse was applied from OCV always with a negative current (i.e., a discharge current) of 0.2C for a duration of 10 s, corresponding to a change in SOC of 0.06%, which we consider to be negligible. From the difference between OCV and the voltage at the end of the pulse (i.e., at 10 s) and the pulse current, the effective resistance was calculated using Ohm's law (for details see reference[45]). To quantify the resistance contributions from anode and cathode, we conducted the DCIR measurements in the same Swagelok T-cell setup with micro-reference electrode that was used for the EIS measurements. Please note that at each SOC, the cell was rested at OCV for 1 h before the 10 s current pulse was applied, followed by a 5 min rest before the impedance measurements were carried out. With this sequence, we expect that the EIS results are not influenced by the DCIR measurements or vice versa. To differentiate between the low frequency resistance obtained by EIS measurements and the DCIR, we will refer to the latter as area specific resistance (ASR, referenced to the geometric surface area). The ASRs measured in the Swagelok T-cells with micro-reference electrode are defined as follows:

$$ASR_{cell} = ASR_{cathode} + ASR_{anode} \quad [5]$$

As the resistances obtained from the DCIR measurements are strongly dependent on time and duration of the current pulse, its value needs to be compared to full EIS measurements in order to understand its physical meaning. Therefore, Figures 3 compares the results from the fitted impedance spectra (EIS, blue lines) with the resistances measured by the DCIR method with 0.2C discharge current pulses for 10 s (DCIR, green lines). Figures 3a–3c depict the anode, cathode, and full-cell resistances versus SOC as the cell is either being charged (square symbols) or being discharged (triangular symbols), whereby the EIS data correspond to the sum of $R_{HFR}+R_1+R_2$ shown in Figure 2a (referred to further on as low frequency resistance) and the DCIR data are the resistance calculated from the 10 s pulse (always a discharge pulse). These resistances are plotted versus the capacity (every Δ20% SOC), starting at ≈47 mAh/g (≡20% SOC) up to ≈235 mAh/g (≡100% SOC for an upper limit of 4.6 V). The EIS based low frequency resistances of the graphite anode (blue symbols/lines in Figure 3a) are roughly constant (≈22–24 Ωcm^2) and independent of whether the cell is being charged or being discharged. The latter behavior is also observed for the DCIR-values of the anode (green symbols/lines in Figure 3a), even though its values (≈29–31 Ωcm^2) are ≈20% higher than the EIS derived resistances. The higher values measured by DCIR can be explained by a visual comparison with Figure 2c, where the green spot marks the EIS data point at 0.1 Hz, which is the approximately equivalent nominal frequency corresponding to a 10 s pulse: its real-axis value is ≈15% higher than the low frequency resistance from the EIS fitting (i.e., ≈25 Ωcm^2 versus ≈22 Ωcm^2), reasonably consistent with the ≈20% higher 10 s DCIR value.

In contrast to the anode resistances, EIS and DCIR results for the cathode (Figure 3b) show a strong SOC dependent behavior and substantial differences between the charge (square symbols) and the discharge (triangular symbols) pathway (note: charge/discharge pathway refers to whether the cell is being charged/discharged; the pulse is always a discharge pulse). At first, we want to focus on the comparison between the resistance values based on the low frequency EIS resistance (blue symbols/lines in Figure 3b) and the DICR values (green symbols/lines in Figure 3b). Again, the former are generally lower than the latter, which we ascribe to the same effect as discussed above, namely that the real part of the resistance at 0.1 Hz (see green dot in Figure 2b) is higher than the low frequency resistance. One exception is the resistance at 235 mAh/g (≡100% SOC for an upper limit of 4.6 V), for which the EIS derived value is higher (Figure 3b); furthermore, while the EIS based resistance at 235 mAh/g should be the same for the charge and the discharge pathway, it is ≈20% higher for the former, even though these measurements are only separated by a 1 h OCV phase. To explain these differences, it is noted that in contrast to all other cathode EIS data, the Nyquist spectra at 235 mAh/g (≡100%

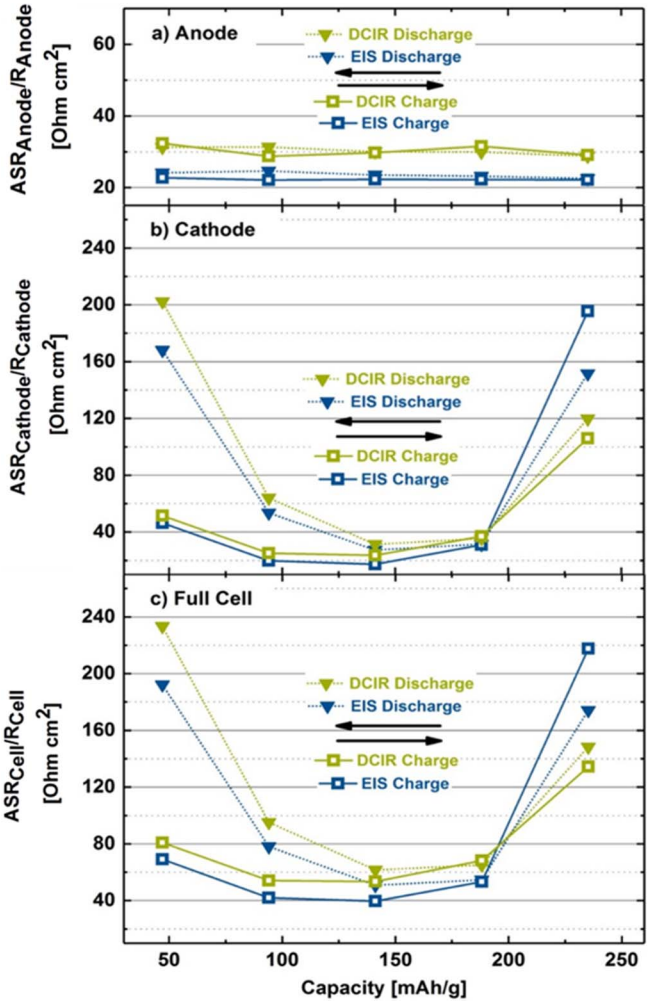

Figure 3. Resistances vs. SOC during the charge and the discharge pathway of a graphite//HE-NCM cell at 0.2C and 25°C (for cycle 6, see Figure 1), obtained from the EIS-based low frequency resistance (blue symbols/lines) and from discharge current pulses (DCIR; green symbols/lines), using a Swagelok T-cell with a micro-reference electrode. Impedance spectra were evaluated with the equivalent circuit shown in Figure 2a, while DCIR values were calculated by Ohm's law. a) Anode resistances; b) cathode resistances; and, c) full-cell resistances. The DCIR values were determined from 10 s long 0.2C discharge current pulses; impedance spectra were recorded from 100 kHz to 60 mHz with an amplitude of 0.9 mA. After charge/discharge to a certain SOC, the cell was held at OCV for 1 h before the DCIR was measured, followed by another 5 min at OCV before recording EIS data.

SOC) do not show the shape of a semi-circle (data not shown), but show a blocking electrode behavior, analogous to what can be observed for an LNMO cathode ($LiNi_{0.5}Mn_{1.5}O_4$),[47] for which all lithium can be fully extracted at 100% SOC, as is the case for the HE-NCM material. In that case, the charge-transfer reaction is hindered and capacitive coupling becomes the main process during the impedance measurement, as was shown by Landesfeind et al.[47] for a fully delithiated LNMO cathode, for which nearly perfect blocking conditions were obtained. Due to this phenomenon, namely that the EIS response of a fully delithiated cathode active material is dominated by capacitive coupling, the charge-transfer resistances obtained by fitting EIS data at 100% SOC generally show large and unreliable values, explaining the discrepancy for the two EIS measurements at 235 mAh/g in Figure 3b. As this phenomenon does not occur for discharge pulse measurements, we expect that the DCIR-based values for the cathode resistance at 235 mAh/g (≡100% SOC) are accurate and more reliable than the EIS-based values.

Finally, Figure 3c shows the full-cell resistance based on EIS (blue symbols/lines) and DCIR (green symbols/lines) measurements, which of course are simply the summation of the anode and cathode impedance. Comparing the anode and cathode contribution of the full-cell resistance (Figure 3), it is obvious that the SOC dependency and the hysteresis between the charge and the discharge pathway is caused by the cathode, while the anode only adds a more minor linear offset to the full-cell resistance. Owing to the reasonably good correlation between the EIS- and DCIR-based resistances as well as the simply linear offset and the overall minor contribution of the anode (particularly at low and high SOC), the SOC dependence of the HE-NCM resistance and its hysteresis are largely reflected by the full-cell DCIR resistances. Owing to the simplicity of full-cell DCIR measurements, requiring no reference electrode and no EIS measurements, we will now use the full-cell DCIR resistances (based on 0.2C discharge pulses over 10 s) to further investigate the unusual SOC dependence of the resistance and its hysteresis of HE-NCM cathode active materials cycled in graphite//HE-NCM full-cells. Here it should be noted that our study does not focus on the absolute resistance values, i.e., that the scope of this work is not to quantify absolute impedance build-up values, but that we rather want to characterize the charge/discharge pathway dependence of HE-NCM cathode active materials. In our opinion, the full-cell current pulse based DCIR method offers a reliable and quick access to the approximate cathode area specific resistance (ASR) for the practical and well-proven coin-cell design for long-term cycling studies.

Structural changes due to high voltage activation.—Figure 4a depicts the cycling stability of graphite//HE-NCM full-cells (coin-cells) cycled up to 4.1 V (red symbols/line, continuously cycled to 4.1 V) and cells cycled up to 4.7 V for the first-cycle activation process (black symbols/line, with subsequent cycles only up to 4.6 V). Cells cycled between 2.0 V and 4.1 V show a very good cycling stability, but since the HE-NCM was not activated, only very little capacity can be extracted from the cell (<100 mAh/g). In contrast, when HE-NCM is activated (i.e., cycled beyond the potential plateau at 4.5 V in the first cycle), a tremendous increase in the specific capacity of HE-NCM to ≈250 mAh/g is observed. Nonetheless, the cycling performance of the material deteriorates rather quickly, which can be explained by several mechanisms triggered by the cycling to high voltages, like oxygen release from the surface-near regions,[21,23,24] irreversible transition metal migration,[18,28,35] and anionic redox in the bulk.[26–28,43] After every 6 fast 0.5C/1C cycles, 4 diagnostic cycles with a charge and discharge rate of 0.2C were applied (corresponding to the procedure shown in Figure 1). From Figure 4a it can be seen that the discharge capacity for the slow (0.2C) and the fast discharge rate (1C) are essentially the same, pointing towards a continuous capacity loss caused by loss of active lithium or by loss of active cathode material due to side reactions.[24] However, Figure 4a clearly points out that cycling to high voltages (e.g. 2.0–4.6V in a full-cell) is required in order to achieve high capacities that make the material interesting for commercial applications and one has to deal with the structural drawbacks that are associated with the high-voltage activation.

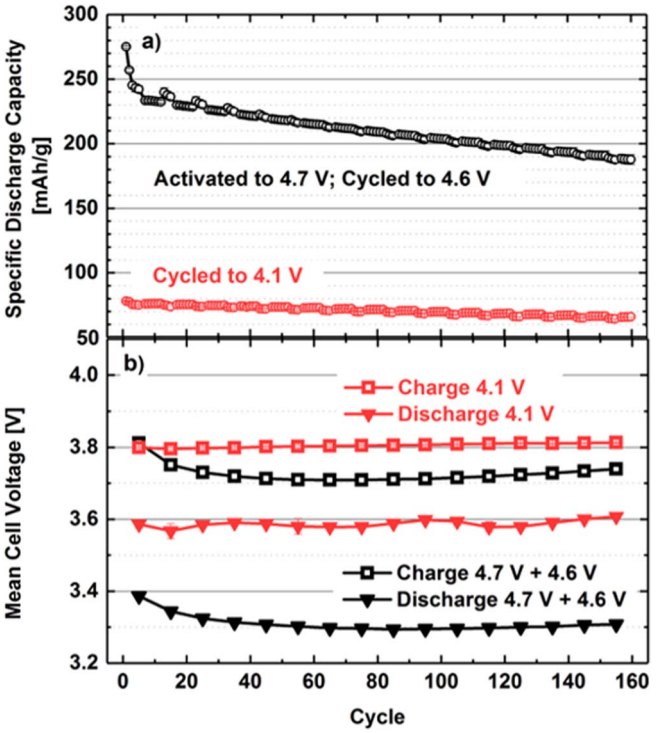

Figure 4. Electrochemical cycling of graphite//HE-NCM full-cells (coin-cells) at 25°C according to the procedure shown in Figure 1. Cells with activated HE-NCM (one cycle to 4.7 V) are shown in black and were cycled between 2.0–4.6 V (initial activation cycle between 2.0–4.7 V), cells with non-activated HE-NCM are shown in red and were cycled between 2.0–4.1 V. Full-cell resistances were measured every 10 cycles by the DCIR method in 10% SOC intervals during charge and discharge. a) Specific discharge capacities for cells with activated (black) and non-activated (red) HE-NCM; b) corresponding charge-averaged mean cell voltages at 0.2C (for CC charge/discharge). For the determination of the mean voltage, the last 0.2C cycle of each sequence (Figure 1a) was used; e.g. cycle 5, 15, 25, and so on. The mean cell voltage was calculated as defined by Jung et al.[9] $\bar{V}_{charge/discharge} = \int V_{charge/discharge} \cdot dQ_{charge/discharge} / \int \cdot dQ_{charge/discharge}$.

The charge-averaged charge (square symbols) and discharge (triangular symbols) voltages for the 0.2C cycles (the last of each 0.2C shown in Figure 1a, prior to the DCIR measurements; e.g., cycle 5, 15, 25 and so on) are shown in Figure 4b, indicating that the cells with non-activated HE-NCM cycled between 2.0 V and 4.1 V show no voltage fading and a voltage-hysteresis of only ≈200 mV (here defined as the difference between the mean charge and discharge voltage). On the other hand, the cells with activated HE-NCM cycled between 2.0 V and 4.6 V show a much larger voltage-hysteresis of ≈400 mV, in addition to a substantial voltage-fading over 160 cycles of ≈180 mV in the mean discharge voltage and ≈160 mV in the mean charge voltage (see Figure 4b). This points towards a major transformation of the bulk HE-NCM material, a phenomenon which has been examined by many different groups and has been ascribed to transition metal migration within the bulk material for both lithium- and manganese-rich HE-NCM[18,35] as well as for related lithium-rich materials.[33] It has been suggested that the charge/discharge voltage-hysteresis might be correlated to reversible transition metal migration between the lithium and the transition metal layer,[18,35,50] while recent studies showed that transition metal migration also correlates with the reversible anionic oxygen redox within the bulk material.[27,28] Furthermore, it was suggested that reversible transition metal movement might occasionally result in an irreversible trapping of the transition metals in the lithium layer,[18,35] causing bulk material changes which lead to voltage fading.[18,19,33,35]

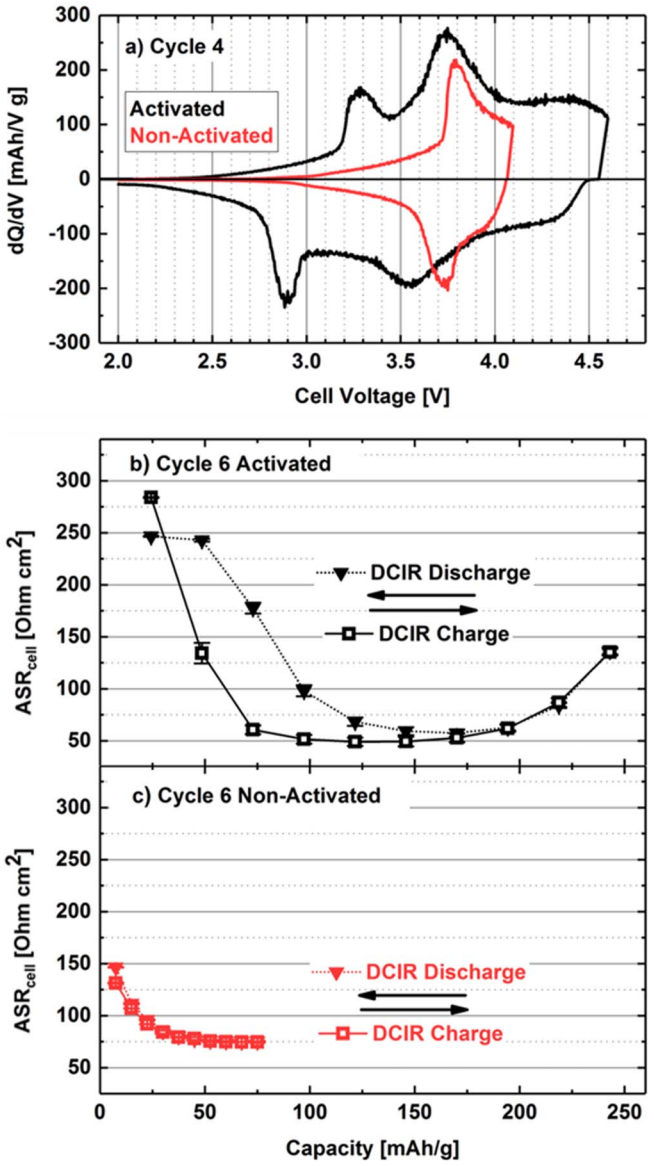

Figure 5. a) Full-cell dQ/dV of cycle 4 at 0.2C (taken from the data set of Figure 4) for cells with activated (black) and non-activated (red) HE-NCM at 25°C. The corresponding full-cell DCIR-based resistances (10 s long 0.2C discharge pulses at 25°C) from cycle 6 are shown for b) the activated, and c) the non-activated HE-NCM. DCIR measurements were conducted in 10% SOC intervals, always following a 1h OCV period.

Further differences between cells with non-activated HE-NCM cycled up to 4.1 V (red line) and with activated HE-NCM (first cycle to 4.7 V) cycled up to 4.6 V (black line) can be seen in Figure 5a, showing the differential capacity curves for the fourth cycle at 0.2C. The potentials that were recorded with the reference electrode during the initial cycles (data not shown) show that the full-cell dQ/dV is not strongly affected by the graphite anode and reflects the behavior of the HE-NCM cathode; the behavior of the dQ/dV is also in line with half-cell data reported in earlier studies using the exact same material.[23,24,35] Clearly, for non-activated HE-NCM, a fully reversible behavior without voltage-hysteresis is observed (with charge/discharge peaks at ≈3.8/3.7 V), contrary to the large voltage-hysteresis in the drastically different differential capacity curves of activated HE-NCM. The first distinct difference is the appearance of a charge peak at already ≈3.3 V for the activated HE-NCM, which in a previous study we showed to be due to an oxygen depleted surface layer produced by the lattice oxygen release from the near-surface layer of the HE-NCM particles.[24] We previously showed by careful quantification of the capacity contribution of this first charge peak that it represents a reversible rocksalt-to-spinel transformation upon delithiation.[24,51,52] This surface layer appeared in HRTEM images as cation disordered surface phase and was referred to as M'_3O_4 spinel type layer, as TEM did not allow to distinguish between the two phases (due to the poor electron density of Li).[24] From the careful quantification shown by Teufl et al.,[24] we expect that this surface layer is electrochemically active and thus can reversibly transform between spinel and rocksalt during cycling. As mentioned above we expect a disordered M'_3O_4 spinel type surface layer, while the term rocksalt refers to the overlithiated stoichiometry of this M'_3O_4 surface layer. The existence of such an overlithiated disordered spinel phase (referred to as rocksalt phase) suggests that the lithium content of this surface layer differs substantially between the charged and the discharged state (delithiation expected around 3.3 V), which can be rationalized by the capacity contribution of this surface layer, as shown in a previous study.[24] In this study we therefore refer it to as oxygen depleted surface layer and suggest it to have a rocksalt like structure at low SOCs and a spinel type structure above 3.3 V. A further dQ/dV characteristic of activated HE-NCM seen in Figure 5a is the disappearance of the discharge peak at ≈3.7 V, which is reversible for non-activated HE-NCM, concomitant with the occurrence of a new discharge peak at a ≈1 V lower potential (i.e., at ≈2.9 V). This ≈1 V hysteresis was already noted by Croy et al.,[50] and can be rationalized by reversible transition metal migration and reversible oxygen redox in the bulk of the HE-NCM material.[18,28,35]

The full-cell DCIR measurements taken during cycle 6 of the data set shown in Figure 4 (in 10% SOC intervals, according to the procedure depicted in Figure 1) can be seen in Figure 5b for the activated and in Figure 5c for the non-activated HE-NCM. The latter shows resistances which are identical along the charge and discharge pathway, as expected for traditional layered oxides, with a value of ≈70 Ωcm^2 over a wide range; only at very low SOCs (i.e., at <25 mAh/g, corresponding to <40% SOC for the non-activated HE-NCM), the resistance increases up to ≈150 Ωcm^2, which can be rationalized by the lower lithium mobility in nearly fully lithiated layered oxides.[53–55] A strikingly different behavior is observed for the cells with activated HE-NCM (Figure 5b): Upon charging (open squares), very high resistances of ≈280 Ωcm^2 are obtained at ≈25 mAh/g (≡10% SOC), which rapidly decrease to a minimum of ≈50 Ωcm^2 at around 120 mAh/g (≡50% SOC), followed by a gradual increase to ≈135 Ωcm^2 by the end-of-charge along the charge pathway (i.e., at 245 mAh/g, ≡100% SOC), which is in line with the behavior reported in the literature.[38,39] Even more interesting is the behavior during discharge of the activated HE-NCM (filled triangles), which first follows the resistance observed along the charge pathway down to 145 mAh/g (≡60% SOC), but upon further discharge becomes much larger than that measured along the charge pathway. For example, the resistance at ≈45 mAh/g (≡20% SOC) along the discharge pathway is ≈240 Ωcm^2, much higher than the ≈135 Ωcm^2 obtained along the charge pathway at the same SOC, clearly indicating a higher energy barrier for lithium reintercalation into the HE-NCM material. After discharging the cell down to ≈25 mAh/g (≡10% SOC), this resistance hysteresis diminishes again.

Our interpretation of the observed resistance hysteresis is as follows: We believe that the rapid resistance drop along the charge pathway (open squares Figure 5b) from 25 mAh/g (≡10% SOC; ≈3.1 V) to 45 mAh/g (≡20% SOC; ≈3.3 V) is caused by the rocksalt-to-spinel transformation of the oxygen depleted surface layer formed on the HE-NCM particles by lattice oxygen release during activation and subsequent cycling;[24] upon its delithiation, this surface layer changes from a poorly lithium ion conducting rocksalt to a well conducting spinel.[51,52] This surface layer was shown to be delithiated during charge in the potential range between ≈3.0–3.5 V.[24] During discharge, the surface layer will relithiate and back-transform into a rocksalt structure, which will lead again to the very high resistance observed towards the end of the discharge. With regards to the large resistance hysteresis at low SOC, we expect that during discharge in the range from 145 mAh/g (≡50% SOC) to 45 mAh/g (≡20% SOC), the

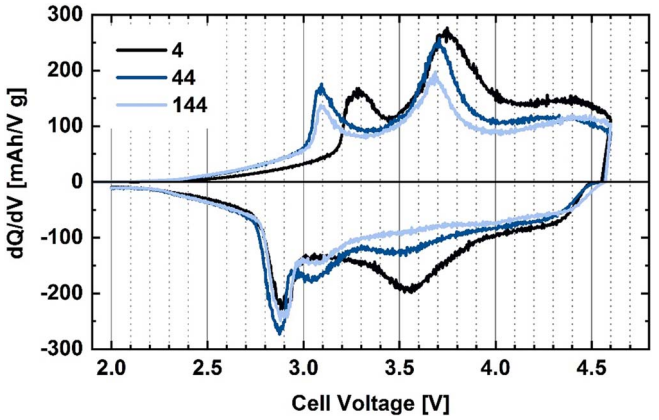

Figure 6. Full-cell dQ/dV of cycle 4 (black line), cycle 44 (dark blue line) and cycle 144 (light blue line) measured at 0.2C for cells with activated HE-NCM at 25°C (taken from the data set of Figure 4).

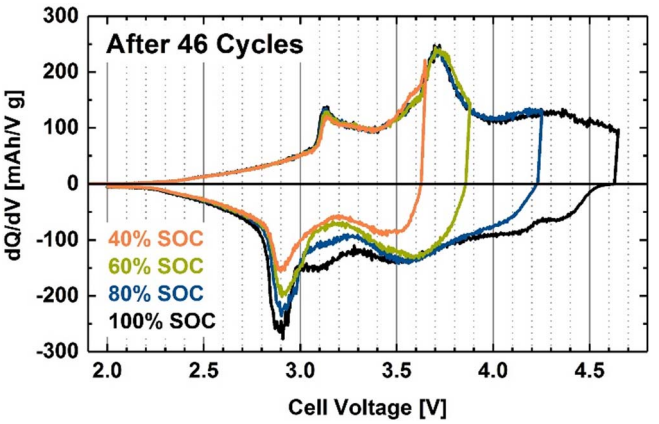

Figure 7. Full-cell dQ/dV of activated HE-NCM (at 4.7 V in the first cycle) at 0.2C after 46 cycles between 2.0–4.6 V according to the procedure shown in Figure 1, except that the upper charge cutoff in the DCIR measurement cycle (red cycle in Figure 1) was modified as follows: in a first cycle it the upper SOC was increased to 40% (orange), in a second cycle, to 60% SOC (green), in a third cycle to 80% SOC (blue), and in a fourth cycle to 100% (black), with 100% SOC being defined by the ≈225 mAh/g obtained for cycling at 0.2C between 2.0–4.6 V.

discharge resistance is strongly affected by the extent of reversible and irreversible migration of transition metals that occupy the lithium diffusion paths. The resistance hysteresis would then be related to a hysteresis in the extent of transition metal occupation in the lithium layer, which within a given charge/discharge cycle would have to correspond to a hysteresis in the reversible occupation of the transition metals in the lithium layer, as will be discussed in detail later on.

Ongoing structural changes during the first 144 cycles can be seen in the dQ/dV plots in Figure 6, where several differences can be noted, particularly between cycle 4 and cycle 44. Comparing the first charge peak of cycle 4 (Figure 6; black line) to cycle 44 (Figure 6; dark blue line) and cycle 144 (Figure 6; light blue line), it is apparent that this peak changes mostly during the initial cycles, where the surface restructuration mainly takes place. It has been reported that the surface restructuration after oxygen release occurs during the first 25 cycles, which is in good accordance with this peak shifting from ≈3.3 V to ≈3.1 V during the first 44 cycles, with little further changes up to 144 cycles. Furthermore, increasing hysteresis and voltage-fading can be seen during discharge, especially for the peak at ≈3.5 V during discharge that is present in cycle 4 and has disappeared after 44 cycles. In summary, the major transformations occur during the initial cycles and only minor differences can be seen between cycle 44 and cycle 144 in Figure 6. This is in good accordance with the voltage characteristics of the activated HE-NCM shown in Figure 4b, where the main part of the voltage-fading is shown to occur during the first 50 cycles. As the major structural changes already occur during the initial cycles (Figure 4b and Figure 6), we conducted the further analysis of the resistance behavior during cycle 46 where the extent of capacity fading is still low (≈240 mAh/g for cycle 6 and ≈225 mAh/g for cycle 46; see Figure 4a).

Influence of the upper cutoff on the reversibility of the resistance.—As shown in Figure 5, charge/discharge pathway dependency of the resistance is obtained for cells with activated HE-NCM cycled between 2.0 V and 4.6 V (after first-cycle activation to 4.7 V), which is definitely not visible for cells with non-activated HE-NCM cycled only up to 4.1 V. In order to determine the point from which the resistance hysteresis starts to occur for cells with activated HE-NCM (at 4.7 V in the first cycle), the cells were cycled between 2.0 V and 4.6 V according to the procedure shown in Figure 1, except that the maximum SOC value of the diagnostic cycle during which the DCIR-values are measured (see red cycle in Figure 1) was modified as follows: a first diagnostic cycle was done from 0% SOC (2.0 V) to 40% SOC and back to 0% SOC (2.0 V), recording the DCIR at 10% SOC intervals (100% SOC being defined at 4.6 V, corresponding to ≈225 mAh/g); this was followed by a subsequent diagnostic cycle from 0-60-0% SOC, then from 0-80-0% SOC, and finally from 0-100-0% SOC. For simplicity, these four diagnostic cycles were counted as one cycle and they were carried out each tenth cycle. The results for this sequence after 46 cycles are shown in Figure 7 and Figure 8.

The resistances measured during charge (open squares) and discharge (closed triangles) for cells with activated HE-NCM charged to different SOCs after 46 cycles are shown in Figure 8, and the corresponding dQ/dV plots are shown in Figure 7, both for cases where the cells are charged/discharged to 40% SOC (orange), 60% SOC (green), 80% SOC (blue) and 100% SOC (≡4.6 V, black). Figure 8a shows the resistance for a charge up to only 40% SOC (corresponding to ≈90 mAh/g obtained at ≈3.7 V) followed by a complete discharge to 2.0 V, illustrating that only a negligible difference in resistance between charge/discharge pathways is observed. However, upon increasing the upper cutoff potential by charging the cell to 60% SOC (≈135 mAh/g obtained at ≈3.9 V, Figure 8b), 80% SOC (≈180 mAh/g obtained at ≈4.3 V, Figure 8c), and finally 100% SOC (≈225 mAh/g obtained at ≈4.6 V, Figure 8d), it becomes obvious that the resistance hysteresis between charge and discharge pathways develops and substantially grows with increasing SOC.

Comparison with the dQ/dV plots from Figure 7 now allows to draw a correlation between the pathway dependence of the resistances and the electrochemical characteristics of the activated HE-NCM. From Figure 7 it can be clearly seen that the capacity charged in the high voltage region (>4.0 V) can only be regained during discharge at potentials below 3.0 V, so that this high irreversibility in the dQ/dV plot of ≈1 V, also reported in the literature[50] mirrors the above observed resistance hysteresis. It has been shown that with increasing SOC also the voltage hysteresis between charge and discharge increases, suggesting this must be caused by concomitant changes in the bulk of the HE-NCM material.[56] For a related lithium-rich layered oxide, Assat et al.[43] recently suggested that high voltage charging would lead to oxygen anionic redox, which on one hand enables high capacities, but owing to its slow kinetics also leads to voltage hysteresis and high impedances. Later on, Gent et al.[28] also provide evidence that the oxygen anionic redox is coupled intimately with reversible transition metal migration. The latter, we believe, is reflected in the here observed charge/discharge pathway dependence of the resistance, which only develops at high SOCs (>40%, see Figure 8).

Transition metal migration and its influence on the resistance.—Transition metal migration in lithium-rich layered oxides is a well-known phenomenon and has been the object of numerous studies. It has been shown that reversible and irreversible transition metal

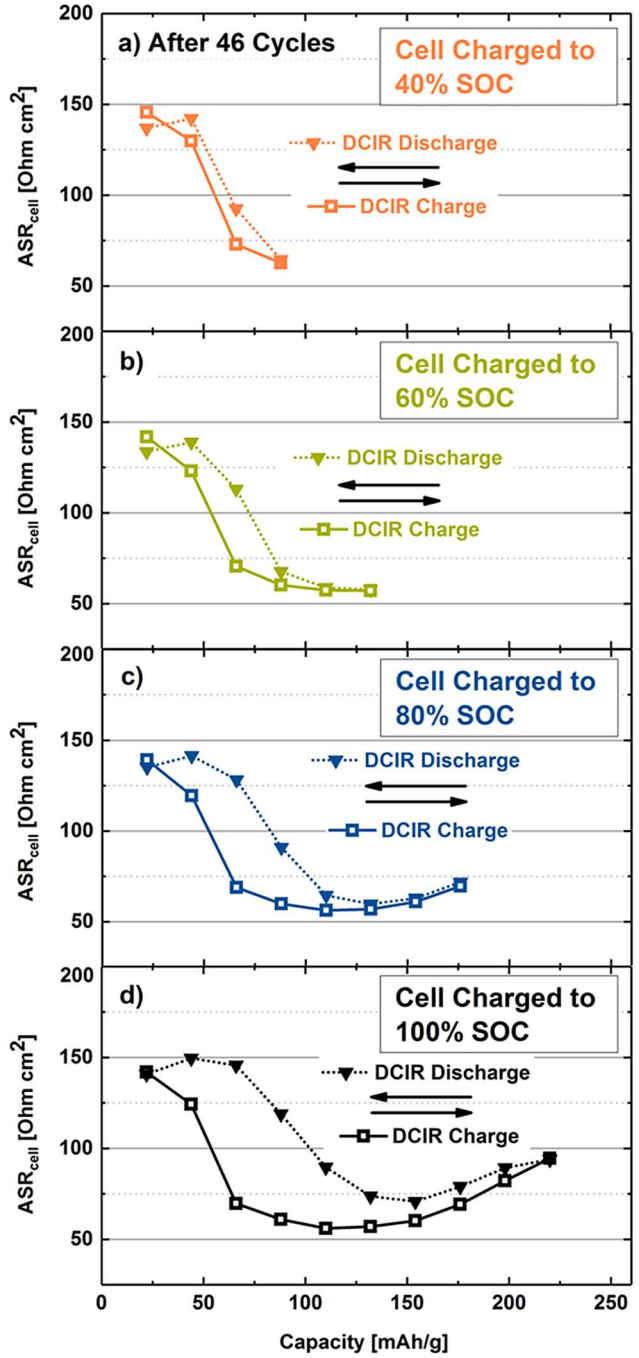

Figure 8. Full-cell resistances of activated HE-NCM (at 4.7 V in the first cycle) obtained by DCIR (10 s long 0.2C discharge pulses at 25°C) for different upper cutoff SOC-values during four DCIR measurement cycles, corresponding to the dQ/dVs shown in Figure 7. Prior to taking the here shown DCIR-based resistances at 10% SOC intervals, the cells were cycled for 46 cycles between 2.0 and 4.6 V according to Figure 1 and then cycled between 0% SOC (at 2.0 V) and different upper SOC values of: a) first 40% SOC, b) then 60% SOC, c) then 80% SOC, and, d) finally 100% SOC (4.6 V), whereby 100% SOC correspond to the ≈225 mAh/g obtained for cycling at 0.2C between 2.0–4.6 V.

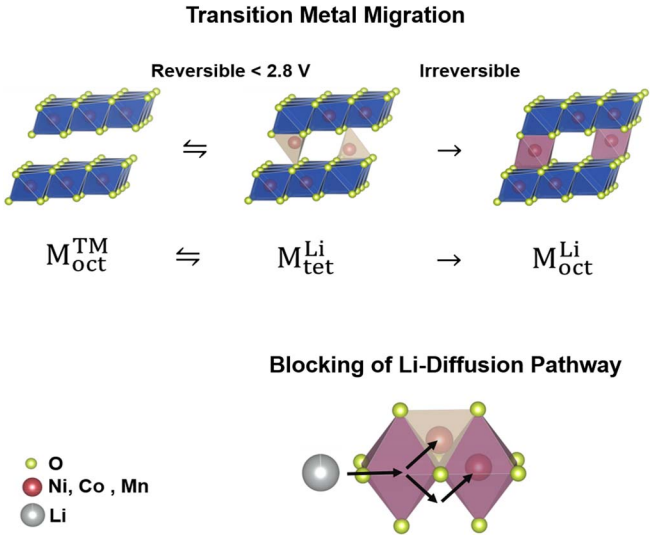

Scheme 1. Upper part: schematic illustration of the transition metal and the lithium layers, depicting the suggested reversible transition metal migration into tetrahedral positions in the lithium layer (M_{tet}^{Li}) and irreversible migration into octahedral positions in the lithium layer (M_{oct}^{TM}) during cycling, as shown by Kleiner et al.[35] Lower part: retarding effect of migrated transition metals (marked by red spheres for both tetrahedral and octahedral sites in the lithium layer) on lithium diffusion within lithium-rich layered oxide materials.

migration, even if the fraction of migrated transition metals is fairly small, has a detrimental effect on actual cell performance of these materials;[18,29,32,33,35,57] on the other hand, however, it has also been suggested that transition metal migration might be the reason why HE-NCMs can be cycled reversibly to 100% SOC (referenced to the lithium in the lithium layer).[28,35] Based on these studies, our cell resistance measurements in Figure 8 thus indicate that at high degrees of delithiation (i.e., at high SOCs) transition metals are prone to migrate reversibly into thermodynamically favorable positions, proposed to be the tetrahedral and octahedral sites in the lithium layer.[35] Scheme 1 depicts our current view of the bulk transition metal movements between the layers, suggesting that during delithiation transition metals first migrate into tetrahedral positions of the lithium layer (M_{tet}^{Li}, see upper panel in Scheme 1),[18,35] a process which was suggested to be almost entirely reversible.[28,35] Kleiner et al.[35] recently hypothesized that over the course of cycling, transition metals might also occasionally further migrate into octahedral positions in the lithium layer (M_{oct}^{Li}), deduced from long-term powder diffraction data which showed that the transition metal occupancy of octahedral sites in the lithium layer is independent of SOC and increases upon cycling, viz., from M_{oct}^{Li} ≈2% after the first activation cycle to M_{oct}^{Li} ≈5% after 100 cycles. Furthermore, these authors showed that transition metals in tetrahedral positions of the lithium layer occur exclusively in the charged state (i.e., at high SOC) and that tetrahedral migration is reversible during discharge, with the fraction of transition metals moving reversibly into tetrahedral sites remaining essentially constant over cycling (M_{tet}^{Li} ≈8%). Based on first-principles calculations, van der Ven and Ceder[53] suggested that lithium diffusion in the lithium layer of layered oxides takes place between octahedral sites via passage through the tetrahedral sites in between. However, based on the above hypotheses, at high SOC transition metals would occupy tetrahedral (reversibly) as well as octahedral (irreversibly) positions within the lithium layer, so that they would occupy the positions required for lithium diffusion, as is shown schematically in the lower panel of Scheme 1, which represents these lithium diffusion path and their blocking by transition metals. If the above discussed reversible transition metal occupancy of tetrahedral sites were to exhibit a hysteresis, i.e., if transition metal back-migration into the transition metal layer were to occur at a lower SOC along the discharge pathway compared to its migration into lithium layer tetrahedral sites during the charge pathway, the observed resistance hysteresis with respect to charge/discharge pathways could be understood.

Based on the principal mechanisms of transition metal migration on an atomic scale, we now want to turn to the effect of blocked lithium diffusion paths and its implications onto the cell resistance during

lithium re-intercalation, as shown in Figure 8. During the charge at low SOCs, a rapid resistance decrease can be observed due to the rocksalt-to-spinel transition of the oxygen depleted surface layer. As one would expect, no pathway dependence is observed for this process as long as the SOC corresponds <90 mAh/g (Figure 8a). As the upper cutoff is increased to 135 mAh/g (Figure 8b), the charge resistance remains low, but now the onset of a noticeable pathway dependence of the resistance can be seen during discharge, suggesting the onset of reversible TM migration. As the SOC goes beyond 60% SOC, the discharge resistance strongly increases due to reversible TM migration (Figure 8c) which has been suggested to be coupled to the anion redox phenomenon.[28] Assuming that TM back-migration is kinetically slow, the appearance of a strong resistance pathway dependence, namely a higher resistance during the discharge can be explained; the latter becomes even more pronounced for a higher upper SOC (Figure 8d). As the results from Figure 8 are essentially recorded within the same cycle, the hysteresis is observed at presumably the same extent of irreversible transition metal migration. This means that the resistance pathway hysteresis must be related to reversible rather than irreversible TM migration. We expect that additional irreversible migration can enhance the resistance hysteresis, but the overall phenomenon is closely coupled to reversible TM migration.

While Assat et al.[43] suggested based on EIS, GITT, and PITT measurements with the model compound $Li_2Ru_{0.75}Sn_{0.25}O_3$ that the resistance pathway-dependence and the sluggish kinetics are caused by the reversible oxygen redox within the material, our data and analysis suggest that reversible cation migration might be the reason for the pathway-dependence of the resistance by blocking the lithium diffusion paths. In a recent study by Gent et al.,[28] the oxygen redox mechanism was closely correlated to the reversible migration of transition metals and described as dynamic process expressed as: $\{O^{2-} + TM\} \rightarrow \{O^{-} + TM_{mig}\} + e^{-}$. In this case, our findings and the study by Assat et al.[43] can be correlated, as oxygen redox and transition metal migration into tetrahedral sites of the lithium layer would both occur at high voltages (i.e., at high SOC) and thus cause the pathway-dependence and high activation energies for lithium re-intercalation. This hypothesis is supported by our observation that the pathway-dependence of the resistance only occurs at high cutoff voltages and that it can be eliminated upon complete discharge of the HE-NCM material.

Gowda et al.[38] carried out a detailed study on the high impedance at low SOCs of Li- and Mn-rich NCMs. They observed a sharp resistance increase at low SOCs which they concluded not to be caused by an interfacial resistance; in contradiction we suggest that this sharp increase is caused by a disordered surface layer that stems from oxygen release during the initial cycles. The different observation can be explained by the higher Li_2MnO_3 content of 0.50 of the material used by Gowda et al.[38] In a previous study from Teufl et al.[24] it was shown that these high Li_2MnO_3 contents cause oxygen release and spinel formation in the bulk material and not only at the particle surface, as shown for the material used in this study. Therefore, they could observe a higher impact of the disordered phase onto the overall impedance of the material. They also suggested that this sharp increase of the resistance at low SOCs is not caused by the hysteresis, which is in one line with our observation that a disordered phase from oxygen release causes this sharp increase. While Gowda et al.[38] observed this sharp increase below 3.5V (equal to 40% SOC), we could only observe it below 30% SOC (see Figure 5 and Figure 8) which can be explained by the lower oxygen release expected for the material used in this study.[24] Furthermore, Gowda et al.[38] could observe a path dependent resistance >3.5 V (equal to 40% SOC) and suggested transition metal migration as possible reason which is in good accordance with the results shown in Figure 8 and the conclusions from this study.

Conclusions

In this study we analyzed the resistance behavior of over-lithiated manganese-rich NCM (HE-NCM) at various SOCs during charge and discharge and showed a correlation between structural changes, electrochemical characteristics, and the resistance measurements. A pathway-dependent resistance hysteresis was observed during charge and discharge for HE-NCM that is activated in the first-cycle to a high upper cutoff voltage, accompanied by a large charge/discharge voltage hysteresis and a gradual voltage-fading upon extended cycling. This is not observed for a non-activated HE-NCM material, while high-voltage activation (up to 4.8V vs. Li^+/Li) is required to achieve reasonable capacities. By a systematic variation of the upper cutoff potential for activated HE-NCM, we could show that the pathway-dependent resistance hysteresis increases with increasing upper cutoff voltages, at which the oxygen redox is believed to occur. Our data suggest that the pathway-dependence of the resistance can be rationalized by a hysteresis in the reversible transition metal migration, meaning that transition metals migrate into tetrahedral sites in the Li layer at high potentials and only migrate back into the transition metal layer upon discharge below 3V.

Acknowledgment

The authors want to thank BASF SE who supported this work within the BASF SE Battery Research Network. Furthermore, we want to gratefully acknowledge Karin Kleiner, Benjamin Strehle, and Frederick Chesneau for very fruitful discussions and Patrick Krieg for his contribution to this work.

ORCID

Tobias Teufl https://orcid.org/0000-0001-5889-5204
Daniel Pritzl https://orcid.org/0000-0002-9029-107X
Sophie Solchenbach https://orcid.org/0000-0001-6517-8094

References

1. J. B. Goodenough and K. S. Park, *J. Am. Chem. Soc.*, **135**(4), 1167 (2013).
2. D. Andre, S.-J. Kim, P. Lamp, S. F. Lux, F. Maglia, O. Paschos, and B. Stiaszny, *J. Mater. Chem. A*, **3**(13), 6709 (2015).
3. M. M. Thackeray, C. Wolverton, and E. D. Isaacs, *Energ. Environ. Sci.*, **5**(7), 7854 (2012).
4. K. Mizushima, P. Jones, P. Wiseman, and J. B. Goodenough, *Mat. Res. Bull.*, **15**(6), 783 (1980).
5. J. Choi and A. Manthiram, *J. Electrochem. Soc.*, **152**(9), A1714 (2005).
6. I. Belharouak, Y. K. Sun, J. Liu, and K. Amine, *J. Power Sources*, **123**(2), 247 (2003).
7. Z. Lu, D. D. MacNeil, and J. R. Dahn, *Electrochem. Solid-State Lett.*, **4**(12), A200 (2001).
8. M.-H. Kim, H.-S. Shin, D. Shin, and Y.-K. Sun, *J. Power Sources*, **159**(2), 1328 (2006).
9. R. Jung, M. Metzger, F. Maglia, C. Stinner, and H. A. Gasteiger, *J. Electrochem. Soc.*, **164**(7), A1361 (2017).
10. L. de Biasi, A. O. Kondrakov, H. Geßwein, T. Brezesinski, P. Hartmann, and J. Janek, *J. Phys. Chem. C*, **121**(47), 26163 (2017).
11. M. M. Thackeray, S.-H. Kang, C. S. Johnson, J. T. Vaughey, R. Benedek, and S. A. Hackney, *J. Mater. Chem.*, **17**(30), 3112 (2007).
12. Z. Lu and J. R. Dahn, *J. Electrochem. Soc.*, **149**(7), A815 (2002).
13. Z. Lu, L. Y. Beaulieu, R. A. Donaberger, C. L. Thomas, and J. R. Dahn, *J. Electrochem. Soc.*, **149**(6), A778 (2002).
14. C. S. Johnson, J. S. Kim, C. Lefief, N. Li, J. T. Vaughey, and M. M. Thackeray, *Electrochem. Commun.*, **6**(10), 1085 (2004).
15. F. La Mantia, F. Rosciano, N. Tran, and P. Novák, *J. Appl. Electrochem.*, **38**(7), 893 (2008).
16. A. R. Armstrong, M. Holzapfel, P. Novák, C. S. Johnson, S.-H. Kang, M. M. Thackeray, and P. G. Bruce, *J. Am. Chem. Soc.*, **128**(26), 8694 (2006).
17. H. Yu, H. Kim, Y. Wang, P. He, D. Asakura, Y. Nakamura, and H. Zhou, *Phys. Chem. Chem. Phys.*, **14**(18), 6584 (2012).
18. J. R. Croy, M. Balasubramanian, K. G. Gallagher, and A. K. Burrell, *Acc. Chem. Res.*, **48**(11), 2813 (2015).
19. D. Mohanty, J. Li, S. C. Nagpure, D. L. Wood, and C. Daniel, *MRS Energy & Sustainability*, **2**, (2015).
20. N. Yabuuchi, K. Yoshii, S. T. Myung, I. Nakai, and S. Komaba, *J. Am. Chem. Soc.*, **133**(12), 4404 (2011).
21. H. Koga, L. Croguennec, M. Ménétrier, P. Mannessiez, F. Weill, and C. Delmas, *J. Power Sources*, **236**, 250 (2013).
22. C. Genevois, H. Koga, L. Croguennec, M. Ménétrier, C. Delmas, and F. Weill, *J. Phys. Chem. C*, **119**(1), 75 (2014).
23. B. Strehle, K. Kleiner, R. Jung, F. Chesneau, M. Mendez, H. A. Gasteiger, and M. Piana, *J. Electrochem. Soc.*, **164**(2), A400 (2017).
24. T. Teufl, B. Strehle, P. Müller, H. A. Gasteiger, and M. A. Mendez, *J. Electrochem. Soc.*, **165**(11), A2718 (2018).

25. E. McCalla, A. M. Abakumov, M. Saubanère, D. Foix, E. J. Berg, G. Rousse, M.-L. Doublet, D. Gonbeau, P. Novák, G. Van Tendeloo, D. R., and J. M. Tarascon, *Science*, **350** (6267), 1516 (2015).
26. H. Koga, L. Croguennec, M. Menetrier, K. Douhil, S. Belin, L. Bourgeois, E. Suard, F. Weill, and C. Delmas, *J. Electrochem. Soc.*, **160**(6), A786 (2013).
27. D. H. Seo, J. Lee, A. Urban, R. Malik, S. Kang, and G. Ceder, *Nat. Chem.*, **8**(7), 692 (2016).
28. W. E. Gent, K. Lim, Y. Liang, Q. Li, T. Barnes, S.-J. Ahn, K. H. Stone, M. McIntire, J. Hong, J. H. Song, Y. Li, A. Mehta, S. Ermon, T. Tyliszczak, D. Kilcoyne, D. Vine, J.-H. Park, S.-K. Doo, M. F. Toney, W. Yang, D. Prendergast, and W. C. Chueh, *Nat. Commun.*, **8**(1), 2091 (2017).
29. M. Jiang, B. Key, Y. S. Meng, and C. P. Grey, *Chem. Mater.*, **21**(13), 2733 (2009).
30. H. Liu, Y. Chen, S. Hy, K. An, S. Venkatachalam, D. Qian, M. Zhang, and Y. S. Meng, *Adv. Energy Mater.*, **6**(7), 1502143 (2016).
31. D. Mohanty, A. S. Sefat, J. Li, R. A. Meisner, A. J. Rondinone, E. A. Payzant, D. P. Abraham, D. L. Wood 3rd, and C. Daniel, *Phys. Chem. Chem. Phys.*, **15**(44), 19496 (2013).
32. D. Mohanty, J. Li, D. P. Abraham, A. Huq, E. A. Payzant, D. L. Wood, and C. Daniel, *Chem. Mater.*, **26**(21), 6272 (2014).
33. M. Sathiya, A. M. Abakumov, D. Foix, G. Rousse, K. Ramesha, M. Saubanere, M. L. Doublet, H. Vezin, C. P. Laisa, A. S. Prakash, D. Gonbeau, G. VanTendeloo, and J. M. Tarascon, *Nat. Mater.*, **14**(2), 230 (2015).
34. A. van Bommel, L. J. Krause, and J. R. Dahn, *J. Electrochem. Soc.*, **158**(6), A731 (2011).
35. K. Kleiner, B. Strehle, A. R. Baker, S. J. Day, C. C. Tang, I. Buchberger, F.-F. Chesneau, H. A. Gasteiger, and M. Piana, *Chem. Mater.*, **30**(11), 3656 (2018).
36. M. Bettge, Y. Li, K. Gallagher, Y. Zhu, Q. Wu, W. Lu, I. Bloom, and D. P. Abraham, *J. Electrochem. Soc.*, **160**(11), A2046 (2013).
37. K. G. Gallagher, S.-H. Kang, S. U. Park, and S. Y. Han, *J. Power Sources*, **196**(22), 9702 (2011).
38. S. R. Gowda, D. W. Dees, A. N. Jansen, and K. G. Gallagher, *J. Electrochem. Soc.*, **162**(7), A1374 (2015).
39. W. Mao, G. Ai, Y. Dai, Y. Fu, X. Song, H. Lopez, and V. Battaglia, *J. Electrochem. Soc.*, **163**(14), A3091 (2016).
40. J. Zheng, W. Shi, M. Gu, J. Xiao, P. Zuo, C. Wang, and J. G. Zhang, *J. Electrochem. Soc.*, **160**(11), A2212 (2013).
41. S.-H. Kang, W.-S. Yoon, K.-W. Nam, X.-Q. Yang, and D. P. Abraham, *J. Mater. Sc.*, **43**(14), 4701 (2008).
42. H. Yu, Y. Wang, D. Asakura, E. Hosono, T. Zhang, and H. Zhou, *RSC Adv.*, **2**(23), 8797 (2012).
43. G. Assat, C. Delacourt, D. A. D. Corte, and J.-M. Tarascon, *J. Electrochem. Soc.*, **163**(14), A2965 (2016).
44. S. Solchenbach, D. Pritzl, E. J. Y. Kong, J. Landesfeind, and H. A. Gasteiger, *J. Electrochem. Soc.*, **163**(10), A2265 (2016).
45. H. G. Schweiger, O. Obeidi, O. Komesker, A. Raschke, M. Schiemann, C. Zehner, M. Gehnen, M. Keller, and P. Birke, *Sensors (Basel)*, **10**(6), 5604 (2010).
46. D. Pritzl, A. Bumberger, M. Wetjen, J. Landesfeind, S. Solchenbach, and H. Gasteiger, *J. Electrochem. Soc.*, **166**(4), A582 (2019).
47. J. Landesfeind, D. Pritzl, and H. A. Gasteiger, *J. Electrochem. Soc.*, **164**(7), A1773 (2017).
48. M. Gaberscek, J. Moskon, B. Erjavec, R. Dominko, and J. Jamnik, *Electrochem. Solid-State Lett.*, **11**(10), A170 (2008).
49. J. Landesfeind, J. Hattendorff, A. Ehrl, W. A. Wall, and H. A. Gasteiger, *J. Electrochem. Soc.*, **163**(7), A1373 (2016).
50. J. R. Croy, K. G. Gallagher, M. Balasubramanian, Z. Chen, Y. Ren, D. Kim, S.-H. Kang, D. W. Dees, and M. M. Thackeray, *J. Phys. Chem. C*, **117**(13), 6525 (2013).
51. P. G. Bruce, A. R. Armstrong, and L. Gitzendanner, *J. Mater. Chem.*, **9**, 193 (1998).
52. M. M. Thackeray, *Prog. Solid State Chem.*, **25**, 1 (1997).
53. A. Ven and G. Ceder, *J. Power Sources*, **97**, 529 (2001).
54. I. Buchberger, S. Seidlmayer, A. Pokharel, M. Piana, J. Hattendorff, P. Kudejova, R. Gilles, and H. A. Gasteiger, *J. Electrochem. Soc.*, **162**(14), A2737 (2015).
55. S.-H. Kang, D. P. Abraham, W.-S. Yoon, K.-W. Nam, and X.-Q. Yang, *Electrochim. Acta*, **54**(2), 684 (2008).
56. J. R. Croy, K. G. Gallagher, M. Balasubramanian, B. R. Long, and M. M. Thackeray, *J. Electrochem. Soc.*, **161**(3), A318 (2014).
57. F. Dogan, B. R. Long, J. R. Croy, K. G. Gallagher, H. Iddir, J. T. Russell, M. Balasubramanian, and B. Key, *J. Am. Chem. Soc.*, **137**(6), 2328 (2015).

3.1.2. Oxygen release from the near-surface region

This section presents the article "Oxygen Release and Surface Degradation of Li- and Mn-Rich Layered Oxides in Variation of the Li_2MnO_3 Content".[60] It was submitted in June 2018 and published in August 2018 as peer-reviewed publication in the *Journal of the Electrochemical Society*. It is published as an open access article and distributed under the terms of the Creative Commons Attribution Non-Commercial Non-Derivatives 4.0 License. The permanent web-link to the article is provided under: http://jes.ecsdl.org/content/165/11/A2718.full. The paper was presented by Tobias Teufl at the 231st Meeting of the Electrochemical Society (May 28th – June 1st, 2017) in New Orleans, Louisiana, USA (Abstract Number: 036).

The plateau at ≈4.5 V vs. Li^+/Li during the first-cycle activation step of Li- and Mn-rich NCMs was initially ascribed to an electrochemical activation of redox inactive Li_2MnO_3, leading to a release of bulk lattice oxygen and to an active $LiMnO_2$ phase that was suggested to serve for charge compensation upon lithium extraction to capacities >200 mAh/g.[59, 74, 131, 132] It was suggested that this bulk oxygen release leads to a layered-to-spinel transformation in the bulk of the material and therefore causes phenomena like the voltage-hysteresis and voltage-fading.[62, 121, 122, 133, 134] However, exact quantification by Strehle et al.[73] and Luo et al.[75] proved that the extent of the oxygen release is an order of magnitude too small to be explained by bulk Li_2MnO_3 activation. Furthermore, Strehle et al.[73] showed that the oxygen release is not an electrochemical reaction, but rather a chemically driven side reaction that occurs on the surface of the particles, leading to an oxygen deficient spinel-type surface layer.

In this study, we show a detailed analysis of the oxygen release behavior and the electrochemical properties of overlithiated NCMs with different Li_2MnO_3 domains. We show that the oxygen-release increases with the Li_2MnO_3 content and prove that oxygen release is not the main reason for voltage fading and voltage-hysteresis. These data are complemented with HRTEM analysis of the pristine and the cycled materials, showing the formation of a disordered, spinel-type surface layer. By careful quantification of the OEMS data and the electrochemical half-cell data, the extent of this surface layer is quantified and the characteristic signature of this surface spinel in dQ/dV plots is shown. We prove that oxygen

release and spinel formation for Li_2MnO_3 contents of 0.33 and 0.42 occurs exclusively at the surface of the HE-NCM particles, while a Li_2MnO_3 content of 0.50 leads to a partial collapse of the bulk structure, so that a spinel-type phase can also be observed in the bulk of the particles. As most of the previous literature had focused on Li_2MnO_3 contents of 0.50, the findings presented herein can explain why these previous studies concluded that bulk oxygen release would occur, which then would lead to a layered-to-spinel transformation in the bulk material.

Author contributions

T.T. and B.S. carried out the OEMS experiments. T.T. and M.M. did the electrochemical analysis. P.M. carried out the TEM analysis. T.T. wrote the manuscript and H.A.G. edited the manuscript. All authors discussed the results.

Oxygen Release and Surface Degradation of Li- and Mn-Rich Layered Oxides in Variation of the Li_2MnO_3 Content

Tobias Teufl,[1,2,*,z] Benjamin Strehle,[2,*] Philipp Müller,[1] Hubert A. Gasteiger,[2,] and Manuel A. Mendez[1]**

[1] *BASF SE Ludwigshafen, New Battery Materials and Systems, D-67056 Ludwigshafen, Germany*
[2] *Chair of Technical Electrochemistry, Department of Chemistry and Catalysis Research Center, Technical University of Munich, D-85748 Garching, Germany*

In this study, we will show how the oxygen release depends on the Li_2MnO_3 content of the material and how it affects the actual voltage fading of the material. Thus, we compared overlithiated NCMs (x Li_2MnO_3 • (1-x) $LiMeO_2$; Me = Ni, Co, Mn) with x = 0.33, 0.42 and 0.50, focusing on oxygen release and electrochemical performance. We could show that the oxygen release differs vastly for the materials, while voltage fading is similar, which leads to the conclusion that the oxygen release is a chemical material degradation, occurring at the surface, while voltage fading is a bulk issue of these materials. We could prove this hypothesis by HRTEM, showing a surface layer, which is dependent on the amount of oxygen released in the first cycles and leads to an increase of the charge-transfer resistance of these materials. Furthermore, we could quantitatively deconvolute capacity contributions from bulk and surface regions by dQ/dV analysis and correlate them to the oxygen loss. As a last step, we compared the gassing to the base NCM ($LiMeO_2$, Me = Ni, Co, Mn), showing that surface degradation follows a similar reaction pathway and can be easily modulated by controlling the amount of Li_2MnO_3.

 [DOI: 10.1149/2.0691811jes]

Manuscript submitted June 15, 2018; revised manuscript received July 31, 2018. Published August 24, 2018. This was Paper 36 presented at the New Orleans, Louisiana, Meeting of the Society, May 28–June 1, 2017.

To face future issues, as global warming, air pollution, as well as the consumption of fossil fuels, an alternative is required to cover the future demand of energy and mobility in an environmentally friendly and sustainable way. In this context, lithium-ion batteries are viable options for large scale energy storage and for electric vehicles, as they have been used to power consumer electronics for many years.[1,2] Since graphite is an excellent anode material at potentials of ≈0.1 V vs. Li^+/Li with a roughly 2-fold higher specific capacity of about 360 mAh/g compared to currently used cathode active materials (CAMs), many efforts have been undertaken to increase the specific capacity and energy density of CAMs. As first practical cathode active material Lithium-Cobalt-Oxide (LCO) was investigated by Goodenough et al. in the 1980s, exhibiting a specific capacity of about 140 mAh/g and having a layered structure composed of lithium and transition metal layers.[3] As these layered structures showed good structural stability during lithium extraction and insertion, and therefore good capacity retention, many attempts have been undertaken to further develop alternative layered structures which would offer higher capacity. One promising attempt that led to the currently used Lithium-Nickel-Cobalt-Manganese-Oxides (NCMs) is to change the occupancy of the transition metal layer by not using exclusively cobalt, but also introducing nickel and manganese into the transition metal layer; hereby it was found that nickel shows a high redox activity, while manganese helps to stabilize the structure during lithium extraction.[4–6] By using different transition metals and metal compositions, a playground has been created that allows to tune the properties of the material: while initially a Ni:Co:Mn ratio of 1:1:1 was used (also referred to as NCM-111), trends nowadays favor the so-called Ni-rich NCMs, for example with a Ni:Co:Mn ratio of 8:1:1, which yield higher capacities at practicable potentials.[6,7] However, it has been shown that all NCM materials show structural instabilities at high state-of-charge (SOC), i.e., at a high degree of delithiation, leading to oxygen release from the near-surface region accompanied by the formation of a resistive surface layer; ultimately, this leads to rapid capacity fading and limits the practical capacity of NCM materials to <200 mAh/g.[8–10]

Therefore, in the 2000s the concept of lithium- and manganese-rich NCM materials was investigated by preparing a Li_2MnO_3 domain within an NCM material in a certain composition, leading to x Li_2MnO_3 • (1-x) $LiMeO_2$ (Me = Ni, Co, Mn), also referred to as High-Energy NCM (HE-NCM), with which high reversible capacities of ≈250 mAh/g can be achieved.[11] However, these materials exhibit serious issues that so far has hindered its commercialization, such as a decrease of the average discharge voltage over extended charge/discharge cycling (commonly referred to as voltage fading), a large hysteresis between charge and discharge voltage, as well as high impedance.[12–14] Since the discovery of this class of materials, researchers have been trying to find an explanation for these high reversible capacities, as the capacities exceed the theoretical capacity limit that could be explained by the classical view of transition metal cation redox. Initially, it was thought that during the first cycle activation plateau at ≈4.5 V vs. Li^+/Li an electrochemical activation of redox inactive Li_2MnO_3 would take place, leading to a release of bulk lattice oxygen and to an electrochemically active $LiMnO_2$ phase which could charge compensate Li extraction to capacities >200 mAh/g.[15–18] This oxygen release was ascribed to cause strong structural changes within the bulk material, ultimately leading to a layered-to-spinel transformation of the particles. This transformation of the bulk material was believed to lead to the HE-NCM specific phenomena such as voltage fading and hysteresis.[12,19–22] However, this activation was suggested to be accompanied by an oxygen release from the bulk of the material, which was suggested from XRD data by Lu et al. in 2002.[19,20] At first sight, this seemed consistent with the mass spectrometrically detected O_2 and CO_2 evolution starting during the activation plateau, which was interpreted to indicate the release of Li_2O from the bulk of the material during activation and accompanying structural changes within the bulk material.[15,17,18,23,24] However, the exact quantification of the released oxygen by Strehle et al. and Luo et al. revealed that the amount of released oxygen is an order of magnitude too low to be consistent with the assumed electrochemical oxygen release[25,26] and also that the O_2 evolution does not start until right after the activation plateau (only <10 $\mu mol_{O2}/g_{AM}$ during the plateau, but >100 $\mu mol_{O2}/g_{AM}$ following thereafter; shown by Strehle et al.).[25] Both observations suggested that the observed oxygen release cannot be ascribed to a loss of oxygen from the bulk of the material, but that the oxygen is only being released from the near-surface

*Electrochemical Society Member.
**Electrochemical Society Fellow.
[z]E-mail: tobias-maximilian.teufl@basf.com

region of the HE-NCM material.[25] While this contradicted most of the literature on the mechanistics of the HE-NCM activation process, it was in accordance with the conclusions drawn by earlier work based on careful XRD, neutron diffraction, and high-resolution transmission electron microscopy.[27–29]

Thus, more recent studies propose that bulk and surface of these overlithiated materials show distinctly different properties, rationalized by a bulk-shell model.[25,27–29] It has been suggested that oxygen release takes places in near-surface region, leading to a chemical layered-to-spinel transformation and a concomitant impedance buildup by the formed resistive surface layer. This phenomenon has also been shown to be one of the main fading mechanisms for traditional NCM materials.[10,30] In contradiction to the bulk oxygen release, the recent literature gives strong evidence that reversible anionic oxygen redox participation in the bulk material can serve for charge compensation and therefore explain the high reversible capacities within this class of materials.[31–34] Therefore, it is suggested that high degrees of delithiation and reversible oxygen redox trigger reversible and irreversible transition metal migration within the bulk material, leading to voltage fading and to the large charge/discharge voltage hysteresis due to the hindered lithium diffusion within the bulk material.[14,35–38] In contradiction to the hypothesis of bulk oxygen release and bulk structural transformation, recent studies give clear evidence that the bulk structure is preserved, while a relatively small fraction of transition metals (about 10% over 100 cycles)[35] migrate reversibly and over extended charge/discharge cycling irreversibly between the transition metal and the lithium layers, leading to changes of the bulk material thermodynamics like the charge and discharge potentials as well as to the observed voltage fading.[25,35]

In this study, we will examine the effect of oxygen release onto the bulk and the surface structure of HE-NCM and correlate it with the macroscopic electrochemical performance of the material. These studies will be conducted with HE-NCM materials with different amounts of the Li_2MnO_3 phase (x = 0.33, 0.42 and 0.50 if referenced to x Li_2MnO_3 • (1-x) $LiMeO_2$), comparing the materials in terms of their oxygen release, their half- and full-cell performance as well as their impedance growth. These data will be complemented with high-resolution transmission electron microcopy (HRTEM) analysis of pristine and charge/discharge cycled materials. By on-line electrochemical mass spectrometry (OEMS) and HRTEM we prove that oxygen release above 4.6 V vs. Li^+/Li leads to a restructuration of the near-surface region, the extent of which increases with increasing over-lithiation and with increasing amounts of oxygen released during the first few cycles. Furthermore, while large differences are observed in the amount of oxygen released for the different materials, their electrochemical performance as well as their voltage fading behavior does not correlate with the extent of oxygen release. Thus, we propose that oxygen release does not have an influence on the bulk properties of HE-NCM, but rather affects the extent of surface restructuration/degradation.

Experimental

Electrode preparation.—HE-NCM with the compositions 0.33 Li_2MnO_3 • 0.67 $LiMeO_2$, 0.42 Li_2MnO_3 • 0.58 $LiMeO_2$, and 0.50 Li_2MnO_3 • 0.50 $LiMeO_2$ was obtained from BASF SE (Germany) and synthesized by the same procedure. While the exact Ni:Co:Mn ratio of the base NCM cannot be disclosed, the $LiMeO_2$ domain was held constant for all materials used in this study, while only the amount of Li_2MnO_3 was varied from 0.00 up to 0.50. The sum formula for the materials was x Li_2MnO_3 • (1-x) $LiMeO_2$ (x = 0.00, 0.33, 0.42, 0.50), whereby the x = 0.42 material is identical what that used by Strehle et al.[25] For coin cell testing, inks for cathode electrode preparation consisted of 92.5 wt% HE-NCM (BASF SE, Germany), 3.5 wt% polyvinylidene-fluoride binder (PVDF, Solef 5130, Solvay, Belgium), 2 wt% conductive carbon (Super-C65, Timcal, Switzerland; BET area of ≈65 m^2/g), and 2 wt% graphite (SFG6L, Timcal, Switzerland; BET area of ≈17 m^2/g). The materials were dispersed in N-methyl pyrrolidine (NMP, anhydrous, Sigma-Aldrich, USA) and coated onto aluminum foil (16 μm). Dried electrodes were calendered to a density of 2.3 g/cm^3, calandered electrodes had final electrode thickness of 20 μm. For electrochemical testing, electrodes with a diameter of 14 mm were punched out, ending up with an active material loading of ≈6.5 mg/cm^2, corresponding to ≈1.6 mAh/cm^2, based on a nominal reversible capacity of 250 mAh/g.

Electrodes for OEMS measurements were prepared by dispersing 96 wt% HE-NCM or the base NCM without Li_2MnO_3 (BASF SE, Germany), 2 wt% conductive carbon (Super-C65, Timcal, Switzerland), and 2 wt% PVDF binder (Kynar HSV 900, Arkema, France) in NMP (anhydrous, Sigma-Aldrich, USA). A high solid content of 71% for the slurry was chosen to enable coating onto a porous stainless-steel mesh (SS316, aperture 26 μm, wire diameter 25 μm, The Mesh Company Ltd., UK). The slurry was coated with a wet film thickness of 20 μm onto the stainless-steel mesh, yielding a HE-NCM loading of ≈8.5 mg/cm^2, corresponding to ≈2.1 mAh/cm^2. Electrodes for OEMS experiments were punched out with a diameter of 15 mm and compressed for 20 s with 2.5 tons.

Graphite electrodes were commercial electrodes with a graphite loading of ≈6.7 mg/cm^2, corresponding to ≈2.4 mAh/cm^2 (based on a theoretical capacity of 360 mAh/g); for electrochemical testing, graphite electrodes with a diameter of 15 mm were punched out. All anode and cathode electrodes were dried overnight under vacuum in an oven within the glove box (O_2, H_2O < 0.1 ppm, MBraun, Germany) at 120°C and were not exposed to air after the drying procedure. For some experiments, graphite anodes were preformed in coin half-cells: cells were cycled for two cycles with a discharge rate of C/15 down to 0.025 V vs. Li^+/Li followed by a 1 h CV step at this potential and a subsequent charge at C/15 up to 1.5 V vs. Li^+/Li; then, the cells were disassembled at 1.5 V in a glove box (O_2, H_2O < 0.1 ppm, MBraun, Germany). These preformed graphite electrodes were used for full-cell assembly without any further washing step.

On-line electrochemical mass spectrometry (OEMS).—For OEMS experiments, electrodes coated onto a stainless-steel mesh (see above) were used to have a porous medium as current collector in order to allow diffusion from the electrode to the capillary.[25] For OEMS measurements a custom-made cell is used; the cell design as well as the OEMS setup were reported previously.[39] OEMS cells were assembled with Li metal counter electrode, two porous polyolefin separators (2500, Celgard, USA), a HE-NCM or NCM working electrode and 120 μl of electrolyte composed of FEC:DEC (2:8 g:g) and 1 M $LiPF_6$ (BASF SE, Germany). The cells were connected to the mass spectrometer, held for 4 h at OCV (open circuit voltage), and then charged to 4.8 V vs. Li^+/Li at a C/10 rate, followed by a 1 h CV step at 4.8 V vs. Li^+/Li; the discharge to 2.0 V vs. Li^+/Li and the second charge/discharge cycle were conducted at C/5 rate between 4.8 V vs Li^+/Li (+1 h CV) and 2.0 V vs Li^+/Li (C-rates here are calculated based on a nominal capacity of 250 mAh/g). For quantification of the mass spectrometer currents, a calibration gas containing H_2, O_2, CO_2, C_2H_4 (each 2000 ppm) in Argon (Linde AG, Germany) was used. All currents were normalized to the current at m/z = 36 (Ar isotope) in order to correct for effects of minor pressure and temperature deviations, and afterwards the currents m/z = 32 (O_2) and m/z = 44 (CO_2) were converted into gas concentration.

Electrochemical characterization.—Galvanostatic cycling was carried out in 2032-type coin-cells (Hohsen Corp., Japan) at 25°C in a temperature controlled oven (Binder, Germany) and using a battery cycler (Series 4000, Maccor, USA). Half-cells were assembled in an argon filled glove box (O_2, H_2O < 0.1 ppm, MBraun, Germany) using a Li metal anode with a diameter of 17 mm, three glass fiber separators (glass microfiber, GF/A, VWR, Germany), and an HE-NCM cathode (coated on Al current collector) with a diameter of 14 mm. The cells were filled with 120 μL electrolyte (FEC:DEC (2:8 g:g) with 1 M $LiPF_6$; BASF SE, Germany). For impedance measurements in symmetrical cells, charge/discharge cycled half-cells were charged to 50% SOC in the final cycle (based on the preceding complete charge-discharge cycle) and afterwards the cathodes were harvested in an argon filled glove box. Subsequently, two harvested cathodes from cells cycled with the same procedure were reassembled for impedance

measurements into a symmetric coin cell with one thick glass fiber separator (300 μm thickness; glass microfiber filter, GF/D, VWR, Germany) and 95 μL of the same FEC:DEC electrolyte. For full-cell experiments in 2032 coin-cells, a graphite anode with a diameter of 15 mm and a cathode with a diameter of 14 mm were assembled with one polyethylene separator (2500, Celgard, USA) and with 14 μL of electrolyte based on FEC:DEC with 1 M $LiPF_6$ with an additional confidential co-solvent to improve full-cell cycling stability. For proof of reproducibility, at least two independent measurements were carried out and the here presented cycling data show the average values while the error bars reflect the maximum and minimum of the measured values.

All cells were allowed to rest for 2 hours prior to electrochemical testing and C-rates are referenced to a nominal capacity of 250 mAh/g. For half-cells, the first activation cycle was conducted at C/10 up to 4.8 V, followed by a 1 h CV-step at this potential and a discharge at C/5 to 2.0 V. The second charge/discharge cycle was conducted at C/5 and also charged up to 4.8 V, followed by 1 h CV-step at 4.8 V and a discharge at C/5 to 2.0 V (up to this point identical with the OEMS cycling procedure). The subsequent charge/discharge cycles at C/5 had a reduced upper cutoff potential of 4.7 V without a CV-step and the same lower cutoff potential of 2.0 V (CC/CC charge/discharge procedure).

Full-cells were activated in the first cycle at a C-rate of C/15 to 4.7 V (corresponding to ≈4.8 V vs. Li^+/Li, as in the half-cell and OEMS measurements), followed by a 1-hour CV-step at this potential (CCCV charge), and then discharged at C/15 to 2.0 V (CC); in subsequent cycles, the upper cutoff and CV-step potential were reduced to 4.6 V. Afterwards 4 cycles at C/10 were applied (CCCV), followed by a rate test for which the cell was charged/discharged for 3 cycles each at 0.2C (CCCV)/0.5C (CC), 0.5C (CCCV)/1C (CC), 0.5C (CCCV)/2C (CC), 0.5C (CCCV)/3C (CC), whereby all CV-steps were terminated after 1 h or when the current decreased below 0.01C. The rate test was followed by 250 cycles with a charge rate of 0.5C (CCCV) and a discharge rate of 1C (CC), the CV-step defined as above.

High-resolution transmission electron microscopy (HRTEM).— Cathodes for HRTEM measurements were obtained from half-cell coin-cells which had been cycled at C/5 for 2 or 50 cycles (see above for cell assembly and half-cell cycling procedure). The electrodes were harvested at 0% SOC (cells discharged to 2.0 V), corresponding to a fully lithiated cathode material. After cycling, cathodes were harvested in an argon filled glove-box and then washed for 5 minutes first in an FEC:DEC (2:8 g:g) solvent mixture and then in pure DEC (BASF SE, Germany). Subsequently, the electrodes were dried overnight at room temperature inside the glove box.

Samples for transmission electron microscopy (TEM) were prepared by focused ion beam (FIB) milling using a Strata 400 dualbeam machine (FEI Company, Hillsboro, USA). Samples were immediately imaged at 200 keV by HRTEM on FEI Tecnai G20 and FEI Osiris microscopes. The local crystal structure of oriented crystallites was analyzed by Fourier-analysis of the images using the Digital Micrograph software (Gatan, Pleasanton, USA: version 2.11).

Results

Electrochemical activation plateau.—Table I lists the different HE-NCM and NCM materials by their compositions, given as x Li_2MnO_3 • (1-x) $LiMeO_2$ (Me = Ni, Co, Mn) with x = 0.00, 0.33, 0.42 and 0.50. The shown total theoretical capacities (Q) are calculated for a theoretical complete delithiation using Faraday's law:

$$Q = \frac{n_{Li}\ F}{M} \qquad [1]$$

with F being the Faraday constant (96485 As/mol), M being the molar mass of the (HE-)NCM, and n_{Li} being the moles of lithium per mol of (HE-)NCM. Furthermore, the fraction of the capacity arising from the NCM domain and from the Li_2MnO_3 domain can be calculated individually from the given stoichiometry and molecular weight and is also shown in Table I. From these results, one can see that higher

Table I. Chemical formulas/compositions, theoretical capacity and BET surface areas for materials with Li_2MnO_3 content of 0.00, 0.33, 0.42 and 0.50; Li_2MnO_3 was varied with the same $LiMeO_2$ component, ending up in a constant Ni:Co ratio and a variation in the amount of Li and Mn for the different compositions. The total theoretical capacity is calculated for 100% delithiation of the material, according to Equation 1; furthermore, shown are the nominal theoretical capacities of the $LiMeO_2$ and the Li_2MnO_3 domains.

	Theoretical capacity [mAh/g]			
Composition	Total	$LiMeO_2$	Li_2MnO_3	BET [m^2/g]
0.00 Li_2MnO_3 • 1.00 $LiMeO_2$	279	279	0	0.5
0.33 Li_2MnO_3 • 0.67 $LiMeO_2$	346	174	172	6.5
0.42 Li_2MnO_3 • 0.58 $LiMeO_2$	363	148	215	6.5
0.50 Li_2MnO_3 • 0.50 $LiMeO_2$	377	126	251	6.0

Li_2MnO_3 contents lead to a higher share of capacity arising from the Li_2MnO_3 domain, but also the theoretical total capacity of the overall compound can be increased substantially with increasing lithium content. Also shown in Table I are the BET areas, which are essentially identical for the HE-NCM materials, but more than an order of magnitude lower for the NCM material. Therefore, for better comparability, gas evolution rates from OEMS experiments will be also normalized to the BET area (in units of μmol/m^2).

Figure 1 depicts the first cycle activation for all three compositions in half-cells, showing the first cycle charge-discharge curves

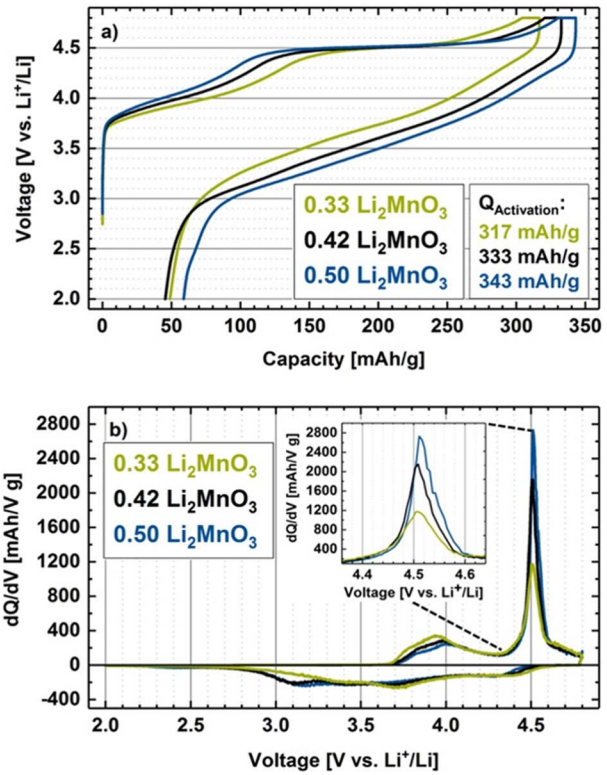

Figure 1. (a) Voltage vs. capacity for the first activation cycle in half-cells of HE-NCM with 0.33, 0.42, and 0.50 Li_2MnO_3 content (see Table I); the first charge capacity $Q_{Activation}$ is given in the figure. (b) Corresponding dQ/dV plots, show an increasing peak at 4.5 V with increasing Li_2MnO_3 contents (the inset is a zoom into the 4.5 V region). Cells were activated with metallic-Li as counter electrode at C/10 up to 4.8 V followed by a 1 h CV-step at 4.8 V and then discharged at C/5 to 2.0 V at 25°C in FEC:DEC (2:8 g:g) with 1 M $LiPF_6$.

in Figure 1a and the corresponding dQ/dV plot in Figure 1b, both showing a longer activation plateau and a higher amount of capacity in this plateau with increasing Li_2MnO_3 content. The first charge capacities are given in Figure 1a, reaching 317 mAh/g for a Li_2MnO_3 content of 0.33, 333 mAh/g for 0.42 Li_2MnO_3, and 343 mAh/g for 0.50 Li_2MnO_3. Comparing the measured capacities from Figure 1 to the total theoretical capacities listed in Table I, the apparent degree of delithiation is 92% for the materials with 0.33 and 0.42 Li_2MnO_3 and 91% for the material with 0.50 Li_2MnO_3. While the degree of delithiation is similar for different Li_2MnO_3 contents, one should note that delithiation beyond 90% of the overall amount of lithium is unique for this class of materials and cannot be achieved for classical NCM materials without irreversibly destroying the material.[10] However, this high delithiation cannot be explained by only taking cationic redox into account, given that Mn^{IV} in Li_2MnO_3 is redox inactive. Therefore, it is clear that another mechanism is responsible for charge compensation. While some groups expect electrochemical activation of Li_2MnO_3 to MnO_2 accompanied by bulk oxygen release,[11] more recent publications give strong evidence that anionic oxygen redox might serve for charge compensation at high delithiation.[26,31–33] The specific role of oxygen release HE-NCM particularly during the first activation cycle will be analyzed and discussed later on.

Focusing now on the quantitative effect of the Li_2MnO_3 on the capacity in the activation plateau, we defined the capacity gained during the plateau as the capacity gained between 4.40 V and 4.60 V. The thus obtained capacities during the activation plateau are 116 mAh/g for 0.33 Li_2MnO_3, 159 mAh/g for 0.42 Li_2MnO_3, and 190 mAh/g for the 0.50 Li_2MnO_3 content, showing a clear correlation between the Li_2MnO_3 content and the activation plateau capacity.[40] On the other hand, Figure 1a shows also that the capacity loss during the first discharge increases with increasing Li_2MnO_3 content, resulting in a comparable first-cycle irreversible capacity loss of 49 mAh/g for 0.33 and 46 mAh/g for 0.42 Li_2MnO_3, while the HE-NCM with the higher 0.50 Li_2MnO_3 content shows a much higher value of 60 mAh/g. In the discussion section, we will examine in detail the possible origins and explanations for this high irreversible capacity loss during activation, and how it influences the actual full-cell performance of the material.

Effect of the activation in full-cells.—For further analysis of the high irreversible capacity during the first charge/discharge cycle of HE-NCMs, full-cells were assembled, in the same way as the half-cells discussed in Figure 1, using a preformed graphite counter electrode instead of a lithium counter electrode. The graphite electrode was preformed in the same electrolyte in order to eliminate anode SEI losses (detailed information can be found in the experimental section). The upper cutoff potential was lowered from 4.8 V for the half-cells to 4.7 V in the full-cells, so that the upper cutoff potential of the cathode corresponded to ≈4.8 V vs. Li^+/Li in both cases. Figure 2a shows the corresponding first charge/discharge potential profiles for the different HE-NCMs. Comparable first-cycle irreversible capacities can be observed for the full-cells with preformed graphite electrodes and the Li metal half-cells (see Table II). By using preformed graphite electrodes, a capacity loss caused by the graphite anode is not expected, as a preformed SEI already exists which should prevent further electrolyte decomposition.

After the first cycle, the discharged cells were disassembled and the graphite anodes were harvested in order to determine the amount of cyclable lithium present in the graphite anode in the discharged HE-NCM//graphite full-cell. This was done by assembling half-cells with the harvested graphite electrodes with lithium counter electrodes and discharging them to 1.5 V at 0.1C in order to obtain the residual capacity in the graphite anodes, whereby this value was normalized to the mass of the cathode that was used during the full-cell activation, providing comparable results for the different cathode materials. Figure 2b shows that the residual capacity in the graphite anodes depends on the Li_2MnO_3 content of the cathode used during full-cell activation, and as one might expect, a higher Li_2MnO_3 content leads to a higher residual capacity stored in the anode. Table II compares the

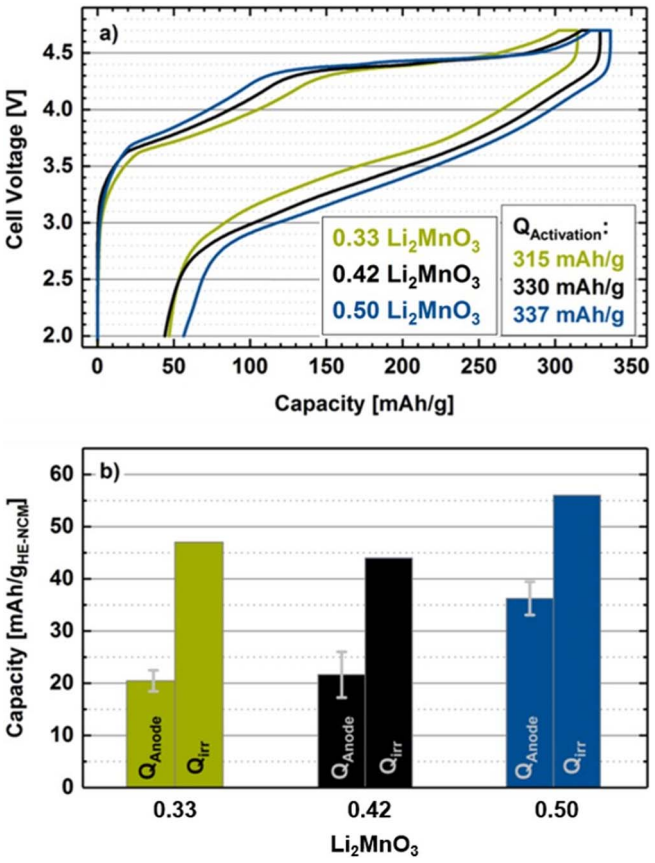

Figure 2. (a) Voltage curves for the first activation cycle in a full-cell of HE-NCM with 0.33, 0.42, and 0.50 Li_2MnO_3 content (see Table I), using preformed graphite anodes (see experimental section). (b) Residual capacity of the preformed graphite anodes after the first charge/discharge cycle (Q_{Anode}), obtained from the delithiation of harvested graphite anodes in half-cells to 1.5 V at C/10 (referenced to the cathode loading), as well as the irreversible first-cycle capacities (Q_{irr}) derived from Figure 2a (error bars for the residual capacities are derived from two independent measurements). Full-cells were charged at C/10 up to 4.7 V followed by a 1 h CV-step at 4.7 V and then discharged at C/5 to 2.0 V at 25°C in FEC:DEC (2:8 g:g) with 1 M $LiPF_6$.

first-cycle irreversible capacities measured during full-cell and half-cell activation as well as the residual capacity stored in the graphite anodes. From this it can be concluded that a higher first-cycle irreversible capacity leads to a higher amount of cyclable lithium within the graphite anode. In other words, a high irreversible capacity during the first charge does not necessarily mean that a high amount of lithium is lost irreversibly, but rather that after the HE-NMC activation not all of the extracted lithium can be reinserted into the cathode active

Table II. First-cycle irreversible capacities (Q_{irr}) during the first charge/discharge cycle for HE-NCMs with different Li_2MnO_3 content, taken from Figure 1a and Figure 2a, respectively. Also, the residual capacity obtained from preformed graphite anodes shown in Figure 2b is compared to the first-cycle irreversible capacity loss, showing an offset of ≈20 – 27 mAh/g.

	Q_{irr} [mAh/g]		
Li_2MnO_3	Half-cell	Full-cell	Residual capacity in preformed graphite [mAh/g]
0.33	49	47	20
0.42	46	44	22
0.50	60	56	36

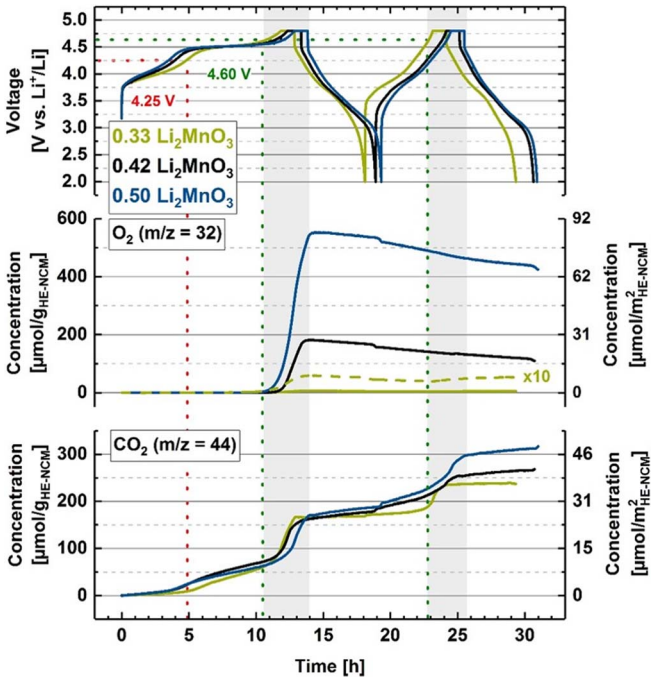

Figure 3. OEMS measurements for the first two charge/discharge cycles in a half-cell with three different HE-NCM compositions (see also Table I). Upper panel: charge/discharge voltage vs. time; middle/lower panel: evolution of the concentrations of concomitantly evolved O_2/CO_2 given in units of either $\mu mol/g_{AM}$ (left axes) or $\mu mol/m^2{}_{AM}$ (right axes). Cells were charged at C/10 rate to 4.8 V, followed by 1 h CV-step at 4.8 V and a consecutive discharge at C/5 to 2.0 V and another full charge/discharge cycle at C/5. Cells were composed of metallic Li counter electrode and a Celgard separator (CG2500) and experiments were conducted at 25°C in FEC:DEC (2:8 g:g) with 1 M $LiPF_6$. The vertical dashed red line indicates the first onset of CO_2 evolution, and the vertical dashed green lines mark the potential of 4.6 V where the onset of O_2 evolution occurs.

material (even though for mechanistically different reasons, an irreversible capacity loss is also observed for NCM 111).[41,42] However, for all compositions an offset between capacity loss during the first cycle and the cyclable lithium capacity in the graphite anodes of about 20 – 27 mAh/g is observed. This capacity offset must correspond to an irreversible loss of active lithium in side-reactions during the first charge/discharge cycle and cannot be assigned to typical anode SEI losses, as the SEI was already preformed on the graphite electrodes. The specific reactions leading to this phenomenon are unfortunately not clear at this time. However, Figure 2 shows that an increasing Li_2MnO_3 content leads to a higher amount of active lithium within a HE-NCM//Graphite full-cell. Thus, it is expected that this additional lithium can be utilized for SEI formation or stored in the graphite anode as lithium reservoir that can be utilized during cycling. Therefore, the full-cell performance is expected to be improved for higher Li_2MnO_3 which will be discussed later.

Oxygen release during activation.—To examine the effect of different Li_2MnO_3 onto the oxygen release of overlithiated NCM materials and to get insights if electrochemical Li_2MnO_3 activation accompanied by bulk oxygen release is feasible, results of the OEMS measurements on all three compositions are shown in Figure 3. The upper panel shows the galvanostatic charge/discharge profiles between 2.0 and 4.8 V against a Li counter electrode, and the middle/lower panels depict the concentration of the concomitantly evolved O_2/CO_2; concentrations are given in terms of both $\mu mol/g_{AM}$ (left axis) and $\mu mol/m^2_{AM}$ (right axis), whereby the latter surface normalized concentration will be used in the discussion section for comparison with the stochiometric NCM material. The first onset of CO_2 evolution can be observed at 4.2 V, followed by a rapid increase in CO_2 upon the onset of oxygen release at 4.6 V vs. Li^+/Li, i.e., at the end of the first charge activation plateau. Quite striking when comparing the different HE-NCMs is that the amount of evolved CO_2 is essentially identical for all materials, the extent of O_2 release decreases substantially with decreasing Li_2MnO_3.

However, concerning the origin of CO_2 from stochiometric and overlithiated layered oxides, there is an ongoing debate: while Luo et al.[26] suggested that the main part of CO_2 evolved from overlithiated oxides derives from electrolyte oxidation with lattice oxygen, it has been proposed by Renfrew et al.[43] that CO_2 evolution is exclusively triggered by the decomposition of Li_2CO_3 surface impurities. However, Jung et al.[8,10,44] and Strehle et al.[25] proposed another concept for stochiometric and overlithiated layered oxides, respectively, suggesting that CO_2 evolution starting at 4.2 V vs. Li^+/Li before the onset of oxygen release is produced by the oxidation of surface impurities, while the released oxygen is suggested to react with the carbonate electrolyte causing CO_2 evolution, consistent with the concomitant rapid increase in CO_2 concentration. While the exact mechanism leading to CO_2 evolution is still subject to ongoing discussions, we will here adopt the mechanistic view proposed by Strehle et al. and Jung et al. As mentioned above, a rather striking observation is the ≈100-fold variation in the amount of oxygen released by the end of the first activation charge for the different Li_2MnO_3 contents: ≈6 µmol/g (≈1 $\mu mol/m^2$) for 0.33 Li_2MnO_3, ≈180 µmol/g (≈28 $\mu mol/m^2$) for 0.42 Li_2MnO_3, and ≈550 µmol/g (≈85 $\mu mol/m^2$) for 0.50 Li_2MnO_3 content. If compared to the amount of O_2 which would be expected for the historically proposed bulk activation of Li_2MnO_3 (1600 µmol/g for 0.33 Li_2MnO_3, 2000 µmol/g for 0.42 Li_2MnO_3, and 2350 µmol/g for 0.50 Li_2MnO_3), bulk oxygen release does not seem to be a feasible mechanism for these overlithiated materials. As already shown in a previous study, oxygen release caused by a chemical layer-to-spinel transformation leading to the formation of a resistive surface layer and concomitant oxygen release from near-surface regions can explain the phenomena of oxygen release for HE-NCMs[25] as well as for classical NCM materials.[9,10] In these reports as well as in our present study, the main part of the oxygen evolution is detected during the first charge of the material, while rather small amounts of O_2 evolution can be detected during the second cycle. The continuous oxygen consumption during the cycling procedure indicated by the decreasing O_2 concentration after the first charging cycle (see middle panel in Figure 3) is ascribed to a gradual reduction of oxygen to Li_2O_2 on the lithium counter electrode, shown by Yabuuchi et al. to occur below 3.0 V vs. Li^+/Li.[22] Furthermore, a more sudden oxygen consumption can be observed when the cathode is cycled below 3.0 V vs. Li^+/Li (e.g., at ≈19 h in Figure 3), whereby the initially formed superoxide radical causes a sharp CO_2 increase due to reaction with the electrolyte.[22] During the first charging cycle, the onset of O_2 evolution is accompanied by a rapid increase of the CO_2 evolution rate, as discussed above. However, while no further evolution of O_2 can be observed in the second cycle, further CO_2 evolution can be detected at the potential where O_2 started to evolve in the first cycle (≈4.6 V), indicating further oxygen release from the cathode material, even if no molecular O_2 evolution can be detected anymore.

Galvanostatic cycling of half-cells.—As a next step, Figure 4 shows the half-cell cycling data for all three different compositions over 50 cycles at a rather slow rate of C/5 and with a high amount of electrolyte (120 µl). Figure 4a depicts the discharge capacity retention for the materials, whereby the material with the highest Li_2MnO_3 content also shows the highest initial capacities, as expected from Table I and Figure 1. The capacity of the 0.50 Li_2MnO_3 material (blue symbols) decreases strongly during the first 20 cycles, resulting in a capacity loss of 28 mAh/g between cycle 3 and cycle 50 (253 mAh/g to 225 mAh/g), while the capacity fading of the 0.42 Li_2MnO_3 over the same cycles is much lower (255 mAh/g to 240 mAh/g), amounting to a capacity loss of 15 mAh/g. The lowest capacity fading of roughly 7 mAh/g between cycle 3 and 50 is observed for the 0.33 Li_2MnO_3 (247 mAh/g to 240 mAh/g). Comparing this with the results from Figure 3 suggests that a higher oxygen release leads to more extensive

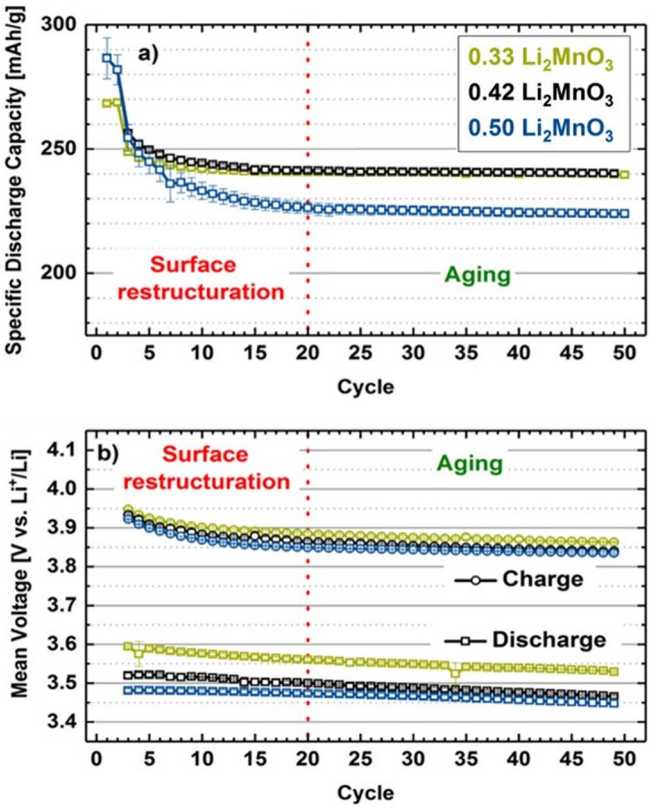

Figure 4. Electrochemical cycling at C/5 rate of the different HE-NCM compositions at 25°C using a Li counter electrode, FEC:DEC (2:8 g:g) with 1 M $LiPF_6$ electrolyte, and a glassfiber separator. The first activation cycle was carried out at C/10 to 4.8 V where the potential was held for 1 h and then the cell was discharged at C/5 to 2.0 V, followed by an analogous second activation cycle at C/5 (up to 4.8 V + 1 h CV); all further cycling (i.e., starting at the third cycle) was carried out at C/5 rate without any CV-steps (CC charge/discharge) between 2.0 V and 4.7 V. (a) shows the specific discharge capacity as a function of the cycle number (note that the first two discharge capacities are cycled up to 4.8 V followed by 1 h CV), while (b) shows the corresponding mean charge and discharge voltage (as defined by Eq. 1 in Jung et al.[10]). All data points represent the average of at least two independent measurements and the error bars reflect the maximum and minimum of the measured values.

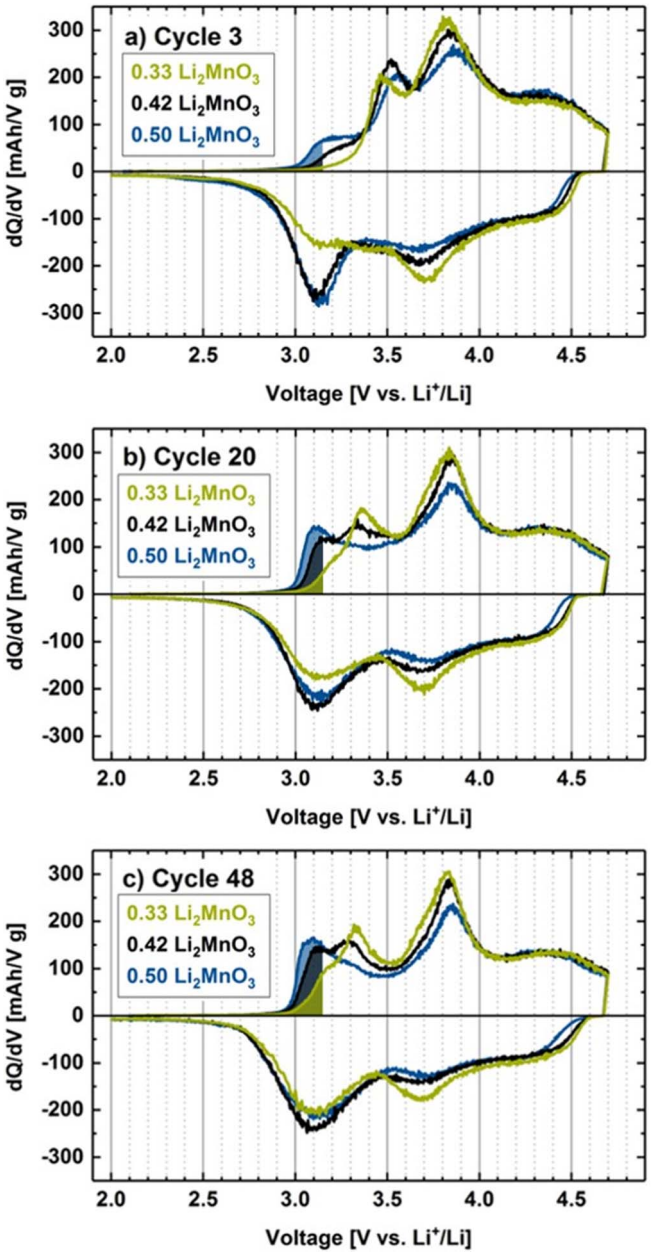

Figure 5. Electrochemical cycling of the different HE-NCM compositions at 25°C using a Li counter electrode, FEC:DEC (2:8 g:g) with 1 M $LiPF_6$ electrolyte, and a glassfiber separator. The activation and cycling procedure is that same as that shown/described in Figure 4. All dQ/dV plots were recorded at C/5 for cycle 3 (a), cycle 20 (b) and cycle 48 (c). The shaded areas in the charging cycles represent the hypothesized rocksalt-to-spinel transition.

surface degradation and a concomitant decrease of the electrochemical performance; the effect of oxygen release on active material loss will be discussed and quantified in the discussion section. As oxygen release is hypothesized to be correlated to the voltage hysteresis and the hysteresis between charge and discharge,[11,45] one might pose the question whether the large differences in oxygen release shown in Figure 3 also have such a big influence onto the voltage fading of the different materials. The mean charge and discharge voltages are shown in Figure 4b. It can be seen that the mean charge voltage fading is comparable for all three materials, showing a fading of ≈90-100 mV between cycle 3 and 50 for all materials. The same observation can be made for the mean discharge voltage fading, which does not differ largely between the different materials (≈40–70 mV). Thus, while the O_2 release increases by almost two orders of magnitude as the Li_2MnO_3 content is increased, the differences in voltage fading are rather minor, which suggests that the main cause of the voltage fading of HE-NCMs is not related directly to the oxygen release. Therefore, the oxygen release is a side reaction occurring at the HE-NCM near-surface region,[25] while reversible and irreversible transition metal migration in the bulk material cause the main voltage fading and the high hysteresis.[35,45,46]

Figure 5 depicts the dQ/dV plots for cycle 3, cycle 20, and cycle 48 extracted from the cycling data shown in Figure 4. Hereby, cycle 3 is the first C/5 cycle between 2.0 V and 4.7 V and therefore is subjected to the same cycling conditions as cycle 20 and 48. For the characterization of the mean voltages as well as the evolution of the spinel surface layer, we will focus on the charging curve of the materials, as the discharge shows very high impedances and limitations of Li diffusion within the bulk of the material, which is part of a separate study.[14] The most striking differences can be observed by a peak in the dQ/dV plot growing at roughly 3.1 V during the charge (shadowed areas in Figure 5). In Figure 5a and Figure 5b it can be seen that the area under this peak is largest for the 0.50 Li_2MnO_3 material that also has the highest O_2 release, while for the material with the lowest oxygen release (0.33 Li_2MnO_3) the area under this peak is lowest. Therefore, we suggest that this peak might be correlated to an oxygen deficient, spinel-like electrochemically active

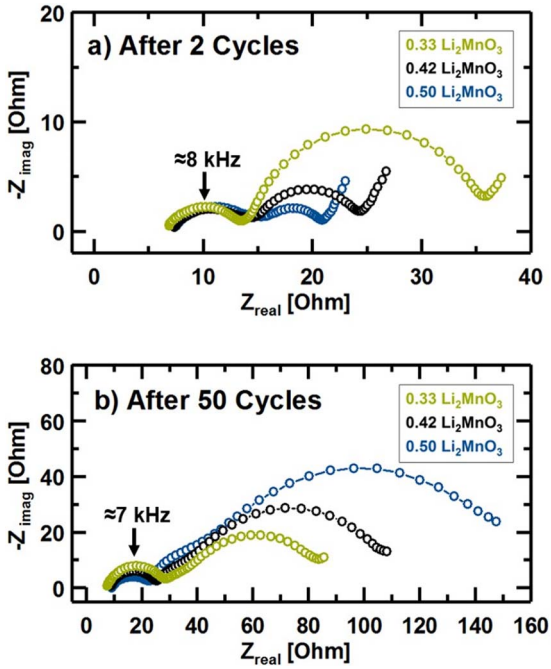

Figure 6. Impedance spectra measured in symmetric coin cells with cathodes harvested at 50% SOC (a) after the two-cycle activation procedure and (b) after a total of 50 cycles according to the procedure shown in Figure 4. Symmetric cells were built with a 300 μm glassfiber separator and with 95 μL of 1 M $LiPF_6$ in FEC:DEC (2:8 g:g) electrolyte. Impedance spectra were measured at the OCV at 50% SOC (between 300 kHz and 30 mHz with an amplitude of 10 mV).

surface structure, which would also be consistent with the observations by Bruce et al. and Thackeray, who proposed the rocksalt-to-spinel transition ($Li_2Mn_2O_4 \rightarrow LiMn_2O_4 + Li^+ + e^-$) at such potentials.[47,48] Comparing the evolution of the area under these peaks, it can be clearly seen that it increases substantially from cycle 3 to cycle 20, while it remains relatively constant between cycle 20 and cycle 48. This behavior reflects the evolution of the capacity loss with cycling, which is most pronounced during the first 20 cycles, while afterwards the capacity stays approximately constant (Figure 4a). Thus, the capacitive contribution from the first charging peak in the dQ/dV plot seems to correlate with the capacity loss, which we will further quantify in the discussion section, including the relationship of this feature with the extent of oxygen release.

Impedance spectroscopy in symmetric cells.—It has been reported in the literature that surface degradation of layered oxides, caused by oxygen release, can lead to spinel and rocksalt like structures at the surface of the cathode material, leading to drastic increases in the charge transfer resistance, which in turn might be the cause of the so-called rollover failure.[10,49] Figure 6 shows impedance spectra measured in symmetric cells for HE-NCM electrodes with the three different compositions (a) after 2 activation cycles, and (b) after another 48 cycles (total of 50 cycles) according to the procedure in Figure 4. Impedance spectra were acquired at OCV following a charge to 50% SOC (based on the preceding full charge-discharge cycle). All Nyquist plots show two distinct semi-circles, one at high frequencies that shows the same resistance for all the materials both at cycle 2 and 50 (increasing from ≈8 to ≈20 Ω), and one at lower frequencies which differs significantly for the different compositions. Previous studies have shown that the semi-circle at high frequencies for cathode electrodes can be assigned to a contact resistance at the interface of the cathode electrode with the aluminum current collector,[50,51] which can also be rationalized by considering the electrode capacitance corresponding to this first semi-circle:

$$C = \frac{1}{R\ 2\ \pi\ f_{max}} \quad [2]$$

where C is the capacitance, R is the diameter of the semi-circle (divided by two in this case of a symmetric cell), and f_{max} is the frequency corresponding to the apex of the first semi-circle. For the data shown in Figure 6a, the resistance for one electrode is R ≈8 Ω and f_{max} ≈8 kHz, equating to an electrode capacitance of ≈5 μF, which is similar for all HE-NCM compositions. To understand its origin, one may normalize it by either the surface area of the current collector (≈1.5 cm^2 for the 14 mm diameter electrodes) or by the total surface area of the cathode electrode (≈730 cm^2, based on the mass of HE-NCM and conductive carbons in the electrode multiplied by their BET surface area), yielding either ≈3.2 μF/cm^2 or ≈0.007 μF/cm^2, respectively. If compared to the typical double layer capacitance which is on the order of ≈10^1 μF/cm^2, it is clear that the first semi-circle occurs due to a contact resistance at the interface between the electrode and the current collector. Detailed studies onto the origin of those contact resistances are reported elsewhere.[50,51]

The second semi-circle at lower frequencies can then be assigned to a charge-transfer resistance (R_{CT}), which clearly differs largely for the different HE-NCM materials. First examining their impedance directly after the two activation cycles (Figure 6a), it can be seen that R_{CT} decreases with increasing Li_2MnO_3 content and thus with increasing oxygen release (Figure 3). This could be rationalized by assuming either that the oxygen vacancies in the surface layer largely increase the lithium ion mobility and/or that the surface restructuration increases the porosity at the surface of the cathode material, concomitant with an increase in interfacial surface area and thus a lowering of the apparent charge transfer resistance.

Interestingly, the above discussed trend of a decreasing charge transfer resistance with increasing Li_2MnO_3 content reverses over the course of cycling (Figure 6b). Even though the resistance represented by the second semi-circle increases for all HE-NCMs from cycle 2 to cycle 50 (Figure 6b), it increases by a much larger factor for the 0.50 Li_2MnO_3 (≈15-fold) compared to the 0.33 Li_2MnO_3 material (≈2.5-fold), so that after 50 cycles the 0.50 Li_2MnO_3 material now shows the highest impedance and therefore also the highest impedance buildup. As the thickness of the oxygen-deficient phase after the activation is expected to increase with the extent of O_2 release and thus with the extent of overlithiation, the gradual transformation of this surface layer from perhaps an initially highly conductive disordered layered structure into a more resistive ordered spinel or rocksalt structure could explain the increase in the cycling induced impedance buildup with the extent of overlithiation. This hypothesis will be examined in the following by HRTEM analysis of pristine and cycled HE-NCMs.

High-resolution TEM measurements.—Figure 7 shows representative HRTEM images of the near-surface region for the material with an intermediate extent of overlithiation (0.42 Li_2MnO_3) for the pristine material (a), after 2 cycles (b), and after 50 charge-discharge cycles (c), following the same cycling protocol as that shown/described in Figure 4. For the pristine material, a layered structure without any crystalline surface layer but with a thin amorphous surface layer can be seen, which we ascribe to carbonate and hydroxide surface impurities. The HRTEM image taken after 2 charge/discharge cycles (Figure 7b), i.e., after most of the oxygen has been released from the active material, clearly still shows a layered surface structure for which, however, a slight loss of density in the near-surface regions can be observed. This provides first hints that the release of oxygen initiates changes in the surface structure. After 50 charge/discharge cycles, Figure 7c clearly shows the presence of a pronounced surface layer with a thickness of roughly 4 nm, whereby the corresponding FFT image in Figure 7d indicates strong cation mixing within the spinel-type surface layer. These findings are consistent with the HRTEM analysis by Genevois et al.[29] on chemically delithiated HE-NCM, indicating a strong surface restructuration after several charge/discharge cycles.

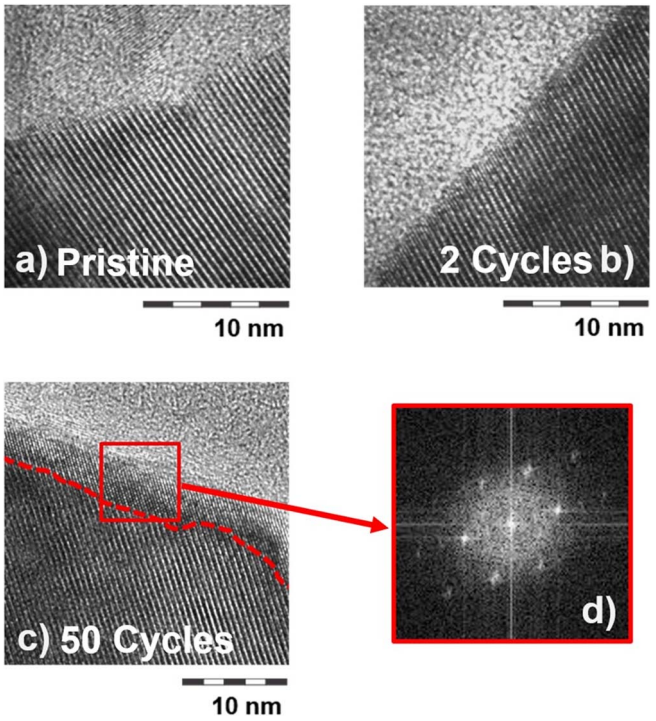

Figure 7. HRTEM analysis of the near-surface region of the 0.42 Li_2MnO_3 HE-NCM material (a) in its pristine state, (b) after 2 cycles, and (c) after 50 cycles (the cycling procedure is according to that described in Figure 4). (d) shows the corresponding FFT image for the material after 50 cycles, taken in the red marked region in (c).

Furthermore, the here presented HRTEM measurements support one of our above assumptions used to interpret the EIS measurements shown in Figure 6, namely the initial formation of surface layer with reduced density after activation and the associated O_2 release, followed by a densification[28] and spinel-type surface layer formation upon extended charge/discharge cycling.

HRTEM images for all HE-NCM compositions were also collected after 50 cycles. The 0.33 Li_2MnO_3 material is shown in Figures 8a–8c. Figure 8a shows an entire primary particle, displaying a perfectly layered bulk material as demonstrated by the FFT image (Figure 8b), with a surface-layer in the range of 1–2 nm. The latter is marked by the red dashed line and magnified in Figure 8c; unfortunately, this layer was too thin to take an FFT image. The HRTEM image of an entire primary particle of the 0.42 Li_2MnO_3 material is shown in Figure 8d, which also is a well-ordered layered bulk material, as demonstrated by the FFT image taken from the center of the particle (Figure 8f). However, the restructuration of the surface is much more pronounced for this material, showing a surface layer thickness in the range of 4 nm and even thicker in some areas (marked by the red dashed line in Figure 8d). The FFT image from the surface layer (Figure 8e) is in line with the image shown in Figure 7d, showing strong cation mixing in a spinel-type surface layer. Finally, the HRTEM images for the 0.50 Li_2MnO_3 material are shown in Figures 8g–8i. In these images it can be observed that the formation of a spinel-type structure is now not only limited to the surface, but also alters the bulk material. The FFT image in Figure 8h from one area within the particle indicates an intact layered structure, while Figure 8i from a different region within the same particle already shows cation mixing within the bulk material and changes of the layered structure. In summary, all these observations present strong evidence that the higher oxygen release during activation produced by higher degrees of overlithiation leads to an increasingly pronounced growth of surface layers, initially formed as reduced density layered structures and transformed upon cycling into spinel-type phases with strong cation mixing.

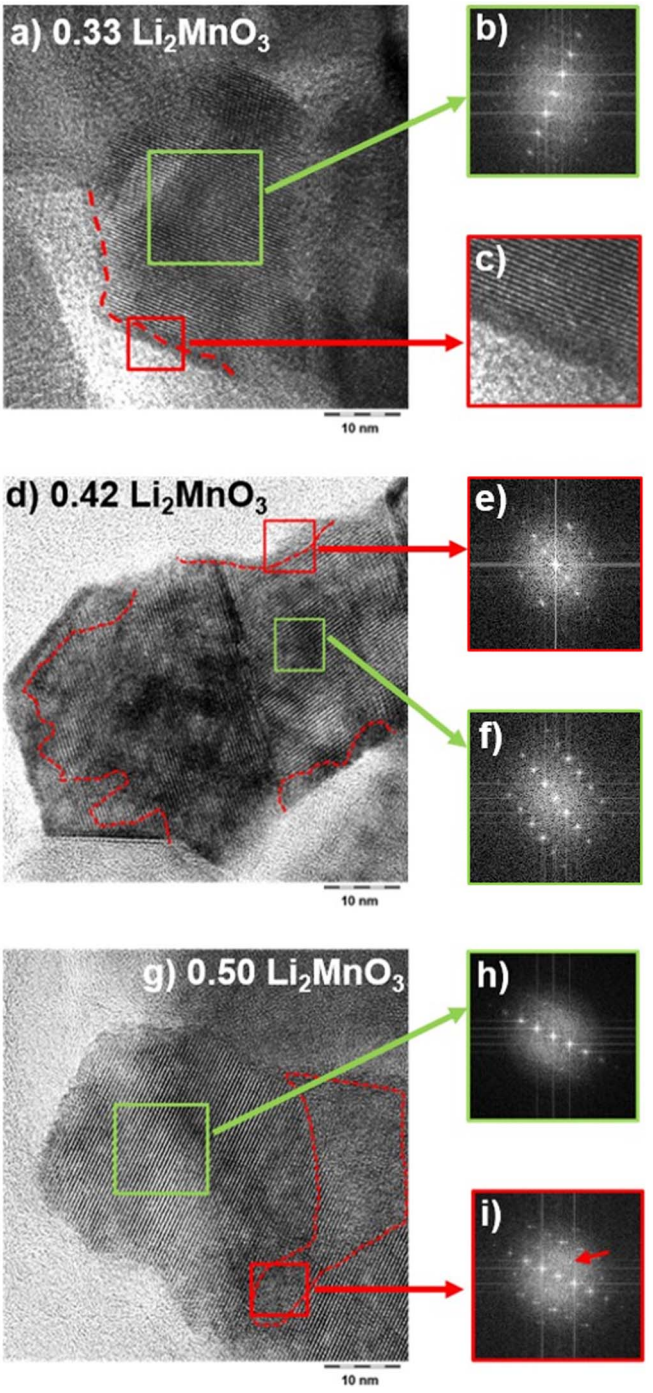

Figure 8. HRTEM images showing particle degradation for HE-NCMs with (a, c) 0.33 Li_2MnO_3, (d) 0.42 Li_2MnO_3, and (g) 0.50 Li_2MnO_3 content. Corresponding FFT images after 50 cycles from the marked regions in the HR-TEM images are shown: (b) for the bulk of the 0.33 Li_2MnO_3 material; (e) and (f) for the surface and bulk, respectively, of the 0.42 Li_2MnO_3 material; (h) and (i) for the bulk and surface, respectively, of the 0.50 Li_2MnO_3 material.

Discussion

***Estimation of spinel-type surface layer thickness.*—**Strehle et al. have recently shown that the oxygen evolution in Li- and Mn-rich layered oxides occurs *i*) right after the activation plateau and *ii*) also continues during the OCV at 4.8 V. Based on these results it was proposed that oxygen release from the bulk material seems to be unlikely, which led to the conclusion that high voltage charging and high degrees of delithiation destabilize the material's surface and ultimately

Table III. Li_2MnO_3 content, molar mass and theoretically required oxygen release for a 100% conversion into a spinel structure for HE-NCMs delithiated at 4.6 V ($n(O_2^{theo})$, see Equation 8),[10,25] calculated acc. to Equations 4–8.

Li_2MnO_3 content	Molar mass [g/mol]	100% O_2 conversion [μmol/g]
0.33	88.4	2941
0.42	86.8	2880
0.50	85.2	3521

result in a surface restructuration of the material.[25] Similar behavior was also shown to occur for stochiometric NCM materials, leading to a chemically driven formation of a spinel and/or rocksalt surface layer upon delithiation.[10] Such chemically driven spinel and/or rocksalt formation have been shown and intensively characterized for the thermally induced transformation of partially delithiated NCMs.[52,53] The general chemical reaction for spinel formation is given in Equation 3. Since rocksalt structures could not be observed by HRTEM measurements (see Figure 7 and Figure 8), the surface layer thickness is estimated only assuming the formation of a spinel surface layer.[10,25]

$$Li_xMe_yO_2 \rightarrow \frac{x+y}{3} Li_{3-\frac{3y}{(x+y)}} Me_{\frac{3y}{(x+y)}} O_4 + \frac{3-2(x+y)}{3} O_2 \uparrow \quad [3]$$

As starting compound for the spinel formation according to Equation 3, it is assumed that material restructuration starts at the oxygen onset potential, so the starting compound for the material restructuration is the partially delithiated phase at 4.6 V during the first charge, as already suggested by Strehle et al.[25] Thus, the amount of lithium that remains in the structure at the oxygen onset (x-value in Eq. 3) needs to be estimated using Equation 4

$$\Delta x_{Li} = \frac{QM}{F} \quad [4]$$

with Q being the capacity reached at the oxygen onset during the first charge (from Figure 3), M being the molar mass of the pristine HE-NCM, and F being the Faraday constant. With these calculations, residual lithium contents of $Li_{0.25}$ (0.33 Li_2MnO_3), $Li_{0.29}$ (0.42 Li_2MnO_3), and $Li_{0.25}$ (0.50 Li_2MnO_3) are found and can be further replaced into the general equations for spinel formation (Equations 3). The resulting transformations into the spinel phase for the different materials are shown in Equations 5 to 7.

Spinel formation for the 0.33 Li_2MnO_3 material delithiated to 4.6 V:

$$Li_{0.25}Me_{0.86}O_2 \rightarrow 0.37\ Li_{0.68}Me_{2.32}O_4 + 0.26\ O_2 \uparrow \quad [5]$$

Spinel formation for the 0.42 Li_2MnO_3 material delithiated to 4.6 V:

$$Li_{0.29}Me_{0.83}O_2 \rightarrow 0.37\ Li_{0.78}Me_{2.22}O_4 + 0.25\ O_2 \uparrow \quad [6]$$

Spinel formation for the 0.50 Li_2MnO_3 material delithiated to 4.6 V:

$$Li_{0.25}Me_{0.80}O_2 \rightarrow 0.35\ Li_{0.71}Me_{2.29}O_4 + 0.30\ O_2 \uparrow \quad [7]$$

These equations give the theoretical loss of oxygen per mole of HE-NCM for a 100% layered-to-spinel conversion (O_2^{theo}), from which the moles of oxygen released for a 100% conversion of the entire particle into the spinel ($n(O_2^{theo})$) can be easily calculated according to formula 8, using the molar mass of the different HE-NCM compositions. Table III shows the molar mass values for the different compositions, as well as the theoretical oxygen release which would be required for a 100% of spinel formation calculated from the equations above.

$$n\left(O_2^{theo}\right) = \frac{O_2^{theo}}{M} \quad [8]$$

The ratio of oxygen release expected for a 100% phase transformation ($n(O_2^{theo})$) into a spinel structure and the actual oxygen evolution measured by OEMS ($n(O_2^{meas})$) can be used to calculate the molar fraction of layered material converted into a spinel-type structure.

$$x_{surface\ layer} = \frac{n\left(O_2^{meas}\right)}{n\left(O_2^{theo}\right)} \quad [9]$$

To translate the molar fraction into a surface layer thickness, the approximate particle radius is estimated from the BET areas (A_{BET}) given in Table I according to Equations 10, with $\rho_{HE\text{-}NCM}$ being the crystallographic density of the pristine material ($\rho_{HE\text{-}NCM} = 4.2\ g/cm^3$).

$$r = \frac{3}{A_{BET}\ \rho_{HE-NCM}} \quad [10]$$

From the radius and the molar fraction of the spinel phase, the surface layer thickness can be easily assumed using Equations 11 and 12. More detailed information regarding these calculations have been reported by Strehle et al. and Jung et al.[10,25]

$$r' = r\left(1 - x_{surface\ layer}\right)^{1/3} \quad [11]$$

$$t_{surface\ layer} = r - r' \quad [12]$$

Based on the equations and assumptions discussed above, all results from the OEMS measurements and the results of the above calculations are summarized in Table IV. For the gas quantification two different models are taken into account: Model I is based on the amount of O_2 and CO_2 released above 4.6 V during the first charge, while Model II is based on the amount of O_2 and CO_2 released above 4.6 V during the first and the second charge, whereby the evolved amount of gases are taken from Figure 3 (from the gray shaded regions). As mentioned before, the assumption that the CO_2 evolved at high potentials is formed by lattice oxygen from the cathode material is still subject of ongoing discussions,[10,26,43] but recent measurements with ^{13}C labeled EC are in support of this.[44] Furthermore, the amount of evolved CO was not considered, as it is negligible with the here used FEC-based electrolytes (data not shown).

From Table IV it can be seen that the oxygen evolution strongly depends on the material composition and is nearly 100-times higher for the 0.50 Li_2MnO_3 compared to the 0.33 Li_2MnO_3 material. This is consistent with the increase of the surface (and bulk) restructuration with increasing lithium content observed in the HRTEM analysis (see Figure 8). In contrast, it is surprising that the amount of evolved CO_2 is essentially independent of the HE-NCM composition and the amount of evolved oxygen, suggesting that the reaction between electrolyte and lattice oxygen saturates at a high level of oxygen release from HE-NCM. Furthermore, since the CO_2 evolution at high potentials during the second charge is also likely due to the reaction of electrolyte with lattice oxygen (more apparent in the OEMS study by Jung et al. on NCMs),[10] Model II is assumed to be the more representative scenario.

From the total amount of CO_2 and O_2 evolved at ≥4.6 V, which we believe are reaction products of the electrolyte with lattice oxygen, the molar fraction of the resulting spinel surface layer as well as its thickness can be estimated; these are given for the different materials in Table IV. For the 0.33 Li_2MnO_3 material, a roughly 2 nm thick surface layer could be detected by HRTEM, which is consistent with the spinel layer thickness calculated for Model II (see Table IV). A similarly good quantitative agreement is found for the 0.42 Li_2MnO_3 material, with HRTEM images showing surface layers of roughly 4 nm, the same as the thickness predicted by Model II. However, for the 0.50 Li_2MnO_3 material the simple surface layer model fails, as oxygen depletion proceeds into the bulk of the material, leading to large domains of bulk degradation (see Figures 8g–8i). Nevertheless, when comparing semi-quantitatively the HRTEM images of the 0.50 Li_2MnO_3 material after 50 cycles, the molar fraction of ≈20 mol% of spinel based on the gas evolution data (Table IV) seems to be a realistic value. Please note that the results discussed above and shown in Table IV suggest the formation of a M'_3O_4 (M' = Li + Me) type spinel, as discussed in previous publications.[10,25] Another possible spinel structure formed upon oxygen release might be a $LiMn_2O_4$ type spinel layer, which would lead to a lower oxygen loss per mole

Table IV. Amounts of O_2 and CO_2 evolved at ≥4.6 V in the 1st (Model I) as well as in the 1st + 2nd cycle (Model II) from HE-NCMs with different Li_2MnO_3 contents (from the OEMS data in Figure 3). The molar fraction of the spinel surface layer ($x_{surf.\ layer}$) is calculated from the sum of O_2 and CO_2 detected at ≥4.6 V according to the chemical reactions given in Equations 3–9 and the surface layer thickness ($t_{surf.\ layer}$) is calculated from Equations 10–12.

		Gas evolution (≥4.6 V) [µmol/g_{AM}]				
Li_2MnO_3 content	Model	Total	O_2	CO_2	$x_{surf.\ layer}$ [mol%]	$t_{surf.\ layer}$ [nm]
0.33	I	96	6	90	3.3	1.2
	II	146	6	140	5.0	1.9
0.42	I	265	180	85	9.2	3.5
	II	305	180	125	11	4.0
0.50	I	650	550	100	19	7.3
	II	695	550	145	20	7.8

of converted HE-NCM, so that for the same amount of oxygen release a thicker spinel-type surface layer would be expected, based on the following general equation:

$$Li_xMe_yO_2 \rightarrow \frac{y}{2} Li_{\frac{2x}{y}}Me_2O_4 + (1-y)\ O_2 \uparrow \quad [13]$$

Conducting the same calculations (Model II in Table IV), as shown in Equation 5–12, for the formation of a $LiMn_2O_4$ type spinel layer, the following amounts of spinel ($x_{surf.\ layer}$ in mol%) will be obtained for the different materials: 9.2 mol% (0.33 Li_2MnO_3), 16.5 mol% (0.42 Li_2MnO_3) and 29.6 mol% (0.50 Li_2MnO_3), ending up with surface layers ($t_{surf.\ layer}$ in nm) from 3.5 nm (0.33 Li_2MnO_3) to 6.4 nm (0.42 Li_2MnO_3) up to 12 nm for the 0.50 Li_2MnO_3 HE-NCM. Comparing these values to the calculations for the M'_3O_4 spinel layer, with predicted spinel fractions and thicknesses ranging from 5–20 mol.% and from 1.9–7.8 nm, respectively (see Model II, Table IV), one can see that the formation of a $LiMn_2O_4$ type spinel would result in a ~1.5 fold larger estimated for the amount and the thickness of the spinel surface layer. Therefore, one should keep in mind that the here projected surface spinel layer amounts/thicknesses do depend on the actual phase that is formed after the oxygen release and as such are just rough estimates. However, taking into regard that the spinel forms due to cation migration at room temperature, we rather expect a disordered spinel with the stoichiometry M'_3O_4 than a well ordered $LiMe_2O_4$ phase, as obtained from high temperature synthesis.

In summary, by correlating HRTEM images/analysis with the OEMS experiments we have proven that the oxygen release during the HE-NCM activation cycles is accompanied by the formation of a surface spinel-like layer and is not due to a bulk restructuration, as suggested in earlier reports.[25,27–29] However, using a material with a very high lithium content, like the 0.50 Li_2MnO_3 material in this study, a partial bulk transformation can be observed, amounting to ≈20 mol% of the material being converted into a spinel-like phase (calculated from the oxygen evolution, shown in Model II from Table IV). While the TEM data are statistically not sufficient to provide exact quantitative surface layer thickness values for averaged over the entire material, they fit well to the quantification from the OEMS results. The partial bulk conversion for highly overlithiated HE-NCMs (≈20 mol%) now also explains previous studies from which it was concluded that the activation of HE-NCMs leads to a bulk transformation to a spinel-like phase.[19,20,22,54] For example Yabuuchi et al. and Mohanty et al. have suggested bulk structural changes during the first charge due to oxygen removal from the bulk of the material based on X-ray diffraction studies, both conducted with overlithiated HE-NCM with 0.50 Li_2MnO_3 content.[22, 54] Clearly, the results of structural, non-spatially resolved measurements are strongly dependent on the extent of overlithiation and perhaps on the synthesis of HE-NCM materials, which is the reason for the different mechanistic hypotheses which can be found in the literature. However, recent approaches using spatially resolved techniques[38] lead to the same conclusions as presented in our study.

Evolution of the surface layer during cycling.—Now we want to discuss the evolution of the structural transformation during cycling, considering the OEMS measurements (Figure 3), the impedance spectroscopy analysis (Figure 6), and the HRTEM data (Figure 7 and Figure 8). The OEMS experiments show the first CO_2 onset at 4.2 V, which we believe is correlated to the oxidation of surface contaminants at potentials as low as 4.2 V,[25,44] i.e., at a potentials far below the observed onset of oxygen evolution. At a potential of ≥4.6 V, strong oxygen release occurs during the first charge cycle, accompanied by a striking increase in CO_2 evolution, whereby it was shown that oxygen from the lattice is released as molecular oxygen and, at least partially as singlet oxygen,[55] leading to CO_2 formation from the reaction of reactive oxygen (surface) species with the electrolyte.[10,26,55] While only traces of oxygen were detected by OEMS during the second charge cycle, a boost in CO_2 evolution at ≥4.6 V (where the onset of oxygen evolution is observed in the first cycle) still suggests further reaction with lattice oxygen.

In contradiction to the OEMS analysis, which shows substantial O_2 and CO_2 evolution at ≥4.6 V in the first two cycles, HRTEM investigations of the 0.42 Li_2MnO_3 material (Figure 7) do not show any structural changes at the surface of the material after 2 cycles, implying that although the main part of the oxygen is released, the layered structure is still preserved. However, a clear structural surface transformation into a spinel-like layer can be observed after 50 consecutive charge/discharge cycles for all HE-NCM compositions, the thickness of which correlates nicely with the gas evolution in the first two cycles (see above). Another key observation is that the impedance spectra in Figure 6 are consistent with the HRTEM measurements: i) after 2 cycles, the HE-NCMs with the highest oxygen release showed the lowest charge-transfer resistance (Figure 6a), which we associate with the formation of a layered surface structure with abundant vacancies caused by the high oxygen release, allowing for fast lithium diffusion; and, ii) the impedance spectra after 50 cycles showed the highest charge-transfer resistance for the material with the highest oxygen release (Figure 6b), suggesting that the initial oxygen-vacant layered surface structure underwent a structural transformation into a spinel-like phase, inhibiting lithium diffusion, particularly for the thicker layers formed at the more lithium-rich HE-NCMs. From these observations emerges the hypothesis that the release of lattice oxygen does not immediately induce a phase transformation of the formed oxygen-depleted surface layer. Instead, the above presented data suggest that only the de-lithiation/lithiation processes over the course of subsequent cycling leads to a progressive phase transformation of the layered oxygen-vacant surface region. The half-cell cycling data from Figure 4 provide strong evidence that this phase transformation process indeed takes place during the first 20 cycles, leading to the observed capacity loss due to the gradual transformation of the layered oxygen-vacant surface region into a spinel-like surface layer. This hypothesis is schematically depicted in Scheme 1.

Correlation between capacity fading and spinel surface layer formation.—In the following, the effect of the surface layer formation and its subsequent restructuration shall be examined more quantitatively and correlated to the half-cell cycling performance of the material. It was shown in Figure 4a that a higher Li_2MnO_3

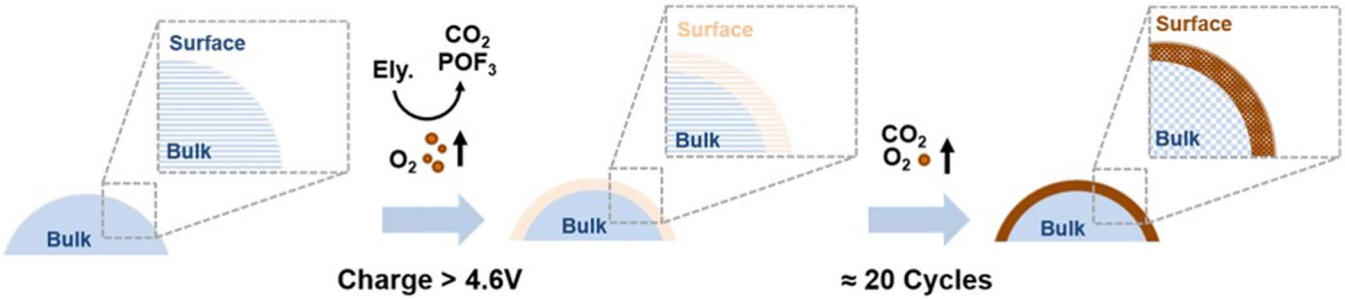

Scheme 1. Schematic presentation of the gas evolution processes and of the hypothesized mechanism of the spinel-type surface layer formation. Left panel: During the initial part of the first charge of (HE)-NCMs, surface impurities are decomposed at potentials below 4.6 V, accompanied by CO_2 evolution. Upon charging to ≥ 4.6 V, O_2 is released from the oxide lattice, also forming CO_2 by interaction of reactive oxygen (surface) species with the electrolyte. This leads to the formation of an oxygen deficient layered surface structure. Right panel: Over ≈20 subsequent charge/discharge cycles, the initially formed surface layer is converted into a resistive spinel-type surface layer. Furthermore, cation migration in the bulk material, happening independently of the O_2 release from the near-surface regions, leads to the observed voltage fading over extended cycling, evidence for which is reported in a previous study.[35]

content and thus also a higher oxygen release leads to faster capacity fading. Furthermore, the corresponding dQ/dV plots for the charging cycles show the evolution of a new phase between 2.0 V and 3.15 V (shaded areas in Figure 5), the capacitive contribution of which increases mainly during the first 20 cycles and is the larger the higher the Li_2MnO_3 content of the material and the higher the oxygen release. As it is has been shown in the literature that spinel structures delithiate at roughly the same potential,[47,48] it is conceivable that the lithiation capacity between 2.0 V and 3.15 V corresponds to the lithiation of a spinel-like surface layer formed by the structural surface transformation upon oxygen release. If this were true, part of the capacity fading should be ascribable to the lower capacity of the resulting spinel vs. the initially present layered surface phase. To examine this hypothesis, Table V compares the measured capacity losses between cycle 3 and cycle 48 ($Q_{loss}^{meas.}$) of the three HE-NCMs (data from Figure 4a) with the charge capacities between 2.0 V and 3.15 V for cycle 48 (referred to as $Q_{spinel}^{meas.}$) that correspond to the capacities under the shadowed areas in Figure 5c.

To quantitatively evaluate this hypothesis that the lower capacity of the spinel surface layer formed by oxygen release can be attributed to the observed capacity loss, we estimate the capacity contributions from the layered bulk structure of the HE-NCM ($Q_{layered}^{est.}$) and that of the surface spinel layer formed over cycling ($Q_{spinel}^{est.}$). The capacity of the former can be estimated by taking the observed capacity of the HE-NCMs after the two activation cycles (≈250 mAh/g in the third cycle, see Figure 4), at which point the spinel-layer has not yet been formed, and multiplying it with the remaining fraction of layered material, using the value of the mol% of spinel estimated by the OEMS data (taken from Table IV, Model II):

$$Q_{layered}^{est.} = (1 - x_{spinel}) \bullet 250\ mAh/g \quad [14]$$

Similarly, assuming the theoretical reversible capacity of a spinel to be roughly 140 mAh/g,[47] the estimated capacity of the surface layer after surface restructuration can be calculated by multiplying the mol% of spinel (taken from Table IV, Model II) with the theoretical capacity of a spinel:

$$Q_{spinel}^{est.} = x_{spinel} \bullet 140\ mAh/g \quad [15]$$

Thus, the capacity fade caused by the formation of a surface spinel layer ($Q_{loss}^{est.}$) would correspond to the difference between the initially observed capacity of the HE-NCMs (≈250mAh/g) and subtracting the estimated capacity contributions from the remaining layered bulk structure and the surface spinel layer:

$$Q_{loss}^{est.} = 250\ mAh/g - \left(Q_{layered}^{est.} + Q_{spinel}^{est.}\right) \quad [16]$$

In Table V, the actually measured values of $Q_{loss}^{meas.}$ (from Figure 4) and $Q_{spinel}^{meas.}$ (Figure 5) are compared with their estimated values derived from the OEMS measurements (O_2 + CO_2 from Model II, see Table IV). The striking agreement between the measured and estimated capacity losses ($Q_{loss}^{meas.}$ vs. $Q_{loss}^{est.}$) and between the measured and estimated contributions of the spinel surface layer to the capacity ($Q_{spinel}^{meas.}$ vs. $Q_{spinel}^{est.}$), provides strong evidence that the capacity fading of HE-NCMs is caused by the formation of a spinel surface layer with a lower intrinsic capacity compared to the originating layered structure.

Examination of voltage fading.—Despite the large changes in the extent of surface spinel formation and oxygen release as a function of Li_2MnO_3 content, the extent of voltage fading does seem rather independent of the Li_2MnO_3 content (see Figure 4b). Thus, we conclude that the oxygen release and the associated surface layer formation is not the main driving force for the observed voltage fading. To a smaller extent, however, it does influence the mean charge voltage, as the capacity contribution for charging the surface spinel layer at 2.0 to ≈3.15 V increases with increasing Li_2MnO_3 content (see Figure 5) and thus with increasing oxygen release (Figure 3). Nevertheless, since the capacity contribution from the surface spinel layer does not exceed 10% of the overall capacity (see Table V), it is not surprising that the charge voltage fading of the 0.50 Li_2MnO_3 material is only insignificantly larger for the 0.50 Li_2MnO_3 compared to the other materials (see Figure 4b). As oxygen release cannot be responsible for the observed voltage fading, the probable reason is that the reported

Table V. Capacity loss measured from half-cell cycling in Figure 4 ($Q_{loss}^{meas.}$) and capacity loss estimated by the amount of surface degradation ($Q_{loss}^{est.}$), as shown in Table IV. These values can be compared to the measured capacity of the spinel layer from Figure 5 ($Q_{spinel}^{meas.}$) and to the estimated capacity of the spinel layer ($Q_{spinel}^{est.}$) according to Equations 14–16.

	Capacity loss [mAh/g]		Capacity surface layer [mAh/g]	
Li_2MnO_3	Q_{loss}^{meas}	$Q_{loss}^{est.}$	Q_{spinel}^{meas}	$Q_{spinel}^{est.}$
0.33	7	6	8	7
0.42	15	12	18	15
0.50	28	22	25	28

transition metal movement within the layered bulk material leads to changes of the thermodynamic potentials, at least at low C-rates, where differences in impedance are less critical: reversible transition metal movement leading to the charge/discharge voltage hysteresis and irreversible transition metal movement to voltage-fading.[35,38,46]

At higher C-rates, the substantially larger impedance growth for more the more lithium-rich materials (see Figure 6) may lead to overall lower mean discharge voltages. Unfortunately, it is not possible to quantify this effect on the basis of the impedances shown only for 50% SOC in Figure 6, as the impedance for HE-NCMs is known to be strongly dependent on SOC.[14]

Effect of different Li_2MnO_3 contents onto full-cell performance.—So far, all data discussed in this study focused onto the half-cell performance and the structural changes of the cathode material. While the capacity and capacity fading in half-cells at low/moderate C-rate is mainly limited by the real capacity of the cathode material (impedance effects usually being small) and by cycling induced capacity changes, the performance of full-cells at faster C-rates can in addition be limited by impedance growth, cell balancing, and the loss of active lithium (also via crosstalk effects between the anode and the cathode). Therefore, in order to predict the performance of actual battery cells with a new cathode material, full-cell data are required, whereby also the amount of electrolyte added to the cells plays an important role. Wagner et al. showed that the mass ratio of electrolyte to cathode active material in large-scale commercial cells is on the order of m_{ely}:m_{CAM} ≈1:3,[56] which is typically ≈10-fold lower than what is used in coin cells (or other small-scale test cells). In the following, in order to most closely approach the value in large-scale cells, we used a ratio of m_{ely}:m_{CAM} ≈1:1, the lowest ratio with which we could still obtain reproducible coin cell data.

From Figure 9a it can be seen that the capacity fading for all the HE-NCM materials is similar over the first 50 cycles. After 50 cycles, the discharge capacity at 1C ranges from 200–220 mAh/g, only ≈20 mAh/g lower than the discharge capacity at C/5 in the half-cells (see Figure 4a). Beyond 50 cycles, the full-cell capacity of the material with 0.50 Li_2MnO_3 content (blue line in Figure 9a) actually surpasses that of the other materials, which can be explained by the larger lithium reservoir produced in the graphite anode (see Table II).

The mean discharge voltage observed in full-cells (Figure 9b) follows the same order as in half-cells (Figure 4b), being the lower the higher Li_2MnO_3 content. Over the first 50 cycles, all materials exhibit a ≈2-fold higher mean discharge voltage-fading at 1C in full-cells compared to that in half-cells at C/5, which most likely is due to the significant impact of the cathode impedance on cell voltage at the high current densities at 1C (2.1 mA/cm^2), so that an increase in the charge transfer resistance over extended cycling will have a larger effect on voltage-fading. Finally, one of the most important factors for the practical assessment of the materials is their specific discharge energy, i.e. the product of capacity and mean discharge potential, shown in Figure 9c. It demonstrates that essentially identical specific discharge energy values and fading rates are observed for all HE-NCMs, independent of their Li_2MnO_3 content. Nevertheless, regarding their practical application in large-scale cells, the 0.33 Li_2MnO_3 material is superior, as it would release the least amount of gas during the first two formation cycles, namely ≈0.25 $mmol_{O2+CO2}/g_{AM}$ (≡ 6 cm^3_{O2+CO2}/g_{AM}) for the 0.33 Li_2MnO_3 material vs. ≈0.90 $mmol_{O2+CO2}/g_{AM}$ (≡ 22 cm^3_{O2+CO2}/g_{AM}) for the 0.50 Li_2MnO_3 material (see Figure 3).

O_2 and CO_2 evolution of HE-NCM vs. NCM.—Jung et al. recently reported a similar oxygen release from stoichiometric NCM materials, also caused by a chemical spinel transformation at the particle surface.[10] The onset potential for oxygen evolution and the amount of oxygen release was shown to be strongly dependent on the nickel content of the material, whereby oxygen release was always observed at ≈80% SOC. To compare the oxygen release from HE-NCM and stoichiometric NCM, the here used base NCM material for the HE-

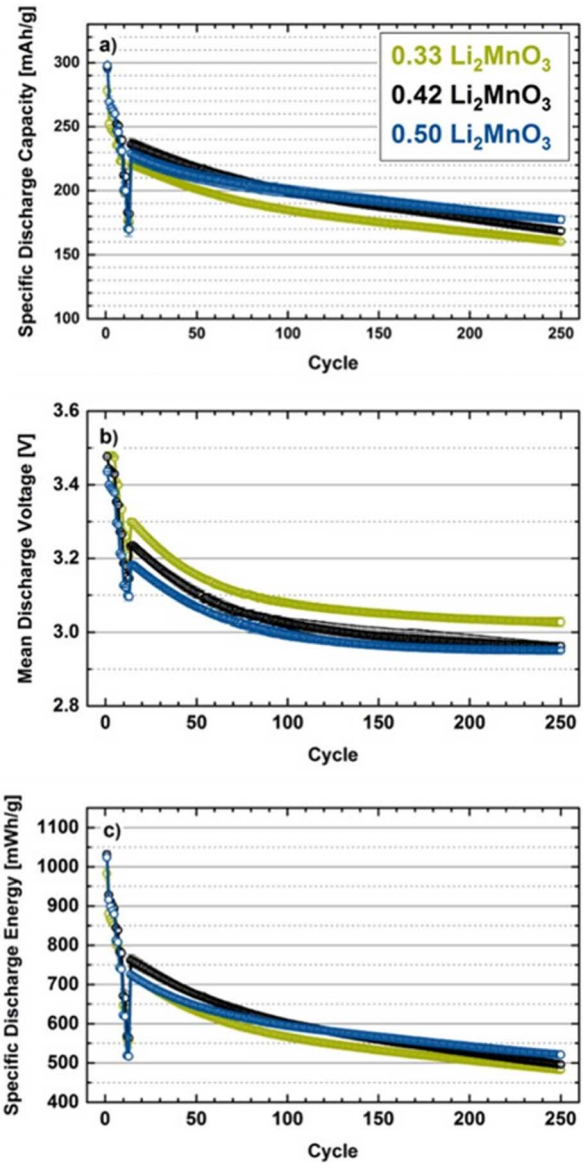

Figure 9. Electrochemical cycling of the different HE-NCM compositions in full-cells at 25°C, using a graphite anode, 14 µL of FEC:DEC (2:8 g:g) with 1 M $LiPF_6$ electrolyte with a proprietary co-solvent (m_{ely}: m_{CAM} ≈1:1) and a Celgard separator. The first activation cycles were carried out at C/15 to 4.7 V where the potential was held for 1 h and then the cell was discharged at C/15 to 2.0 V. This was followed by a rate test (up to 3C) between 2.0 V and 4.6 V, while further cycling was carried out at C/2 charge (+1h CV) rate and 1 C discharge between 2.0 V and 4.6 V. (a) Shows the specific discharge capacity as a function of the cycle number, (b) shows the mean discharge voltages, and (c) shows the specific discharge energy referenced to the cathode active material weight. All data points represent the average of at least two independent measurements and the error bars reflect the maximum and minimum of the measured values.

NCMs (referred to as 0.00 Li_2MnO_3 • 1.00 $LiMeO_2$ in Table I) was also investigated by OEMS. Results for the gas evolution of the base NCM are shown in Figure 10, using the same procedure that was used for the HE-NCMs (see Figure 3). In contrast to the HE-NCMs, oxygen evolution already occurred at 4.52 V and is also mainly observed during the first cycle. Furthermore, a strong increase in the CO_2 evolution was observed at the onset of oxygen evolution in the first cycle; in the second cycle, CO_2 evolution was observed at the potential where O_2 evolution had started in the first cycle, analogous to the OEMS data with the HE-NCM materials (see Figure 3). These data strongly suggest that oxygen release and subsequent surface restructuration for HE-NCM and stochiometric NCM materials follow

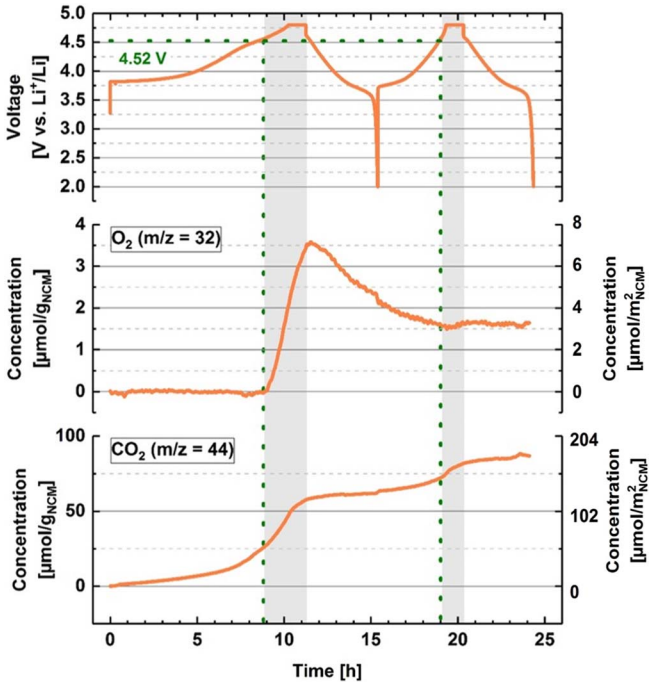

Figure 10. OEMS measurements for the stochiometric NCM (0.00 Li_2MnO_3 • 1.00 $LiMeO_2$, see Table I, using the same cell setup and procedure as in Figure 3 for the HE-NCMs. Upper panel: charge/discharge voltage vs. time; middle/lower panel: evolution of the concentrations of concomitantly evolved O_2/CO_2 given in units of either µmol/g_{AM} (left axes) or µmol/m^2_{AM} (right axes).

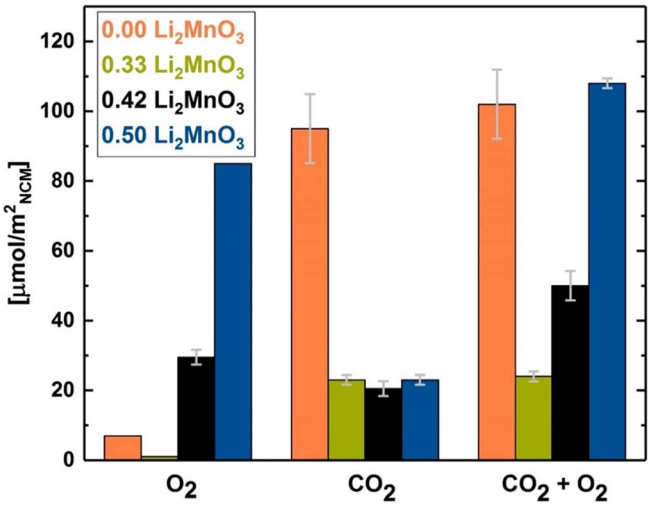

Figure 11. O_2 and CO_2 (after oxygen onset) evolution of the first two cycles are shown for the three different materials from Figure 3 (0.33, 0.42 and 0.50 Li_2MnO_3), data for 0.00 Li_2MnO_3 are from Figure 10. Total gas amounts were quantified during the first and the second cycle above the oxygen onset potential, depicted by the gray areas in Figure 3 and Figure 10. The error bars shown in this figure are derived from two separate OEMS measurements for each material.

very similar mechanisms, in both cases leading to reactions of lattice oxygen with the electrolyte via a surface reaction[57] and/or the reaction with released singlet oxygen.[55] In addition, for the stochiometric base NCM ("0.00 Li_2MnO_3") and the 0.33 Li_2MnO_3 HE-NCM, the SOC at which oxygen evolution can be observed is essentially identical (≈77%). Increasing the Li_2MnO_3 content however leads to oxygen evolution even at lower SOCs, namely at ≈72% for the 0.42 Li_2MnO_3 material and at ≈69% for the 0.50 Li_2MnO_3 material (all HE-NCM data from Figure 3). The shift of the onset of oxygen evolution to lower SOC values with increasing Li_2MnO_3 content indicates that the near-surface region of the material becomes less stable with increasing Li_2MnO_3 content, which is consistent with the observation that the thickness of the restructured surface layer increases with increasing Li_2MnO_3 content (see Figure 8), extending all the way into the bulk for the 0.50 Li_2MnO_3 material.

To compare the total amount of oxygen evolved from the different HE-NCMs and the stoichiometric NCM, all data for the gas evolution were normalized to the respective BET surface area (see Table I), as the surface area of the stoichiometric NCM was more than ten times smaller than that of the HE-NCMs. For the O_2 quantification, the O_2 evolved during the first two cycles is shown; for CO_2 quantification, the CO_2 evolved above the oxygen onset potential during the first and the second cycle is shown (gray areas in Figure 3 and Figure 10). Figure 11 shows that the 0.33 Li_2MnO_3 material evolves even less oxygen than the stoichiometric base NCM material, while a further increase of the Li_2MnO_3 content substantially increases the released amount of oxygen. Surprisingly, the surface normalized amount of evolved CO_2 for the three HE-NCM materials is essentially identical, despite the largely different oxygen release, while the base NCM releases much higher amounts of CO_2. This observation could be rationalized by either one of the following hypotheses: i) at the high absolute oxygen release rates from the high surface area HE-NCMs, the surface reaction between lattice oxygen and the electrolyte could become rate-limiting, so that a significant fraction of the oxygen is released as molecular oxygen without any further reaction with the electrolyte; or, ii) oxygen released from the surface at high rates as singlet oxygen[55] could form gas bubbles, in which reactive singlet O_2 can decay to triplet oxygen within the gas phase, while the reaction of singlet oxygen with the electrolyte to CO_2 would be limited to the gas/electrolyte interface. It is also conceivable that the latter may be influenced by particle morphology, whereby the hierarchical structure of the HE-NCM particles (consisting of primary agglomerates composed of smaller primary particles with interstitial pores) could lead to a formation/trapping of oxygen gas bubbles in contrast to NCM particles which have no internal void volume.

Despite the so far not clearly understood differences in the evolved CO_2/O_2 ratios for the different materials, the comparison of the total amount of lattice oxygen released from the materials (represented by the sum of $CO_2 + O_2$; see right-hand-side bars in Figure 11) suggests that low amounts of Li_2MnO_3 added to the base NCM can increase the active material stability at high SOCs. This stabilization may explained by the compensation of repulsive forces between the transition metal layers at low lithium content, produced by the loss of lithium from the transition metal layer, thereby creating vacancies within the transition metal layers. These repulsive forces would furthermore be reduced by the reported reversible oxygen redox,[26,32,33] whereby it is conceivable that the creation of vacancies in the transition metal layer during the first activation cycle is responsible for enabling oxygen redox processes.[38] However, increasing the Li_2MnO_3 content leads to an increased lithium occupation in the transition metal layer in the pristine material[58] that will be extracted during the first activation charge, leading to a destabilization of the surface at increasingly lower SOCs, as was discussed above.

Conclusions

In this study, we systematically compared HE-NCM materials with different amounts of Li_2MnO_3 using on-line electrochemical mass spectrometry (OEMS), high-resolution transmission electron microscopy (HRTEM) and electrochemical characterization methods, in order to understand the oxygen release as well as its influence on the active material structure and the electrochemical performance. We could show quantitatively that the half-cell capacity loss at low C-rates during the first 50 cycles can be ascribed to the formation of a surface spinel layer which can be estimated from the gas

evolution. HRTEM shows that the surface layer thickness increases with increasing Li_2MnO_3 content, hereby the thickness was in excellent agreement with the layer thickness estimated from the OEMS experiments, except the 0.50 Li_2MnO_3 material, for which spinel formation occurs all the way into the bulk of the material.

The oxygen release and the total gas release differ vastly for the different materials, even though the full-cell initial capacity, the capacity retention and the voltage fading are rather similar for all materials, which ends up in full-cell energies and energy fading that are essentially identical over 250 cycles. However, for practical applications in large-scale cells the initial gas evolution is a critical factor where the material with 0.33 Li_2MnO_3 outperforms the other materials, having a nearly 4 times lower initial gas evolution (6 cm^3/g_{CAM}) compared to the 0.50 Li_2MnO_3 material (22 cm^3/g_{CAM}). Furthermore, the increase in impedance is more critical for the 0.50 Li_2MnO_3 compared to the other materials, leading to improved rate performance for lower Li_2MnO_3 contents.

Acknowledgment

This work was supported by BASF SE within its BASF SE Battery Research Network. The authors want gratefully acknowledge A. Freiberg, K. Kleiner and R. Jung for their contribution to this work and for the very fruitful discussions.

ORCID

Tobias Teufl https://orcid.org/0000-0001-5889-5204

References

1. J. B. Goodenough and K. S. Park, *J. Am. Chem. Soc.*, **135**(4), 1167 (2013).
2. D. Andre, S.-J. Kim, P. Lamp, S. F. Lux, F. Maglia, O. Paschos, and B. Stiaszny, *J. Mater. Chem. A*, **3**(13), 6709 (2015).
3. K. Mizushima, P. Jones, P. Wiseman, and J. B. Goodenough, *Mat. Res. Bull.*, **15**(6), 783 (1980).
4. Z. Lu, D. D. MacNeil, and J. R. Dahn, *Electrochem. Solid-State Lett*, **4**(12), A200 (2001).
5. J. Choi and A. Manthiram, *J. Electrochem. Soc.*, **152**(9), A1714 (2005).
6. I. Belharouak, Y. K. Sun, J. Liu, and K. Amine, *J. Power Sources*, **123**(2), 247 (2003).
7. M.-H. Kim, H.-S. Shin, D. Shin, and Y.-K. Sun, *J. Power Sources*, **159**(2), 1328 (2006).
8. R. Jung, M. Metzger, F. Maglia, C. Stinner, and H. A. Gasteiger, *J. Phys. Chem. Lett.*, **8**(19), 4820 (2017).
9. D. Streich, C. Erk, A. Guéguen, P. Müller, F.-F. Chesneau, and E. J. Berg, *J. Phys. Chem. C*, **121**(25), 13481 (2017).
10. R. Jung, M. Metzger, F. Maglia, C. Stinner, and H. A. Gasteiger, *J. Electrochem. Soc.*, **164**(7), A1361 (2017).
11. M. M. Thackeray, S.-H. Kang, C. S. Johnson, J. T. Vaughey, R. Benedek, and S. A. Hackney, *J. Mat. Chem.*, **17**(30), 3112 (2007).
12. J. R. Croy, M. Balasubramanian, K. G. Gallagher, and A. K. Burrell, *Acc. Chem. Res.*, **48**(11), 2813 (2015).
13. S. R. Gowda, D. W. Dees, A. N. Jansen, and K. G. Gallagher, *J. Electrochem. Soc.*, **162**(7), A1374 (2015).
14. T. Teufl, D. Pritzl, S. Solchenbach, H. A. Gasteiger, and M. Mendez, *manuscript in preparation*.
15. A. R. Armstrong, M. Holzapfel, P. Novák, C. S. Johnson, S.-H. Kang, M. M. Thackeray, and P. G. Bruce, *J. Am. Chem. Soc.*, **128**(26), 8694 (2006).
16. C. S. Johnson, J. S. Kim, C. Lefief, N. Li, J. T. Vaughey, and M. M. Thackeray, *Electrochem. Commun.*, **6**(10), 1085 (2004).
17. F. La Mantia, F. Rosciano, N. Tran, and P. Novák, *J. Appl. Electrochem.*, **38**(7), 893 (2008).
18. P. Lanz, H. Sommer, M. Schulz-Dobrick, and P. Novák, *Electrochim. Acta*, **93**, 114 (2013).
19. Z. Lu, L. Y. Beaulieu, R. A. Donaberger, C. L. Thomas, and J. R. Dahn, *J. Electrochem. Soc.*, **149**(6), A778 (2002).
20. Z. Lu and J. R. Dahn, *J. Electrochem. Soc.*, **149**(7), A815 (2002).
21. D. Mohanty, J. Li, S. C. Nagpure, D. L. Wood, and C. Daniel, *MRS Energy & Sustainability*, **2**, (2015).
22. N. Yabuuchi, K. Yoshii, S. T. Myung, I. Nakai, and S. Komaba, *J. Am. Chem. Soc.*, **133**(12), 4404 (2011).
23. A. Guéguen, D. Streich, M. He, M. Mendez, F. F. Chesneau, P. Novák, and E. J. Berg, *J. Electrochem. Soc.*, **163**(6), A1095 (2016).
24. D. Streich, A. Guéguen, M. Mendez, F. Chesneau, P. Novák, and E. J. Berg, *J. Electrochem. Soc.*, **163**(6), A964 (2016).
25. B. Strehle, K. Kleiner, R. Jung, F. Chesneau, M. Mendez, H. A. Gasteiger, and M. Piana, *J. Electrochem. Soc.*, **164**(2), A400 (2017).
26. K. Luo, M. R. Roberts, R. Hao, N. Guerrini, D. M. Pickup, Y.-S. Liu, K. Edström, J. Guo, A. V. Chadwick, L. C. Duda, and P. G. Bruce, *Nat. Chem.*, **8**, 684 (2016).
27. H. Koga, L. Croguennec, M. Menetrier, K. Douhil, S. Belin, L. Bourgeois, E. Suard, F. Weill, and C. Delmas, *J. Electrochem. Soc.*, **160**(6), A786 (2013).
28. H. Koga, L. Croguennec, M. Ménétrier, P. Mannessiez, F. Weill, and C. Delmas, *J. Power Sources*, **236**, 250 (2013).
29. C. Genevois, H. Koga, L. Croguennec, M. Ménétrier, C. Delmas, and F. Weill, *J. Phys. Chem. C*, **119**(1), 75 (2014).
30. R. Petibon, L. Madec, D. W. Abarbanel, and J. R. Dahn, *J. Power Sources*, **300**, 419 (2015).
31. S. Muhammad, H. Kim, Y. Kim, D. Kim, J. H. Song, J. Yoon, J.-H. Park, S.-J. Ahn, S.-H. Kang, and M. M. Thackeray, *Nano Energy*, **21**, 172 (2016).
32. E. McCalla, A. M. Abakumov, M. Saubanère, D. Foix, E. J. Berg, G. Rousse, M.-L. Doublet, D. Gonbeau, P. Novák, G. Van Tendeloo, D. R., and J. M. Tarascon, *Science*, **350**(6267), 1516 (2015).
33. D. H. Seo, J. Lee, A. Urban, R. Malik, S. Kang, and G. Ceder, *Nat. Chem.*, **8**(7), 692 (2016).
34. H. Koga, L. Croguennec, M. Ménétrier, P. Mannessiez, F. Weill, C. Delmas, and S. Belin, *J. Phys. Chem. C*, **118**(11), 5700 (2014).
35. K. Kleiner, B. Strehle, A. R. Baker, S. J. Day, C. C. Tang, I. Buchberger, F.-F. Chesneau, H. A. Gasteiger, and M. Piana, *Chem. Mater.*, (2018), *in press*,.
36. G. Assat, C. Delacourt, D. A. D. Corte, and J.-M. Tarascon, *J. Electrochem. Soc.*, **163**(14), A2965 (2016).
37. B. Qiu, M. Zhang, Y. Xia, Z. Liu, and Y. S. Meng, *Chem. Mat.*, **29**(3), 908 (2017).
38. W. E. Gent, K. Lim, Y. Liang, Q. Li, T. Barnes, S.-J. Ahn, K. H. Stone, M. McIntire, J. Hong, J. H. Song, Y. Li, A. Mehta, S. Ermon, T. Tyliszczak, D. Kilcoyne, D. Vine, J.-H. Park, S.-K. Doo, M. F. Toney, W. Yang, D. Prendergast, and W. C. Chueh, *Nat. Commun.*, **8**(1), 2091 (2017).
39. N. Tsiouvaras, S. Meini, I. Buchberger, and H. A. Gasteiger, *J. Electrochem. Soc.*, **160**(3), A471 (2013).
40. J. R. Croy, K. G. Gallagher, M. Balasubramanian, B. R. Long, and M. M. Thackeray, *J. Electrochem. Soc.*, **161**(3), A318 (2013).
41. J. Choi and A. Manthiram, *Electrochem. Solid-State Letters*, **8**(8), C102 (2005).
42. I. Buchberger, S. Seidlmayer, A. Pokharel, M. Piana, J. Hattendorff, P. Kudejova, R. Gilles, and H. A. Gasteiger, *J. Electrochem. Soc.*, **162**(14), A2737 (2015).
43. S. E. Renfrew and B. D. McCloskey, *J. Am. Chem. Soc.*, **139**(49), 17853 (2017).
44. R. Jung, P. Strobl, F. Maglia, C. Stinner, and H. A. Gasteiger, *manuscript in preparation*.
45. J. R. Croy, K. G. Gallagher, M. Balasubramanian, Z. Chen, Y. Ren, D. Kim, S.-H. Kang, D. W. Dees, and M. M. Thackeray, *J. Phys. Chem. C*, **117**(13), 6525 (2013).
46. M. Sathiya, A. M. Abakumov, D. Foix, G. Rousse, K. Ramesha, M. Saubanere, M. L. Doublet, H. Vezin, C. P. Laisa, A. S. Prakash, D. Gonbeau, G. VanTendeloo, and J. M. Tarascon, *Nat. Mater.*, **14**(2), 230 (2015).
47. M. M. Thackeray, *Prog. Solid State Chem.*, **25**, 1 (1997).
48. P. G. Bruce, A. R. Armstrong, and L. Gitzendanner, *J. Mat. Chem.*, **9**, 193 (1998).
49. J. C. Burns, A. Kassam, N. N. Sinha, L. E. Downie, L. Solnickova, B. M. Way, and J. R. Dahn, *J. Electrochem. Soc.*, **160**(9), A1451 (2013).
50. D. Pritzl, A. Bumberger, M. Wetjen, J. Landesfeind, S. Solchenbach, and H. Gasteiger, *manuscript in preparation*.
51. J. Landesfeind, D. Pritzl, and H. A. Gasteiger, *J. Electrochem. Soc.*, **164**(7), A1773 (2017).
52. S.-M. Bak, K.-W. Nam, W. Chang, X. Yu, E. Hu, S. Hwang, E. A. Stach, K.-B. Kim, K. Y. Chung, and X.-Q. Yang, *Chem. Mat.*, **25**(3), 337 (2013).
53. S. M. Bak, E. Hu, Y. Zhou, X. Yu, S. D. Senanayake, S. J. Cho, K. B. Kim, K. Y. Chung, X. Q. Yang, and K. W. Nam, *ACS Appl. Mater. Interfaces*, **6**(24), 22594 (2014).
54. D. Mohanty, S. Kalnaus, R. A. Meisner, K. J. Rhodes, J. Li, E. A. Payzant, D. L. Wood, and C. Daniel, *J. Power Sources*, **229**, 239 (2013).
55. J. Wandt, A. T. S. Freiberg, A. Ogrodnik, and H. A. Gasteiger, *Materials Today*, 2018, *in press*,.
56. F. T. Wagner, B. Lakshmanan, and M. F. Mathias, *J. Phys. Chem. Lett.*, **1**(14), 2204 (2010).
57. T. M. Østergaard, L. Giordano, I. E. Castelli, F. Maglia, B. K. Antonopoulos, Y. Shao-Horn, and J. Rossmeisl, *J. Phys. Chem. C*, **122**(19), 10442 (2018).
58. H. Liu, Y. Chen, S. Hy, K. An, S. Venkatachalam, D. Qian, M. Zhang, and Y. S. Meng, *Adv. Energy Mat.*, **6**(7), 1502143 (2016).

3.2. Challenges for battery cycle-life using lithium- and manganese-rich layered oxides

Based on the previously discussed fundamental understanding of the cathode active material itself, this part of the thesis analyzes the challenges encountered during full-cell operation of Li- and Mn-rich layered oxides. This section gives a clear view of the compatibility of the cathode active material with the electrolyte. The first section discusses the necessity of EC-free electrolytes for Li- and Mn-rich layered oxides and shows that the interaction of EC with the released lattice oxygen from the cathode active material causes a rapid cell failure. The significance of this observation for Ni-rich NCM materials is also discussed, which explains the recently developed concept of EC-free electrolytes, shown by the research group of Jeff Dahn.[91] While the replacement of EC by FEC as co-solvent in the electrolyte shows a strong improvement in the battery cycling performance with Li-and Mn-rich layered oxides, the second section of this part shows that the thermal stability of FEC in $LiPF_6$ containing electrolytes is limited. The reactivity of FEC with $LiPF_6$ at elevated temperatures leads to strong gassing and enhanced transition metal dissolution that can limit the cycle-life of Li- and Mn-rich layered oxides. Later on, **Section 3.3** presents a possible solution to mitigate oxygen release for Ni-rich NCMs.

3.2.1. Impact of the oxygen release onto the cyclability in EC- and FEC-based electrolytes

This section presents the manuscript "Operating EC-based Electrolytes with Li- and Mn-Rich NCMs: The Role of O_2-Release onto the Choice of the Cyclic Carbonate".[60] It will soon be submitted to a peer-reviewed journal for publication. The manuscript was presented by Tobias Teufl at the 233rd Meeting of the Electrochemical Society (May 13th – 18th, 2018) in Seattle, Washington, USA (Abstract Number: 063).

Full-cell operation of Li- and Mn-rich NCMs requires with EC-based electrolytes is characterized by rapid capacity fading, resulting in a poor cycle-life. Replacement of EC by FEC leads to a strong improvement in cycle-life. A similar approach was followed by the research group of Jeff Dahn, who investigated EC-free electrolytes for which EC is replaced by FEC and other co-solvents, leading to a strong performance improvement of NCM 424 full-cells when cycled to potentials >4.4 V.[87-91] In the literature there is still a lack of mechanistic understanding of the poor cycling performance of EC-based electrolytes at high cutoff voltages. Some researchers suggest that FEC is less prone towards electrochemical oxidation compared to EC,[93, 94, 135] while other groups suggest the formation of a passivating surface layer on the cathode due to FEC, leading to a so-called cathode-electrolyte-interface (CEI).[95] However, the existence of such a surface layer could not be proven by surface analysis[96] and no improvement of FEC was observed if a spinel cathode was used instead of a layered oxide cathode.[96, 136]

In this study, we discuss the impact of oxygen release on the degradation of EC- and FEC-based electrolytes. For this, we show that the use of EC-based electrolytes with Li- and Mn-rich NCMs leads to rapid cell failure, while OEMS proves that the anodic stability measured versus a carbon electrode is similar for both EC and FEC. By a pre-activation of the Li- and Mn-rich NCMs in single-layer pouch-cells, we can remove the majority of the oxygen released in the first cycles from the CAM. Afterwards, the pouch-cells are disassembled, the electrodes are washed in DEC, and coin-cells with new electrolyte are assembled. After this procedure, a similar cycling performance for EC- and FEC-based electrolytes can be obtained. Thus, we expect that it is rather the oxygen release that makes

EC-based electrolytes unsuitable for high-voltage cycling of layered oxide cathodes, instead of the high operating potential itself. To prove this hypothesis, NCM-622 full-cells are assembled with EC- and FEC-based electrolytes and cycled below and above the onset potential for oxygen release. As expected, similar capacity retention can be observed for both electrolytes when the cells are cycled below the onset potential for oxygen release. In stark contrast, the EC-based electrolyte shows a rapid failure when cycled above the onset potential for oxygen release, while the FEC-based electrolyte shows still a sufficient cycling performance. With these experiments, we can show unequivocally that it is not the high operating voltage itself that makes EC unsuitable for high-voltage operation, as suggested in literature, but that it is rather the oxygen release from the layered oxide cathodes that leads to detrimental decomposition products in EC-containing electrolytes.

Author contributions

T.T. and P.K. carried out the OEMS experiments. T.T. and P.K. did the electrochemical analysis. T.T. and D.P. drafted the manuscript. All authors were discussing the results and the data. T.T. wrote the manuscript.

Operating EC-based Electrolytes with Li- and Mn-Rich NCMs: The Role of O_2-Release onto the Choice of the Cyclic Carbonate

Tobias Teufl [a, b, #], Daniel Pritzl [b], Patrick Krieg [a], Benjamin Strehle [b], Manuel A. Mendez [a] and Hubert A. Gasteiger [b]

[a]*BASF SE Ludwigshafen, New Battery Materials and Systems, D-67056 Ludwigshafen, Germany*

[b]*Chair of Technical Electrochemistry, Department of Chemistry and Catalysis Research Center, Technical University of Munich, D-85748 Garching, Germany*

[#]corresponding author

Abstract

Li- and Mn-rich layered oxides are a promising class of cathode materials for future lithium-ion batteries. However, they suffer from fast capacity fading in standard EC-containing electrolytes and therefore fluorinated alternatives, such as FEC, are required to improve their full-cell performance, which increases the cost of the electrolyte. In this study, we will analyze the reasons for the bad cycling performance of EC-containing electrolytes at high-voltages (≈4.7 V vs. Li^+/Li). By on-line electrochemical mass spectrometry (OEMS), we will show that the oxidative stability of EC is sufficient for these applications, but the electrolyte heavily reacts with the lattice oxygen released from the cathode material. Furthermore, we will show that the use of EC-based electrolytes above the oxygen onset potential leads to a resistance build-up causing a rapid rollover fading, while FEC does not show such a dramatic impedance increase. Last, we will correlate the oxygen release of NCM-622 to the requirement of EC-free electrolytes for stoichiometric NCM materials, when cycled above 4.4 V.

Introduction

Electric vehicles (such as Audi's new etron) are the most promising approach to make future mobility sustainable and environmentally more friendly.[1, 2] Lithium-Ion batteries serve as reasonable energy storage device for electric vehicles, as they can achieve high energy densities and they are already used in customer electronics for many years.[2, 3] However, for mass market penetration of BEV's (battery electric vehicles), todays lithium-ion batteries need to be improved in terms of energy density, while lowering cost at the same time.[4] Hereby, one of the main requirements is the optimization of the cathode active material (CAM), as the cathode has limited capacity and a significant cost contribution.[4] One of the most promising future CAMs are the so-called Li- and Mn-rich NCMs (x Li_2MnO_3 • (1-x) $LiNi_aCo_bMn_cO_2$) that are based on the layered LCO structure.[5, 6]

While these materials can achieve high reversible capacities of > 250 mAh/g, their practical cycling performance shows several issues that hindered their commercialization so far.[7, 8] It has been shown that all layered oxides release lattice oxygen from the surface upon delithiation above 80% state-of-charge (SOC), leading to a drastic degradation of the CAM and the electrolyte and therefore causing a rapid capacity decay.[9-11] However, the Li- and Mn-rich NCMs are always charged to more than 90% delithiation in order to achieve these high reversible capacities, which means that these type of materials are always operated above the oxygen onset potential, ending up with oxygen release and surface degradation during the initial cycles.[12, 13] Furthermore, the Li- and Mn-rich NCMs are operated at potentials > 4.5 V vs. Li^+/Li and therefore require a very challenging full-cell chemistry to mitigate rapid capacity fading and high impedance build-up.[12] Especially, ethylene-carbonate (EC) containing electrolytes are problematic when they are used in

a realistic full-cell setup together with a Li- and Mn-rich NCM cathode, leading to a rapid cell fading.

The research group of Jeff Dahn showed that EC-containing electrolytes are also very critical in graphite//NCM-424 full cells, when charged to potentials > 4.4 V;[14-17] they showed that replacing EC by a variety of different SEI forming carbonates could significantly improve the high voltage performance of layered oxides.[16-18] In particular they showed that fluorinated electrolytes (e.g. FEC) can strongly improve the high voltage performance in full-cells containing a layered oxide cathode and evaluated EC-free electrolytes for high voltage applications;[14, 15] a concept that was investigated by Gmitter at al.[19] In literature it is suggested that FEC is less prone to electrochemical oxidation compared to EC and therefore provides better cycling performance at high voltages.[20-22] Other researchers suggest the formation of a passivating surface layer on the cathode due to FEC,[23] however detailed surface analysis by other groups could not prove the existence of such a passivating surface layer and an improved cycling performance of graphite//LNMO cells could not be prooved.[22, 24, 25] Recently, it has been shown that EC can heavily react with lattice oxygen released from layered oxide cathode materials.[9, 10, 26] In this respect, Wandt et al.[26] and Freiberg et al.[27] showed that singlet oxygen can be released from the cathode material that leads to an oxidation of EC, forming oxidative instable species, such as VC and H_2O_2. Furthermore, it is suggested that also a surface reaction between the activated oxygen and EC takes place that leads to a chemical electrolyte decomposition.[28-30]

In this study, we will analyze the pure anodic stability of EC and FEC and we will carefully investigate the role of the oxygen release onto the cyclability in EC- and FEC-based electrolytes. We can show that Li- and Mn-rich NCMs show much better cycling when EC is replaced by FEC, therefore we used a realistic full-cell setup with an electrolyte/CAM weight ratio (m_{ely}:m_{CAM}) of

≈1:1. By on-line electrochemical mass spectrometry (OEMS) we could then show that EC and FEC show rather good anodic stabilities up to 5.0 V vs. Li^+/Li, while the oxygen release leads to a strong chemical electrolyte oxidation. By a pre-activation step prior to cycling we can prove that the oxygen release strongly alters the EC-based electrolyte and is the main failure mechanism when Li- and Mn-rich NCMs are cycled in EC-containing electrolytes. At the end we show that the sensitivity of EC towards O_2 release does not only account for Li- and Mn-rich NCMs but is also the main issue when NCM-622 is cycled above 4.4 V in standard EC-based electrolytes.

Experimental

Electrode preparation.—NCM-622 with the composition $LiNi_{0.6}Co_{0.2}Mn_{0.2}O_2$ and Li- and Mn-rich NCM with the compositions $0.33\ Li_2MnO_3 \bullet 0.67\ LiMeO_2$ (Me = Co, Ni, Mn) were both obtained from BASF SE (Germany). For coin cell testing of Li- and Mn-rich NCM, inks for cathode electrode preparation consisted of 92.5 wt.% CAM (BASF SE, Germany), 3.5 wt.% polyvinylidene-fluoride binder (PVDF, Solef 5130, Solvay, Belgium), 2 wt.% conductive carbon (Super-C65, Timcal, Switzerland; BET area of ≈62 m^2/g), and 2 wt.% graphite (SFG6L, Timcal, Switzerland; BET area of ≈17 m^2/g). The materials were dispersed in N-methyl pyrrolidine (NMP, anhydrous, Sigma-Aldrich, USA) and coated onto aluminum foil (16 μm). Dried electrodes were calendered to a density of 2.3 g/cm^3, calendered electrodes had final electrode thickness of 20 μm. For electrochemical testing, electrodes with a diameter of 14 mm were punched out, ending up with an active material loading of ≈6.5 mg/cm^2, corresponding to ≈1.6 mAh/cm^2, based on a nominal reversible capacity of 250 mAh/g. NCM-622 coin cell electrodes contained of 94 wt.% CAM (BASF SE, Germany), 3 wt.% polyvinylidene-fluoride binder (PVDF, Solef 5130, Solvay, Belgium) and 3 wt.% conductive carbon (Super-C65, Timcal, Switzerland; BET area of ≈62 m^2/g).

The materials were dispersed in N-methyl pyrrolidine (NMP, anhydrous, Sigma-Aldrich, USA) and coated onto aluminum foil (16 μm). Dried electrodes were calendered to a density of 3.2 g/cm^3, calendered electrodes had final electrode thickness of 32 μm. For electrochemical testing, electrodes with a diameter of 14 mm were punched out, ending up with an active material loading of ≈10.1 mg/cm^2, corresponding to ≈1.6 mAh/cm^2, based on a nominal reversible capacity of 160 mAh/g.

Electrodes for OEMS measurements were prepared by dispersing 96 wt.% CAM (BASF SE, Germany), 2 wt.% conductive carbon (Super-C65, Timcal, Switzerland), and 2 wt.% PVDF binder (Kynar HSV 900, Arkema, France) in NMP (anhydrous, Sigma-Aldrich, USA). A high solid content of 71% for the slurry was chosen to enable coating onto a porous stainless-steel mesh (SS316, aperture 26 μm, wire diameter 25 μm, The Mesh Company Ltd., UK). The slurry was coated with a wet film thickness of 20 μm onto the stainless-steel mesh, yielding a HE-NCM loading of ≈8.5 mg/cm^2. Electrodes for OEMS experiments were punched out with a diameter of 15 mm and compressed for 20 s with 2.5 tons. The carbon black electrodes for the OEMS measurements were prepared by dispersing 1.0 g conductive carbon (Super-C65, Timcal, Switzerland), and 1.0 g PVDF binder (Kynar HSV 900, Arkema, France) in 18 g NMP (anhydrous, Sigma-Aldrich, USA). The slurry was coated with a wet film thickness of 240 μm onto a polyethylene separator (Celgard 2500, USA), yielding a carbon loading of ≈0.8 mg$_C$/cm^2. Electrodes for OEMS experiments were punched out with a diameter of 15 mm.

Graphite electrodes used with Li- and Mn-rich NCMs were commercial electrodes with a graphite loading of ≈6.7 mg/cm^2, corresponding to ≈2.4 mAh/cm^2 (based on a theoretical capacity of 360 mAh/g), while the commercial graphite electrodes used with the NCM622 had a higher loading of graphite loading of ≈8.3 mg/cm^2 (corresponding to ≈3.0 mAh/cm^2) to guarantee

sufficient balancing up to 4.6 V; for electrochemical testing, graphite electrodes with a diameter of 15 mm were punched out. All anode and cathode electrodes were dried overnight under vacuum in an oven within the glovebox (O_2, H_2O < 0.1 ppm, MBraun, Germany) at 120 °C and were not exposed to air after the drying procedure.

On-line electrochemical mass spectrometry (OEMS).—For OEMS experiments, electrodes coated onto a stainless-steel mesh (see above) were used to have a porous medium as current collector in order to allow diffusion from the electrode to the capillary.[13] For OEMS measurements a custom-made cell is used; the cell design as well as the OEMS setup were reported previously.[31] For the OEMS measurement with NCM622 a one-compartment OEMS cells was used. The cells were assembled with Li metal counter electrode, a glassfiber separator (200 µm thickness, VWR, Germany), a NCM working electrode and 300 µl of electrolyte composed of FEC-only or EC-only, each with 1.5M $LiPF_6$ (BASF SE, Germany). The cells were connected to the mass spectrometer, held for 4 h at OCV (open circuit voltage), and then charged to 5.0 V vs. Li^+/Li at a C/15 rate (C-rates here are calculated based on a nominal capacity of 250 mAh/g). For the measurements of the oxidative stability with the carbon black electrodes we used a custom made sealed two-compartment cell that separates the anode and the cathode department by a lithium-ion conductive glass ceramic (Ohara Corp., Japan).[32] This cell setup allows to separate the gasses from the electrolyte oxidation from the lithium counter electrode and avoids crosstalk effects; this is important to determine the exact onset of the electrolyte oxidation on a carbon electrode, the setup was developed in our group and reported in a separate study.[32] The cells were assembled with Li metal counter electrode, a glassfiber separator (200 µm thickness, VWR, Germany) and 200 µl of electrolyte in the lower compartment and a carbon black working electrode, a polyester separator

(Freudenberg, Germany) and 100 µl of electrolyte composed of FEC-only or EC-only, each with 1.5M $LiPF_6$ (BASF SE, Germany) in the upper compartment. The cells were connected to the mass spectrometer, held for 4 h at OCV (open circuit voltage), and then charged to 5.5 V vs. Li^+/Li at a scan rate of 0.1 mV/s. For quantification of the mass spectrometer currents, a calibration gas containing H_2, O_2, CO_2, C_2H_4 (each 2000 ppm) in Argon (Linde AG, Germany) was used. All currents were normalized to the current at m/z = 36 (Ar isotope) in order to correct for effects of minor pressure and temperature deviations, and afterwards the currents m/z = 32 (O_2) and m/z = 44 (CO_2) were converted into gas concentration.

Electrochemical characterization.—Galvanostatic cycling was carried out in 2032-type coin-cells (Hohsen Corp., Japan) at 25 °C in a temperature-controlled oven (Binder, Germany) and using a battery cycler (Series 4000, Maccor, USA). For full-cell experiments in 2032 coin-cells, a graphite anode with a diameter of 15 mm and a cathode with a diameter of 14 mm were assembled with one polyethylene separator (2500, Celgard, USA) and with 14 µL (for Li- and Mn-rich NCM) or 21 µL (for NCM-622 due to higher CAM mass) of electrolyte based on FEC:DEC = 2:8 wt.% with 1M $LiPF_6$ or EC:DEC = 2:8 wt.% with 1M $LiPF_6$ (BASF SE, Germany).

All cells were set for a rest period of 2 hours prior to electrochemical testing and C-rates are referenced to a nominal capacity of 250 mAh/g (Li- and Mn-rich NCM) or 160 mAh/g (NCM-622). Li- and Mn-rich NCM full-cells were activated in the first cycle at a C-rate of C/15 to 4.7 V (CC) and then discharged at C/15 to 2.0 V (CC); in subsequent cycles, the upper cutoff was reduced to 4.6 V. Afterwards 3 cycles at C/10 were applied (CC), followed by a rate test for which the cell was charged/discharged for 3 cycles each at 0.2C (CCCV)/0.5C (CC), 0.5C (CCCV)/1C (CC), 0.5C (CCCV)/2C (CC), 0.5C (CCCV)/3C (CC), whereby all CV-steps

were terminated after 1 h or when the current dropped below 0.01C. The rate test was followed by lifetime testing composed of repetition units with 3 cycles at C/10 (CC) and 30 cycles at a charge rate of 0.5C (CCCV) and a discharge rate of 1C (CC), the CV-step defined as above. For the NCM-622 full-cells the same cycling procedure was used, but the upper cutoff was the same for all cycles; the cells were charged between 3.00 V – 4.35 V and 3.00 V – 4.60 V respectively.

Some electrodes were pre-activated prior to cycling; therefore, the first charge/discharge cycle was carried out in a single-layer pouch cell with a capacity of ≈40 mAh. The single-layer pouch cells were assembled with the exact same materials, using one polyethylene separator (2500, Celgard, USA) and 1 mL of electrolyte based on FEC:DEC = 2:8 wt.% with 1M $LiPF_6$ or EC:DEC = 2:8 wt.% with 1M $LiPF_6$ (BASF SE, Germany); each electrolyte was the same that was afterwards used for the corresponding coin-cell cycling. The activation in the pouch-cells was carried out under the same conditions as in the coin-cells (C/15 charge/discharge to 4.7 V); the pouch cell was degassed twice during the first cycle (at 4.0 V during charge and at 4.0 V during discharge). After the first cycle the discharged cell was opened, and coin-cell electrodes were punched out (anode 15 mm diameter, cathode 14 mm diameter). The electrodes were afterwards washed in pure DEC (without $LiPF_6$) and coin-cells were assembled from the pre-activated materials. The pre-activated coin-cells were assembled with the same amount of electrolyte and the same separator and were cycled with the same procedure; the cycling procedure started the second cycle (C/10 to 4.6 V) as the activation cycle was carried out in the pouch cell.

Results and Discussion

Full-cell performance of Li- and Mn-rich NCMs in EC and FEC based electrolytes.—To evaluate the actual cycling performance and the lifetime of cathode materials using different cell chemistries it is crucial that the materials are tested within a reasonable cell setup. The full-cell performance is not only given by the CAM capacity, but can also be affected by impedance growth, cell balancing and active lithium loss (also via crosstalk effects between anode and cathode are possible). Therefore, reasonable full-cell data are required in order to predict the battery lifetime of a certain cell chemistry, whereby the amount of electrolyte plays a major role. Wagner et al.[33] showed that the mass ratio of electrolyte to cathode active material in large-scale commercial cells is on the order of m_{ely}:m_{CAM} ≈1:3, which is typically ≈10-fold lower than what is used in lab scale cells. For this reason, we limited the amount of electrolyte in this study in order to most closely approach the value in large-scale cells. In particular, we used a ratio of m_{ely}:m_{CAM} ≈1:1, the lowest ratio with which we could still obtain reproducible coin cell data.

A Li- Mn-rich NCM with the composition 0.33 Li_2MnO_3 • 0.67 $LiMeO_2$ was used for full-cell cycling, the composition was optimized in a previous study regarding its gassing behavior.[12] **Figure 1** shows the capacity fading for Li- and Mn-rich NCM cycled in a EC:DEC (2:8 wt.%) and a FEC:DEC (2:8 wt.%) solution, both containing 1M $LiPF_6$; it can be seen that during 1C cycling (starting from cycle 18) the EC-based electrolyte shows a rapid capacity fading which is similar to a rollover mechanism, as shown by Burns et al.[34] and Jung et al.[9] which is not the case in the FEC-based electrolyte. The cell with the EC-containing electrolyte (black lines, **Figure 1**) shows a rapid capacity decay during 1C cycling from 191 ± 5 mAh/g in cycle 18 to only 98 ± 15 mAh/g (51% retention at 1C) during cycle 48, while the FEC-based electrolyte (blue lines, **Figure 1**) does not only show a higher capacity of 215 ± 3 mAh/g (cycle 18), but also a much better capacity

retention, retaining 165 ± 3 mAh/g (77% retention at 1C) even after 113 cycles. To differentiate between kinetic losses and the loss of active lithium, C/10 cycles were included to the cycling procedure all 10 cycles. Interestingly, the EC-based electrolyte shows good capacity retention at C/10, resulting in 177 ±13 mAh/g after 50 cycles, compared to 98 ± 15 mAh/g at 1C during cycle 48, ending up in a difference of ≈79 mAh/g between operation at 1C and C/10. In comparison the FEC-based full-cells show much smaller deviations between 1C and C/10 rate, ending up in a difference of ≈27 mAh/g (cycle 48 compared to cycle 50). Therefore we suggest that the failure of the EC-containing electrolytes can be explained by a high impedance growth rather than a loss of active lithium, a similar rapid capacity fade has been shown for EC-based electrolytes with layered NCM cathodes;[9] in this regard Burns et al.[34] introduced the term rollover mechanism. The EC-containing cells in **Figure 1** were already stopped after 50 cycles, as they have already reached their end-of-life at 1C (< 80% capacity retention) and therefore showed increasing error bars.

It has been shown in literature that EC plays a critical role when NCM materials are cycled to potentials > 4.4 V[14] and many approaches have been made to design EC-free electrolytes to improve their high voltage stability.[18, 19] So far it is suggested that the anodic stability of EC is crucial when the cell is operated at high voltages and FEC improves the cell performance due to higher oxidative stability.[20-22] However, it turned out that the cycling performance of a high voltage spinel (LNMO, operated at 4.9 V vs. Li^+/Li) cannot be improved by replacing EC by FEC.[24, 35] Furthermore, it was shown that FEC can lead to reactions with $LiPF_6$ forming oxidative instable species, such as VC.[35, 36] For this reason, we will evaluate the oxidative stability of EC and FEC with 1.5M $LiPF_6$ on a pure carbon electrode in order to get information about the anodic stabilities of the different cyclic carbonates.

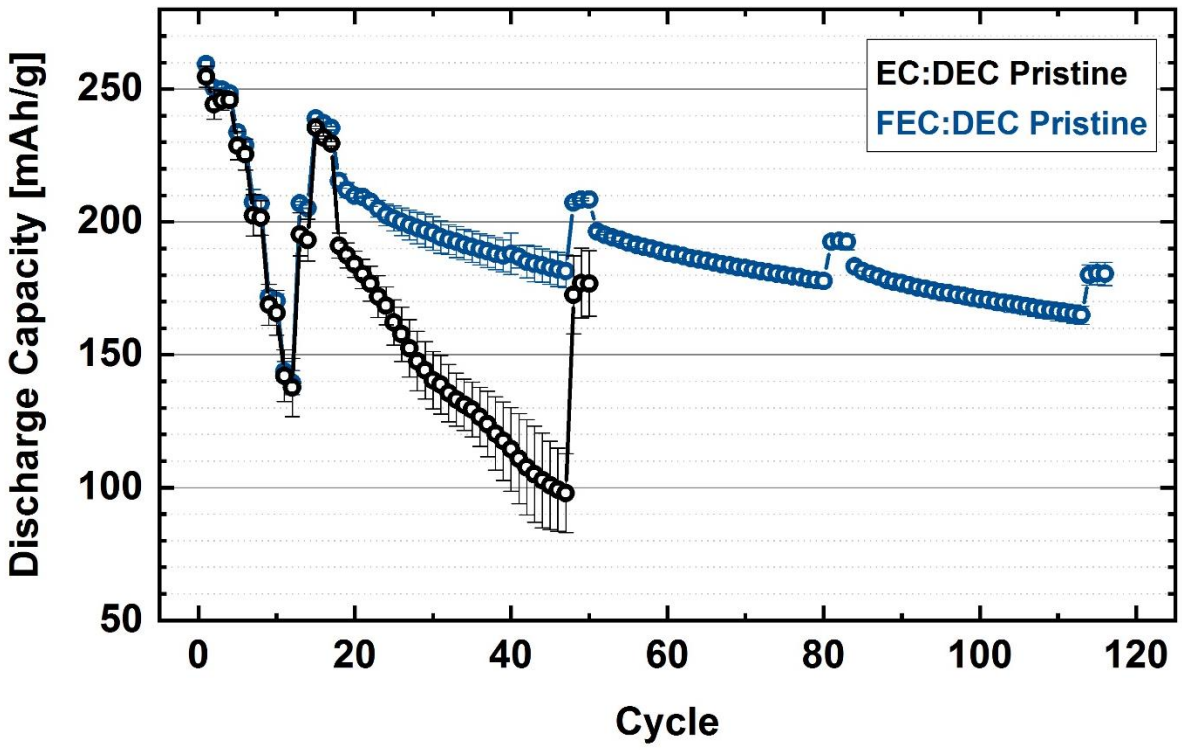

Figure 1. Electrochemical cycling of 0.33 Li_2MnO_3 Li- and Mn-rich NCM at 25°C using a graphite counter electrode, 14 µL of electrolyte (m_{ely}:m_{CAM} ≈ 1:1) and a Celgard 2500 separator; activation was carried out at C/15 (CC 2.0 – 4.7 V), followed by a rate test (up to 3C) between 2.0 – 4.6 V, while further cycling was carried out at 0.7C (CCCV) charge and 1C discharge between 2.0 and 4.6 V. Each thirty cycles C/10 cycles were applied as diagnostic cycles.

Anodic stability of EC and FEC on a carbon electrode.— So far it is suggested that the oxidative instability of EC hinders its application in cells charged to potentials of 4.4 V or higher.[20] In order to investigate the onset potential of EC and FEC, we investigated EC-only and FEC-only mixed with 1.5M $LiPF_6$. Therefore, we performed on-line electrochemical mass spectrometry (OEMS), using pure carbon black electrodes without any cathode active material which allows us to not only track the current response but also the CO_2 signal from electrolyte oxidation. Following not only

the current but also the CO_2 signal is necessary to differentiate between further parasitic reactions, such as PF_6^- intercalation into the carbon black, and electrolyte oxidation. Furthermore, we use a sealed two-compartment cell setup that avoids crosstalk between the electrodes and allows to separately detect gasses from electrolyte oxidation and electrolyte reduction on the lithium counter electrode, the setup is reported elsewhere.[32] Therefore, we can show the pure gas evolution from the electrolyte oxidation on the carbon electrode. **Figure 2** shows the current profile (upper panel) and the CO_2 evolution (lower panel m/z = 44) for FEC + 1.5 M $LiPF_6$ and EC + 1.5M $LiPF_6$ during a linear sweep voltammetry experiment from OCV (≈ 3V vs. Li^+/Li) up to 5.5 V vs. Li^+/Li. The gas evolution from the EC oxidation (black lines, **Figure 2**) starts around 4.8 V vs. Li^+/Li and shows a strong increase above 5.0 V vs. Li^+/Li, which is in one line with the results shown by Pritzl et al.[37] The results in **Figure 1** suggest that FEC has a much better anodic stability compared to EC, however, the results for FEC depicted in **Figure 2** (blue lines) indicate similar results for the anodic stability of FEC and EC. The results in **Figure 2** clearly prove that the onset potential of the current signal, as well as for the CO_2 evolution is essentially the same for EC and FEC, while the slope for the FEC oxidation seems to be even slightly higher compared to the EC oxidation. While the cycling data shown in **Figure 1** show a significant improvement when EC is replaced by FEC for high voltage applications, **Figure 2** suggests that the anodic stability of the electrolyte is not improved if FEC is used as cyclic carbonate instead of EC. However, Jung et al.[9, 10] recently suggested that electrolyte decomposition is mainly triggered by chemical oxidation due to reactions with the lattice oxygen instead of electrooxidation and therefore the oxygen release might significantly influence the cycling performance and the choice of the electrolyte. To further understand the strong deviations in the cycling performance in EC- and FEC-based electrolytes we will in the following analyze the effect of the oxygen release from the Li- and Mn-rich NCM on the full-cell performance.

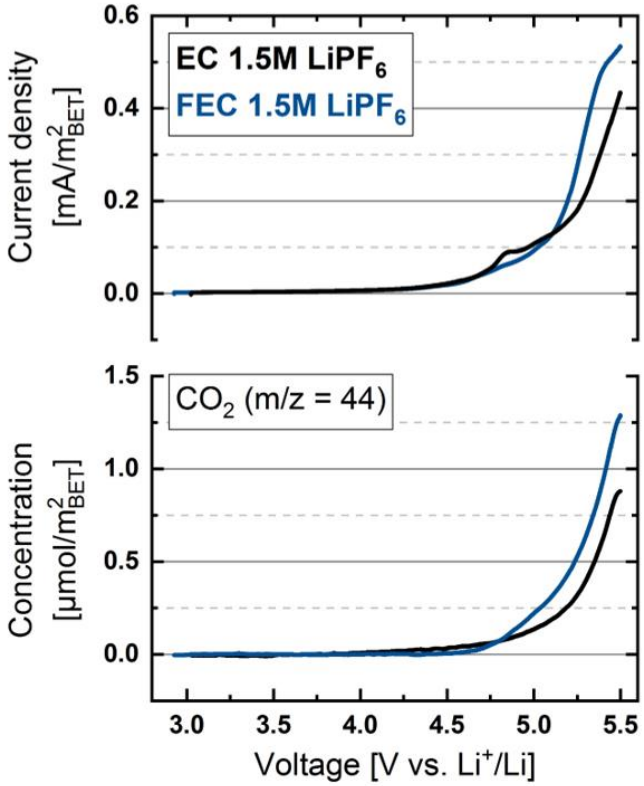

Figure 2. Anodic current (upper panel) and CO_2 evolution (lower panel) from EC and FEC electrolytes, each containing 1.5M $LiPF_6$. A linear scan (0.1 mV/s) was carried out from OCV (≈ 3 V vs. Li^+/Li) to 5.5 V vs. Li^+/Li. The OEMS experiments were performed in a sealed two-compartment using a carbon working and a lithium counter electrode, the cell setup is shown elsewhere.

Cycling performance of pre-activated Li- and Mn-rich NCMs.— Jung et al.[9, 10] showed that oxygen release from layered NCM cathodes causes strong electrolyte decomposition and is the dominating source of electrolyte decomposition up to ≈4.9 V vs. Li^+/Li at 25 °C. Wandt et al.[26] and Freiberg et al.[27] proved that singlet oxygen is released from stoichiometric and from Li- and Mn-rich NCMs and leads to rapid reactions with the electrolyte. Furthermore, it is shown in literature that the main part of the oxygen release from Li- and Mn-rich NCMs already occurs during the first activation cycle, showing a strong O_2 and CO_2 evolution during the first charge.[12, 13, 38, 39] This means that a large part of the electrolyte is already decomposed during the first cycle, while side-

reactions level out during the further cycling. To investigate the influence of the oxygen release on the full-cell capacity retention we pre-activated (1st cycle) the electrodes in pouch-cells, washed them, punched small electrodes and reassembled them for comparison in the same coin full cell setup as the pristine materials (see detailed description in the experimental section). The first cycle pre-activation in the pouch-cells was carried out according to the same procedure that was used for the pristine coin-cells, whereby the pouch-cells were degassed twice; the first degassing step was carried out at 4.00 V during the first charge to remove the gasses that were evolved during the SEI formation. The second degassing step was carried out at 4.00 V during the first discharge in order to remove the gasses that were evolved during the activation, especially O_2 has to be removed before complete discharge, as it has been shown that O_2 can be reduced to Li_2O_2 on the CAM surface when cycled below 3.00 V.[12, 40] With this pre-activation procedure we can remove the decomposition products caused by the high oxygen release during the first cycle, after the pre-activation coin-cells were assembled with the washed electrodes, fresh electrolyte and a new separator to improve the cycle life by mitigating the first cycle oxygen release in the actual cell.

The results for the pristine and the pre-activated electrodes in FEC:DEC = 2:8 wt.% 1M $LiPF_6$ are shown in **Figure 3**. It can be seen that the pre-activation helps to improve the capacity retention in the FEC-based electrolyte, but both cells showing a constant lithium loss and no rollover mechanism. The pre-activated cell has a remaining capacity of 187 ± 3 mAh/g at 1C after 113 cycles (85% retention at 1C), while the cell that was normally cycled has a capacity of 165 ± 3 mAh/g (77% retention at 1C), which means that the pre-activation in the FEC-based electrolyte could improve the cycle performance by 22 mAh/g (≈13%) after 113 cycles. This is already a significant improvement if one considers that the same materials and the same cell setup was used and shows that the oxygen release also has an influence on the lifetime in FEC-based electrolytes but does not cause a rapid cell failure but rather a continuous capacity loss.

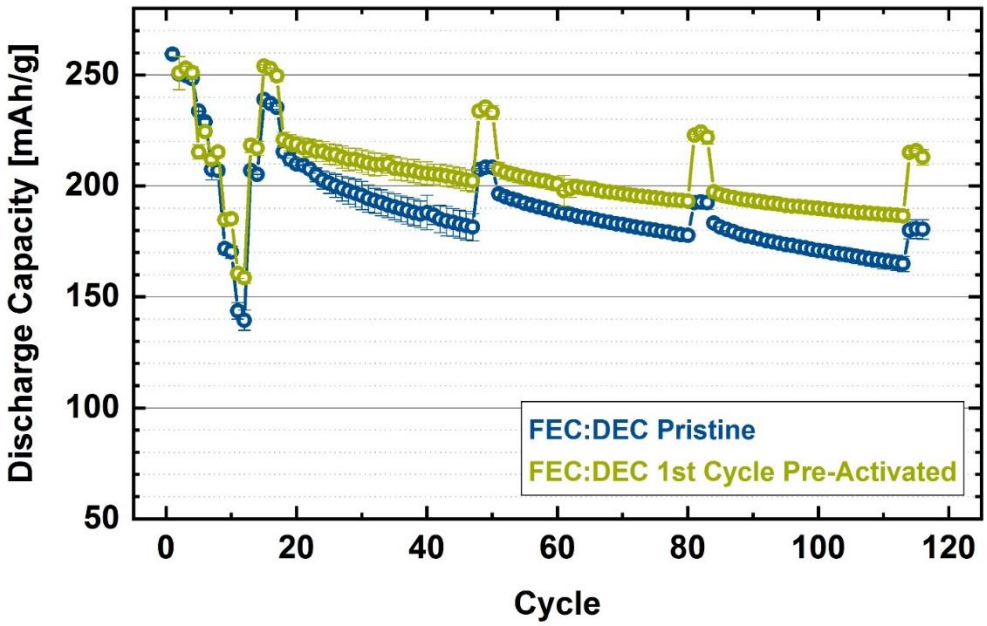

Figure 3. Electrochemical Cycling of 0.33 Li_2MnO_3 Li- and Mn-rich NCM at 25°C using a graphite counter electrode, 14 µL of a FEC:DEC (2:8 wt.%) 1M $LiPF_6$ electrolyte and a Celgard 2500 separator; activation was carried out at C/15 (CC 2.0 – 4.7 V), followed by a rate test (up to 3C) between 2.0 – 4.6 V, while further cycling was carried out at 0.7C (CCCV) charge and 1C discharge between 2.0 and 4.6 V. Each thirty cycles C/10 cycles were applied as diagnostic cycles.

To now analyze the influence of the oxygen release and the chemical electrolyte degradation on the full-cell performance with an EC:DEC = 2:8 wt.% 1M $LiPF_6$ electrolyte, the pre-activation was also carried out in the EC-based electrolyte solution. **Figure 4a** depicts the cycling of the pristine and the pre-activated electrodes in the EC-containing electrolyte (pre-activated samples from **Figure 3** were added as reference). As already shown **Figure 1** the pristine electrodes in EC-based electrolyte suffer from a rapid capacity decay at a rate of 1C in the EC-containing electrolyte. In stark contrast, it is shown in **Figure 4a** that the pre-activated electrodes can be cycled in the EC-containing electrolyte without the rapid rollover mechanism, which can be rationalized by the fact that in this case the main oxygen release was carried out before the coin-

cell assembly. While the pristine sample had only a 1C capacity retention of 98 ± 15 mAh/g (51% retention at 1C) after 48 cycles, the pre-activated cell could maintain 185 ± 4 mAh/g (88% retention at 1C) at the same rate after 48 cycles, showing a significant improvement due to a simple pre-activation step, while all materials are exactly the same for both experiments. As discussed in the beginning a large rate dependence is observed for the pristine EC-based cell, ending up in a difference of ≈79 mAh/g between 1C (cycle 48) and C/10 (cycle 50); pointing towards a high resistance build-up. Interestingly, the pre-activated EC-based materials do not show a rapid rollover failure and show only a small rate dependence, ending up in a ≈9 mAh/g higher capacity at C/10 (cycle 50) compared to the fast 1C rate (cycle 48). From these results we suggest that the reaction of EC with the lattice oxygen released from the CAM causes high kinetic losses, leading to a similar rollover mechanism as suggested in literature.[9, 34]

To prove this hypothesis, the potential curves for the first 1C cycle and the last 1C cycle (cycle 8 and cycle 48) for the pristine and the pre-activated materials are shown in **Figure 4b**, for both cycles the charge rate was 0.5C and the discharge was carried out at 1C rate. In cycle 8 the voltage profiles for the pristine and the pre-activated materials nearly overlap and show only little overpotentials and equal capacity. The picture changes after 48 cycles, while the pre-activated material shows still decent capacities and only slightly increased overpotentials, the pristine material shows a high capacity loss and a large overpotential during charge. The potential curves clearly show that the combination of oxygen release and EC-based electrolytes leads to high resistance build-up and kinetic limitations that cause a rapid capacity decay. **Figure 4b** also indicates that especially the charge of the full-cell (intercalation into graphite) is kinetically limited and causes a high overpotential and a capacity loss.

There is an ongoing discussion about the exact decomposition mechanism of EC during the oxygen release. Wandt et al.[26] clearly showed that singlet oxygen is released from NCM materials which can be correlated to the O_2 and CO_2 evolution. Based on this observation Freiberg et al.[27] could show that singlet oxygen reacts with EC, forming VC and H_2O_2, both are oxidative instable species at potentials > 4.5 V Li^+/Li. In contrast, Yu et al.[29] suggested a dehydrogenation of EC due to activated oxygen on the surface of the CAM, leading to a ring-opening and oligomerization of EC. However, there is clear evidence for the existence of both mechanisms, but at the moment it is not clear which mechanism is more detrimental for the battery performance. Regarding the observation from **Figure 4**, both mechanisms could explain the impedance increase and the rollover after the oxygen release. If VC is formed due to the reaction with singlet oxygen, it is known that VC is oxidative not stable at such potentials and it was shown that the oxidation of large amounts VC within a cell can lead to poly-VC layers that cause an impedance build-up and a rapid cell failure.[37] On the other hand, dehydrogenation, as described by Yu et al.[29], can lead to oligomerization of EC that could also rationalize resistive polymer layers within a full-cell, causing a high resistance build-up.[29] So far it is not clear which mechanism exactly causes this rapid failure, but from the data shown in **Figure 3** and **Figure 4** it is clear that the decomposition products of EC lead to a rapid resistance build-up, while the performance FEC-based electrolyte is less sensitive towards oxygen release.

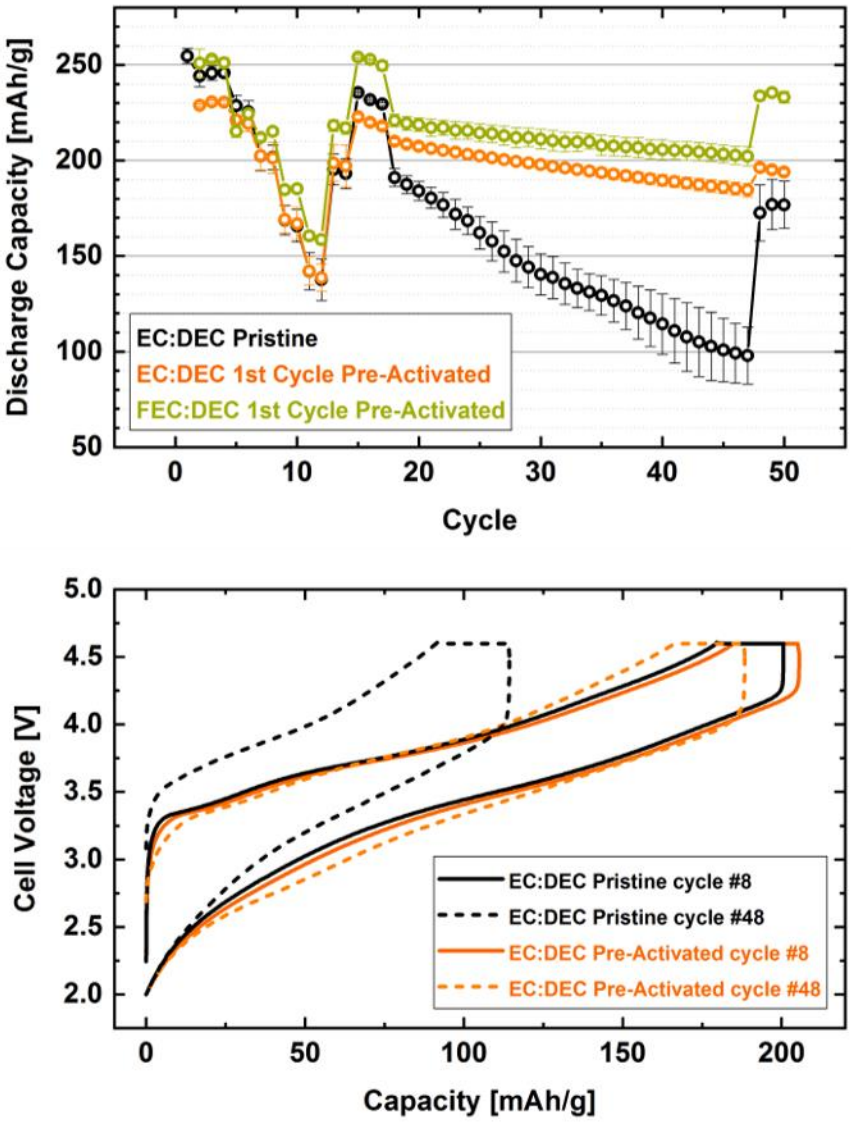

Figure 4. Electrochemical Cycling of 0.33 Li_2MnO_3 Li- and Mn-rich NCM at 25°C using a graphite counter electrode, 14 µL of a EC:DEC (2:8 wt.%) 1M $LiPF_6$ electrolyte and a Celgard 2500 separator; activation was carried out at C/15 (CC 2.0 – 4.7 V), followed by a rate test (up to 3C) between 2.0 – 4.6 V, while further cycling was carried out at 0.7C (CCCV) charge and 1C discharge between 2.0 and 4.6 V. Each thirty cycles C/10 cycles were applied as diagnostic cycles.

Relevance for Ni-rich NCM materials.— So far, we only focused on the Li- and Mn-rich NCMs, now we want to show the impact of the oxygen release onto the cycling performance of a NCM-622 in dependence of the upper cutoff potential. At first the gas evolution from the NCM-622 in EC 1.5M $LiPF_6$ and FEC 1.5M $LiPF_6$ was measured by OEMS, pure EC/FEC model electrolytes are sufficient in the OEMS to improve the sensitivity of the measurement by an increased signal to noise ratio.[41] **Figure 5** shows the results from the OEMS measurements, whereas the upper panel shows the galvanostatic charge profiles from OCV (≈3 V) up to 5.0 V against a Li counter electrode and the middle/lower panels depict the concentration of the evolved O_2 (m/z = 32, middle panel) and CO_2 (m/z = 44, lower panel) given in µmol/g_{AM}. In both electrolytes a total capacity of ≈ 265 mAh/g is reached upon charge to 5.0 V vs. Li^+/Li. The oxygen onset potential (**Figure 5**; middle panel) occurs for both electrolytes at ≈4.47 V vs. Li^+/Li and is followed by a sharp increase in the CO_2 evolution which is in god accordance with the results reported by Jung et al.[9, 42] A first CO_2 onset can be observed in both electrolytes starting at ≈4.10 V vs. Li^+/Li (**Figure 5**; lower panel). Adopting the concept reported by Jung et al.[42] the first CO_2 evolution stems from the reaction of surface impurities, while the CO_2 evolution at higher potentials can be rationalized by the reaction of lattice oxygen with the electrolyte, similar as reported for the Li- and Mn-rich NCM.[12, 13] As mentioned above the gas evolution of NMC-622 in EC + 1.5M $LiPF_6$ and the FEC + 1.5M $LiPF_6$ electrolyte shows the same onset potentials for the O_2 and the CO_2 evolution, as shown in **Figure 5**. Quantification after the first charge to 5.0 V vs. Li^+/Li shows similar amounts of ≈4 µmol/g O_2 for EC and FEC, while CO_2 evolution in EC corresponds to ≈55 µmol/g and ≈30 µmol/g CO_2 for FEC. The different amounts of CO_2 already indicate different degradation mechanisms for EC and for FEC. From the results from **Figure 1** we clearly suggest that the decomposition products of the reaction with EC and lattice oxygen lead to high resistance build-up and are much more detrimental for the full-cell performance compared to the decomposition

products of FEC. While the exact mechanisms are not clear at the moment, this could for example be rationalized by the formation of polymeric species due to the reaction of EC and lattice oxygen, as discussed above.[27, 29] To further prove this hypothesis, graphite//NCM-622 full-cells were assembled with EC:DEC = 2:8 wt.% or FEC:DEC = 2:8 wt.% electrolytes and cycled below and above the oxygen onset potential; if our hypothesis is correct, the use of EC:DEC = 2:8 wt.% above the oxygen onset potential should lead to a rapid rollover failure. The oxygen onset potential of ≈4.47 V vs. Li^+/Li (**Figure 5**), corresponds to an upper full-cell cutoff of ≈ 4.37 V and will serve as guideline for the cycling experiments.

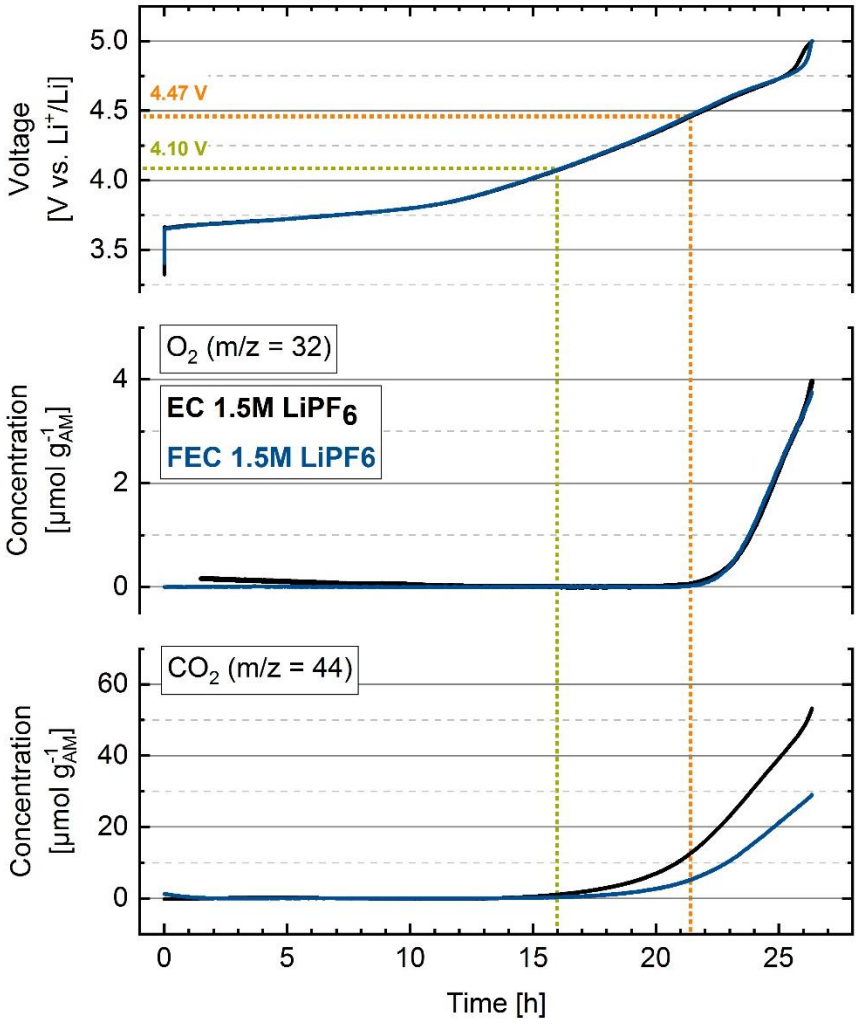

Figure 5. OEMS measurements for the first charge cycles in a half-cell for NCM-622 using EC + 1.5M $LiPF_6$ or FEC + 1.5M $LiPF_6$ as electrolyte at 25 °C. Upper panel: charge voltage vs. time and capacity; middle/lower panel: evolution of the concentration of concomitantly evolved O_2/CO_2 given in µmol/g_{AM}. Cells were charged at C/15 rate to 5.0 V and cells were composed of metallic Li counter electrode and a glassfiber separator. The vertical dashed green line indicates the CO_2 onset potential at 4.10 V vs. Li^+/Li and the vertical orange line indicates the O_2 onset potential at 4.47 V vs. Li^+/Li.

In order to investigate the effect of the oxygen release on the cycling performance of EC-containing electrolytes during high voltage cycling of stoichiometric layered NCM materials, we have assembled graphite//NCM-622 full-cells with a m_{ely}:m_{CAM} ≈ 1:1, containing EC:DEC = 2:8 wt.% or FEC:DEC = 2:8 wt.%. One set of the cells were cycled to a full-cell upper

cutoff of 4.35 V, which is slightly below the oxygen onset potential (**Figure 5**) and one set of cells were cycled to an upper full-cell cutoff of 4.60 V, which is above the oxygen onset potential (**Figure 5**), but the pure anodic electrolyte stability is still sufficient (**Figure 2**). Despite the adjusted cutoff potentials, the cells were cycled with the same protocol that was used for the Li- and Mn-rich NCMs shown before. **Figure 6** depicts the results of the cycling experiments, it can be seen that for the cells cycled to 4.35 V (orange and green line) both electrolytes show good cycling performance and no deviation between both electrolytes can be observed, which can be explained by the absence of oxygen release, as shown in **Figure 5**. In stark contrast, a strong deviation between the EC-based (black lines **Figure 6**) and the FEC-based (blue lines **Figure 6**) electrolyte can be seen if the cell is cycled above the oxygen onset potential. The cells with the FEC-based electrolyte show a continuous capacity decay and a remaining capacity at 1C after 48 cycles of ≈171 ± 1 mAh/g, while the cells with the EC-based electrolyte show a rapid rollover failure at 1C and only a remaining capacity of ≈111 ± 7 mAh/g after 48 cycles, although the cells have already reached their end-of -life (< 80% capacity retention) after 25 cycles. Again, a high deviation of ≈49 mAh/g between the capacity at 1C and the capacity at C/10 can be observed if the EC-based electrolyte is cycled above the oxygen onset potential (black line **Figure 6**), pointing towards a high resistance build-up. In contrast, only a difference of ≈13 mAh/g between the capacity at 1C and at C/10 occurs if the FEC-based electrolyte is cycled to 4.60 V (blue line **Figure *6***). Beside the rapid failure of the EC-based electrolyte after the oxygen evolution, one has to mention that also the cycling stability of the cells containing FEC-based electrolyte is not unaffected by the oxygen release. In particular, the cells with the FEC-based electrolyte loose ≈41 mAh/g between cycle 18 and 148 if they are cycled to 4.60 V (blue line **Figure 6**) and only about ≈7 mAh/g if the upper cutoff is limited to 4.35 V (green line **Figure 6**). This can be explained by the degradation of the cathode active material due to the oxygen release and by the fact that also

FEC reacts with the lattice oxygen (**Figure 5**). Although the FEC-based electrolytes do not cause a high resistance build-up and a rapid rollover failure, they might still form decomposition products that might cause side reactions, such as decomposition of the conductive salt[35, 43] transition metal migration[44-46] and probably clogging of the separator pores.

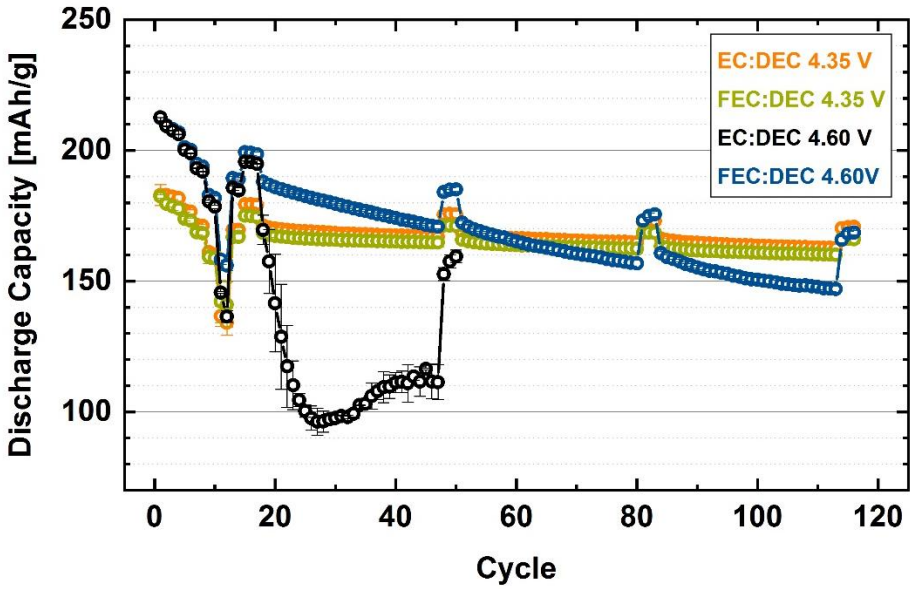

Figure 6. Electrochemical Cycling of NCM-622 at 25°C using a graphite counter electrode, 21 µL of a EC-DEC (2-8 wt.%) 1M $LiPF_6$ or a FEC-DEC (2-8 wt.%) 1M $LiPF_6$ electrolyte and a Celgard 2500 separator; activation was carried out at C/15, followed by a rate test (up to 3C), while further cycling was carried out at 0.7C (CCCV) charge and 1C discharge. The lower cutoff potential was held constant at 3.0 V, the upper cutoff was 4.35 V or 4.60 V, as indicated in the figure. Each thirty cycles C/10 cycles were applied as diagnostic cycles.

Conclusions

In this study we discussed the high voltage cycling performance of stoichiometric and overlithiated layered oxides with EC-containing electrolytes. In particular we could show that in a realistic full-cell setup (m_{ely}:m_{CAM} ≈ 1:1) Li- and Mn-rich NCMs cannot be cycled in EC-based electrolytes, due to a high resistance build-up causing a rapid rollover failure. Replacement of EC by FEC as co-solvent could sufficiently improve the cycling performance of Li- and Mn-rich NCMs and prevent a rollover failure. By on-line electrochemical mass spectrometry (OEMS) we could show that the anodic stability of EC compared to FEC cannot be the reason for these strong deviations in the cycling performance, while both carbonates can be chemically decomposed by lattice oxygen, released from the layered NCM cathode. Therefore, we showed by a pre-activation of Li- and Mn-rich NCMs that the oxygen release strongly alters the cycling performance of the EC-based electrolyte, while the FEC-based electrolyte is affected to a much smaller extent. By a systematic variation of the upper cutoff potential of graphite//NCM-622 cells we showed that the same mechanism accounts for stoichiometric NCMs and that oxygen release is the reason why layered oxides cannot be cycled in EC-based electrolytes above 4.4 V.

Acknowledgement

This work was supported by BASF SE within its BASF SE Battery Research Network.

Literature

1. D. Larcher and J. M. Tarascon, *Nat. Chem.*, **7** (1), 19-29 (2015).
2. J. B. Goodenough and K. S. Park, *J. Am. Chem. Soc.*, **135** (4), 1167-1176 (2013).
3. M. M. Thackeray, C. Wolverton, and E. D. Isaacs, *Energy & Environ. Sc.*, **5** (7), 7854 (2012).
4. D. Andre, S.-J. Kim, P. Lamp, S. F. Lux, F. Maglia, O. Paschos, and B. Stiaszny, *J. Mat. Chem. A*, **3** (13), 6709-6732 (2015).
5. K. Mizushima, P. Jones, P. Wiseman, and J. B. Goodenough, *Mater. Res. Bull.*, **15** (6), 783-789 (1980).
6. M. M. Thackeray, S.-H. Kang, C. S. Johnson, J. T. Vaughey, R. Benedek, and S. A. Hackney, *J. Mater. Chem.*, **17** (30), 3112 (2007).
7. S. Hy, H. Liu, M. Zhang, D. Qian, B.-J. Hwang, and Y. S. Meng, *Energy Environ. Sci.*, **9** (6), 1931-1954 (2016).
8. J. R. Croy, M. Balasubramanian, K. G. Gallagher, and A. K. Burrell, *Acc. Chem. Res.*, **48** (11), 2813-2821 (2015).
9. R. Jung, M. Metzger, F. Maglia, C. Stinner, and H. A. Gasteiger, *J. Electrochem. Soc.*, **164** (7), A1361-A1377 (2017).
10. R. Jung, M. Metzger, F. Maglia, C. Stinner, and H. A. Gasteiger, *J. Phys. Chem. Lett.*, **8** (19), 4820-4825 (2017).

11. D. Streich, C. Erk, A. Guéguen, P. Müller, F.-F. Chesneau, and E. J. Berg, *J. Phys. Chem. C*, **121** (25), 13481-13486 (2017).

12. T. Teufl, B. Strehle, P. Müller, H. A. Gasteiger, and M. A. Mendez, *J. Electrochem. Soc.*, **165** (11), A2718-A2731 (2018).

13. B. Strehle, K. Kleiner, R. Jung, F. Chesneau, M. Mendez, H. A. Gasteiger, and M. Piana, *J. Electrochem. Soc.*, **164** (2), A400-A406 (2017).

14. J. Xia, M. Nie, J. C. Burns, A. Xiao, W. M. Lamanna, and J. R. Dahn, *J. Power Sources*, **307** 340-350 (2016).

15. J. Xia, K. J. Nelson, Z. Lu, and J. R. Dahn, *J. Power Sources*, **329** 387-397 (2016).

16. J. Xia, R. Petibon, D. Xiong, L. Ma, and J. R. Dahn, *J. Power Sources*, **328** 124-135 (2016).

17. R. Petibon, J. Xia, L. Ma, M. K. G. Bauer, K. J. Nelson, and J. R. Dahn, *J. Electrochem. Soc.*, **163** (13), A2571-A2578 (2016).

18. L. Ma, S. L. Glazier, R. Petibon, J. Xia, J. M. Peters, Q. Liu, J. Allen, R. N. C. Doig, and J. R. Dahn, *J. Electrochem. Soc.*, **164** (1), A5008-A5018 (2016).

19. A. J. Gmitter, I. Plitz, and G. G. Amatucci, *J. Electrochem. Soc.*, **159** (4), A370-A379 (2012).

20. K. Xu, *Chem. Rev.*, **114** 11503 (2014).

21. L. Hu, Z. Zhang, and K. Amine, *Electrochem. Commun.*, **35** 76-79 (2013).

22. L. Hu, Z. Xue, K. Amine, and Z. Zhang, *J. Electrochem. Soc.*, **161** (12), A1777-A1781 (2014).

23. E. Markevich, G. Salitra, K. Fridman, R. Sharabi, G. Gershinsky, A. Garsuch, G. Semrau, M. A. Schmidt, and D. Aurbach, *Langmuir*, **30** (25), 7414-7424 (2014).

24. B. Aktekin, R. Younesi, W. Zipprich, C. Tengstedt, D. Brandell, and K. Edström, *J. Electrochem. Soc.*, **164** (4), A942-A948 (2017).

25. T. Teufl, D. Pritzl, S. Solchenbach, H. A. Gasteiger, and M. Mendez, *manuscript submitted*.

26. J. Wandt, A. T. S. Freiberg, A. Ogrodnik, and H. A. Gasteiger, *Materials Today*, **21**, 218 (2018).

27. A. T. S. Freiberg, M. K. Roos, J. Wandt, R. de Vivie-Riedle, and H. A. Gasteiger, *J. Phys. Chem. A*, **122** (45), 8828-8839 (2018).

28. T. M. Østergaard, L. Giordano, I. E. Castelli, F. Maglia, B. K. Antonopoulos, Y. Shao-Horn, and J. Rossmeisl, *J. Phys. Chem. C*, **122** (19), 10442-10449 (2018).

29. Y. Yu, P. Karayaylali, Y. Katayama, L. Giordano, M. Gauthier, F. Maglia, R. Jung, I. Lund, and Y. Shao-Horn, *J. Phys. Chem. C*, **122** (48), 27368-27382 (2018).

30. L. Giordano, P. Karayaylali, Y. Yu, Y. Katayama, F. Maglia, S. Lux, and Y. Shao-Horn, *J. Phys. Chem. Lett.*, **8** (16), 3881-3887 (2017).

31. N. Tsiouvaras, S. Meini, I. Buchberger, and H. A. Gasteiger, *J. Electrochem. Soc.*, **160** (3), A471-A477 (2013).

32. M. Metzger, B. Strehle, S. Solchenbach, and H. A. Gasteiger, *J. Electrochem. Soc.*, **163** (5), A798-A809 (2016).

33. F. T. Wagner, B. Lakshmanan, and M. F. Mathias, *J. Phys. Chem. Lett.*, **1** (14), 2204-2219 (2010).

34. J. C. Burns, A. Kassam, N. N. Sinha, L. E. Downie, L. Solnickova, B. M. Way, and J. R. Dahn, *J. Electrochem. Soc.*, **160** (9), A1451-A1456 (2013).

35. T. Teufl, D. Pritzl, S. Solchenbach, M. Mendez, and H. A. Gasteiger, *in preparation.*

36. K. Kim, I. Park, S.-Y. Ha, Y. Kim, M.-H. Woo, M.-H. Jeong, W. C. Shin, M. Ue, S. Y. Hong, and N.-S. Choi, *Electrochimica Acta*, **225** 358-368 (2017).

37. D. Pritzl, S. Solchenbach, M. Wetjen, and H. A. Gasteiger, *J. Electrochem. Soc.*, **164** (12), A2625-A2635 (2017).

38. A. R. Armstrong, M. Holzapfel, P. Novák, C. S. Johnson, S.-H. Kang, M. M. Thackeray, and P. G. Bruce, *J. Am. Chem. Soc.*, **128** (26), 8694-8698 (2006).

39. T. Zünd, B. Strehle, D. Hochfilzer, and H. A. Gasteiger, *in preparation.*

40. N. Yabuuchi, K. Yoshii, S. T. Myung, I. Nakai, and S. Komaba, *J. Am. Chem. Soc.*, **133** (12), 4404-4419 (2011).

41. M. Metzger, C. Marino, J. Sicklinger, D. Haering, and H. A. Gasteiger, *J. Electrochem. Soc.*, **162** (7), A1123-A1134 (2015).

42. R. Jung, P. Strobl, F. Maglia, C. Stinner, and H. A. Gasteiger, *J. Electrochem. Soc.*, **165** (11), A2869-A2879 (2018).

43. A. Guéguen, D. Streich, M. He, M. Mendez, F. F. Chesneau, P. Novák, and E. J. Berg, *J. Electrochem. Soc.*, **163** (6), A1095-A1100 (2016).

44. J. A. Gilbert, I. A. Shkrob, and D. P. Abraham, *J. Electrochem. Soc.*, **164** (2), A389-A399 (2017).

45. R. Jung, F. Linsenmann, R. Thomas, J. Wandt, S. Solchenbach, F. Maglia, C. Stinner, M. Tromp, and H. A. Gasteiger, *J. Electrochem. Soc.*, **166** (2), A378-A389 (2019).

46. J. Wandt, A. Freiberg, R. Thomas, Y. Gorlin, A. Siebel, R. Jung, H. A. Gasteiger, and M. Tromp, *J. Mater. Chem. A*, **4** (47), 18300-18305 (2016).

3.2.2. Thermal stability of FEC-based electrolytes

This section presents the manuscript "Thermal Stability of FEC-Based Electrolytes for High-Voltage Li-Ion Batteries". It will soon be submitted to a peer-reviewed journal for publication. The manuscript was presented by Tobias Teufl at the 234th Meeting of the Electrochemical Society (September 30th – October 4th, 2018) in Cancun, Mexico (Abstract Number: 456).

It has been shown in various studies that high-voltage operation of EC-containing electrolytes with layered oxide-based cathode materials shows insufficient cycling performance and leads to a rapid capacity fading.[91] In particular, we could show in a previous study that EC as electrolyte component does not allow stable cycling in cases where oxygen is released from the cathode active material.[137] As it is well known that oxygen release occurs during the activation of Li- and Mn-rich layered oxides,[60, 73-75, 79, 138] EC-based electrolytes cannot be used in combination with this class of cathode materials.[137] For this reason, if EC is replaced by FEC as co-solvent, a strong improvement of the cycling performance can be observed.[137] However, it has been shown by Kim et al.[98] that high amounts of FEC within the electrolyte can lead to a certain reactivity with $LiPF_6$, which is particularly critical during high temperature cell operation. As a consequence, protic and acidic products can evolve within the electrolyte and lead to detrimental side reactions with the electrodes, such as transition-metal dissolution.

In this study, we show a detailed analysis of the reactivity of FEC with $LiPF_6$ and its impact on the cell chemistry and the cell performance. By a combination of the detection of gaseous reaction products by OEMS and an analysis of the liquid reaction products by ^{1}H-NMR, we can prove one of the mechanisms suggested by Kim et al.[98] In particular, we can show that the most critical reaction products are HF and VC (vinylene carbonate). As a consequence, impedance growth on the anode and the cathode side can be observed; at the same time, the evolved HF leads to an increased detection of manganese on the anode side, which is known to have a critical influence onto cycling performance.[53, 81, 84] In addition, it turns out that the formation of VC leads to strong gas-evolution when high-voltage cells are used with FEC-based electrolytes which, can be rationalized by the anodic instability of VC

at potentials >4.3 V vs. Li^+/Li.[52] This understanding is not only of high importance for high-voltage cathode active materials, but also for cells with silicon containing anodes, where typically high amounts of FEC within the electrolyte are required.[35] These results suggest that the amount of FEC in the electrolyte has to be limited, especially for high temperature applications. Furthermore, we expect that the high temperature performance of oxygen releasing cathode materials can be optimized by replacing FEC as co-solvent.

Author contributions

T.T. carried out the OEMS measurements and cycled the pouch-cells. The NMR experiments and the ICP-MS measurements were carried out at the analytical department of BASF SE (Ludwigshafen). D.P. carried out the cycling and impedance experiments. All authors discussed the data. T.T. and D.P. wrote the manuscript.

Thermal Stability of FEC-Based Electrolytes for High-Voltage Li-Ion Batteries

Tobias Teufl,[a, b,=] Daniel Pritzl,[b,=] Sophie Solchenbach,[b] Manuel A. Mendez,[a] and Hubert A. Gasteiger[b]

[a]*BASF SE Ludwigshafen, Lithium-Ion Battery Research, D-67056 Ludwigshafen, Germany*
[b]*Chair of Technical Electrochemistry, Department of Chemistry and Catalysis Research Center, Technical University of Munich, D-85748 Garching, Germany*

[=] Authors contributed equally

Abstract

Fluoroethylene-carbonate (FEC) is often used as co-solvent for high-voltage materials, as well as for silicon-based anode materials. However, FEC as co-solvent shows a limited thermal stability when used together with $LiPF_6$ as conductive salt and leads to a chemical electrolyte decomposition that can strongly trigger side reactions in a lithium-ion battery. In this study, we will show a detailed analysis of the reaction mechanism of FEC with $LiPF_6$ and will show that vinylene-carbonate (VC), HF and PF_5 can evolve if FEC is used as co-solvent. By using a full-cell setup, equipped with a gold-wire reference electrode (GWRE), we can show that these side reactions do not only lead to a resistance increase on the cathode, as well as on the anode side, but also trigger transition metal dissolution. By comparison of FEC and ethylene-carbonate (EC) as cyclic carbonate, we prove that FEC has no advantage at high-voltage operation compared to EC, if no oxygen is evolved from the cathode material (in this case LNMO). In the end we use commercial multi-layer pouch-cells to analyze the gassing of EC- and FEC-based electrolytes. Here we could clearly show that FEC-based electrolytes lead to strong swelling of multi-layer pouch-cells, which can be rationalized by the oxidation VC starting at 4.3 V vs. Li^+/Li.

Introduction

Typical anode materials for lithium-ion batteries exhibit low reversible voltages < 0.5 V vs. Li^+/Li in order to increase the overall energy output of a lithium-ion cell.[1, 2] While this is sufficient for increasing energy density, the stability window of the typical carbonate electrolytes is exceeded at these low cutoff potentials, leading to electrolyte reduction on the anode.[3] For this purpose, additives have been investigated that can form an effective passivation layer during the first charge and therefore prevent further electrolyte reduction, while guarantee sufficient Li-ion conductivity into the anode.[4, 5] In this regard, especially VC and FEC are widely used as SEI forming additives which are added to the electrolyte in rather small amounts (≈1-2 wt.%) , to form a more stable SEI compared to EC.[4, 6, 7] However, it has been shown that especially for silicon anodes FEC is an important cell component to effectively passivate the silicon anode.[8-10] The large volume expansion of silicon during lithium insertion leads to a continuous cracking of the SEI layer, that causes ongoing FEC consumption and the need of high amount of FEC in electrolytes used for silicon anodes.[8, 10] A similar behavior was also shown for lithium metal anodes where lithium plating and stripping leads to destabilization of the SEI layer;[8, 11] in this regard it has been suggested that replacement of EC by FEC leads to an improved performance of lithium metal anodes.[12]

However, FEC is not only used as additive to passivate the anode side, but also as co-solvent for high voltage and high energy cathode materials with increased upper cutoff potentials.[13, 14] In this regard it has been clearly shown by the group of Jeff Dahn that NCM-424//Graphite cells that are operated at 4.5 V show strongly improved cycle performance when FEC is used as co-solvent instead of EC[15] and in general fluorination of electrolyte components turned out to be advantageous for high-voltage applications.[13] It has been suggested in literature that the oxidative

stability of FEC exceeds the oxidation potential of EC and thus leading to improved cycle life for EC-free electrolytes with FEC as cyclic carbonate.[4, 16-18] In contradiction, other groups suggested that FEC can form a passivating surface layer on the cathode material, leading to a so-called cathode-electrolyte-interface (CEI) that can prevent the electrolyte from further oxidation.[19, 20] However, surface analysis of LNMO electrodes after cycling could not prove the existence of such a passivating inorganic surface layer.[21] Recently, it was shown that oxygen release from layered oxides has a drastic impact on the full-cell cycling performance[22] and leads to a much more pronounced electrolyte degradation compared to electrooxidation below 4.8 V vs. Li^+/Li.[23-27] In this respect, we could prove that FEC shows less sensitivity towards oxygen evolution from the layered oxides compared to EC which now clarifies the effectiveness of FEC-based electrolytes together with layered oxides cycled to high cutoff potentials.[28] This however suggests that FEC does not show any advantage at high voltage cycling for cathode materials that do not release oxygen, such as the LNMO high voltage spinel compound.[22-24]

While FEC exhibits a much better oxidative stability compared to VC,[19, 29, 30] which is also reasonable compared to EC,[28, 31] the thermal stability of FEC as co-solvent is part of ongoing discussions and seems to be more critical compared to the non-fluorinated EC.[32] It was shown in LNMO//LTO cells that increasing amounts of FEC lead to a decreasing cell performance and form thick polymer species on the LNMO cathode that might potentially lead to an increase in impedance.[21] Furthermore, it was recently shown that FEC-based electrolytes exhibit lower thermal stability and form HF that leads to transition metal dissolution from the cathode and decreasing cycling performance.[32] In this study it was also discussed that electrolyte solutions containing $LiPF_6$ and FEC blackens after 3-days storage at 60 °C and show a strong acidic pH after the storage experiment.[32] Furthermore, higher gassing during cycling was observed with FEC-based electrolytes compared to EC-based base electrolytes; the gasses were mainly determined to be

CO_2,[33, 34] while other studies also showed increased POF_3 evolution in FEC containing electrolytes, stemming from $LiPF_6$ decomposition.[35, 36]

In this study we will compare the thermal stability of EC and FEC solutions with 1.5M $LiPF_6$ and we will carefully analyze the gaseous decomposition products during a heating experiment by on-line electrochemical mass spectrometry (OEMS).[37] Furthermore, we will then analyze and quantify the decomposition products after 3 weeks storage at 60 °C that are dissolved in the electrolyte, therefore we will apply ^{1}H-NMR spectroscopy. After the high temperature storage, we will also analyze the oxidative stability of the FEC 1.5M $LiPF_6$ solution before and after storage using a carefully designed OEMS experiment in a two-compartment cell.[38] By the addition of 1000 ppm VC, we will prove the decomposition mechanism suggested from the OEMS and the ^{1}H-NMR data. After that we will show the actual effect on the cell chemistry, using LNMO//graphite full-cells. Here we can show that FEC-based electrolytes exhibit a higher impedance build-up, increased transition metal dissolution and strong gassing, compared to its EC-based analogous.

Experimental

Electrode preparation.— $LiNi_{0.5}Mn_{1.5}O_4$ (LNMO) cathodes were prepared by mixing LNMO (BASF SE, Germany), carbon black (Super-C65, Timcal, Switzerland), and polyvinylene difluoride (PVDF, Kynar HSV 900, Arkema, France) at a mass ratio of 92/5/3 with NMP (N-methyl pyrrolidone, anhydrous, Sigma-Aldrich, Germany) in a planetary mixer (Thinky Corp.) for 15 min. The ink was coated onto an aluminum foil (MTI, 18 µm) with a doctor blade coater and dried at 50 °C in a convection oven for at least 3 h. The final LNMO coating had a loading of ≈13.6 mg_{LNMO}/cm^2, corresponding to ≈1.9 mAh/cm². Electrodes with a diameter of 11 mm (≡0.95 cm^2) were punched out and compressed to ≈30% porosity with a KBr press. Graphite electrodes were prepared by mixing graphite (T311, SGL Carbon, Germany) and PVDF at a mass ratio of 95/5 with NMP by applying the same procedure as for the positive electrodes. The graphite ink was coated onto copper foil (MTI, ≈12 µm) and dried in a convection oven at 50 °C for 3 h. The loading of the graphite coating was ≈6.5 $mg_{graphite}/cm^2$ corresponding to ≈2.4 mAh/cm². The electrodes were punched out with a diameter of 11 mm and compressed to a porosity of ≈30%. Both types of electrodes were dried under dynamic vacuum at 120 °C overnight in a vacuum oven (Büchi, Switzerland) and then transferred into an Argon-filled glovebox (MBraun, Germany) without exposure to air.

The carbon black electrodes for the OEMS measurements were prepared by mixing 1.0 g conductive carbon (Super-C65, Timcal, Switzerland), and 1.0 g PVDF binder (Kynar HSV 900, Arkema, France) in 18 g NMP (anhydrous, Sigma-Aldrich, USA) in a planetary mixer (Thinky Corp.) for 5min. The slurry was coated with a wet film thickness of 240 µm onto a polyethylene separator (Celgard 2500, USA), yielding a carbon loading of ≈0.8 mg_C/cm^2. Electrodes for OEMS experiments were punched out with a diameter of 15 mm.

On-line electrochemical mass spectrometry (OEMS).— To detect decomposition products during thermal treatment of EC 1.5M $LiPF_6$ and FEC 1.5M $LiPF_6$ (both <20 ppm H_2O BASF SE, Germany), a test-protocol used by Metzger et al.[39] and Solchenbach et al.[40] was adopted. Therefore, the standard OEMS cell was filled only with 240 µL electrolyte without any separator or electrodes and heated stepwise up to 60 °C, the cell setup is reported elsewhere.[37] The cells were assembled at room temperature inside a glovebox and then cooled down to 10 °C previously to the measurement and connected to the OEMS. The cell was then heated stepwise from 10 °C to 25 °C to 45 °C and finally to 60 °C, whereas each temperature was set for three hours in order to detect the decomposition products. For the measurements of the oxidative stability with the carbon black electrodes we used a custom made sealed two-compartment cell that separates the anode and the cathode department by a lithium-ion conductive glass ceramic (Ohara Corp., Japan).[38] This cell setup allows to separate the gasses from the electrolyte oxidation from the lithium counter electrode and avoids crosstalk effects; this is important to determine the exact onset of the electrolyte oxidation on a carbon electrode, the setup was developed in our group and reported in a separate study.[38] The cells were assembled with Li metal counter electrode, a glassfiber separator (200 µm thickness, VWR, Germany) and 200 µl of electrolyte in the lower compartment and a carbon black working electrode, a polyester separator (Freudenberg, Germany) and 100 µl of electrolyte composed of FEC-only or EC-only, each with 1.5M $LiPF_6$ (both <20 ppm H_2O BASF SE, Germany) in the upper compartment. The cells were connected to the mass spectrometer, held for 4 h at OCV (open circuit voltage), and then charged to 5.5 V vs. Li^+/Li at a scan rate of 0.1 mV/s. For quantification of the mass spectrometer currents, a calibration gas containing H_2, O_2, CO_2, C_2H_4 (each 2000 ppm) in Argon (Linde AG, Germany) was used. All currents were normalized to the current at m/z = 36 (Ar isotope) in order to correct for effects of minor pressure and temperature

deviations, and afterwards the currents m/z = 32 (O_2) and m/z = 44 (CO_2) were converted into gas concentration.

Electrochemical characterization.— Impedance measurements were conducted with a gold-wire reference electrode (GWRE).[41] Graphite//LNMO cells were cycled 2x at C/10 (25 °C, Formation) with a constant current constant voltage (CCCV) charge with a cut-off for the CV phase of C/20 and a constant current CC discharge. Afterwards, cycling with a C/2 CCCV charge and a CC discharge at 1C was carried out. The cells were cycled in the voltage range between 3.5 V and 4.8 V. Prior to the impedance measurement, the gold wire was lithiated with a constant current of 150 nA for 1 hour. Impedance spectra were recorded at 50% SOC after formation and after 100 charge/discharge cycles under open-circuit conditions at 25 °C with a 1 hour rest phase before starting the measurement. The impedance was recorded with an amplitude of 10 mV in the frequency range of 100 kHz to 100 mHz using a potentiostat (VMP 300, Biologic, France).

Multi-layer pouch-cells used for the gassing analysis were commercial Graphite//NCM-111 and Graphite//LNMO cells (Li-Fun Technologies, China) with a nominal capacity of 200 mAh. Prior to cell assembly the fresh cells were dried at 60 °C under vacuum overnight and then filled in an argon filled glovebox with 700 mL electrolyte. As electrolyte EC:DEC (2:8 by volume; BASF SE, Germany) 1M $LiPF_6$ or FEC:DEC (2:8 by volume; BASF SE, Germany) 1M $LiPF_6$ were used; cells were evacuated and sealed inside the glovebox. For cell formation the cells were charged at 25 °C to 20% SOC at a rate of C/10 and then stored for 18h at 45 °C, afterwards the cells were degassed to remove formation gasses and cycled at 45 °C. The first two cycles after formation were carried out at C/10 charge (CC) and C/10 discharge (CC), before the cells were cycled for 100

cycles with a 0.5C charge (CCCV) rate and 1C discharge (CC) rate, where the CV-step was terminated after 1h or at a current cutoff of C/20.

Further characterization.—The amount of gasses evolved during cycling was measured for the multi-layer pouch-cells after 100 charge/discharge cycles. The gas volume was measured by the Archimedes method that has been reported by Aiken et al.[42], the gas volumes are referenced to the volume that was measured after the initial degassing step.

To analyze the decomposition products solved in the electrolyte, FEC with 1.5M $LiPF_6$ was stored within a glovebox for 3 weeks at 60 °C. Decomposition products in the electrolyte were analyzed by ^{1}H-NMR spectroscopy (Bruker AV3-500p, 500 MHz), NMR was measured for the fresh electrolyte and after three weeks storage without using any further solvent.

For ICP-MS measurements the GWRE cells from the impedance measurements were opened in the discharged state and the graphite anodes were taken without any further washing step. The graphite anodes were dissolved in acid and analyzed by ICP-MS. Gases from the multi-layer pouch cells were analyzed by GC-MS. Hereby, the gasses were extracted under nitrogen with a syringe from the cells and analyzed by GC-MS.

Results and Discussion

Thermal stability of EC and FEC with $LiPF_6$.— It has been shown in literature that the mixture of FEC and $LiPF_6$ blackens during high temperature storage and forms acidic species within the liquid electrolyte solution.[32] We expect to get profound mechanistic information about the decomposition products by the analysis of the gaseous decomposition products. According to the mechanistic suggestions from Kim et al.[32], formation of PF_5 and CO_2 seems to be viable during thermal reaction of FEC and $LiPF_6$. While CO_2 can be easily detected in the OEMS, Solchenbach et al.[40] have shown that our OEMS setup is unable to differentiate between PF_5 and POF_3. This means that both, PF_5 (m/z = 107) and POF_3 (m/z = 85) will always be detected as "POF_3" (m/z = 85) in our OEMS setup, which can be rationalized by the high reactivity of PF_5 towards trace moisture.[40] We will conduct OEMS analysis of a FEC + 1.5M $LiPF_6$ and an EC + 1.5M $LiPF_6$ mixture at different temperatures and take a look at the masses m/z = 44 (corresponding to CO_2) and m/z = 85 (corresponding to POF_3 and PF_5) to analyze the gases that form during thermal decomposition. **Figure 1** shows the temperature dependent reactivity of a fresh FEC + 1.5M $LiPF_6$ and a fresh EC + 1.5M $LiPF_6$ mixture, showing equal signals at m/z = 44 (CO2) for both electrolytes and a strong deviation for m/z = 85 (POF_3/PF_5). The upper panel in **Figure 1** shows the temperature set point, starting from 10 °C and heating stepwise up to 60 °C; each temperature was held for 3h, as validated by Metzger et al.[39] and Solchenbach et al.[40] The middle panel depicts the signal for the mass m/z = 44, whereas the left y-axis gives the absolute number of the signal and the right y-axis gives the amount of a hypothetical CO_2 evolution (in ppm). Despite the signal on m/z = 44, we do not expect significant CO_2 evolution from electrolytes in **Figure 1** for three main reasons: first of all only negligible thermal decomposition of EC-based electrolytes is suggested up to 60 °C[43, 44]; in particular Metzger et al.[39] showed no CO_2 evolution

stemming from EC hydrolysis up to 60 °C. Furthermore, both carbonates, EC and FEC, cause a background signal at m/z = 44 that increases with increasing vapor pressure and therefore with temperature which can explain the temperature depended signal at m/z = 44. Whereas the higher vapor pressure of FEC compared to EC can therefore explain the slightly higher signal of the FEC based mixture. As last point one has to mention that the hypothetical amounts of CO_2 calibrated in ppm are very small (≈280 ppm, see **Figure *1*** middle panel, right scale) and cannot explain a decomposition mechanism, if compared to the signals for EC hydrolysis from Metzger et al. (≈ 5000 ppm)[39] which is an order of magnitude higher. In stark contrast, one can clearly see in the lower panel in **Figure *1*** that the POF_3/PF_5 signal (m/z = 85) differs substantially for the two electrolytes. It can be seen that $LiPF_6$ shows rather good stability in EC up to 60 °C and therefore causes only a small signal on m/z = 85 and only at 60 °C. In contradiction, it is shown that a signal on m/z = 85 can already be detected at 25 °C for the FEC + 1.5M $LiPF_6$ mixtures, giving clear evidence for enhanced $LiPF_6$ decomposition in the FEC mixture. Due to the lack of oxygen source for the POF_3 evolution (H_2O <20 ppm) we suggest that the POF_3 signal is caused by the presence of PF_5 that will also be detected as POF_3, as mentioned before.[40] Calibration into ppm gives roughly ≈10350 ppm of PF_5 that is formed towards the end of the experiment shown in **Figure 1**.

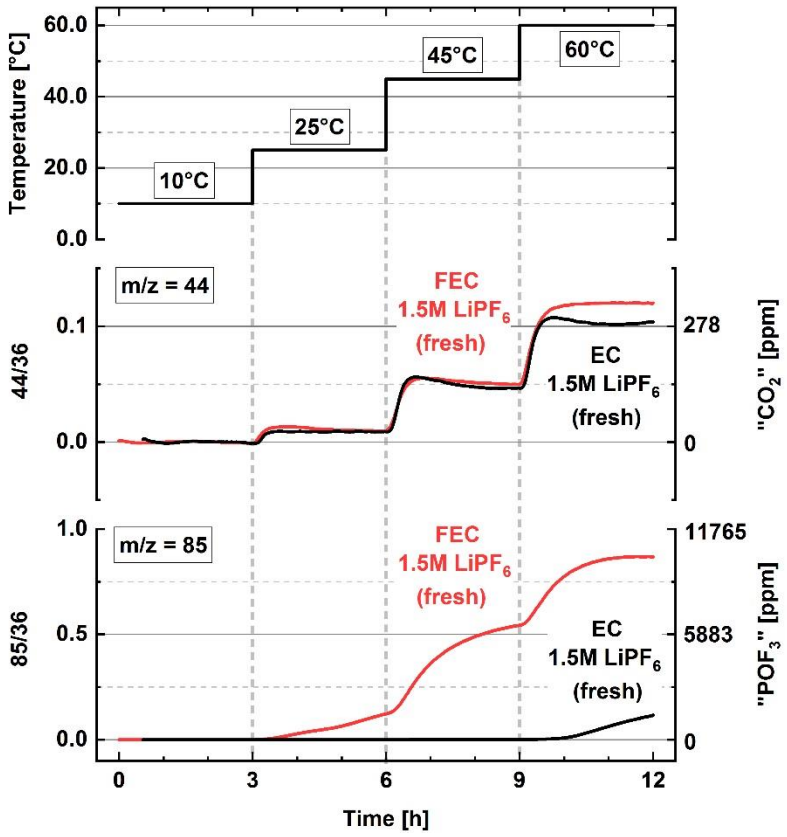

Figure 1. Temperature set points vs. time are shown in the upper panel, the middle panel shows the corresponding signal for m/z = 44 for EC (black) and FEC (red) with 1.5M $LiPF_6$. The lower panel shows m/z = 85 which can be assigned to POF_3, as well as PF_5 evolution as previously reported.[40] Absolut signals are shown on the left y-axis, while the right y-axis gives the hypothetical concentrations in ppm.

To summarize the findings from the OEMS experiment shown in **Figure 1**, one can conclude that the EC + 1.5M $LiPF_6$ mixture shows good thermal stability up to 60 °C, as suggested in literature.[39, 43, 44] For the FEC + 1.5M $LiPF_6$ mixture, no pronounced CO_2 evolution can be observed up to 60 °C, while the $LiPF_6$ decomposition can already be tracked at 25 °C and strongly increases with temperature. This gassing behavior shows good agreement with the mechanism that was suggested by Kim et al.[32] which is shown in **Scheme 1**. According to this mechanism the only

gaseous product that is formed during thermal decomposition is PF_5 which we could prove by the data shown in **Figure 1**. While gaseous PF_5 is tracked by OEMS (**Figure 1**) one should find a certain amount of VC in the liquid phase after thermal treatment. For this purpose, a FEC + 1.5M $LiPF_6$ mixture was stored for three weeks at 60 °C in a polymer vial inside an argon filled glovebox. ^{1}H-NMR was measured for the fresh FEC + 1.5M $LiPF_6$ sample and the sample that was aged for three weeks at 60 °C and the results are shown in **Figure 2**. The fresh electrolyte mixture is shown in the upper panel (black lines) of **Figure 2** and shows the pure FEC signals with an integral ratio of ≈2:1, as expected for FEC.[45] In the lower panel (red lines) in **Figure 2**, the same electrolyte after 3 weeks high temperature storage is shown. It can be seen that an additional small signal is observed at ≈7.25 ppm which indeed can be ascribed to VC formation,[46] the integral ratio allows quantification and leads to an overall VC concentration of 1051 ppm after 60 °C storage, which further supports the mechanism shown in black in **Scheme 1.**

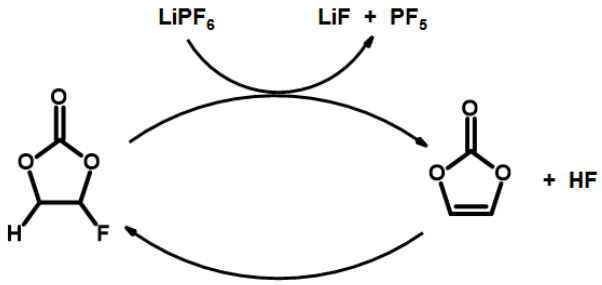

Scheme 1. Decomposition mechanism of FEC in the presence of $LiPF_6$ as proposed by Kim et al.,[32] leading to LiF, gaseous PF_5, HF and VC. An equilibrium saturation of VC is expected, while PF_5 leaves the electrolyte solution.

While the mechanism suggested in **Scheme 1** is qualitatively in good accordance with the decomposition products shown in **Figure 1** and **Figure 2**, a quantitative discrepancy can be observed in the amount of reaction products formed. From the mechanism shown in **Scheme 1**, a ratio between VC and PF_5 of 1:1 would ideally be expected, however after 3 weeks storage at 60 °C only about ≈1000 ppm VC are found in the electrolyte (**Figure 2**) mixture, while the OEMS

experiment with a total duration of only 12h (**Figure 1**; only 3h at 60 °C) already shows the presence of ≈10000 ppm PF_5 which is an order of magnitude higher compared to the VC found after 3 weeks storage. We expect that the VC concentration reaches an equilibrium concentration within a stored solution, while the gaseous PF_5 continuously leaves the solution (see **Scheme 1**). Thus, it is suggested that an equilibrium between FEC, VC and HF limit the actual VC concentration, as long as VC is not removed from the solution. As a consequence, new VC should be formed, once VC is removed (e.g. by oxidation), which will be discussed at the end of this study.

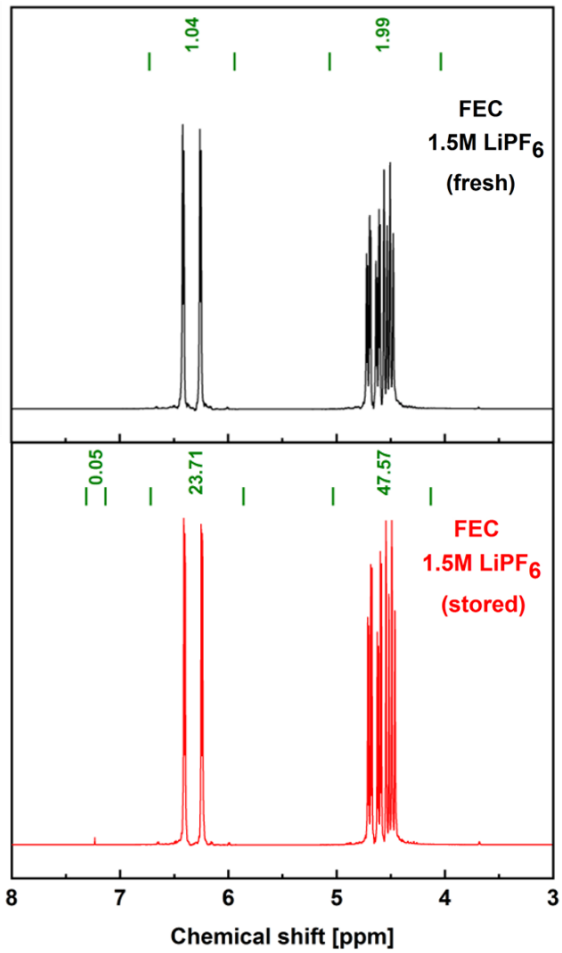

Figure 2. ^{1}H-NMR spectra for the fresh FEC + 1.5M $LiPF_6$ (black) mixture and after 3 weeks storage at 60 °C (red). The green lines/numbers indicate the integral ratios of the different signals.

Investigation of the oxidative stability of fresh and stored FEC + $LiPF_6$.— Pritzl et al.[30] could show by OEMS that VC is oxidative not stable at potentials >4.3 V vs. Li^+/Li and that CO_2 is the only gas that is produced by VC oxidation. We have shown in the previous section that VC can form in the FEC + 1.5M $LiPF_6$ solution, now we will investigate the oxidative stability of the fresh FEC + 1.5M $LiPF_6$ mixture and the same solution after 3 weeks storage at 60 °C which was also analyzed by ^{1}H-NMR (lower panel **Figure 2**). To investigate the oxidative stability, we performed on-line electrochemical mass spectrometry (OEMS), using a pure carbon black electrode as cathode which allows us to not only track the current response but also the CO_2 signal from electrolyte oxidation. Following not only the current but also the CO_2 signal is necessary to differentiate between further parasitic reactions, such as PF_6^- intercalation into the carbon black and electrolyte oxidation. Furthermore, we use a sealed two-compartment cell setup[38] that avoids crosstalk between the electrodes and allows to separately detect gasses from electrolyte oxidation and electrolyte reduction on the lithium counter electrode. Therefore, we can show the pure gas evolution from the electrolyte oxidation on the carbon electrode. **Figure 3** shows the current profile (upper panel) and the CO_2 evolution rate (lower panel m/z = 44) for the fresh FEC + 1.5 M $LiPF_6$ and the same electrolyte after 3 weeks 60 °C storage during a linear sweep voltammetry experiment from OCV (≈3V vs. Li^+/Li) up to 5.5 V vs. Li^+/Li. Data for the fresh FEC + 1.5M $LiPF_6$ electrolyte (black lines, **Figure 3**) show only the response of the base solution without any further oxidation currents or any further CO_2 evolution, as shown by Teufl et al.[28] In contradiction, the same FEC + 1.5M $LiPF_6$ electrolyte after 3 weeks 60 °C storage (red lines, **Figure 3**) shows a strong oxidation current starting from ≈4.7 V vs. Li^+/Li with a related CO_2 evolution at the same potential. This characteristic oxidation peak can be rationalized by the oxidation of VC impurities in the stored electrolyte, as shown for pure VC by Pritzl et al.[30] By ^{1}H-NMR spectroscopy (**Figure *2***) a VC concentration of ≈1000 ppm in the stored FEC + 1.5M $LiPF_6$ solution was found. Therefore,

we conducted a comparative experiment where we added 1000 ppm of VC to the fresh FEC + 1.5M $LiPF_6$ electrolyte, the results are also shown in **Figure 3** (green lines). Addition of 1000 ppm VC is in good accordance with the stored electrolyte, where ^{1}H-NMR analysis suggested a VC concentration of roughly 1000 ppm. These results further prove the existence of VC and the mechanism shown in **Scheme 1**, furthermore these results point towards a critical point for the cell performance, as the thermal decomposition leads to an oxidative less stable electrolyte mixture.

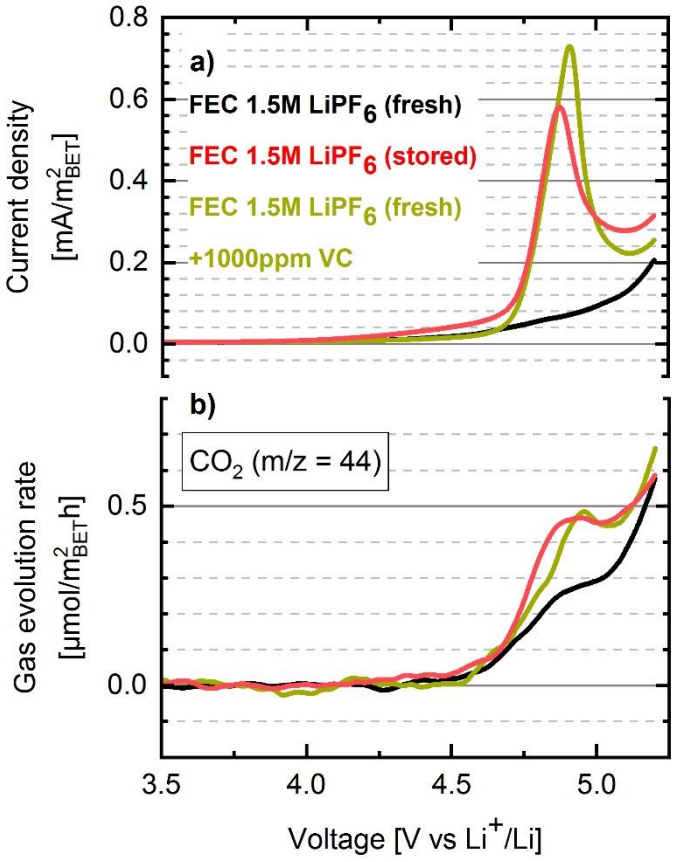

Figure 3. Oxidative current (upper panel) and CO_2 evolution (lower panel) of FEC electrolyte solutions, each containing 1.5M $LiPF_6$. The black line shows fresh mixed FEC + 1.5M $LiPF_6$, while the red line shows the electrolyte after 3weeks storage at 60 °C. The green line shows fresh mixed FEC + 1.5M $LiPF_6$ with addition of 1000 ppm VC. A linear scan (0.1 mV/s) was carried out from OCV (≈3 V vs. Li^+/Li) to 5.5 V vs. Li^+/Li. The OEMS experiments were performed in a sealed two-compartment using a carbon working and a lithium counter electrode, the cell setup is shown elsewhere.[38]

Cycling performance of graphite//LNMO full-cells with EC- and FEC-based electrolytes.— Next, we want to investigate the effect of FEC at elevated temperatures (45 °C) and at high operating cathode voltages (up to 4.9 V vs. Li^+/Li). Therefore, graphite//LNMO cells equipped with a gold-wire reference electrode (GWRE) were assembled. LNMO was chosen as cathode material, as it shows now oxygen release and therefore guarantees a fair comparison of the EC- and FEC-based electrolytes.[22] For one set of cells an EC:DEC (2:8 vol.%, 1M $LiPF_6$) based electrolyte (control) was used and for another set of cells an FEC:DEC (2:8 vol.%, 1M $LiPF_6$) based electrolyte was used. The impedance was recorded after two formation cycles (C/10, 25 °C) at 50% SOC. After 100 charge/discharge cycles with a C/2 charge and 1C discharge at 45 °C the impedance was recorded again. **Figure 4b** shows the specific discharge capacity at 1C versus the cycle number and **Figure 4a** shows the coulombic efficiency versus cycle number.

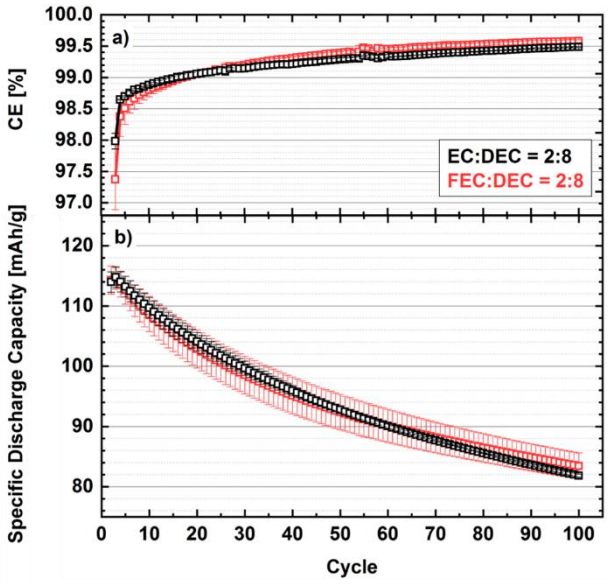

Figure 4. Electrochemical cycling of graphite//LNMO cells at 45 °C using 60 µL of electrolyte and two Freudenberg 2190 separators. The black lines show the performance of an EC:DEC (2:8 vol.%, 1M $LiPF_6$) electrolyte, while the corresponding FEC:DEC (2:8 vol.%, 1M $LiPF_6$) electrolyte is shown in red. The two formation cycles were carried out at C/10 (3.5 – 4.8 V) and at 25 °C, followed by 0.5C charge (+1h CV) and 1C discharge cycling between 3.5 and 4.8 V at 45 °C. The upper panel shows the coulombic efficiency and the lower panel shows the capacity retention, for

clarity the two formation cycles at 25 °C are not shown. A GWRE was used to measure impedance after formation and after cycling, the impedance spectra are shown in **Figure 5** and **Figure 6**, the cell setup is reported elsewhere.[41]

The specific discharge capacity versus cycle number is almost identical for both electrolytes and starts with 115 (±2) mAh/g_{LNMO} after formation. After 100 charge/discharge cycles the specific discharge capacity is 83 (±2) mAh/g_{LNMO}. The coulombic efficiency is also identical for both electrolytes and reaches a value of 99.5% after 100 cycles. This data suggests that the fading of graphite//LNMO cells at 45 °C shows no dependency if EC or FEC is used as cyclic carbonate. These results underline the effect that both EC and FEC are at their anodic stability limit if cycled up to 4.9 V vs. Li^+/Li at 45 °C and FEC shows no improvement over EC regarding high voltage stability (without O_2-release). In order to get more insight into the ageing process, the impedance spectra for the different electrolytes are shown in **Figure 5** (cathode impedance spectra) and in **Figure 6** (anode impedance spectra). The impedance of the LNMO cathode after formation (**Figure 5a**) is identical for both cells cycled with FEC and EC. At highest frequencies the onset of a contact resistance ($R_{Contact}$) between current collector and LNMO coating is observed as already shown in former studies.[47, 48] As the electrodes contain 5% of carbon black this feature is very small. At medium frequencies, a semicircle is observed containing both the charge transfer resistance (R_{CT}) and the pore resistance (R_{Pore}). At lowest frequencies the onset of Warburg diffusion can be seen, representing concentration gradients in the liquid electrolyte.[47] The diameter of the semicircle ($R_{CT} + R_{Pore}$) is corresponds to ≈3 Ωcm² for both electrolytes after formation. After 100 charge/discharge cycles at 45 °C, the impedance spectra differ significantly (see **Figure 5b**). The cells cycled with the EC-based electrolyte show a pronounced high frequency semicircle stemming from an increased contact resistance between the current collector and cathode coating $R_{Contact}$. This was also observed in Pritzl et al.[48] and there correlated with protic species (e.g. HF) from

electrochemical electrolyte oxidation. $R_{Contact}$ has a value of ≈11 Ωcm² after 100 cycles for the EC-based electrolyte. The cathode impedance after 100 cycles for the FEC-based electrolyte is larger than the impedance with the EC based electrolyte. First the contact resistance $R_{Contact}$ has a value of 21 Ωcm² what is a factor two higher compared to the EC-based electrolyte (11 Ωcm²). This can easily be rationalized by the formation of HF from the thermal decomposition of the FEC-based electrolyte (see **Scheme 1**) and thus corroding the aluminum current collector as shown by Pritzl et al.[48] Next also the semi-circle at medium frequencies (R_{CT} + R_{Pore}) is higher for the FEC based electrolyte with a value of 17 Ωcm² compared to 7 Ωcm² for the EC-based case. As the thermal decomposition leads to the formation of vinylene-carbonate (VC) the higher semicircle at medium frequencies can be rationalized by the oxidation of VC which leads to the formation of poly(VC) and thus to an increase of R_{CT} on the cathode side. The effect of VC oxidation with LNMO cathodes was already shown by Pritzl et al.[30]

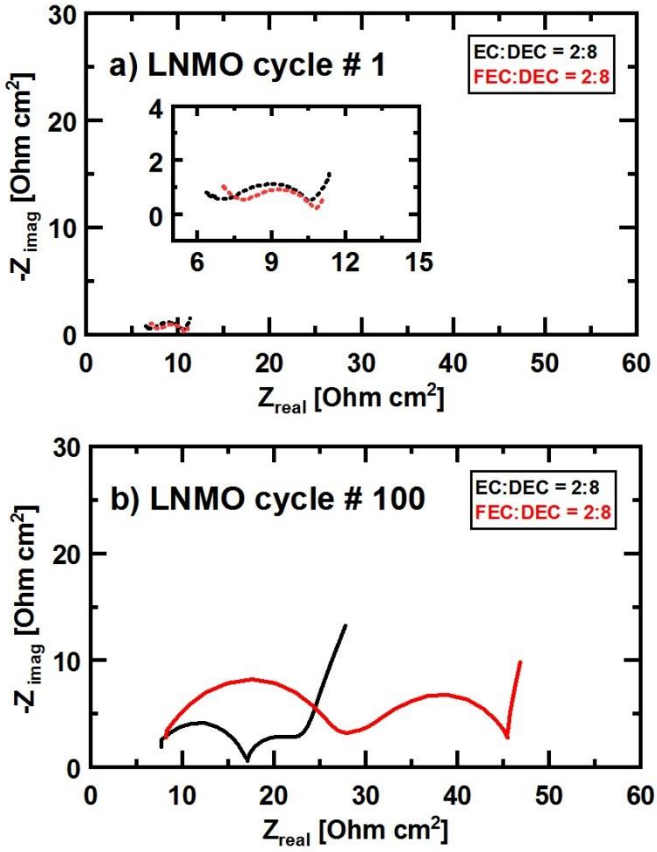

Figure 5. Cathode impedances obtained from graphite//LNMO cells (shown in **Figure 4**) measured with a GWRE after the two formation cycles (a, c) and after 100 charge/discharge cycles (b, d). Impedance was measured at 50% SOC and 25 °C from 100 kHz to 100 mHz with a current amplitude of 0.6 mA. Impedances measured for EC:DEC (2:8 vol.%, 1M $LiPF_6$) are shown in black, impedances measured in FEC:DEC (2:8 vol.%, 1M $LiPF_6$) are shown in red.

The anode impedance after formation is shown in **Figure 6a**. The impedance consists both of charge transfer resistance (R_{CT}) and the resistance of the solid electrolyte interphase (R_{SEI}). The anode resistance after formation (R_{Anode}) is 6 Ωcm² for the EC-based electrolyte and 17 Ωcm² FEC-based electrolyte. The higher initial anode impedance with the FEC-based electrolyte is reasonable as FEC is not only a co-solvent but also an additive which is reduced at higher potentials than EC and could therefore form a more resistive SEI on the anode. After 100 charge/discharge cycles the

resistance of the anode with a FEC-based electrolyte (70 Ωcm²) is substantially higher than the resistance of the cells with EC (50 Ωcm²). Also, at highest frequencies a small semicircle with a diameter of 8 Ωcm² for both cells with EC and FEC electrolyte is observed. This feature was also observed by Pritzl et al.[49] and attributed to an increased resistance between the anode and the separator interphase induced by manganese dissolution. The authors observed the semi-circle only in blocking conditions (absence of a charge transfer process) and not at 50% SOC as measured here. One reason why this contribution to the anode impedance can be observed in the spectra at 50% SOC (this study) could be the fact that here cells are cycled at 45 °C and in the study of Pritzl et al.[49] only at 40 °C. The higher temperature could lead to an enhanced transition metal dissolution.

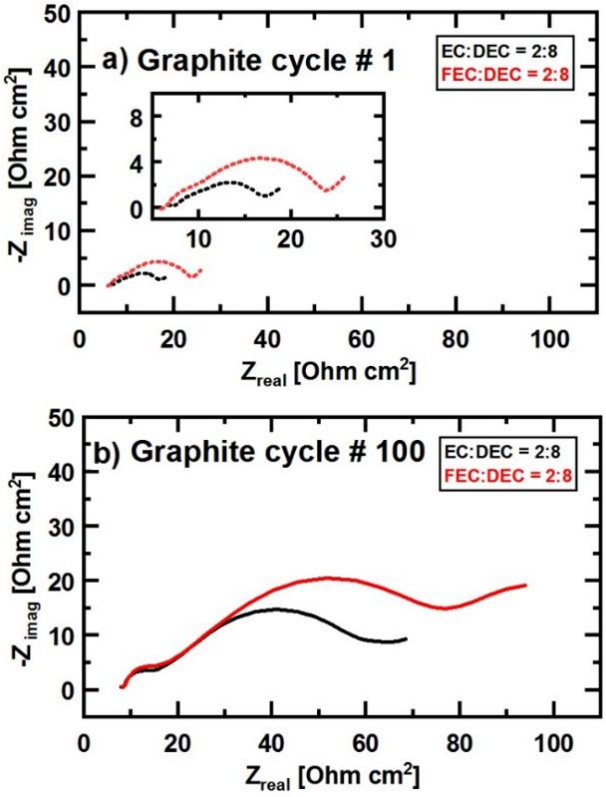

Figure 6. Anode impedances obtained from graphite//LNMO cells (shown in **Figure 4**) measured with a GWRE after the two formation cycles (a, c) and after 100 charge/discharge cycles (b, d). Impedance was measured at 50% SOC and 25 °C from 100 kHz to 100 mHz with a current amplitude of 0.6 mA. Impedances measured for EC:DEC (2:8 vol.%, 1M $LiPF_6$) are shown in black, impedances measured in FEC:DEC (2:8 vol.%, 1M $LiPF_6$) are shown in red.

The higher anode impedance for the cells cycled in FEC can on the one hand be rationalized by the formation of VC (induced by the thermal decomposition of FEC) and such a reduction on the anode, which would increase the interface resistance of the anode. On the other side, the formation of HF upon FEC decomposition could also lead to an increased manganese dissolution. Therefore, the anodes of the T-cells with GWRE were extracted from the cells after the 100th cycle and the amount of dissolved manganese was determined by ICP-MS. The results of these measurements can be seen in **Figure 7**. The amount of manganese on the graphite anode for cells with EC in the

electrolyte equals to 0.012 mg. For cells cycled with FEC as electrolyte the amount of manganese n the anode is 0.018 mg. These results underline the detrimental effect of HF which can the lead to enhanced transition metal dissolution and hence explain a higher anode impedance with cells cycled in an FEC-based electrolyte compared to an EC-based electrolyte at elevated temperatures (45 °C). The nickel content of the cycled graphite anodes was also analyzed and was below the detection limit.

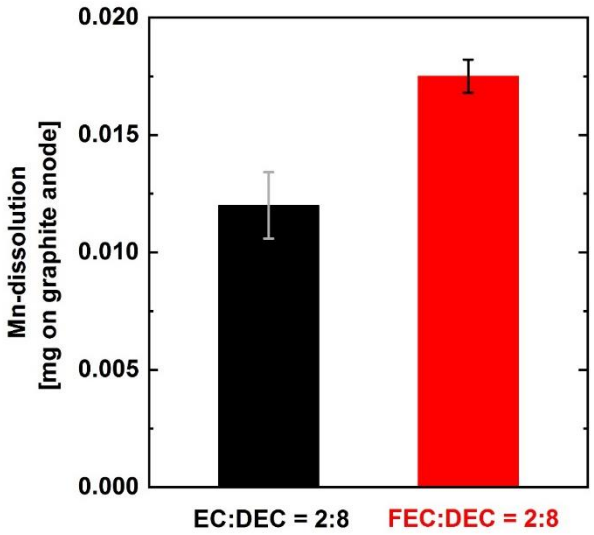

Figure 7. Amount of manganese on the graphite counter electrode was determined by ICP-MS, the anodes were taken from the cells shown in **Figure 4**. The black bar shows the manganese deposited on anodes cycled in EC:DEC (2:8 vol.%, 1M $LiPF_6$), the red bar shows the amount of manganese of anodes cycled in FEC:DEC (2:8 vol.%, 1M $LiPF_6$).

Gas evolution of EC- and FEC-based electrolytes in commercial cells.— In a last step we want to evaluate the gas evolution with EC- and FEC-based electrolytes in 200 mAh pouch cells. Therefore, graphite//LNMO cells were used to investigate the different electrolytes at high voltages (upper cutoff 4.9 V vs. Li^+/Li) and NCM-111//graphite cells were used to investigate the electrolytes at moderate voltages (upper cutoff 4.3 V vs. Li^+/Li). Note: oxygen release for NCM-111 was shown to occur at potentials above 4.5 V vs. Li^+/Li, while for LNMO it has been shown that no oxygen release occurs at all;[23, 50] therefore we do not expect a influence by oxygen release from the cathode materials on these measurements. After formation (see experimental) all cells were degassed to remove the formation gasses and afterwards the gas volume was measured by Archimedes as baseline prior to cycling. Then the cells were cycled for 100 cycles at 45 °C at a 0.5C charge (+1h CV) and a 1C discharge rate, after cycling Archimedes was again measured to obtain the gas volumes shown in **Figure 8**. The cycling performance for the graphite//LNMO cells was similar to the cells shown in **Figure 4** and details for the Archimedes method are reported by Aiken et al.[42]

Figure 8 depicts images of the cycled cells and the gas volumes in mL for the graphite//NCM-111 and the graphite//LNMO cells, containing each a electrolyte mixture composed EC:DEC (2:8 vol.%, 1M $LiPF_6$) or FEC:DEC (2:8 vol.%, 1M $LiPF_6$). For all graphite//NCM-111 cells, as well as for the graphite//LNMO cells with the EC-based electrolyte essentially no gassing was measured during 100 cycles and the values for these cells are within the error bars of the measurement. In stark contrast it is shown that the graphite//LNMO cells with the FEC-based electrolyte show a strong swelling that can be visually seen in the picture of the cell (**Figure 8**) and that was quantified to be ≈5.7 mL. This strong swelling can be rationalized by the formation of VC from FEC (**Scheme 1)** which can then be oxidized to CO_2 starting above 4.3 V vs. Li^+/Li (see **Figure 3**). Therefore, VC can be oxidized in the graphite//LNMO cells (upper

cutoff 4.9 V vs. Li^+/Li), but not in the graphite//NCM-111 cells (upper cutoff 4.3 V vs. Li^+/Li) for which no gassing is observed. The gas volume from the graphite//LNMO cells with FEC-based electrolyte (**Figure 8**) can then be translated into moles:

$$n = \frac{V}{V_m} = \frac{0.0057\ L}{22.4\ \frac{L}{mol}} = 254\ \mu mol \quad (1)$$

GC-MS analysis of the evolved gases from the cells in **Figure 8**, showed that the two main gasses evolved during cycling are CO_2 (35 vol.%) and H_2 (53 vol.%), meaning that 89 µmol CO_2 are evolved during cycling. Assuming a ratio of CO_2:VC of 1:1 upon VC oxidation, as shown by Pritzl et al.[30], the amount of VC that is oxidized during 100 charge/discharge cycles in the cells from **Figure 8** corresponds to 89 µmol. Assuming a VC concentration of 1000 ppm (**Figure 2**) and an electrolyte volume of 700 µL that was used for multi-layer pouch-cell cycling, a volume of 0.7 µL VC in the electrolyte is expected. From this volume the moles of VC expected can be estimated using the molar mass (86.05 g/mol) and the density (1.36 g/cm^3) of VC:

$$n = \frac{\rho V}{M} = \frac{1.36\frac{g}{cm^3}\ 0.0007\ cm^3}{86.05\ \frac{g}{mol}} = 11\ \mu mol \quad (2)$$

Assuming again a ratio of CO_2:VC of 1:1, the effective CO_2 from 1000 ppm VC within the electrolyte would correspond to 11 µmol, which is a factor of 8 lower compared to the 89 µmol measured during cell operation. This discrepancy can be explained by the equilibrium between

FEC and VC, as shown in **Scheme 1**, meaning that once the VC is removed from the solution (in this case by oxidation), new VC will form in this equilibrium and therefore the effective gas evolution can be higher as one would assume from the NMR shown in **Figure 2**. Furthermore, the 53 vol.% H_2 that were determined by the gas-analysis of the multi-layer pouch-cells can be explained by the formation of H^+ upon electrolyte/VC oxidation[30, 38] that can then be reduced on the graphite anode.[38, 51] H_2 could not be determined in the OEMS experiments shown in **Figure 3**, as the two-compartment setup does not allow crosstalk between the anode and the cathode departments, detailed analysis is shown by Metzger et al.[38] Therefore, we have shown that VC oxidation leads to strong gassing in commercial cells that contain high FEC as co-solvent once they are charged to potentials >4.3 V vs. Li^+/Li. This can cause serious issues, such as pressure build-up inside the cell and cell swelling. Furthermore, this is also critical if silicon anodes are paired with high voltage cathode materials, as silicon anodes typically require large excess of FEC.[8]

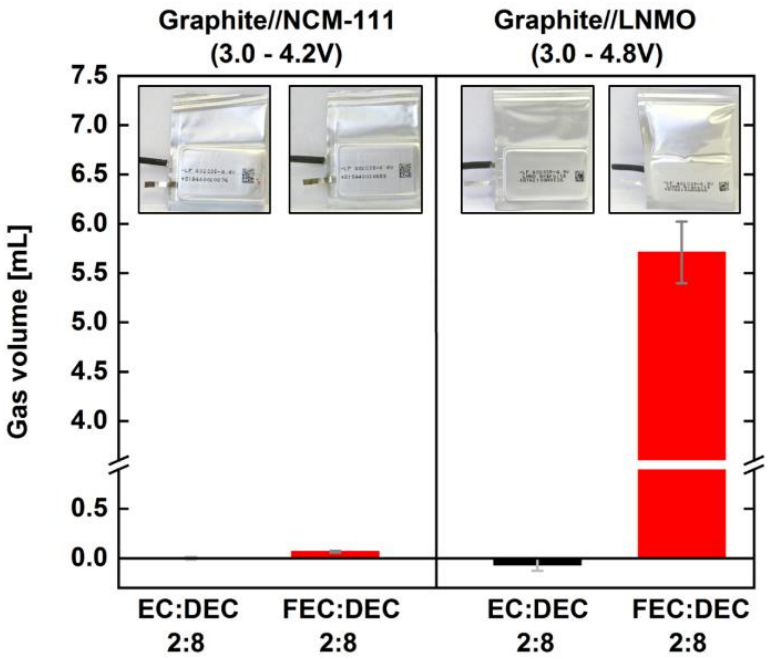

Figure 8. Gas evolution measured by Archimedes method[42] and corresponding images of multi-layer pouch-cells cycled with FEC:DEC (2:8 vol.%, 1M $LiPF_6$) electrolyte and EC:DEC (2:8 vol.%, 1M $LiPF_6$) electrolyte. Graphite//LNMO cells were cycled for 100 cycles between 3.0 and 4.8 V at 45 °C and graphite//NCM-111 cells were

cycled between 3.0 and 4.2 V at 45 °C. For formation the cells were charged to 20% SOC at 25 °C and stored at 60 °C overnight, afterwards the cells were degassed to remove formation gasses and cycled for 100 cycles with 0.5C charge and 1C discharge rate at 45 °C; cells were commercial cells and were obtained from LiFun and each data set consist of at least two cells.

Conclusions

We could show in this study that FEC can react with $LiPF_6$ and thus can lead to thermal instabilities of the electrolyte. The products of this reactions are VC, HF and PF_5, whereas HF can trigger side reactions in the cell, such as transition metal migration and VC is oxidative not stable at potentials above 4.3 V vs. Li^+/Li. By a Swagelok® T-cell equipped with a reference electrode we could prove that for graphite//LNMO cells impedance build-up and manganese migration gets more pronounced in FEC-based electrolytes, compared to the EC-based analogous, while FEC did not improve the cycle life of the graphite//LNMO cells. In the end we used multi-layer pouch-cells with a nominal capacity of 200 mAh to show that FEC-based electrolytes do not only suffer from higher impedances and increased manganese dissolution but also cause serious gassing issues when they are cycled at 45 °C to high potentials. Furthermore, we could prove that FEC has no advantage when cycled to high voltages with cathodes that do not release oxygen.

Acknowledgement

This work was supported by BASF SE within its BASF SE Battery Research Network. The authors want gratefully acknowledge Anna Freiberg for the very fruitful discussions.

Literature

1. M. M. Thackeray, C. Wolverton, and E. D. Isaacs, *Energ. Environ. Sci.*, **5** (7), 7854 (2012).
2. J. B. Goodenough and K. S. Park, *J. Am. Chem. Soc.*, **135** (4), 1167-1176 (2013).
3. J. B. Goodenough and Y. Kim, *Chem. Mater.*, **22** (3), 587-603 (2010).
4. K. Xu, *Chem. Rev.*, **114** (23), 11503-11618 (2014).
5. E. Peled, *J. Electrochem. Soc.*, **126** (12), 2047-2051 (1979).
6. I. A. Shkrob, J. F. Wishart, and D. P. Abraham, *J. Phys. Chem. C*, **119** (27), 14954-14964 (2015).
7. M. Nie, J. Demeaux, B. T. Young, D. R. Heskett, Y. Chen, A. Bose, J. C. Woicik, and B. L. Lucht, *J. Electrochem. Soc.*, **162** (13), A7008-A7014 (2015).
8. R. Jung, M. Metzger, D. Haering, S. Solchenbach, C. Marino, N. Tsiouvaras, C. Stinner, and H. A. Gasteiger, *J. Electrochem. Soc.*, **163** (8), A1705-A1716 (2016).
9. C. Xu, F. Lindgren, B. Philippe, M. Gorgoi, F. Björefors, K. Edström, and T. Gustafsson, *Chem. Mater.*, **27** (7), 2591-2599 (2015).
10. R. Petibon, V. L. Chevrier, C. P. Aiken, D. S. Hall, S. R. Hyatt, R. Shunmugasundaram, and J. R. Dahn, *J. Electrochem. Soc.*, **163** (7), A1146-A1156 (2016).
11. E. Markevich, G. Salitra, Y. Talyosef, U.-H. Kim, H.-H. Ryu, Y.-K. Sun, and D. Aurbach, *ACS Appl. Energy Mater.*, **1** (6), 2600-2607 (2018).

12. E. Markevich, G. Salitra, P. Hartmann, J. Kulisch, D. Aurbach, K.-J. Park, C. S. Yoon, and Y.-K. Sun, *J. Electrochem. Soc.,* **166** (3), A5265-A5274 (2019).

13. J. Xia, M. Nie, J. C. Burns, A. Xiao, W. M. Lamanna, and J. R. Dahn, *J. Power Sources*, **307** 340-350 (2016).

14. J. Xia, K. J. Nelson, Z. Lu, and J. R. Dahn, *J. Power Sources*, **329** 387-397 (2016).

15. J. Xia, R. Petibon, D. Xiong, L. Ma, and J. R. Dahn, *J. Power Sources,* **328** 124-135 (2016).

16. M. He, C.-C. Su, Z. Feng, L. Zeng, T. Wu, M. J. Bedzyk, P. Fenter, Y. Wang, and Z. Zhang, *Adv. Energy Mater.,* **7** (15), 1700109 (2017).

17. L. Hu, Z. Zhang, and K. Amine, *Electrochem. Commun.*, **35** 76-79 (2013).

18. L. Hu, Z. Xue, K. Amine, and Z. Zhang, *J. Electrochem. Soc.,* **161** (12), A1777-A1781 (2014).

19. E. Markevich, G. Salitra, K. Fridman, R. Sharabi, G. Gershinsky, A. Garsuch, G. Semrau, M. A. Schmidt, and D. Aurbach, *Langmuir*, **30** (25), 7414-7424 (2014).

20. D. Liu, K. Qian, Y.-B. He, D. Luo, H. Li, M. Wu, F. Kang, and B. Li, *Electrochimica Acta*, **269** 378-387 (2018).

21. B. Aktekin, R. Younesi, W. Zipprich, C. Tengstedt, D. Brandell, and K. Edström, *J. Electrochem. Soc.*, **164** (4), A942-A948 (2017).

22. R. Jung, M. Metzger, F. Maglia, C. Stinner, and H. A. Gasteiger, *J. Electrochem. Soc.,* **164** (7), A1361-A1377 (2017).

23. R. Jung, M. Metzger, F. Maglia, C. Stinner, and H. A. Gasteiger, *J. Phys. Chem. Lett.*, **8** (19), 4820-4825 (2017).

24. J. Wandt, A. T. S. Freiberg, A. Ogrodnik, and H. A. Gasteiger, *materials today,***21**, 825 (2018).

25. A. T. S. Freiberg, M. K. Roos, J. Wandt, R. de Vivie-Riedle, and H. A. Gasteiger, *J. Phys. Chem. A,* **122** (45), 8828-8839 (2018).

26. T. M. Østergaard, L. Giordano, I. E. Castelli, F. Maglia, B. K. Antonopoulos, Y. Shao-Horn, and J. Rossmeisl, *J. Phys. Chem. C,* **122** (19), 10442-10449 (2018).

27. Y. Yu, P. Karayaylali, Y. Katayama, L. Giordano, M. Gauthier, F. Maglia, R. Jung, I. Lund, and Y. Shao-Horn, *J. Phys. Chem. C,* **122** (48), 27368-27382 (2018).

28. T. Teufl, D. Pritzl, P. Krieg, B. Strehle, M. Mendez, and H. A. Gasteiger, *manuscript in preparation.*

29. D. Pritzl, S. Solchenbach, and H. A. Gasteiger, *Meeting Abstracts,* **MA2016-02** (4), 567 (2016).

30. D. Pritzl, S. Solchenbach, M. Wetjen, and H. A. Gasteiger, *J. Electrochem. Soc.,* **164** (12), A2625-A2635 (2017).

31. S. Solchenbach, M. Metzger, and H. A. Gasteiger, *Meeting Abstracts*, **MA2015-02** (5), 362 (2015).

32. K. Kim, I. Park, S.-Y. Ha, Y. Kim, M.-H. Woo, M.-H. Jeong, W. C. Shin, M. Ue, S. Y. Hong, and N.-S. Choi, *Electrochimica Acta,* **225** 358-368 (2017).

33. D. J. Xiong, L. D. Ellis, R. Petibon, T. Hynes, Q. Q. Liu, and J. R. Dahn, *J. Electrochem. Soc.,* **164** (2), A340-A347 (2017).

34. D. Y. Wang, N. N. Sinha, J. C. Burns, C. P. Aiken, R. Petibon, and J. R. Dahn, *J. Electrochem. Soc.,* **161** (4), A467-A472 (2014).

35. D. Streich, A. Guéguen, M. Mendez, F. Chesneau, P. Novák, and E. J. Berg, *J. Electrochem. Soc.,* **163** (6), A964-A970 (2016).

36. A. Guéguen, D. Streich, M. He, M. Mendez, F. F. Chesneau, P. Novák, and E. J. Berg, *J. Electrochem. Soc.,* **163** (6), A1095-A1100 (2016).

37. N. Tsiouvaras, S. Meini, I. Buchberger, and H. A. Gasteiger, *J. Electrochem. Soc.*, **160** (3), A471-A477 (2013).

38. M. Metzger, B. Strehle, S. Solchenbach, and H. A. Gasteiger, *J. Electrochem. Soc.*, **163** (5), A798-A809 (2016).

39. M. Metzger, B. Strehle, S. Solchenbach, and H. A. Gasteiger, *J. Electrochem. Soc.*, **163** (7), A1219-A1225 (2016).

40. S. Solchenbach, M. Metzger, M. Egawa, H. Beyer, and H. A. Gasteiger, *J. Electrochem. Soc.*, **165** (13), A3022-A3028 (2018).

41. S. Solchenbach, D. Pritzl, E. J. Y. Kong, J. Landesfeind, and H. A. Gasteiger, *J. Electrochem. Soc.*, **163** (10), A2265-A2272 (2016).

42. C. P. Aiken, J. Xia, D. Y. Wang, D. A. Stevens, S. Trussler, and J. R. Dahn, *J. Electrochem. Soc.*, **161** (10), A1548-A1554 (2014).

43. M. Pyschik, M. Winter, and S. Nowak, *Separations*, **4** (3), (2017).

44. V. Kraft, W. Weber, M. Grützke, M. Winter, and S. Nowak, *RSC Adv.*, **5** (98), 80150-80157 (2015).

45. M. Kobayashi, T. Inoguchi, T. Iida, T. Tanioka, H. Kumase, and Y. Fukai, *J. Flu. Chem.*, **120** (2), 105-110 (2003).

46. H.-H. Lee, Y.-Y. Wang, C.-C. Wan, M.-H. Yang, H.-C. Wu, and D.-T. Shieh, *J. Appl. Electrochem.*, **35** (6), 615-623 (2005).

47. J. Landesfeind, D. Pritzl, and H. A. Gasteiger, *J. Electrochem. Soc.*, **164** (7), A1773-A1783 (2017).

48. D. Pritzl, A. Bumberger, M. Wetjen, J. Landesfeind, S. Solchenbach, and H. Gasteiger, *J. Electrochem. Soc.*, **166** (4), A582-A590 (2019).

49. D. Pritzl, J. Landesfeind, S. Solchenbach, and H. A. Gasteiger, *J. Electrochem. Soc.*, **165** (10), A2145-A2153 (2018).

50. B. Strehle, K. Kleiner, R. Jung, F. Chesneau, M. Mendez, H. A. Gasteiger, and M. Piana, *J. Electrochem. Soc.*, **164** (2), A400-A406 (2017).

51. R. Bernhard, M. Metzger, and H. A. Gasteiger, *J. Electrochem. Soc.*, **162** (10), A1984-A1989 (2015).

3.3. Path forward: mitigating oxygen release by washing of nickel-rich layered oxides with pure water

This section presents the manuscript "Washing of nickel-rich cathode materials for lithium-ion batteries – Towards a mechanistic understanding". It will soon be submitted to a peer-reviewed journal for publication. The manuscript was presented by Daniel Pritzl at the 234th Meeting of the Electrochemical Society (September 30th – October 4th, 2018) in Cancun, Mexico (Abstract Number: 234).

Ni-rich cathode materials are very sensitive towards moisture and tend to the formation of surface hydroxides and carbonates.[65, 67] These surface impurities are critical, as they can lead to gelling of the slurry during electrode preparation[56] and to reactions with the electrolyte which leads to gassing and capacity loss during full-cell operation.[56, 67, 68] As a very simple and practical solution, cell manufacturers include an aqueous washing step to remove these surface impurities.[56, 139] It is shown in the literature that such a washing step can reduce LiOH and Li_2CO_3 impurities on the cathode surface[140, 141] and can therefore prevent gelling[140] and significantly lower the gassing during cell operation.[142] However, there is still a lack of understanding if and how washing affects the surface of the nickel-rich cathode material. So far, it is also not totally understood why some researcher claim an improved performance after washing,[140] while others show that it leads to the formation of resistive surface layers and to poor capacity retention.[56, 141]

The purpose of this study is to gain an in-depth understanding of the underlying mechanisms occurring during aqueous washing of Ni-rich cathode materials, and the implications for the handling of those materials. To this purpose, we analyze the washed cathode active material and the washing solution examining two consecutive washing steps. These experiments are carried out under argon in order to exclude any exposure to ambient atmosphere. Surprisingly, LiOH can still be detected during the second washing step, while Li_2CO_3 can be removed completely by a single washing step. This results suggests a Li/H^+ exchange from the Ni-rich cathode material in aqueous solution. By TGA-MS analysis of a washed Ni-rich NCM material we show that the Li/H^+ exchange causes an instable surface

phase during drying, which leads to a spinel (80 - 250°C) or a rocksalt surface structure (>250°C), depending on the drying temperature. As very encouraging and exciting result, we can show that the formation of these surface layers can substantially suppress and even prevent further oxygen release from the cathode material during electrochemical cycling. However, for the conditions used in this study we show that these surface layers also cause a high impedance build-up and lead to an overall deterioration of the cycling performance. These results give a clear understanding about the underlying reactions during the washing of nickel-rich cathode material and present a valuable foundation for the optimization of such washing procedures.

In particular, these results are very encouraging, as it has been shown by Jung et al.[55] that oxygen release for nickel-rich cathode materials limits the upper cutoff potential and thus the extractable capacities. With this study, we open a new pathway towards the design of Ni-rich cathode materials, based on a natively grown and a stabilized surface layer that does not release oxygen during operation. Furthermore, in view of the critical role of oxygen release in Li- and Mn-rich layered oxides discussed in the previous section of this thesis, a similar strategy may also be possible to mitigate the oxygen release from Li- and Mn-rich layered oxides.

Author contributions

The materials were washed by T.T. and D.P. OEMS was carried out by T.T. D.P. and A.T.F.S. and XPS was measured by D.P. Impedance and TGA-MS was measured by D.P. and the mechanism was suggested by J.S., D.P., T.T. and H.A.G. All authors discussed the data and T.T. and D.P. wrote the manuscript and H.A.G edited the manuscript.

Washing of nickel-rich cathode materials for lithium-ion batteries – Towards a mechanistic understanding

Daniel Pritzl [a, #, =], Tobias Teufl [a, b, =], Anna T. S. Freiberg [a], Benjamin Strehle [a], Johannes Sicklinger [a], Heino Sommer [b], Pascal Hartmann [b] and Hubert A. Gasteiger [b]

[a]*Chair of Technical Electrochemistry, Department of Chemistry and Catalysis Research Center, Technical University of Munich, D-85748 Garching, Germany*

[b]*BASF SE Ludwigshafen, New Battery Materials and Systems, D-67056 Ludwigshafen, Germany*

[#]corresponding author

[=]equal contribution

Abstract

Washing is a commonly used method to remove surface impurities of cathode active materials for lithium-ion batteries. However, a clear mechanistic understanding of the washing process has not yet been provided in the literature. In this study, we will investigate the effect of washing of nickel-rich NCM cathodes (85% nickel) with respect to its effect on gassing and impedance build-up. By on-line electrochemical mass spectrometry (OEMS), we will show a drastic reduction of the O_2 release above 80% SOC for a sample washed in water, suggesting that the washing and/or drying process leads to the formation of a more stable surface layer. The modification of the surface can be confirmed by a strong impedance increase of the washed cathode active material measured via a µ-reference electrode in a full-cell. Last, we will propose a comprehensive mechanism about the washing process of nickel-rich NCM materials and identify the drying temperature after washing as the dominant factor influencing the surface properties.

Introduction

Lithium-ion batteries are considered as a viable option for energy storage in electric vehicles (EV's). In order to reach the goal of a widespread application in electrical vehicles, many obstacles have to be overcome with respect to cost, driving range and charging times.[1, 2] The most critical factor for an increase in energy density (and hence an increase in driving range) for future Li-ion batteries is the capacity of the cathode active material (CAM).[2] One of the most promising class of cathode materials therefor are the so called NCM and NCA materials, both having a layered structure with the sum formula $LiMeO_2$ (Me = Ni, Co, Mn for NCM and Me = Ni, Co, Al for NCA). In state of the art vehicles mid nickel NCM-523 (Ni:Co:Mn = 5:2:3) cathodes are already used,[3] showing good structural stability during lithium extraction/insertion and reasonable capacities of ≈160mAh/g.[3] However, to increase the specific capacity with acceptable upper cutoff voltages, recent trends tend to increasing nickel contents, leading to nickel rich NCMs (Ni:Co:Mn ≥ 8:1:1).[4] These nickel-rich materials can lead to reversible capacities of up to ≈180 mAh/g at reasonable cutoff potentials (4.2 V vs. graphite). For these high nickel materials not only manganese can be used to stabilize the structure,[5] but it can also be replaced by aluminum leading to nickel-rich NCA, which Tesla had been using for many years.[3]

However, the increasing capacity of nickel-rich materials comes at the cost of faster capacity fading and higher sensitivity towards storage and cycling conditions.[6, 7] It turned out that Ni-rich materials are very sensitive toward storage under humidity and CO_2 containing atmospheres,[6-9] leading to the formation of large amounts of hydroxides and carbonates on the surface of the particles.[10-16] These surface impurities do not only lead to a deterioration of the capacity retention,[6, 8, 9] but also cause high gas evolution in commercial cells[8, 17-20] and lead to a high pH causing gelation of the slurry during electrode preparation.[21, 22] As a very simple and practical solution to remove surface contaminants most cell and material manufacturer included

a washing step in which the active material is washed in an aqueous solution.[22, 23] This washing step can significantly lower the pH value of the slurry[22, 24] and can thus prevent gelation during the electrode coating process. Kim et al.[25] have also shown that washing of nickel-rich cathodes can efficiently prevent gas evolution during high temperature storage experiments. It has been initially suggested that washing of NCA simply removes carbonate and hydroxide impurities from the cathode material surface and therefore improves the material properties[24] whereas other reports suggest also a reaction with the active material itself.[22, 26] While washing of NCA powder significantly improves the cycling stability at room temperature and C-rates as low as C/5,[24] there is clear evidence that washing of NCA has a negative effect on the 45 °C cycle performance at 1C discharge,[22] pointing towards a thermal instable surface which in consequence leads to the formation of a resistive surface layer.[26] On the other hand, heat treatment of the washed samples could show that a recalcination at 700 °C can regain the initial surface structure and thus recover the electrochemical performance after removal of the surface impurities.[26] While it seems obvious that a NCM surface without any hydroxides or carbonates should perform best, it turned out that synthesis of an entirely virgin surface shows poor electrochemistry and a certain exposure to ambient conditions is required for a sufficient surface termination.[11] In this respect, it has been shown that nickel-rich NCMs strongly tend to the formation of a spinel type structure at SOCs > 80%, induced by oxygen release,[27, 28] leading to chemical electrolyte oxidation[29] and a high impedance build-up,[27] following a similar mechanism thatw as described for Li- and Mn-rich NCMs.[30] At the moment many different surface stabilizations strategies are under investigation to stabilize the surface of nickel-rich layered cathode materials, such as surface sulfatation,[31] recalcination after storage,[8, 9, 32] as well as surface coatings with spinel structures[33] or core-shell particles.[34] Considering the results by Paulsen et al.[11], we suggest that washing of nickel-rich materials does not only remove the surface impurities but also induces a significant reaction with the active material surface, e.g. by lithium proton exchange that has been suggested from literature.[9, 35, 36] While washing of

nickel-rich cathode materials is a well-known industrial process and is already implemented by most of the battery manufacturers there is still a significant lack of scientific literature providing a profound understanding about the exact mechanism and the effect of these washing procedures. Therefore, we think that a detailed understanding of the washing process can open a new path towards surface modification strategies of nickel-rich cathode materials.

In this study we will examine the reactions that occur during the washing of nickel-rich cathode materials in deionized water and its effect onto the electrochemistry and the gas evolution. These studies will be conducted with a Ni-rich material, having the sum formula $LiNi_{0.85}Co_{0.10}Mn_{0.05}O_2$, also referred to as NCM 851005. For this study, we measured the pH during washing, as well as the LiOH and Li_2CO_3 contents of the wash solution. By on-line electrochemical mass spectrometry (OEMS) we could prove that washing has a significant influence on the oxygen release and the gas evolution of the material which can be rationalized by the formation of an oxygen deficient surface layer during the drying step. While washing can prevent oxygen release and can remove hydroxide and carbonate impurities from the surface, we can clearly show by impedance and OEMS that the drying temperature influences the properties of the newly formed interface. Thus, we prove that washing of nickel-rich materials not only removes the surface impurities but also strongly reacts with the materials surface and therefore needs to be analyzed in detail in order to stabilize nickel-rich cathode materials.

Experimental

Washing process of NCM851005 powder — For the washing process, deionized water (18 MΩcm, Merck KGaA, Germany) was used. 20 g of NCM851005 were given into 100 mL of purified water and stirred for 20 minutes. The solution was then filtered, and the washed material dried in a vacuum oven for at least 4h (either at 25 °C or 65 °C, see Table 1). The once washed material was then washed again (20 g material in 100 g of purified water) and the suspension was filtered again. In both wash solutions (from the first and second washing), the concentration of LiOH and Li_2CO_3 were determined by titration with HCl. The pH-measurements and the titration experiments were carried out in an argon atmosphere. All other experiments conducted in ambient air. The material after the second washing was dried for 12h with four different drying conditions: 80 °C, 180 °C and 300 °C in a vacuum oven and one sample was freeze dried and used for further analysis. The freeze drying was carried out in a vessel with washed material, which was put into liquid nitrogen and dynamic vacuum was applied for 12h. The detailed drying conditions of all used materials with water to CAM ratio, atmosphere, drying temperature between first and second washing and final drying temperature are listed in Table 1.

Table 1: Summarized information about the washing procedure with information about the experiment, water to CAM ratio, atmosphere and drying temperatures (under dynamic vacuum).

NCM powder	H_2O/CAM ratio	Atmosphere (washing)	Drying temperature between 1. and 2. Washing in vacuum	Final drying temperature
Pristine	---	air	---	120 °C (12h)
25 °C sample	5/1	air	25 °C for 4h	Freeze dry, 25 °C (12h)
80 °C sample	5/1	air	65 °C for 4h	80 °C (12h)
180 °C sample	5/1	air	65 °C for 4h	180 °C (12h)
300 °C sample	5/1	air	65 °C for 4h	300 °C (12h)

Electrode preparation **—** Electrodes for OEMS measurements were prepared by dispersing 96 wt.% $LiNi_{0.85}Co_{0.10}Mn_{0.5}O_2$ (NCM851005) (BASF SE, Germany), 2 wt.% conductive carbon (Super-C65, Timcal, Switzerland), and 2 wt.% polyvinylene difluoride PVDF binder (Kynar HSV 900, Arkema, France) in N-methyl-2-pyrrolidone NMP (anhydrous, Sigma-Aldrich, USA). A high solid content of 70% for the slurry was chosen to enable coating onto a porous stainless-steel mesh (SS316, aperture 26 μm, wire diameter 25 μm, The Mesh Company Ltd., UK). The slurry was mixed in a planetry mixer (Thinky Corp.) for 10 min. and coated onto the stainless-steel mesh, yielding a NCM loading of ≈12 mg/cm^2, corresponding to ≈3.3 mAh/cm^2 (based on a theoretical capacity of 275 mAh/g for 100% delithiation). Electrodes for OEMS experiments were punched out with a diameter of 15 mm.

For impedance measurements, NCM851005 electrodes were prepared by mixing $LiNi_{0.85}Co_{0.10}Mn_{0.5}O_2$ (NCM851005) (commercial, BASF SE, Germany), carbon black (Super C65, Timcal), and polyvinylene difluoride (PVDF, Kynar) at a mass ratio of 96/2/2 with NMP

(N-methyl pyrrolidone, anhydrous, Sigma-Aldrich, Germany) in a planetary mixer (Thinky Corp.) for 15 min. The ink was coated onto aluminum foil (MTI, 18 µm) with a doctor blade coater and dried afterwards at 50 °C in a convection oven for at least 3h. The final NCM851005 coating had a loading of ≈9 mg_{NCM}/cm^2, corresponding to ≈2 mAh/cm^2 (based on a first charge capacity of 215 mAh/g at 4.2 V cell cut-off). In this specific case, the theoretical capacity was defined by the first charge capacity in order to guarantee sufficient full-cell balancing. Electrodes with a diameter of 11 mm (≡0.95 cm^2) were punched out and compressed to ≈30% porosity with a KBr press.

Graphite electrodes were prepared by mixing graphite (commercial, T311, SGL Carbon, Germany) and PVdF at a mass ratio of 95/5 with NMP by applying the same procedure as for the positive electrodes. The graphite ink was coated onto copper foil (MTI, 12 µm) and dried in a convection oven at 50 °C for 3 h. The loading of the graphite coating was ≈6 $mg_{graphite}/cm^2$ corresponding to ≈2.05 mAh/cm^2 (based on a specific capacity of 340 mAh/g). The electrodes were punched out with a diameter of 11 mm and compressed to a porosity of ≈30%. All anodes were dried under dynamic vacuum at 120 °C. The cathodes were dried at 25 °C (for the freeze dried material), at 80 °C (for the CAM which was dried at 80 °C prior to coating, see Table 1) and all other cathodes at 120 °C for at least 12 h in a vacuum oven (Büchi, Switzerland) and then transferred into an Argon-filled glovebox (MBraun, Germany) without exposure to air.

On-line electrochemical mass spectrometry (OEMS) **—** For OEMS experiments, electrodes coated onto a stainless-steel mesh (see above) were used to have a porous medium as current collector in order to allow fast diffusion of evolved gases from the electrode to the capillary.[37] For OEMS measurements a custom-made one-compartment cell is used; the cell design as well as the OEMS setup were reported previously.[38] OEMS cells were assembled with a lithium metal counter electrode, one glassfiber separator (200 µm thickness, VWR, Germany), a NCM

working electrode and 120 µl of electrolyte composed of EC-only with 1.5M $LiPF_6$ (BASF SE, Germany). The cells were connected to the mass spectrometer, held for 4 h at OCV (open circuit voltage), and then charged to 5.0 V vs. Li^+/Li at a C/10 rate (C-rates here are calculated based on a nominal capacity of 275 mAh/g). For quantification of the mass spectrometer currents, a calibration gas containing O_2 and CO_2, (each 2000 ppm) in Argon (Linde AG, Germany) was used. All currents were normalized to the current at m/z = 36 (Ar isotope) in order to correct for effects of minor pressure and temperature deviations. The currents m/z = 32 (O_2) and m/z = 44 (CO_2) were converted into gas concentration.

Modified OEMS setup for water addition to NCM powder — The above described setup was modified in order to add a defined amount of water to an NCM851005 powder. Consequently, the OEMS cell was replaced by a Swagelok T-fitting, which was connected to the MS system. The other two openings of the Swagelok fitting were equipped with a septum in order to introduce water with a syringe and with a standard closed nut where 0.5 g NCM851005 powder was added. After a 40 minutes rest phase, a syringe with argon from the glovebox was added to the system in order to check for the tightness of the septum. After 60 minutes of recording the mass traces of O_2, H_2O and N_2, 2.5 mL of purified water were dozed to the NCM powder and the mass traces were further recorded.

Electrochemical Impedance Spectroscopy (EIS) **and charge/discharge cycling —** The impedance of the cathode was measured with a gold wire reference electrode (GWRE) as reported in an earlier publication.[39] Before measuring the impedance, two formation cycles of the graphite/NCM851005 cells were carried out at 25 °C in the voltage range of 4.2 V – 3.0 V Cell Voltage. The charging protocol consisted of a constant current constant voltage (CCCV) charge with a cut-off for the CV phase of C/20. The discharge was carried out in CC mode.

After formation, the cells were charged to 50% SOC by a 5h charge with C/10 based on the second discharge capacity. After 1h of a rest phase, the impedance was recorded in potentiostatic mode from 100 kHz to 100 mHz with a perturbation of 10 mV. Afterwards charge discharge cycling was carried out with a CCCV charge to 4.2 V with C/2 and a CC discharge to 3.0 V with 1C at 25 °C for 198 cycles.

X-ray photoelectron spectroscopy (XPS) **—** Surface analysis of the pristine and 2x washed sample (dried at 180 °C) was carried out by X-ray photoelectron spectroscopy (Axis, Supra, Kratos, UK). The powders were pressed to pellets inside an argon-filled glovebox and mounted on an electrically insulated sample holder, which can be transferred from the glovebox into the XPS system without any air exposure. The sample was kept in the pre-antechamber until a pressure of $\approx 10^{-8}$ Torr and was then transferred to the sample analysis chamber (SAC) where the pressure was always kept below $\approx 10^{-9}$ Torr during the whole measurement period. Sample irradiation was carried out with a monochromated Al Kα radiation (1486.6 eV) with an emission current of 15 mA. Survey spectra were recorded for all samples with a stepsize of 0.5 eV and at a pass energy (PE) 160 eV. Elemental spectra were recorded with a stepsize of 0.2 eV and an emission current of 15 mA. For all measurements, a charge neutralizer was used, and the spectra were calibrated to the adventitious carbon peak with a binding energy (BE) of 284.8 eV.

Thermogravimetric Analysis with coupled Mass Spectrometry (TGA-MS) — For TGA-MS analysis a TGA system (Mettler Toledo, Switzerland) coupled to a mass spectrometer (Pfeiffer Vacuum, Germany) was used. All samples analyzed by TGA-MS were dried in a vacuum oven (Büchi, Switzerland) for at least 3 h at 120 °C under dynamic vacuum. The as dried samples, washed twice in water and the pristine NCM851005 were analyzed with the

following protocol: First a conditioning at 25 °C for 10 minutes with an argon flow rate of 200 mL/min. Afterwards the flow rate was changed to 20 mL/min and again a rest phase of 10 minutes at 25 °C was carried out. Then the temperature was increased from 25 °C to 120 °C at 10 K/min. Here, the temperature was held for 40 minutes. The last step includes a heat ramp (10 K/min) to 450 °C with a hold phase of 50 minutes. All mass traces from the MS were normalized to the nitrogen signal (m/z = 28).

Results

Li_2CO_3 & LiOH concentration and pH-value of NCM851005 in water — For the washing process, the cathode material NCM851005 was selected as it is known that the formation of surface contaminants, such as LiOH and Li_2CO_3, is most crucial for nickel-rich materials.[9, 21] For the determination of LiOH and Li_2CO_3, the washing process is carried out in an argon-filled glovebox in order to exclude any effects of CO_2 from the air. 20 g of NCM851005 are dissolved in a solution of 100 mL degassed water and stirred for 20 minutes (referred to as "First Washing"). Afterwards the wash solution is filtered, and the powder is then stored in a drying oven at 65 °C for at least 4h. After that, the powder is washed again in 100 mL of water for 20 minutes (referred to as " Second Washing").

The lithium carbonate content is determined by titration and shown in Figure 1. After the first washing, the amount of lithium carbonate is found to be ≈6.4 ± 0.2 mg Li_2CO_3 per gram NCM (red bar). This would correspond to 6450 ppm of Li_2CO_3 on the surface of the active material which compares well with the high carbonate impurities reported by Noh et al.[21] who found roughly 15000 ppm on their 85% nickel containing NCM material. The differences in ppm might be found in the specific storage conditions and surface areas of the materials, which are

different for each research group. After the first washing, the material is dried in a vacuum oven in the glovebox and then washed again in the glovebox. Interestingly, no more lithium carbonate can be detected in the wash solution after the second washing. The absence of lithium carbonate in the second wash solution can easily be rationalized by the low values of CO_2 in the glovebox, the high solubility of Li_2CO_3 in the washing water, the long washing time and the high water/CAM ratio.

The LiOH content is also determined by titration and the amount after washing the material once is shown in Figure 1. After the first washing ≈4.6 ± 0.35 mg LiOH (0.19 $mmol_{LiOH}$) per gram NCM (1 g_{NCM} = 10.26 $mmol_{NCM}$) (red bar) are found in the wash solution. This corresponds to an amount of LiOH on the cathode active material of ≈4600 ppm. Noh et al.[21] also determined the amounts of LiOH on an 85% nickel containing NCM and found ≈11000 ppm on their material showing that our levels are reasonably high. Generally, one expects that after washing the material once, no more or only little amounts of LiOH from surface impurities should be found in the wash solution as also all Li_2CO_3 has been washed away under these conditions. However, when we analyze the second wash solution we still find ≈2.8 ± 0.15 mg LiOH (0.12 $mmol_{LiOH}$) per gram NCM wash solution (black bar). This would correspond to a LiOH amount on the cathode material of ≈2800 ppm. We think that this amount cannot stem form impurities, which are still left on the surface of the cathode material and the origin of the large amounts of LiOH in the wash solution must be caused by a different mechanism. In order to translate the LiOH concentration from Figure 1 into a molar lithium loss, the molar ratios of lithium loss and lithium in the NCM material have to be taken into account. After washing the sample twice ≈ 0.31 mmol Li^+ were found in the wash solutions as LiOH, which stems from 10.26 mmol NCM (data in Figure 1 are normalized to 1g). Therefore, the mol.% of Li^+ loss from the structure can be calculated:

$$\frac{n_{Li+}}{n_{NCM}} = \frac{0.31\ \text{mmol}}{10.26\ \text{mmol}} = 3\ \text{mol.\%} \quad (1)$$

This means that during the two washing steps in total 3 mol.% of lithium are dissolved from the NCM material; this value will be used for further calculations during the discussions section.

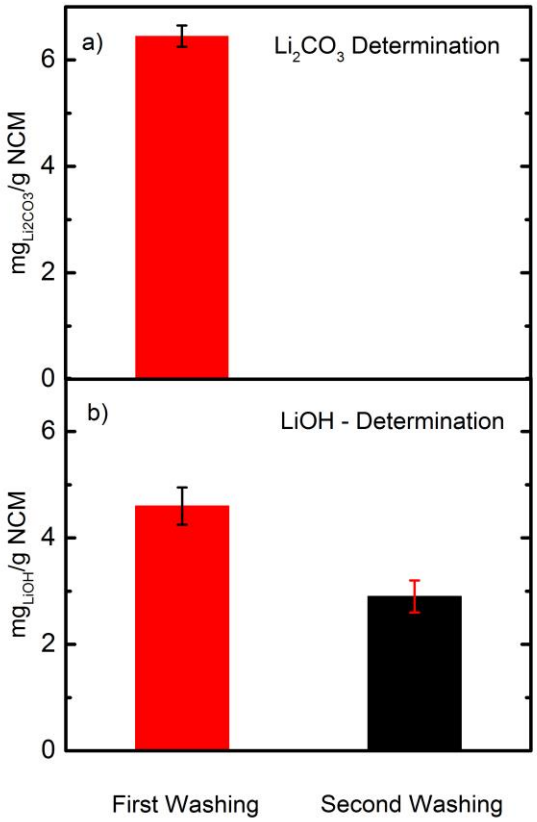

Figure 1: a) Li_2CO_3 & b) LiOH amounts of 20 g NCM851005 powder washed in 100 mL degassed water for 20 minutes under argon atmosphere. The carbonate and hydroxide amounts are determined by titration with HCL. The material was washed once and then the titration was carried out of the wash solution and is referred to as "First Washing". After that, the powder was dried in a vacuum oven in the glovebox at 65 °C for at least 4h. The as-dried powder was then washed again and the wash solution is used for titration and the amounts are referred to as "Second Washing". The error bars show the deviation of three repeat measurements.

In order to understand the behavior of LiOH found in both wash solutions we recorded the pH-value during the first and second washing under argon over the course of 20 minutes, which is identical to the washing experiment (20 g NCM in 100 g water). The results are shown in Figure **2**. By adding NCM851005 to the wash solution for the first time (open round symbols) the pH-value immediately jumps to a value of ≈11.3. After ten minutes, the pH is ≈12.1 and after 20 minutes, the pH saturates with a value of ≈12.2. When the once washed and afterwards dried material is washed again (square symbols), the pH again immediately jumps to a very high value of 11.1. After ten minutes, the pH is 11.5 and after 20 minutes, the pH-value saturates at a value of 11.6. Interestingly, when the materials are put into water a sudden pH jump occurs both for the first- and for the second washing. This implies a fast-chemical reaction must happen which is then controlled via diffusion. Please note that the plateaus observed are caused by the sensitivity of the pH meter of 0.1 pH.

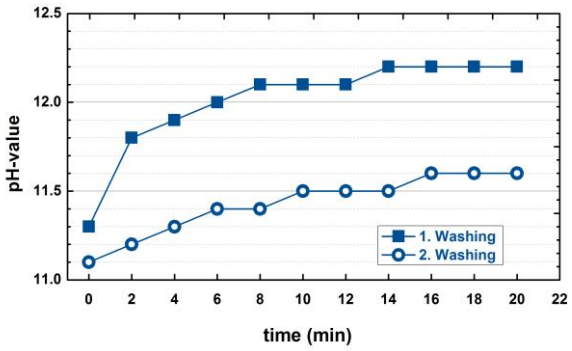

Figure 2: pH-value over time of 20 g NCM851005 in 100 g water while stirring the solution in an argon-filled glovebox. The rectangular symbols show the pH-value when the NCM851005 powder is first washed. The open round symbols show the pH-value of the NCM851005 powder that was washed beforehand and dried afterwards in a vacuum oven at 65 °C for at least 4h.

Next, we have to rationalize these results from a mechanistic perspective. Regarding the mechanism of the washing process, we think that the first step is a proton (H^+) exchange with a lithium ion (Li^+) leading to the formation of LiOH (explaining the strong pH increase) and to a HMO_2 surface. For a nickel-rich material the HMO_2 structure is isostructural with a NiOOH like surface. The reaction path is shown in equation 2. Shkrob et al.[7] have already shown by XRD that a lithium/proton exchange occurs, when the material is exposed to ambient air and stored under improper conditions. Jeong et al.[40] recently published a study, which is related to the washing process of an LCO cathode and they have shown that the first step during washing is a lithium/proton exchange on the surface of the LCO cathode.

$$LiMO_2 + H_2O \rightarrow LiOH + HMO_2 \quad (2)$$

We think that the lithium/proton exchange occurs on the surface of the NCM and penetrates into the structure, which is limiting at the end and leads to the lower Li^+-leaching after the first washing. As a next step, the material washed twice was heated to 180 °C (to remove residual water) and analyzed in terms of residual reactive lithium on the surface via XPS, gassing via on-line electrochemical mass spectrometry (OEMS) and charge transfer resistance changes by impedance spectroscopy with a gold wire reference electrode (GWRE).

Surface- and electrochemical analysis of the 2x washed NCM851005 material (dried at 180 °C) — In order to prove that no more residual lithium (LiOH & Li_2CO_3) is on the surface as claimed by the literature[24], we performed XPS measurements of the pristine NCM851005 material and the NCM851005 material, which was washed 2x and dried at 180 °C. The samples were transferred to the vacuum system of the XPS without any exposure to air. The Li 1s region was recorded from 58 eV to 52 eV BE. In the top panel of Figure 3, the spectrum is shown for the pristine NCM851005 that was received by the material manufacturer. One can nicely observe two peaks in the spectrum. One is located around 54.0 eV (in green) and attributed to the intercalated lithium ($Li_{intercalated}$) and one peak is located at 55.3 eV (in blue), which is attributed to the surface lithium ($Li_{surface}$, = LiOH and Li_2CO_3). The assignment of the peaks is further validated by storing the as received material in humid air, leading to a severe increase of the surface lithium peak (data not shown). Interestingly, when the material is washed twice in argon, no more surface lithium can be detected by XPS whereas the intercalated lithium peak (in green) is still present. This result fits well with the literature where Kim et al.[24] could show by FT-IR measurements that the amounts of LiOH and Li_2CO_3 drastically decrease after washing. With that, we can show that washing leads to a decrease in residual LiOH and Li_2CO_3 on the surface of the cathode material. Next, we want to check if the washing process has an influence on the gassing and the impedance of the NCM851005 material.

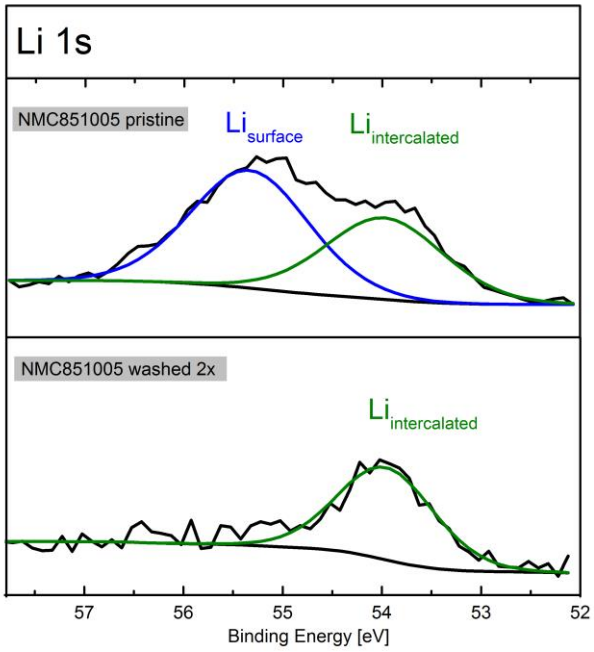

Figure 3: Li 1s region of NCM851005 pristine and washed under argon twice by XPS (data shown in black). The pristine sample (NCM851005 as received) was dried at 120 °C and the washed sample (NCM851005 washed 2x) was dried at 180 °C prior to the measurement. The samples are transferred to the vacuum chamber without any air exposure. For peak fitting, a Shirley background (in black) was subtracted and two peaks with a center energy of 54.0 eV ($Li_{intercalated}$) and 55.3 eV ($Li_{surface}$) and a FWHM of 1.4 were used.

Recently, it has been shown that oxygen release from nickel-rich layered materials significantly alters the electrolyte and mainly causes gas evolution during the first cycles, leading to a strong capacity degradation.[19, 27, 29] Furthermore, it has been shown that hydroxide species on the material surface can react with the electrolyte leading to the formation of CO_2.[8, 19] In order to investigate the effect of a washing step onto the gas evolution of a nickel-rich NCM material, we performed on-line electrochemical mass spectrometry on the pristine and the washed sample. Therefore, we used an electrolyte based on pure EC mixed with 1.5 M $LiPF_6$. This model electrolyte is on the one hand sufficient due to its low vapor pressure, leading to a high sensitivity of the measurement by an increased signal to noise ratio.[41] On the other hand, the only gases that evolve during EC reduction on the lithium counter electrode are CO and ethylene[42-44] which can be clearly differentiated from the O_2 and CO_2 evolved from the

cathode material.[29] Results of the OEMS measurements on both samples are shown in Figure 4. The upper panel shows the galvanostatic charge profiles from OCV (≈3 V) up to 5.0 V against a Li counter electrode, and the middle/lower panels depict the concentration of the concomitantly evolved O_2 (m/z = 32, middle panel) and CO_2 (m/z = 44, lower panel); concentrations are given in terms of μmol/g_{AM} (left axis). The gas evolution for the pristine material is shown by the grey lines in Figure 4, showing a capacity of ≈267 mAh/g during the first charge to 5.0 V vs. Li^+/Li. The O_2 evolution can be observed at 84% SOC (≈4.32 V vs. Li^+/Li) which is in one line with the results reported by Jung et al.[19, 27] and Teufl et al.[30], where the oxygen release is followed by a sharp increase in the CO_2 evolution. In contrast to that, the electrode made from the washed material (red lines, middle and bottom panel in Figure 4) show nearly no gassing up to 5.0 V vs Li^+/Li for both, the O_2 and the CO_2 evolution.

The oxygen release for the pristine NCM in Figure 4 (middle panel) is in accordance with literature and can be rationalized by thermodynamic instabilities of layered oxides at SOC's > 80%.[19, 27, 28, 30] However, concerning the CO_2 evolution during the first charge of layered oxides there is an ongoing debate about its origin; it has been assumed by Luo et al.[45] that the CO_2 evolution completely evolves due to electrolyte oxidation with lattice oxygen, Renfrew et al.[18] proposed the opposite, suggesting that CO_2 evolution is exclusively triggered by the oxidative decomposition of Li_2CO_3 from surface regions. However, Jung et al.[19, 27] showed detailed analysis of the CO_2 evolution, suggesting that the CO_2 evolved at ≈4.2 V vs. Li^+/Li is produced due to surface impurities, while the oxygen released at higher potentials is suggested to react with the carbonate electrolyte causing a rapid increase in the CO_2 evolution.[29] Recently Jung et al.[19] could prove their concept by temperature dependent measurements with an ^{13}C labeled electrolyte showing a reaction of surface hydroxides with the electrolyte at low potentials and a strong reaction of lattice oxygen with the electrolyte > 4.3 V vs. Li^+/Li; for that reason we will adopt the mechanistic view proposed by Jung et al.[27] and Strehle et al.[37] As

mentioned above a striking observation is the variation in the gases evolved from the washed material, compared to the pristine material. By the end of the first charge to 5.0 V vs. Li^+/Li, a total amount of ≈3.1 µmol/g O_2 and ≈171 µmol/g CO_2 can be detected for the pristine sample, in contrast only about ≈0.025 µmol/g O_2 and ≈12 µmol/g CO_2 are evolved from the washed material (capacity ≈244 mAh/g), meaning that the total gas evolution is ≈25-fold lower after the washing procedure. While the titration experiments in Figure 1 were carried out without exposure to air, the electrodes prepared for the OEMS experiments were exposed to air after washing. Therefore, we cannot exclude a minor contribution of surface carbonates to the CO_2 signal after the washing step; However, the 25-fold difference in the gas evolution after washing is very significant and quite striking. As already shown in previous studies, oxygen release caused by a chemical layer-to-spinel/rocksalt formation leading to a resistive surface layer and concomitant oxygen release from near-surface regions can explain the phenomena of oxygen release for stochiometric[27, 28] as well as for overlithiated layered oxides.[30, 37] According to this mechanism we expect that a reaction between the surface of the nickel-rich cathode and the water in the washing solution takes place, leading to strong changes of the surface phases and probably leading to an resistance increase after washing. This resistance increase can already be seen in the voltage profiles in Figure 4 (upper panel), showing an increased overpotential in the initial charge profile after washing and a steep increase of the potential towards the end of the first charge (> 4.5 V vs. Li^+/Li);[6] therefore, a detailed impedance analysis will be shown next.

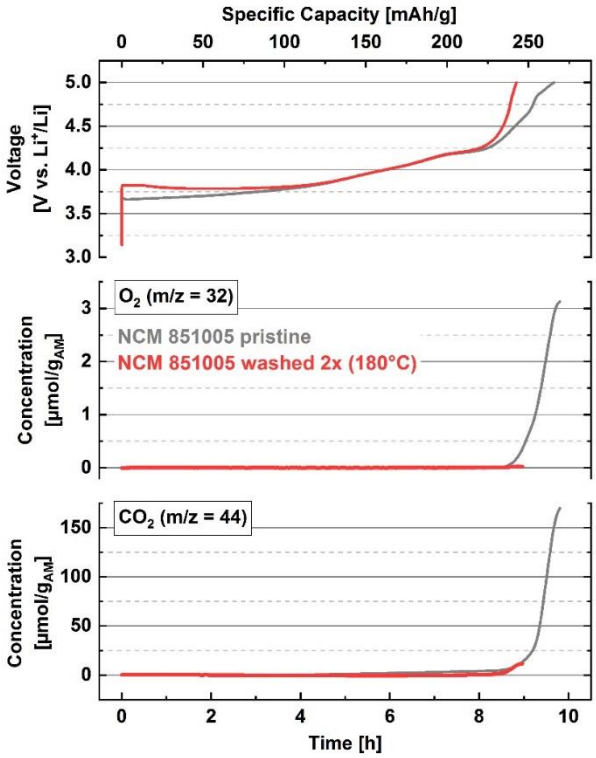

Figure 4: OEMS measurements for the first charge cycles in a half-cell for the pristine and the 2x washed NCM (dried at 180 °C) Upper panel: charge voltage vs. time and capacity; middle/lower panel: evolution of the concentrations of concomitantly evolved O_2/CO_2 given in units of either µmol/g_{AM}. Cells were charged at C/10 rate to 5.0 V. Cells were composed of metallic Li counter electrode and a glassfiber separator and experiments were conducted at 25 °C in EC-only with 1.5M $LiPF_6$. The vertical dashed red line indicates the potential of 4.32 V where the onset of O_2 evolution occurs (≈ 84% SOC; onset determined with zoom).

The OEMS results suggest that surface oxygen is depleted when the material is washed in water; Jung et al.[27] observed such a loss of surface oxygen for NCM materials when they are charged above ≈80% SOC. This oxygen then leads to the chemical oxidation of the electrolyte and a detoriation of the cell performance.[27, 29] During cycling an increase in the overpotential of NCM cathodes was shown when oxygen is released and found a severe increase of the cathode overpotential, which they attribute to the formation of a spinel or rock salt layer.[27] If oxygen is depleted after the washing process, an increase in the charge transfer resistance (R_{CT}) of the cathode material must be observed. For this reason, graphite/NCM851005 cells are

assembled with a gold wire reference electrode (GWRE[39]). This reference electrode allows for the recording of artefact-free half-cell impedance spectra. In this study, cells with a pristine NCM851005 and with a twice-washed cathode are assembled and two formation cycles at C/10 and 25 °C are carried out. Afterwards the cells are charged to 50% SOC (based on the second discharge capacity, roughly 3.7 V - 3.8 V cell voltage) and the impedance is recorded. The impedance spectra of the different NCM851005 cathodes are shown in Figure 5. The high frequency semi-circle observed in both spectra is attributed to a contact resistance ($R_{Contact}$) between the cathode coating and the aluminum current collector. More details on this can be found in the work by Landesfeind et al.[46] The pristine NCM851005 shows a small impedance response with a value for the cathode resistance $R_{Cathode}$ (determined by an R/Q fit) of ≈5 Ωcm². When the same material is washed twice in water $R_{Cathode}$ increases to ≈20 Ωcm² what is an increase of a factor 4. The increase of the $R_{Cathode}$ fits well to the data of Jung et al.[27] for an electrochemically initiated oxygen depletion.

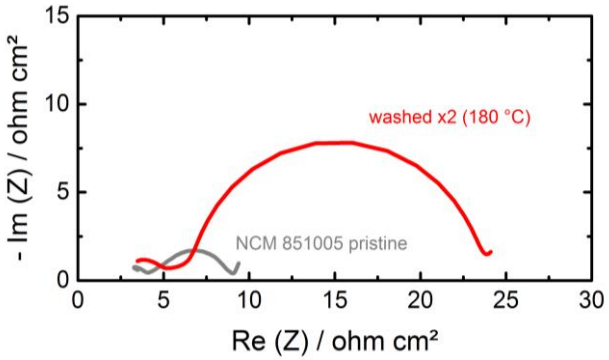

Figure 5: Impedance response of NCM851005 samples (pristine and washed twice and dried at 180 °C) measured versus a gold-wire reference electrode (GWRE) after two formation cycles with C/10 and after a charge to 50% SOC. The grey impedance spectrum represents the NCM851005 material without washing. The red impedance spectrum shows the NCM851005 material washed twice and dried at 180 °C.

Mechanistic understanding of the washing process — Up to now, we have observed a rather continuous formation of LiOH when NCM851005 is added into a solution of water. Further, we have evidence for an oxygen-depleted layer after washing and drying as suggested by OEMS and impedance measurements. Mechanisms that are already suggested in literature can partially explain these results and will be shortly discussed. Mosthev et al.[47] suggested that the extraction of Li^+ from an $LiNiO_2$ powder in an aqueous solution is charge compensated by the evolution of oxygen from the layered lattice. Furthermore, Liu et al.[48] investigated the deterioration of LNO powder under ambient air und suggested that Ni^{3+} from the lattice is reduced to Ni^{2+} and the corresponding oxidation reaction again happens by the oxidation of the lattice oxygen to gaseous O_2. If either of the suggestions in literature were true, the addition of water to a NCM851005 powder should show the evolution of O_2. In order to study this, we used a modified version of our current OEMS setup. A Swagelok T-fitting was connected to the capillary leading to the MS system. To one of the other connections, a septum was installed in order to add water with a syringe and the remaining inlet was equipped with a nut where NCM851005 powder was added.

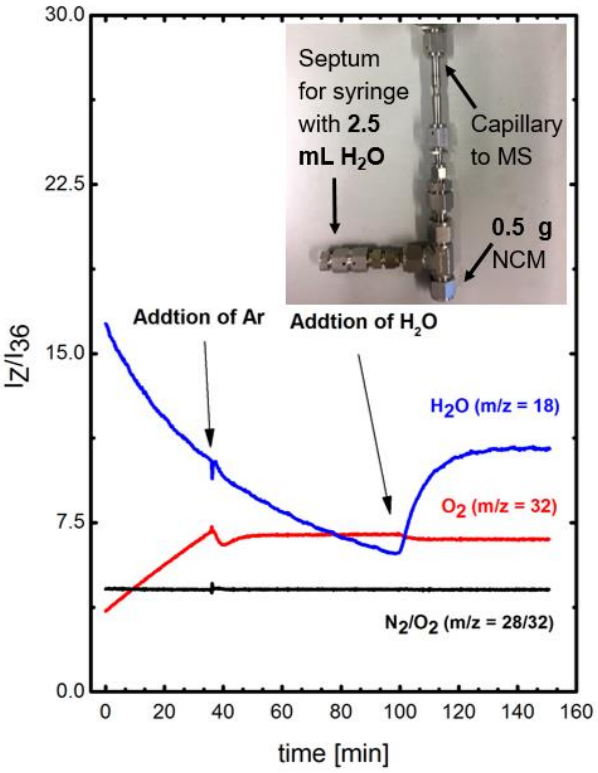

Figure 6: Mass traces of O_2 (m/z = 32, in red), H_2O (m/z = 18, in blue) and of the N_2/O_2 ratio (m/z = 28/32, in black) recorded with a modified version of the OEMS setup. The first 40 minutes consisted of a rest phase followed by the addition of a syringe with pure argon in order to check the stability of the septum. After further 60 minutes, a syringe with 2.5 mL was added to 0.5 g NCM and the mass traces were recorded for further 60 minutes.

After assembly of the cell in an argon-filled glovebox, the mas traces of O_2 (m/z = 32) and of H_2O (m/z = 18) were recorded. The first 40 minutes consisted of a rest period where the residual water amount decreases and the O_2 signal increases. The increase of the oxygen signal can easily be rationalized by a small leakage of the system, as by dividing the mass signal of N_2 (m/z = 28) by the oxygen signal, a straight line is obtained which clearly indicated the intrusion of air. After the rest period of 40 minutes, a syringe with argon from the glovebox atmosphere is added in order to check the tightness of the septum. One can nicely see that during the addition of a syringe, no increase in the oxygen or water masses are observed. After 100 minutes, 2.5 mL of water are added to 0.5 g of powder (same water/CAM ratio as in the previous experiments) and we do not observe any oxygen evolution (red line after 100 minutes) when

water is added to the powder. Therefore, we think that the evolution of lattice oxygen from a nickel-rich material during the contact with water is very unlikely.

Based on our suggested lithium/proton exchange from equation 1, a NiOOH like structure is created on the surface of the NCM material. It is known in the literature, that NiOOH is thermally very instable and starts to decompose already at temperatures as low as 80 °C.[49] The total thermal decomposition after heating the material to 550 °C is then a rocksalt structure (NiO) followed by O_2 and H_2O release. The drying temperature of the washed sample shown in the previous results section was 180 °C; heating a delithiated Ni-rich NCM material in this temperature window we assume the formation of an O_2-deficient layer, which has a M'_3O_4 ($M^{'}$ = Li+Me) spinel-type structure, as suggested by Bak et al.[50] The thermal reduction of the NiOOH phase is shown in equation 5 (Nickel (III)-oxide reduction during drying of the washed powders):

$$2\ NiOOH \rightarrow 2\ \text{"NiO"} + 0.5\ O_2 + H_2O \quad (3)$$

Jeong et al.[40] showed for an LCO cathode material that the washing leads to a CoOOH like structure, which is then thermally decomposed to a CoO or CO_3O_4 structure during the drying process and leads to an impedance increase of the washed material. Based on this concept, we have designed further experiments, which should underline this reaction path. First, we have carried out thermogravimetric analysis (TGA) coupled to a mass spectrometer (MS) of a washed material (compared to a pristine material which was not washed) in order to mimic the drying process. All samples were dried beforehand at 120 °C under dynamic vacuum for at least 3h. The TGA protocol consisted of five parts with argon as carrier gas, including a rest phase (10 minutes) an argon flow rate of 200 mL/min, which is changed to 20 mL/min (and used for all further steps) and held again 10 minutes, both at 25 °C. This is followed by a heat ramp to 120 °C with 10 K/min followed by a hold phase there of 40 minutes. As a next step, the material was heated to 450 °C (10 K/min) and the temperature was held there for 20 minutes. The results

of this experiment are shown in Figure 7. When the flow rate of argon is changed after 10 minutes also the mass signals decrease due to the lower rate now. By ramping the temperature from 25 °C to 120 °C, no severe change in the mass loss (top panel) and no change in the mass traces (middle and bottom panel) is observed. However, when ramping the temperature from 120 °C to 450 °C, first a H_2O evolution takes place (bottom panel) until 250 °C followed by a strong O_2 evolution (middle panel). This oxygen evolution goes hand in hand with a mass loss of 0.4 wt%. In contrast to that, the pristine sample shows only a very little mass loss and no oxygen or water evolution in this temperature range. The thermal reduction of NiOOH first releases water starting from temperatures of 120 °C and probably lower as a mass loss during the 120 °C hold phase can be observed parallel to an increase in the water signal. This is consistent with the results from Pan et al.[49], who showed that NiOOH loses water from the interlayers already at 100 °C. Around 250 °C a strong oxygen release is observed which converts the partially reduced NiOOH structure into a rocksalt phase of NiO (see equation 3). Pan et al.[49] showed that this process happens for a pure NiOOH at 262 °C. We think that first a spinel like structure is formed from the NiOOH phase (loss of water) and followed by the total reduction to a rock salt phase starting from 250 °C (loss of oxygen), which is in one line with the results shown by Bak et al.[50]

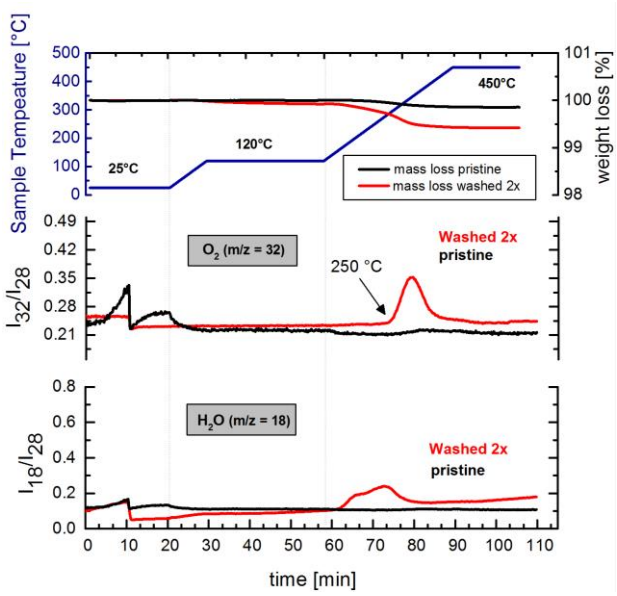

Figure 7: TGA-MS analysis of a 2x washed NCM851005 powder and as reference a NCM851005 material which was stored in an argon-filled glovebox. All materials were dried beforehand in a Büchi oven at 120 °C under dynamic vacuum for at least 3 h. The top panel shows the temperature program with heating ramps and hold phases (left y-axis) and the corresponding mass loss (right y-axis) of the pristine sample (in black) and the sample washed twice (in red). The panel in the middle shows the O_2 signal (m/z = 32) normalized by nitrogen (m/z = 28) of both pristine and washed sample. The bottom panel shows the mass traces of water H_2O (m/z = 18) normalized by the nitrogen signal (m/z = 28).

If this concept is valid, a higher drying temperature must cause a lower gas evolution (O_2 and CO_2) and a higher impedance as the NiOOH phase is more gradually decomposed at higher temperatures. In order to prove this, we have carried out further OEMS and impedance measurements where the cathodes were dried at different temperatures. We have chosen the following conditions for the washed cathodes: One sample was freeze-dried and has seen a maximum temperature of 25 °C. Next, washed CAMs were dried at 80 °C, 180 °C (already shown above), and 300 °C; the OEMS results are shown in Figure 8. As already depicted in Figure 4 the gas evolution of the sample, which was washed and dried at 180 °C, showed nearly no O_2 and CO_2 evolution during the first charge cycle, whereas the pristine sample showed a high gas evolution of ≈3.1 µmol/g O_2 and ≈171 µmol/g CO_2. The systematic variation of the

drying temperature is therefore shown in Figure 8 where the data from Figure 4 (pristine sample and dried at 180 °C) are also included. All samples were washed 2 x 20 minutes as described in the experimental section. As gentle drying procedure, we freeze dried the washed powder and afterwards vacuum dried the electrode at 25 °C. The freeze-dried sample still shows a significant O_2 and CO_2 evolution corresponding to ≈0.35 µmol/g O_2 and ≈90 µmol/g CO_2 detected during the first charge. By increasing the drying temperature to 80 °C a tremendous decrease of the O_2 (≈0.1 µmol/g) and the CO_2 (≈26 µmol/g) can be observed, pointing towards thermal NiOOH decomposition starting already at temperatures around 80 °C. This thermal decomposition at these low temperatures cannot clearly be observed in the TGA experiment. However, we think when the sample is dried in vacuum for 12 h, a thermal reduction can occur (indicated by the OEMS measurement). In the TGA experiment, a fast heat ramp is used and therefore the thermal reduction might not be observed. A further increase of the drying temperature to 180 °C leads to a further decrease of the gas evolution, with decreased amounts of O_2 (0.025 µmol/g) and CO_2 (12 µmol/g) evolution for the sample. Next, we investigated the sample dried at 300 °C in the OEMS, which is also shown in Figure 8. Literally, we cannot detect any O_2 evolution and only very small amounts of CO_2 (6 µmol/g) for the sample dried at 300 °C. From these results we expect that a drying starting from 80 °C might form an oxygen deficient meta-stable surface structure that largely preserves its structure during delithiation and does only release very small amounts of oxygen (e.g. spinel-type phase) but can be thermally decomposed to a thermodynamic more stable phase as shown in Figure 7 e.g. rocksalt structure (when dried at 300 °C), which shows no oxygen evolution at all. Such a thermal instability for delithiated Ni-rich layered oxides was characterized in detail by Bak et al.[50], showing a spinel to rocksalt transformation >200 °C accompanied by oxygen release. Thus, we are confident that the oxygen evolution at drying temperatures >250 °C (Figure 7) stems from surface rocksalt formation of the washed NCM particles. However, Figure 8 does not only give information about the gas evolution during different drying procedures but also about the electrochemistry,

showing an identical charge capacity for the freeze dried sample as observed for the pristine material (both ≈267 mAh/g, Figure 4 and Figure 8). This can be rationalized by the fact that the surface has still a layered structure remaining its electrochemical activity during the first charge without trapping Li^+ in an inactive surface layer. The specific charge capacity of the samples dried at 80 °C, 180 °C and 300 °C is lower with a similar charge capacity of ≈244 mAh/g. From the LiOH determination in Figure 2, we expect a total lithium loss of ≈3% that cannot explain the observed capacity loss (≈23 mAh/g) during the first charge. Therefore, we expect that the lower capacity stems from a phase transformation into a lithium containing spinel and/or rock salt phase leading to a material loss, this finding will in the end be underlined by quantification of the results and the capacity loss. Similar findings have been seen from Teufl et al.[30] who could show a large capacity contribution from a spinel phase to the capacity of a Li- and Mn-rich NCM by a dQ/dV analysis; while for the Li-rich case a Mn spinel can be reversible charged/discharged at potentials around 3 V vs. Li^+/Li,[51, 52] there is no evidence of such a electrochemical active spinel-type phase for Ni-rich NCM materials. Rather we expect that lithium can get trapped within such a surface phase leading to a loss of active lithium by the formation of an electrochemical inactive $(Li+M)_3O_4$ spinel-type phase or a (Li+M)O rocksalt-type phase.[50] To further investigate these findings, impedance measurements for the different samples are shown in Figure 9.

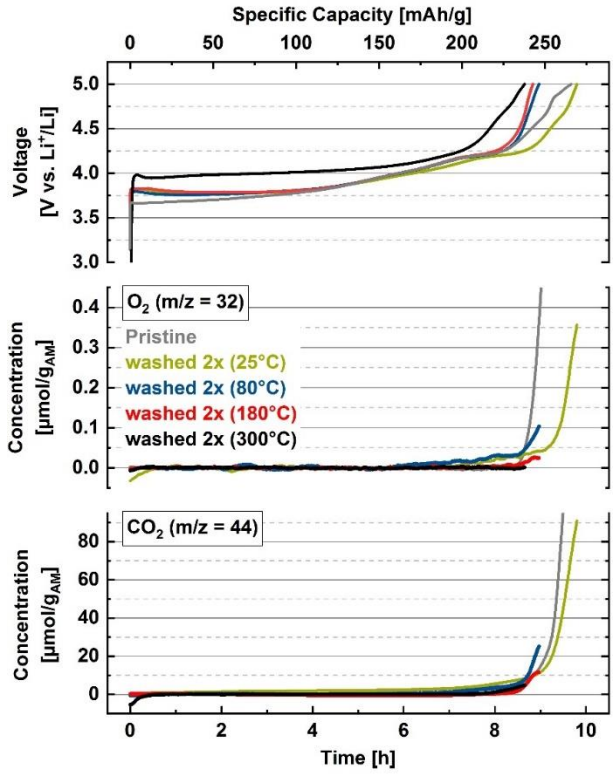

Figure 8: OEMS measurements for the first charge cycles in a half-cell for the 2x washed NCM with different drying temperatures after the washing procedures. Upper panel: charge voltage vs. time and capacity; middle/lower panel: evolution of the concentrations of concomitantly evolved O_2/CO_2 given in units of µmol/g_{AM}. Cells were charged at C/10 rate to 5.0 V. Cells were composed of metallic Li counter electrode and a glassfiber separator and experiments were conducted at 25 °C in EC-only with 1.5M $LiPF_6$.

The impedance of NCM851005 cathodes dried at different temperatures is analyzed with a GWRE in order to analyze the interfacial resistance of the cathode and the data is shown in Figure 9. The resistance ($R_{Cathode}$) of a pristine cathode is in the order of ≈5 Ωcm². When the cathode material is now washed twice in water and then freeze dried and afterwards dried in dynamic vacuum at 25 °C the cathode impedance is in the same order with a value of ≈6 Ωcm². This agrees well with the first part of our mechanism, where only a lithium/proton exchange occurs on the surface. The freeze drying takes away the water from the cathode powder but does avoid the thermal decomposition of the NiOOH phase. The intercalated protons are then charged during the formation cycle and most likely reduced on the graphite anode to H_2 gas.

As we can see from the cathode impedance, drying at maximum 25 °C does not alter the cathode interface. When the drying temperature is switched to 80 °C, we can indeed observe an increase of the cathode resistance with a value of ≈10 Ωcm². This fits also well to the second part of our mechanism and to the TGA measurement from Figure 7, where the thermal reduction of a NiOOH already occurs at 80 °C. When the material is dried at 180 °C, the cathode resistance increases to ≈20 Ωcm², which can be explained by a stronger reduction of the NiOOH phase to an O_2-deficient layer. Interestingly, when the cathode powder is dried at 300 °C the cathode impedance shoots to a very high value of ≈130 Ωcm². At this temperature, we saw a strong oxygen evolution from the cathode material in the TGA-MS measurement (Figure 7) explaining the high cathode impedance. These results are perfectly in line with the phase transformations of delithiated NCM materials suggested by Bak et al.[50]; they clearly showed that a meta-stable spinel phase can form at temperatures between 100 °C and 200 °C, while heating >200 °C clearly ends up with the formation of a rocksalt type phase. This is essentially what can be seen in the impedance spectra (Figure 9b), showing a slight increase in impedance up to 180 °C due to surface-spinel formation, while heating to 300 °C ends up with a very high impedance due to the formation of a resistive rocksalt structure on the surface. In summary, the EIS measurements underline the strong influence of the drying temperature being the main driver for the decreased gassing and increased impedance.

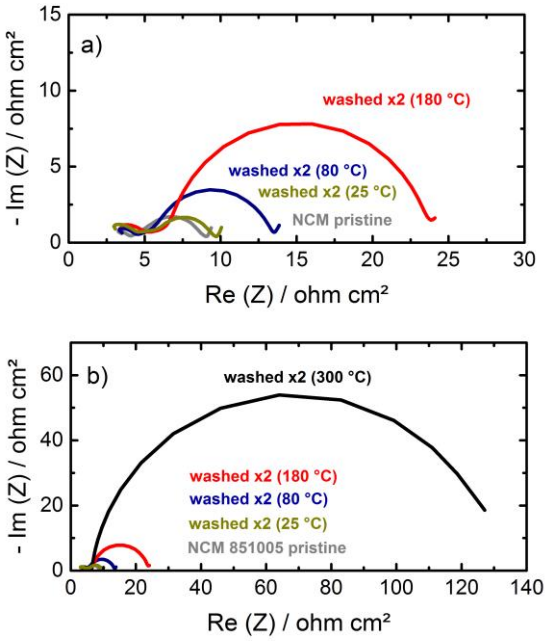

Figure 9: Cathode impedance spectra measured with a gold-wire reference electrode in a graphite//NCM851005 cell configuration. The analyzed cathodes were washed twice in water and then dried with the following conditions as can be seen in panel a): pristine cathode (not washed, dried at 120 °C, in grey), freeze dried cathode (dried at 25 °C, in yellow), dried at 80 °C (in blue) and dried at 180 °C (in red). Panel b) is a zoom out of panel a) in order to show the impedance, or a cathode dried at 300 °C. The impedance was recorded from 100 kHz to 100 mHz with a perturbation of 15 mV at 25 °C.

Influence of harsh washing conditions on the full-cell cycling performance at 25 °C — In order to investigate the effect of different drying conditions for the NCM powders on the cycling performance we have assembled graphite/NCM851005 full cells with a gold wire reference electrode (GWRE). After formation (2 cycles at C/10) and a subsequent charge to 50% SOC the impedance is recorded and shown in Figure 9. After the impedance measurement, the cells are further analyzed by a charge/discharge cycling protocol consisting of a C/2 charge (CCCV) and a 1C (CC) discharge for 198 cycles. The results of this test are shown in Figure 10.

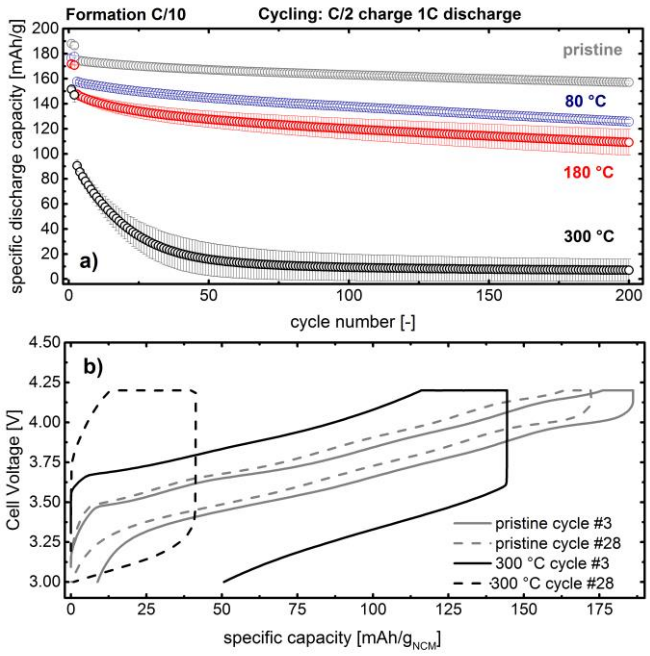

Figure 10: Charge/discharge cycling test of graphite/NCM851005 cells containing a gold-wire reference electrode (GWRE) and an LP57 electrolyte. The cycling is carried out with a CCCV charge to 4.2 V with a cut-off for the CV phase of C/20. The discharge is carried out in CC mode until 3.0 V. a) contains the discharge capacity of the C/10 cycles (2x formation) and the subsequent cycles with a C/2 charge and 1C discharge of the pristine cathode (not washed, dried at 120 °C, in grey), of a NCM cathode dried at 80 °C (in blue), dried at 180 °C (in red) and dried at 300 °C (in black). b) contains the full-cell voltage profiles of the first and 25th cycle during the C/2 charge and 1C discharge protocol of the pristine cathode (in grey) and of NCM dried at 300 °C.

The pristine cathode (in grey) shows a first discharge capacity of 188 ± 1 mAh/g_{NCM} at C/10 which drops to 178 ± 2 mAh/g_{NCM} when the discharge C-rate is increased to 1C. After 200 cycles (formation plus faster cycling), the specific discharge capacity is 157 ± 1 mAh/g_{NCM}. When the cathode material is washed and dried at 80 °C (in blue) the first discharge capacity is 178 ± 2 mAh/g_{NCM} (10 mAh/g less compared to the pristine sample). When the discharge C-rate is increased from C/10 to 1C, the specific discharge capacity is 158 ± 1 mAh/g_{NCM}, which can be explained by the impedance increase after washing and drying at 80 °C. After 200 cycles the specific discharge capacity drops to 126 ± 2 mAh/g_{NCM} By drying the cathode material at 180 °C the first discharge capacity is similar to the sample washed and dried at 80 °C with

175 ± 2 mAh/g_{NCM} and when switching the C-rate to 1C a discharge capacity of 147 ± 3 mAh/g_{NCM} is obtained. This is 11mAh/g lower compared to the cells were the cathode is dried at 80 °C and fits well to a further increased impedance of the cathode (see Figure 9). After 200 cycles the specific discharge capacity is 109 ± 10 mAh/g_{NCM} for electrodes where the powder was dried at 180 °C. For cells cycled at 300 °C very low discharge capacities at C/10 of 151 ± 3 mAh/g_{NCM} are obtained which fit well to the severely increased cathode impedance to a value of ≈130 Ωcm² compared to ≈6 Ωcm² for the pristine material. The first discharge capacity at 1C is 90 ± 5 mAh/g_{NCM} what further underlines the drastic increase in cathode impedance. Interestingly, the cells with the cathode active material dried at 300 °C show also a drastic fading with a final specific discharge capacity of 7 ± 6 mAh/g_{NCM}. In order to understand that, we have to take a closer look into Figure 10 b). Here the voltage profiles of the third cycle (first cycle with 1C discharge) and the 37th cycle are shown. The voltage profiles of the pristine sample (in grey) show very little overpotential and short CV phases as expected for a non-washed material. The voltage profile of the third cycle of the cells with cathodes dried at 300 °C a strong overpotential is observed (compared to the pristine sample). Further, the CV phase is increased during the charge and during discharge, the high impedance causes a capacity drop of approximately 50 mAh/g_{NCM}. After 28 cycles, the impedance must have increased further drastically as the cut-off of 4.2 V is reached immediately. Unfortunately, the impedance after cycling was not recorded, however the voltage profiles clearly indicate a non-stable cathode surface which has a drastic impedance buil-up leading to very low discharge capacities. From this we conclude that washing with high water to CAM ratios (5:1) and drying at 300 °C leads to a very instable structure, which further decomposes when cycled in a real cell configuration. In order to optimize this process with regards to low impedance and stable surfaces after washing, further studies are carried out.

Discussion

Estimated surface layer thickness calculated from LiOH titration — It has been shown in literature that oxygen release at the surface of nickel rich NCM materials can lead to electrochemically formed surface layers on NCM cathode materials.[27, 28] These surface layers lead to an immediate capacity loss during cycling due to significant impedance build-up.[27] In order to get an estimate on the spinel/rocksalt layer thickness after the washing and drying procedure the layer thickness will be estimated from LiOH amounts gained from the titration experiments; details for the calculations of the layer thicknesses are shown by Jung et al.[6, 27] and Strehle et al.[37] As a first step we derive the particle size of a spherical particle from the measured BET surface area, with r being the radius, A_{BET} the BET surface area of the washed material and ρ being the crystallographic density of the NCM material. For the calculation we used the BET surface area that we got after washing, which was as high as 2.4 m^2/g:

$$r = \frac{1}{2} \cdot \frac{6}{A_{\mathrm{BET}} \cdot \rho} = \frac{1}{2} \cdot \frac{6}{2.4\ \mathrm{m^2\ g^{-1}} \cdot 4.8\ \mathrm{g\ cm^{-3}}} \approx 260\ \mathrm{nm} \quad (4)$$

A particle radius of 260 nm is therewith calculated. Knowing the particle size, one can calculate the radius of the bulk particle without the surface layer. Detailed derivation of this calculations can again be found by Strehle et al.[37] and Jung et al.[6, 27] whereas it shall be noted that complete cation disorder is allowed. Hereby the mol-fraction of surface phase is required, this fraction is estimated by the exchange of 3 mol.% lithium by 3 mol.% of protons, as derived from the LiOH titration before and shown in Figure 1. From this estimation we expect a surface phase fraction of $x_{\mathrm{surface\ phase}}$ = 3 mol.%; with these values the radius of the still layered bulk r´ can be calculated:

$$\frac{V_{\text{shell}}}{V} = \frac{r^3 - r'^3}{r^3} = 1 - \left(\frac{r'}{r}\right)^3 = x_{\text{surface phase}} \leftrightarrow r' = r \cdot \left(1 - x_{\text{surface phase}}\right)^{\frac{1}{3}} \quad (5)$$

Plugging in the actual numbers this leads to a radius of 257.4 nm of still layered bulk.

$$r' = r \cdot \left(1 - x_{\text{surface phase}}\right)^{\frac{1}{3}} = 260\ \text{nm} \cdot (1 - 0.03)^{\frac{1}{3}} = 257.4\ \text{nm} \quad (6)$$

Out of this value the thickness of the surface phase $t_{\text{surface phase}}$ can be easily calculated, ending up with roughly 2.6 nm of disordered surface phase.

$$t_{\text{surface phase}} = 2.6\ \text{nm} \quad (7)$$

Estimated surface layer thickness calculated from O_2-loss in TGA-MS — In order to verify this layer thickness, the amount of spinel/rocksalt formed on the surface cannot only be estimated from the LiOH loss, but can also be derived from the mass loss at 250 °C in the TGA-MS experiment shown in Figure 7. At 250 °C the only gas that can be detected is oxygen, which allows the assumption that the 0.4 % mass loss are caused by an oxygen loss during heating (only a minor fraction from the water). These 0.4% weight loss (4 mg_{loss}/g_{CAM}) can therefore be transformed into a O_2 loss of 125 µmol/g_{NCM} ($4_{mg}/32_{g/mol}$) which can be used to calculate the thickness of the rocksalt surface layer. According to Bak et al.[50] the delithiated Ni-rich cathodes undergo a transformation from a M'_3O_4 spinel type structure to a MO rocksalt phase (M = Ni, Co, Mn) at temperatures >200 °C which is accompanied by an oxygen loss and can be ascribed to the following equations:

$$0.33\ M_3O_4 \rightarrow MO + 0.16\ O_2 \quad (8)$$

This equation gives the theoretical loss of oxygen per mole NCM for a 100% spinel to rocksalt transformation (O_2^{theo}), from which the moles of oxygen released for a 100% conversion of the entire particle into the rocksalt ($n(O_2^{theo})$) can be easily calculated according to formula 9, using the molar mass of the NCM851005; detailed information for these calculations can be found by Jung et al.[27], Strehle et al.[37] and Teufl et al.[30]

$$n\ (O_2^{theo}) = \frac{O_2^{theo}}{M} \quad (9)$$

The ratio of oxygen release expected for a 100% phase transformation ($n(O_2^{theo})$) into a rocksalt structure (1638 µmol/g) and the actual oxygen evolution derived from the mass loss in the TGA-MS (Figure 7, 125 µmol/g) can be used to calculate the molar fraction of spinel converted into a rocksalt layer.

$$x_{\text{rocksalt layer}} = \frac{n\ (O_2^{meas})}{n\ (O_2^{theo})} \quad (10)$$

These calculations lead to a fraction of 7.6 mol.% that is transformed into a rocksalt surface layer, this value is now derived from the mass loss in the TGA-MS experiment (Figure 7) and can also be translated into a surface layer thickness with equations 5-7. Discussing this surface transformation to a capacity loss caused by a loss of cathode active material due to the formation of a chemical inactive surface layer, 7.6 mol.% would result in a capacity loss of 21 mAh/g for total delithiation (based on a theoretical capacity of 274 mAh/g). The capacity loss after

washing that can be observed for total delithiation in the OEMS experiment (Figure 4) results in 23 mAh/g, which is in one line with the 21 mAh/g calculated from the mass loss in the TGA. Therefore, we suggest that the capacity loss fur full delithiation at slow C-rates can be explained by lithium captures within the inactive spinel/rocksalt surface layer. The calculation of the surface layer thickness derived from the weight loss in the TGA-MS results in a layer thickness of 6.8 nm, which is substantially thicker than the thickness derived from the pH values of the pure Li/H^+ exchange (2.6 nm as calculated above), this can be explained due to Li^+-mobility during phase transformation. Hereby, one has to note that the first estimation from the pH and the fraction of Li/H^+-exchange accounts for a surface spinel/rocksalt that does not contain any lithium, which is unlikely. The formation of a lithium containing spinel/rocksalt layer would therefore cause a thicker layer assuming the same proton intercalation.

This concept is schematically shown in Scheme 1. Hereby the blue gradient with the thickness d_1 depicts the theoretical layer that is estimated from a pure diffusion process without any Li^+-mobility during the wash and drying process; this hypothetical layer was calculated from the pH values and equals to 2.6 nm. However, in reality the lithium gradient after the washing and drying might look different, which was proven by the layer estimation form the actual oxygen loss during the TGA experiment. This model is shown by the green Li-gradient (Scheme 1) and is expected the more practical one. In addition to the oxygen loss from the TGA-MS the layer with the thickness d_2 can also explain the capacity that is observed during the OEMS experiments which can be rationalized by the quantifications shown above.

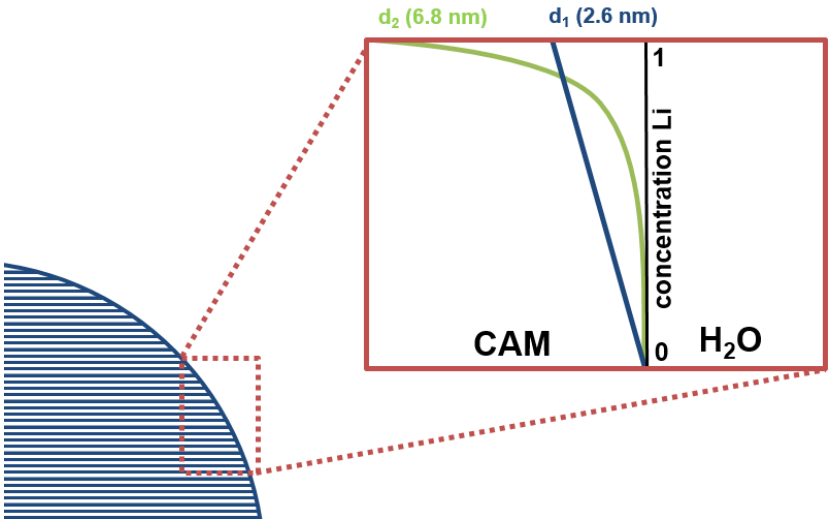

Scheme 1: Schematic presentation of the surface process during the wash and dry procedure of the Ni-rich CAM. The inset shows the particle surface and the different surface layers that we calculated from the pH and from the TGA-MS. The value derived from the pH only takes pure Li^+/H^+ exchange into account, resulting in a thinner, entirely delithiated surface layer. The model for the layer d_2 takes lithium mobility and a lithium gradient into account and the layer thickness was derived from the practical oxygen loss in the TGA-MS experiments.

Conclusions

In this study, we have analyzed the washing process of nickel-rich cathode materials (NCM 851005). We showed that the removal of Li_2CO_3 follows a simple dissolution mechanism, whereas the formation of LiOH proceeds continuously during washing. The washed samples were analyzed in terms of gassing (OEMS) and showed decreased O_2 & CO_2 release above 80% SOC by one order of magnitude going hand in hand with an increased cathode impedance. With a detailed TGA-MS analysis we could show the evolution of oxygen and water during the drying process, which lead us to the conclusion that the first step of the washing must be a lithium/proton exchange on the surface (NiOOH like structure), which is then thermally decomposed in an oxygen-deficient layer. This theory is confirmed by OEMS & Impedance measurements with samples dried at different temperatures, where we could show that the cathode impedance increases with increasing drying temperature and the gassing decreases with increasing drying temperature.

Acknowledgment

Financial support by the BASF SE through its Research Network on Electrochemistry and Batteries is gratefully acknowledged.

References

1. D. Larcher and J. M. Tarascon, *Nat. Chem.*, **7** (1), 19-29 (2015).
2. D. Andre, S.-J. Kim, P. Lamp, S. F. Lux, F. Maglia, O. Paschos, and B. Stiaszny, *J. Mater. Chem. A*, **3** (13), 6709-6732 (2015).
3. G. E. Blomgren, *J. Electrochem. Soc.*, **164** (1), A5019-A5025 (2016).
4. M.-H. Kim, H.-S. Shin, D. Shin, and Y.-K. Sun, *J. Power Sources*, **159** (2), 1328-1333 (2006).
5. P. Rozier and J. M. Tarascon, *J. Electrochem. Soc.*, **162** (14), A2490-A2499 (2015).
6. R. Jung, R. Morasch, P. Karayaylali, K. Phillips, F. Maglia, C. Stinner, Y. Shao-Horn, and H. A. Gasteiger, *Meeting Abstracts*, **MA2017-02** (4), 216 (2017).
7. I. A. Shkrob, J. A. Gilbert, P. J. Phillips, R. Klie, R. T. Haasch, J. Bareño, and D. P. Abraham, *J. Electrochem. Soc.*, **164** (7), A1489-A1498 (2017).
8. J. Sicklinger, M. Metzger, H. Beyer, D. Pritzl, and H. A. Gasteiger, *manuscript in preparation.*
9. N. V. Faenza, L. Bruce, Z. W. Lebens-Higgins, I. Plitz, N. Pereira, L. F. J. Piper, and G. G. Amatucci, *J. Electrochem. Soc.*, **164** (14), A3727-A3741 (2017).
10. J. Paulsen, H.-K. Park, and Y.-H. Kwon, *US 2009/0224201 A1 (2009).*
11. J. Paulsen and J. H. Kim, *WO 2012/107313 A1 (2012).*
12. D.-H. Kim and J. Paulsen, *United States Pat. Appl. 2016036557, WO 2015/128722 A1 (2015).*

13. J. Paulsen, H. P. Hong, and H. S. Ahn, *WO 2015/036882 A2 (2015)*.

14. J. Paulsen, H. P. Hong, and J. D. Oh, *WO 2016/055911 A1 (2016)*.

15. J. R. Dahn, R. Fong, and U. v. Sacken, *US 2, 264, 201 (1993)*.

16. G. V. Zhuang, G. Chen, J. Shim, X. Song, P. N. Ross, and T. J. Richardson, *J. Power Sources,* **134** (2), 293-297 (2004).

17. Y. Kim, *J. Mater. Sc.* **48** (24), 8547-8551 (2013).

18. S. E. Renfrew and B. D. McCloskey, *J. Am. Chem. Soc.*, **139** (49), 17853-17860 (2017).

19. R. Jung, P. Strobl, F. Maglia, C. Stinner, and H. A. Gasteiger, *J. Electrochem. Soc.,* **165** (11), A2869-A2879 (2018).

20. M. Metzger, B. Strehle, S. Solchenbach, and H. A. Gasteiger, *J. Electrochem. Soc.,* **163** (7), A1219-A1225 (2016).

21. H.-J. Noh, S. Youn, C. S. Yoon, and Y.-K. Sun, *J. Power Sources,* **233** 121-130 (2013).

22. J. Kim, H. Lee, H. Cha, M. Yoon, M. Park, and J. Cho, *Adv. Ener. Mater.,* **8** (6), (2018).

23. S. Arimoto, K. Tsuruta, R. Leblanc, and R. Melsert, *US 2017/02946521 A1 (2017)*.

24. J. Kim, Y. Hong, K. S. Ryu, M. G. Kim, and J. Cho, *Electrochem. Solid State Lett.,* **9** A19-A23 (2006).

25. Y. Kim, *J. Solid State Electrochem.,* **17** (7), 1961-1965 (2013).

26. X. Xiong, Z. Wang, P. Yue, H. Guo, F. Wu, J. Wang, and X. Li, *J. Power Sources,* **222** 318-325 (2013).

27. R. Jung, M. Metzger, F. Maglia, C. Stinner, and H. A. Gasteiger, *J. Electrochem. Soc.*, **164** (7), A1361-A1377 (2017).

28. D. Streich, C. Erk, A. Guéguen, P. Müller, F.-F. Chesneau, and E. J. Berg, *J. Phys. Chem. C,* **121** (25), 13481-13486 (2017).

29. R. Jung, M. Metzger, F. Maglia, C. Stinner, and H. A. Gasteiger, *J. Phys. Chem. Lett.,* **8** (19), 4820-4825 (2017).

30. T. Teufl, B. Strehle, P. Müller, H. A. Gasteiger, and M. A. Mendez, *J. Electrochem. Soc.,* **165** (11), A2718-A2731 (2018).

31. J. Sicklinger, H. Beyer, L. Hartmann, F. Riewald, and H. A. Gasteiger, *mansucript in preparation.*

32. Z. Chen, J. Wang, J. Huang, T. Fu, G. Sun, S. Lai, R. Zhou, K. Li, and J. Zhao, *J. Power Sources,* **363** 168-176 (2017).

33. Y. Cho, S. Lee, Y. Lee, T. Hong, and J. Cho, *Adv. Ener. Mater.,* **1** (5), 821-828 (2011).

34. Y.-K. Sun, S.-T. Myung, B.-C. Park, J. Prakash, I. Belharouak, and K. Amine, *Nat. Mater.,* **8** 320 (2009).

35. D. Larcher, M. R. Palacin, G. G. Amatucci, and J.-M. Tarascon, *J. Electrochem. Soc.,* **144** 408-417 (1997).

36. G. G. Amatucci, J. M. Tarascon, D. Larcher, and L. C. Klein, *Solid State Ionics,* **84** (3), 169-180 (1996).

37. B. Strehle, K. Kleiner, R. Jung, F. Chesneau, M. Mendez, H. A. Gasteiger, and M. Piana, *J. Electrochem. Soc.,* **164** (2), A400-A406 (2017).

38. N. Tsiouvaras, S. Meini, I. Buchberger, and H. A. Gasteiger, *J. Electrochem. Soc.,* **160** (3), A471-A477 (2013).

39. S. Solchenbach, D. Pritzl, E. J. Y. Kong, J. Landesfeind, and H. A. Gasteiger, *J. Electrochem. Soc.,* **163** (10), A2265-A2272 (2016).

40. S. Jeong, J. Kim, and J. Mun, *J. Electrochem. Soc.,* **166** (3), A5038-A5044 (2019).

41. M. Metzger, C. Marino, J. Sicklinger, D. Haering, and H. A. Gasteiger, *J. Electrochem. Soc.,* **162** (7), A1123-A1134 (2015).

42. M. Metzger, B. Strehle, S. Solchenbach, and H. A. Gasteiger, *J. Electrochem. Soc.,* **163** (5), A798-A809 (2016).

43. B. Zhang, M. Metzger, S. Solchenbach, M. Payne, S. Meini, H. A. Gasteiger, A. Garsuch, and B. L. Lucht, *J. Phys. Chem. C,* **119** (21), 11337-11348 (2015).

44. S. Solchenbach, G. Hong, A. Freiberg, R. Jung, and H. A. Gasteiger, *J. Electrochem. Soc.,* **165** (14), A3304-A3312 (2018)

45. K. Luo, M. R. Roberts, R. Hao, N. Guerrini, D. M. Pickup, Y.-S. Liu, K. Edström, J. Guo, A. V. Chadwick, L. C. Duda, and P. G. Bruce, *Nat. Chem.*, **8** 684 (2016).

46. J. Landesfeind, D. Pritzl, and H. A. Gasteiger, *J. Electrochem. Soc.,* **164** (7), A1773-A1783 (2017).

47. R. Moshtev, *J. Power Sources,* **81-82** 434-441 (1999).

48. H. S. Liu, *Electrochem. Solid State Lett.,* **7** (7), A190-A193 (2004).

49. J. Pan, Y. Sun, P. Wan, Z. Wang, and X. Liu, *Electrochem. Commun.,* **7** (8), 857-862 (2005).

50. S. M. Bak, E. Hu, Y. Zhou, X. Yu, S. D. Senanayake, S. J. Cho, K. B. Kim, K. Y. Chung, X. Q. Yang, and K. W. Nam, *ACS Appl. Mater. Interfaces*, **6** (24), 22594-22601 (2014).

51. P. G. Bruce, A. R. Armstrong, and L. Gitzendanner, *J. Mater. Chem.,* **9** 193-198 (1998).

52. M. M. Thackeray, *Prog. Solid State Chem.,* **25** 1-71 (1997).

3. Conclusions

The scope of this thesis was not only to understand the main degradation mechanisms of Li- and Mn-rich NCM materials, but also to learn how their chemical interactions in a full-cell limit the battery life. As a first step, the electrochemical properties and the gas evolution of the base materials were investigated, before analyzing their performance in a full-cell with different electrolytes, particularly at elevated temperatures. In the end, a path towards minimizing or even eliminating the oxygen release from layered oxides was suggested by a detailed investigation on the effect of aqueous washing of Ni-rich NCM materials.

At the beginning, we carried out a detailed analysis on the origin of the high and path-dependent impedance of these materials and ascribed these phenomena to structural and electrochemical materials characteristics. We showed that after activation a path dependency of the resistance between charge and discharge can be observed, and that a very high resistance occurs especially at low SOCs. By a careful variation of the upper cutoff potential, we could find that an increase of the upper cutoff potential leads to an increasing discharge resistance which, however, was found to be fully reversible upon complete discharge to 2.0 V. Based on prior work from Kleiner et al.[78] and Gent et al.,[77] we suggest that this hysteresis in the resistance is closely linked to structural bulk phenomena, such as reversible transition metal migration and reversible oxygen redox participation.

Furthermore, the detailed quantification of the oxygen released during the first cycles shown by Strehle et al.[73] suggested the formation of a disordered surface layer that might explain the high impedance at low SOCs. We could prove this hypothesis by the second study carried out in this thesis, namely by a comprehensive analysis of the oxygen release and the occurrence of disordered surface phases in dependence of the Li_2MnO_3 content of Li- and Mn-rich NCMs. Hereby, we quantified the amount of oxygen released during the first two cycles and calculated the theoretical thickness and mole fraction of a spinel-type surface layer caused by oxygen release, as suggested by Strehle et al.[73] The mole fraction of the spinel-type layer was in good agreement with the quantification derived from electrochemical analysis of the capacities in dQ/dV plots. Furthermore, the calculated layer thickness from the OEMS measurements was in very good agreement with HRTEM measurements carried

out for the materials after cycling. The only exception was the material with a very high Li_2MnO_3 content, which showed also a spinel phase in the bulk of the material, while for lower Li_2MnO_3 contents spinel formation was exclusively limited to the surface of the active material particles. However, we could not observe a clear correlation between voltage-fading and oxygen release that has been suggested in the literature.[62] Based on this detailed analysis of the base materials, we focused onto a Li- and Mn-rich NCM with a limited Li_2MnO_3 content of 0.33. While the half-cell cycling of this material shows a rather stable performance, the full-cell performance is very limited and typically leads to a lifetime of <100 cycles in a realistic full-cell setup with standard electrolytes.

Therefore, as a next step, we aimed to better understand the degradation mechanisms in realistic full-cells with Li- and Mn-rich layered oxides. For this, we investigated the differences of EC- and FEC-based electrolytes. It has been reported by the research group of Jeff Dahn that EC-free electrolytes show improved performance with stochiometric NCM materials when cycled to potentials >4.4V, even though the reason for this remained unclear.[91] Also with Li- and Mn-rich NCMs, rapid performance fading can be observed when cycled in EC-based electrolytes, while FEC-based electrolytes show a strong improvement in the lifetime. By OEMS analysis we could show that FEC offers no advantage with respect to the anodic stability compared to EC, so that the improvement in cycling stability by FEC cannot be ascribed to improvements in anodic stability. However, when the majority of the oxygen released during the first activation cycle is removed from the cell by replacing the electrolyte, the lifetime of EC- and FEC-based electrolytes becomes very similar, which suggests that EC-containing electrolytes are not compatible with oxygen releasing cathode active materials. We could prove this with NCM 622 full-cells containing EC-based electrolytes, in which case exceeding the onset potentials for oxygen evolution leads to a rapid cell failure, contrary to what is observed for FEC-based, EC-free electrolytes. As Li- and Mn-rich NCMs always have an oxygen release during the first-cycle activation, replacement of EC by FEC is suitable to strongly improve the lifetime of such full-cells. However, for high amounts of FEC within an $LiPF_6$ containing electrolyte, FEC shows a certain thermal instability, which was part of a further study in this thesis. We could show that FEC and $LiPF_6$ react at elevated temperature and form VC and HF, both of which cause unwanted side reactions within full-cells. On the one hand, HF formation leads to increased

impedances on the anode and the cathode side; on the other hand, HF causes increased Mn-dissolution which is known to alter the full-cell performance.[53, 81, 84] The VC formed upon FEC decomposition can be continuously reduced on the graphite anode, leading to an increased anode resistance and can also be oxidized at voltages >4.3 V vs. Li^+/Li,[52] leading not only to an impedance build-up on the cathode, but also causes strong gassing in large-format cells. From these studies, we could clearly show that FEC is very advantageous for the full-cell performance of Li- and Mn-rich layered oxides if compared to EC. However, we suggest that FEC as co-solvent also has some serious drawbacks during high-temperature operation. Thus, there are two options to enable the application of Li- and Mn-rich NCMs, namely the development of new cyclic carbonate solvents or mitigating lattice oxygen release from these materials, so that EC-based standard electrolytes can be used.

The last part of this thesis shows a potential strategy how oxygen release from layered oxides can be mitigated by washing Ni-rich NCM materials in an aqueous solution. From washing NCM 851005 in argon atmosphere and monitoring pH as well as the LiOH concentrations, we suggest a Li/H^+ exchange during aqueous washing, forming a surface phase that decomposes during a consecutive drying step. TGA-MS analysis suggested spinel or rocksalt formation, depending on the drying temperature. OEMS measurements of the washed materials showed that lattice oxygen release can be mitigated by washing and drying of Ni-rich NCM materials. However, the spinel and rocksalt formation after washing did not only lead to a stabilization of the surface, but also to a drastic impedance increase and a decreased cycle performance of the washed materials. Therefore, while washing is a very promising concept that can help to mitigate oxygen release, the washing conditions from this study need certainly to be optimized. These results are not only important for Ni-rich NCM materials, but also are a promising approach of how the oxygen release in Li- and Mn-rich NCM cathodes can be prevented, which should allow to mitigate its poor full-cell performance caused by lattice oxygen release. Therefore, this thesis gives a clear understanding about the cathode active material and cell performance issues that are observed for Li- and Mn-rich NCMs and shows a promising path towards a future material design to overcome these issues. Thus, the results and the concepts shown in this thesis can help to commercialize Li- and Mn-rich NCMs as cost-effective cathode active materials for lithium-ion batteries.

List of figures

References

1. D. Strohl, *HemmingsDaily*, "Henry Ford and the electric car" (2010) http://blog.hemmings.com/index.php/2010/05/25/henry-ford-and-the-electric-car/ (accessed: 04.05.2019).
2. M. M. Thackeray, C. Wolverton, and E. D. Isaacs, *Energy Environ: Sci:*, **5** (7), 7854 (2012).
3. B. Dunn, H. Kamath, and J.-M. Tarascon, *Science*, **334** (6058), 928-935 (2011).
4. M. S. Whittingham, *Science*, **192** (4244), 1126-1127 (1976).
5. J. B. Goodenough and K. S. Park, *J. Am. Chem. Soc.*, **135** (4), 1167-1176 (2013).
6. M. S. Whittingham, *J. Electrochem. Soc.*, **123** (3), 315-320 (1976).
7. K. Mizushima, P. Jones, P. Wiseman, and J. B. Goodenough, *Mater. Res. Bull.*, **15** (6), 783-789 (1980).
8. G. E. Blomgren, *J. Electrochem. Soc.*, **164** (1), A5019-A5025 (2016).
9. C. Julien, A. Mauger, A. Vijh, and K. Zaghib, *Lithium Batteries*, pp 29-68, Springer, (2016).
10. Y. Nishi, *Electrochem. Soc. Interface*, **25** (3), 71-74 (2016).
11. R. Fong, U. von Sacken, and J. R. Dahn, *J. Electrochem. Soc.*, **137** (7), 2009-2013 (1990).
12. Y. Nishi, H. Azuma, and A. Omaru, "Non-aqueous electrolyte cell", U.S. Pat., 4, 959, 281, 25 Sept. (1990).
13. Y. Nishi, *J. Power Sources*, **100**, 101-106 (2001).
14. D. Andre, S.-J. Kim, P. Lamp, S. F. Lux, F. Maglia, O. Paschos, and B. Stiaszny, *J. Mater. Chem. A*, **3** (13), 6709-6732 (2015).
15. D. Larcher and J. M. Tarascon, *Nat. Chem.*, **7** (1), 19-29 (2015).

16. International Energy Agency, "World Energy Outlook 2017", (2017), https://webstore.iea.org/download/summary/196?fileName=German-WEO-2017-ES.pdf, (accessed 04.05.2019).

17. VTO, U.S. Departement of Energy Vehicle Technologies Office, "FY 2014 Annual Progress Report - Energy Storage R&D" (2015), www.energy.gov/sites/prod/files/2015/04/f21/FY2014_APR_Energy_Storage_R%26D_FINAL_Part1_of_3.pdf, (accessed 15.05.2019).

18. Tesla Motors, Tesla Model 3 technical data, https://www.tesla.com/de_DE/model3, (accessed 04.05.2019).

19. BMW Group, BMW i3 technical data, https://www.bmw.de/de/neufahrzeuge/bmw-i/i3/2017/auf-einen-blick.html, (accessed 04.05.2019).

20. B. Nykvist and M. Nilsson, *Nat. Clim. Change*, **5** (4), 329-332 (2015).

21. O. Gröger, H. A. Gasteiger, and J.-P. Suchsland, *J. Electrochem. Soc.*, **162** (14), A2605-A2622 (2015).

22. London metal exchange, nickel, cobalt, iron and aluminum prices, https://www.lme.com/, (accessed 26.04.2019).

23. C. Banza Lubaba Nkulu, L. Casas, V. Haufroid, T. De Putter, N. D. Saenen, T. Kayembe-Kitenge, P. Musa Obadia, D. Kyanika Wa Mukoma, J.-M. Lunda Ilunga, T. S. Nawrot, O. Luboya Numbi, E. Smolders, and B. Nemery, *Nat. Sustain.*, **1** (9), 495-504 (2018).

24. A. Manthiram, J. C. Knight, S.-T. Myung, S.-M. Oh, and Y.-K. Sun, *Adv. Energy Mater.*, **6** (1), 1501010 (2016).

25. S.-M. Bak, K.-W. Nam, W. Chang, X. Yu, E. Hu, S. Hwang, E. A. Stach, K.-B. Kim, K. Y. Chung, and X.-Q. Yang, *Chem. Mater.*, **25** (3), 337-351 (2013).

26. S. M. Bak, E. Hu, Y. Zhou, X. Yu, S. D. Senanayake, S. J. Cho, K. B. Kim, K. Y. Chung, X. Q. Yang, and K. W. Nam, *ACS Appl. Mater. Interfaces*, **6** (24), 22594-22601 (2014).

27. J. Zheng, S. Myeong, W. Cho, P. Yan, J. Xiao, C. Wang, J. Cho, and J.-G. Zhang, *Adv. Energy Mater.*, **7** (6), 1601284 (2017).

28. K Xu, *Chem. Rev.*, **104**, 4303-4417 (20014).

29. M. Metzger, B. Strehle, S. Solchenbach, and H. A. Gasteiger, *J. Electrochem. Soc.*, **163** (5), A798-A809 (2016).

30. E. Peled, *J. Electrochem. Soc.*, **126** (12), 2047-2051 (1979).

31. E. Peled and S. Menkin, *J. Electrochem. Soc.*, **164** (7), A1703-A1719 (2017).

32. D. Aurbach, K. Gamolsky, B. Markovsky, Y. Gofer, M. Schmidt, and U. Heider, *Electrochim. Acta*, **47** (9), 1423-1439 (2002).

33. F. A. Soto, Y. Ma, J. M. Martinez de la Hoz, J. M. Seminario, and P. B. Balbuena, *Chem. Mater.*, **27** (23), 7990-8000 (2015).

34. K. J. Nelson, G. L. d'Eon, A. T. B. Wright, L. Ma, J. Xia, and J. R. Dahn, *J. Electrochem. Soc.*, **162** (6), A1046-A1054 (2015).

35. R. Jung, M. Metzger, D. Haering, S. Solchenbach, C. Marino, N. Tsiouvaras, C. Stinner, and H. A. Gasteiger, *J. Electrochem. Soc.*, **163** (8), A1705-A1716 (2016).

36. Q. Liu, C. Du, B. Shen, P. Zuo, X. Cheng, Y. Ma, G. Yin, and Y. Gao, *RSC Adv.*, **6** (91), 88683-88700 (2016).

37. J. Wandt, P. Jakes, J. Granwehr, R.-A. Eichel, and H. A. Gasteiger, *Mater. Today*, **21** (3), 231-240 (2018).

38. B. Zhao, R. Ran, M. Liu, and Z. Shao, *Mater. Sci. Eng. R Rep.*, **98**, 1-71 (2015).

39. H. G. Jung, M. W. Jang, J. Hassoun, Y. K. Sun, and B. Scrosati, *Nat. Commun.*, **2**, 516 (2011).

40. R. Bernhard, S. Meini, and H. A. Gasteiger, *J. Electrochem. Soc.*, **161** (4), A497-A505 (2014).

41. R. Bernhard, M. Metzger, and H. A. Gasteiger, *J. Electrochem. Soc.*, **162** (10), A1984-A1989 (2015).

42. M. T. McDowell, S. W. Lee, W. D. Nix, and Y. Cui, *Adv. Mater.*, **25** (36), 4966-4985 (2013).

43. For manganese price see, https://price.metal.com, (accessed 26.04.2019).

44. For nickel, cobalt and manganese prices see, https://www.metalary.com/, (accessed 26.04.2019).

45. D. Liu, W. Zhu, C. Kim, M. Cho, A. Guerfi, S. A. Delp, J. L. Allen, T. R. Jow, and K. Zaghib, *J. Power Sources*, **388**, 52-56 (2018).

46. A. Freiberg, M. Metzger, D. Haering, S. Bretzke, S. Puravankara, T. Nilges, C. Stinner, C. Marino, and H. A. Gasteiger, *J. Electrochem. Soc.*, **161** (14), A2255-A2261 (2014).

47. A. K. Padhi, K. S. Nanjundaswamy, and J. B. Goodenough, *J. Electrochem. Soc.*, **144** (4), 1188-1194 (1997).

48. M. M. Thackeray, *Prog. Solid State Chem.*, **25**, 1-71 (1997).

49. P. G. Bruce, A. R. Armstrong, and L. Gitzendanner, *J. Mater. Chem.*, **9**, 193-198 (1998).

50. K. Amine, H. Tukamoto, H. Yasuda, and Y. Fujita, *J. Electrochem. Soc.*, **143** (5), 1607-1613 (1996).

51. A. Manthiram, K. Chemelewski, and E.-S. Lee, *Energy Environ. Sci.*, **7** (4), (2014).

52. D. Pritzl, S. Solchenbach, M. Wetjen, and H. A. Gasteiger, *J. Electrochem. Soc.*, **164** (12), A2625-A2635 (2017).

53. S. Solchenbach, G. Hong, A. T. S. Freiberg, R. Jung, and H. A. Gasteiger, *J. Electrochem. Soc.*, **165** (14), A3304-A3312 (2018).

54. I. Belharouak, Y. K. Sun, J. Liu, and K. Amine, *J. Power Sources*, **123** (2), 247-252 (2003).

55. R. Jung, M. Metzger, F. Maglia, C. Stinner, and H. A. Gasteiger, *J. Electrochem. Soc.*, **164** (7), A1361-A1377 (2017).

56. J. Kim, H. Lee, H. Cha, M. Yoon, M. Park, and J. Cho, *Adv. Energy Mater.,* **8** (6), (2018).

57. H. Li, M. Cormier, N. Zhang, J. Inglis, J. Li, and J. R. Dahn, *J. Electrochem. Soc.*, **166** (4), A429-A439 (2019).

58. M. M. Thackeray, S.-H. Kang, C. S. Johnson, J. T. Vaughey, R. Benedek, and S. A. Hackney, *J. Mater. Chem.,* **17** (30), 3112 (2007).

59. C. S. Johnson, J. S. Kim, C. Lefief, N. Li, J. T. Vaughey, and M. M. Thackeray, *Electrochem. Commun.,* **6** (10), 1085-1091 (2004).

60. T. Teufl, B. Strehle, P. Müller, H. A. Gasteiger, and M. A. Mendez, *J. Electrochem. Soc.*, **165** (11), A2718-A2731 (2018).

61. J. R. Croy, K. G. Gallagher, M. Balasubramanian, B. R. Long, and M. M. Thackeray, *J. Electrochem. Soc.*, **161** (3), A318-A325 (2014).

62. J. R. Croy, M. Balasubramanian, K. G. Gallagher, and A. K. Burrell, *Acc. Chem. Res.*, **48** (11), 2813-2821 (2015).

63. L. de Biasi, A. O. Kondrakov, H. Geßwein, T. Brezesinski, P. Hartmann, and J. Janek, *J. Phys. Chem. C*, **121** (47), 26163-26171 (2017).

64. D. Streich, C. Erk, A. Guéguen, P. Müller, F.-F. Chesneau, and E. J. Berg, *J. Phys. Chem. C*, **121** (25), 13481-13486 (2017).

65. R. Jung, R. Morasch, P. Karayaylali, K. Phillips, F. Maglia, C. Stinner, Y. Shao-Horn, and H. A. Gasteiger, *J. Electrochem. Soc.* **165** (2), A132-A141 (2018).

66. N. V. Faenza, L. Bruce, Z. W. Lebens-Higgins, I. Plitz, N. Pereira, L. F. J. Piper, and G. G. Amatucci, *J. Electrochem. Soc.,* **164** (14), A3727-A3741 (2017).

67. I. A. Shkrob, J. A. Gilbert, P. J. Phillips, R. Klie, R. T. Haasch, J. Bareño, and D. P. Abraham, *J. Electrochem. Soc.,* **164** (7), A1489-A1498 (2017).

68. R. Jung, P. Strobl, F. Maglia, C. Stinner, and H. A. Gasteiger, *J. Electrochem. Soc.*, **165** (11), A2869-A2879 (2018).

69. R. Jung, M. Metzger, F. Maglia, C. Stinner, and H. A. Gasteiger, *J. Phys. Chem. Lett.*, **8** (19), 4820-4825 (2017).

70. J. R. Croy, K. G. Gallagher, M. Balasubramanian, Z. Chen, Y. Ren, D. Kim, S.-H. Kang, D. W. Dees, and M. M. Thackeray, *J. Phys. Chem. C*, **117** (13), 6525-6536 (2013).

71. M. Sathiya, A. M. Abakumov, D. Foix, G. Rousse, K. Ramesha, M. Saubanere, M. L. Doublet, H. Vezin, C. P. Laisa, A. S. Prakash, D. Gonbeau, G. VanTendeloo, and J. M. Tarascon, *Nat. Mater.*, **14** (2), 230-238 (2015).

72. P. Rozier and J. M. Tarascon, *J. Electrochem. Soc.*, **162** (14), A2490-A2499 (2015).

73. B. Strehle, K. Kleiner, R. Jung, F. Chesneau, M. Mendez, H. A. Gasteiger, and M. Piana, *J. Electrochem. Soc.*, **164** (2), A400-A406 (2017).

74. A. R. Armstrong, M. Holzapfel, P. Novák, C. S. Johnson, S.-H. Kang, M. M. Thackeray, and P. G. Bruce, *J. Am. Chem. Soc.*, **128** (26), 8694-8698 (2006).

75. K. Luo, M. R. Roberts, R. Hao, N. Guerrini, D. M. Pickup, Y.-S. Liu, K. Edström, J. Guo, A. V. Chadwick, L. C. Duda, and P. G. Bruce, *Nat. Chem.*, **8**, 684 (2016).

76. S. Solchenbach, M. Wetjen, D. Pritzl, K. U. Schwenke, and H. A. Gasteiger, *J. Electrochem. Soc.*, **165** (3), A512-A524 (2018).

77. W. E. Gent, K. Lim, Y. Liang, Q. Li, T. Barnes, S.-J. Ahn, K. H. Stone, M. McIntire, J. Hong, J. H. Song, Y. Li, A. Mehta, S. Ermon, T. Tyliszczak, D. Kilcoyne, D. Vine, J.-H. Park, S.-K. Doo, M. F. Toney, W. Yang, D. Prendergast, and W. C. Chueh, *Nat. Commun.*, **8** (1), 2091 (2017).

78. K. Kleiner, B. Strehle, A. R. Baker, S. J. Day, C. C. Tang, I. Buchberger, F.-F. Chesneau, H. A. Gasteiger, and M. Piana, *Chem. Mater.* **30** (11), 3656 (2018).

79. S. E. Renfrew and B. D. McCloskey, *J. Am. Chem. Soc.*, **139** (49), 17853-17860 (2017).

80. Y. Yu, P. Karayaylali, Y. Katayama, L. Giordano, M. Gauthier, F. Maglia, R. Jung, I. Lund, and Y. Shao-Horn, *J. Phys. Chem. C*, **122** (48), 27368-27382 (2018).

81. R. Jung, F. Linsenmann, R. Thomas, J. Wandt, S. Solchenbach, F. Maglia, C. Stinner, M. Tromp, and H. A. Gasteiger, *J. Electrochem. Soc.*, **166** (2), A378-A389 (2019).

82. S. Solchenbach, M. Metzger, M. Egawa, H. Beyer, and H. A. Gasteiger, *J. Electrochem. Soc.*, **165** (13), A3022-A3028 (2018).

83. A. Guéguen, D. Streich, M. He, M. Mendez, F. F. Chesneau, P. Novák, and E. J. Berg, *J. Electrochem. Soc.*, **163** (6), A1095-A1100 (2016).

84. J. A. Gilbert, I. A. Shkrob, and D. P. Abraham, *J. Electrochem. Soc.*, **164** (2), A389-A399 (2017).

85. A. T. S. Freiberg, M. K. Roos, J. Wandt, R. de Vivie-Riedle, and H. A. Gasteiger, *J. Phys. Chem. A*, **122** (45), 8828-8839 (2018).

86. J. Sicklinger, M. Metzger, H. Beyer, D. Pritzl, and H. A. Gasteiger, *manuscript accepted*.

87. J. Xia, M. Nie, J. C. Burns, A. Xiao, W. M. Lamanna, and J. R. Dahn, *J. Power Sources*, **307**, 340-350 (2016).

88. J. Xia, K. J. Nelson, Z. Lu, and J. R. Dahn, *J. Power Sources*, **329** 387-397 (2016).

89. J. Xia, R. Petibon, D. Xiong, L. Ma, and J. R. Dahn, *J. Power Sources*, **328** 124-135 (2016).

90. R. Petibon, J. Xia, L. Ma, M. K. G. Bauer, K. J. Nelson, and J. R. Dahn, *J. Electrochem. Soc.*, **163** (13), A2571-A2578 (2016).

91. L. Ma, S. L. Glazier, R. Petibon, J. Xia, J. M. Peters, Q. Liu, J. Allen, R. N. C. Doig, and J. R. Dahn, *J. Electrochem. Soc.*, **164** (1), A5008-A5018 (2016).

92. K. Xu, *Chem. Rev.*, **114** (23), 11503-11618 (2014).

93. L. Hu, Z. Zhang, and K. Amine, *Electrochem. Commun.*, **35**, 76-79 (2013).

94. L. Hu, Z. Xue, K. Amine, and Z. Zhang, *J. Electrochem. Soc.*, **161** (12), A1777-A1781 (2014).

95. E. Markevich, G. Salitra, K. Fridman, R. Sharabi, G. Gershinsky, A. Garsuch, G. Semrau, M. A. Schmidt, and D. Aurbach, *Langmuir*, **30** (25), 7414-7424 (2014).

96. B. Aktekin, R. Younesi, W. Zipprich, C. Tengstedt, D. Brandell, and K. Edström, *J. Electrochem. Soc.*, **164** (4), A942-A948 (2017).

97. M. Metzger, B. Strehle, S. Solchenbach, and H. A. Gasteiger, *J. Electrochem. Soc.*, **163** (7), A1219-A1225 (2016).

98. K. Kim, I. Park, S.-Y. Ha, Y. Kim, M.-H. Woo, M.-H. Jeong, W. C. Shin, M. Ue, S. Y. Hong, and N.-S. Choi, *Electrochim. Acta*, **225**, 358-368 (2017).

99. Q. Wang, B. Jiang, B. Li, and Y. Yan, *Renew. Sust. Energ. Rev.*, **64** 106-128 (2016).

100. Dutch-Belgium Tesla Forum, public tesla user data, https://docs.google.com/spreadsheets/d/t024bMoRiDPIDialGnuKPsg/edit#gid=826479810, (accessed 04.05.2019).

101. F. Lambert, *electrek*, "Tesla battery degradation at less than 10% after over 160,000 miles, according to latest data", https://electrek.co/2018/04/14/tesla-battery-degradation-data/, (accessed 04.05.2019).

102. F. T. Wagner, B. Lakshmanan, and M. F. Mathias, *J. Phys. Chem. Lett.*, **1** (14), 2204-2219 (2010).

103. M. Sanders, *Avicenne Energy*, "Lithium ion battery raw material supply and demand 2016-2025", aabc conference, 2017 (June 19th 2017), San Francisco, CA, USA.

104. Y. Ding, Z. P. Cano, A. Yu, J. Lu, and Z. Chen, *Electrochem. Energ. Rev.*, **2** (1), 1-28 (2019).

105. S. Solchenbach, D. Pritzl, E. J. Y. Kong, J. Landesfeind, and H. A. Gasteiger, *J. Electrochem. Soc.*, **163** (10), A2265-A2272 (2016).

106. C. P. Aiken, J. Xia, D. Y. Wang, D. A. Stevens, S. Trussler, and J. R. Dahn, *J. Electrochem. Soc.*, **161** (10), A1548-A1554 (2014).

107. H. G. Schweiger, O. Obeidi, O. Komesker, A. Raschke, M. Schiemann, C. Zehner, M. Gehnen, M. Keller, and P. Birke, *Sensors,* **10** (6), 5604-5625 (2010).

108. H. A. Gasteiger, *Lecture*, "Electrochemistry for Energy Materials", Chemistry Departement, Technical University of Munich (2017).

109. A. Lasia "Electrochemical Impedance Spectroscopy and its Applications", *Springer* (2014).

110. N. Tsiouvaras, S. Meini, I. Buchberger, and H. A. Gasteiger, *J. Electrochem. Soc.*, **160** (3), A471-A477 (2013).

111. B. D. McCloskey, D. S. Bethune, R. M. Shelby, G. Girishkumar, and A. C. Luntz, *J. Phys. Chem. Lett.,* **2** (10), 1161-1166 (2011).

112. R. Imhof and P. Novák, *J. Electrochem. Soc.,* **145** (4), 1081-1087 (1998).

113. S. Meini, M. Piana, N. Tsiouvaras, A. Garsuch, and H. A. Gasteiger, *Electrochem. Solid-State Lett.*, **15** (4), A45 (2012).

114. S. Meini, S. Solchenbach, M. Piana, and H. A. Gasteiger, *J. Electrochem. Soc.,* **161** (9), A1306-A1314 (2014).

115. M. Metzger, *PhD thesis*, "Studies on Fundamental Materials Degradation Mechnisms in Lithium-ion Batteries via On-line Electrochemical Mass Spectrometry" (2017).

116. M. Metzger, C. Marino, J. Sicklinger, D. Haering, and H. A. Gasteiger, *J. Electrochem. Soc.,* **162** (7), A1123-A1134 (2015).

117. M. Metzger, J. Sicklinger, D. Haering, C. Kavakli, C. Stinner, C. Marino, and H. A. Gasteiger, *J. Electrochem. Soc.*, **162** (7), A1227-A1235 (2015).

118. B. Strehle, S. Solchenbach, M. Metzger, K. U. Schwenke, and H. A. Gasteiger, *J. Electrochem. Soc.*, **164** (12), A2513-A2526 (2017).

119. C. Genevois, H. Koga, L. Croguennec, M. Ménétrier, C. Delmas, and F. Weill, *J. Phys. Chem. C,* **119** (1), 75-83 (2014).

120. H. Koga, L. Croguennec, M. Ménétrier, P. Mannessiez, F. Weill, and C. Delmas, *J. Power Sources*, **236**, 250-258 (2013).

121. N. Yabuuchi, K. Yoshii, S. T. Myung, I. Nakai, and S. Komaba, *J. Am. Chem. Soc.*, **133** (12), 4404-4419 (2011).

122. D. Mohanty, J. Li, S. C. Nagpure, D. L. Wood, and C. Daniel, *MRS Energy & Sustainability*, **2**, (2015).

123. T. Teufl, D. Pritzl, S. Solchenbach, H. A. Gasteiger, and M. Mendez, *J. Electrochem. Soc.*, **166** (6), A1275-A1284 (2019)..

124. M. M. Thackeray, S. H. Kang, C. S. Johnson, J. T. Vaughey, and S. A. Hackney, *Electrochem. Commun.*, **8** (9), 1531-1538 (2006).

125. G. Assat, C. Delacourt, D. A. D. Corte, and J.-M. Tarascon, *J. Electrochem. Soc.*, **163** (14), A2965-A2976 (2016).

126. S. R. Gowda, D. W. Dees, A. N. Jansen, and K. G. Gallagher, *J. Electrochem. Soc.*, **162** (7), A1374-A1381 (2015).

127. M. Wang, M. Luo, Y. Chen, Y. Su, L. Chen, and R. Zhang, *J. Alloy. Compd.*, **696**, 907-913 (2017).

128. H. Yu, Y. Wang, D. Asakura, E. Hosono, T. Zhang, and H. Zhou, *RSC Adv.*, **2** (23), 8797-8807 (2012).

129. J. Zheng, W. Shi, M. Gu, J. Xiao, P. Zuo, C. Wang, and J. G. Zhang, *J. Electrochem. Soc.*, **160** (11), A2212-A2219 (2013).

130. W. Mao, G. Ai, Y. Dai, Y. Fu, X. Song, H. Lopez, and V. Battaglia, *J. Electrochem. Soc.*, **163** (14), A3091-A3098 (2016).

131. P. Lanz, H. Sommer, M. Schulz-Dobrick, and P. Novák, *Electrochim. Acta*, **93**, 114-119 (2013).

132. F. La Mantia, F. Rosciano, N. Tran, and P. Novák, *J. Appl. Electrochem.*, **38** (7), 893-896 (2008).

133. Z. Lu and J. R. Dahn, *J. Electrochem. Soc.*, **149** (7), A815-A822 (2002).

134. Z. Lu, L. Y. Beaulieu, R. A. Donaberger, C. L. Thomas, and J. R. Dahn, *J. Electrochem. Soc.*, **149** (6), A778-A791 (2002).

135. K. Xu, *Chem. Rev.*, **114**, 11503-11618 (2014).

136. T. Teufl, D. Pritzl, S. Solchenbach, M. Mendez, and H. A. Gasteiger, *manuscript in preparation.*

137. T. Teufl, D. Pritzl, P. Krieg, A. T. S. Freiberg, B. Strehle, S. Solchenbach, M. Mendez, and H. A. Gasteiger, *manuscript in preparation*.

138. D. Streich, A. Guéguen, M. Mendez, F. Chesneau, P. Novák, and E. J. Berg, *J. Electrochem. Soc.*, **163** (6), A964-A970 (2016).

139. S. Arimoto, K. Tsuruta, R. LeBlanc, and R. Melsert, "Drying procedure in manufacturing process for cathode material", U.S. Pat. 0294652 A1, 12 Oct. (1990).

140. J. Kim, Y. Hong, K. S. Ryu, M. G. Kim, and J. Cho, *Electrochem. Solid State Lett.*, **9**, A19-A23 (2006).

141. X. Xiong, Z. Wang, P. Yue, H. Guo, F. Wu, J. Wang, and X. Li, *J. Power Sources*, **222**, 318-325 (2013).

142. Y. Kim, *J. Solid State Electrochem.*, **17** (7), 1961-1965 (2013).

Acknowledgement

First of all, I want to thank my supervisor **Prof. Dr. Hubert A. Gasteiger** for his outstanding support, his enthusiasm and his invaluable guidance during the last years. I am infinitely grateful about all the things that you taught me about electrochemistry and all your knowledge and your experience that you shared with me. It is really outstanding and exceptional how much time and energy you share with us and how you teach us to become passionate and honest researchers. I am really grateful for all the discussions that we had during the last years, it was a fascinating time that I certainly do not want to miss. Thank you!

I also want to thank **Manuel Mendez**, who was my supervisor at BASF, for his great support during the course of my PhD. I am very grateful that I had you as my supervisor. With your great knowledge and your analytical way of thinking you always helped me out. Having such a great scientific support as you at BASF was invaluable during this PhD project and it was always a lot of fun working together with you.

Furthermore, I want to thank **Veronika Pichler** for all the help with the administrative work, for always being in a good mood and all the non-scientific discussions. Your friendliness and frankness are always an enrichment.

I especially want to thank my close friend **Daniel Pritzl** who was my counterpart at TUM. Thanks for the close and successful collaboration during the last years, it was always a pleasure for me to work together with you, during our PhD, as well as during our studies. Furthermore, I want to thank the whole team at TUM, especially I want to thank **Benjamin Strehle**, **Michael Metzger** and **Sophie Solchenbach** for their support with the OEMS setup and all the scientific discussions that we had during the last years. I also have to acknowledge **Michele Piana**, **Karin Kleiner,** **Johannes Landesfeind**, **Roland Jung**, **Johannes**

Sicklinger and **Morten Wetjen** for all the scientific and non-scientific discussions that we had. My starting point into electrochemistry was my master's thesis for which **Jörg Schuster** was a great supervisor, I also want to thank **Johannes Hattendorf** for his support during my master's thesis.

I want to gratefully acknowledge my colleagues from BASF, especially I want to thank **Stefano Meini**, **Jordan Lampert**, **Benjamin Bergner**, **Jörn Kullisch**, **Frederick Chesneau**, **Heino Sommer** and **Johannes Hoecker** for their support. I also want to acknowledge the technicians **Patrick Krieg**, **Lucas Montag**, **Denis Schröder**, **Jürgen Jäger**, **Wolfgang Klaus** and **Diana Fürst** for all the support in the lab and the great working atmosphere.

I also had the great pleasure to stay abroad in the USA at Stanford University. Therefore, I especially want to thank **Prof. Dr. William Chueh** for having me and being a great host. I also want to thank **Peter Csernica**, **Kipil Lim** and **William Gent**, who made this stay unforgettable.

A very special thanks goes to my family who supported me during my whole life and made all of this possible. I want to thank my parents, my grandparents and my brother for their never-ending support.